



Universidade Federal da Bahia  
Instituto de Matemática

Programa de Pós-Graduação em Ciência da Computação

**EFFICIENT SHADOW ANTI-ALIASING  
TECHNIQUES USING SILHOUETTE  
REVECTORIZATION**

Márcio Cerqueira de Farias Macedo

TESE DE DOUTORADO

Salvador  
28 de Maio de 2018



MÁRCIO CERQUEIRA DE FARIAS MACEDO

**EFFICIENT SHADOW ANTI-ALIASING TECHNIQUES USING  
SILHOUETTE REVECTORIZATION**

Esta Tese de Doutorado foi apresentada ao Programa de Pós-Graduação em Ciência da Computação da Universidade Federal da Bahia, como requisito parcial para obtenção do grau de Doutor em Ciência da Computação.

Orientador: Prof. Dr. Antônio Lopes Apolinário Júnior

Salvador  
28 de Maio de 2018

Ficha catalográfica elaborada pelo Sistema Universitário de Bibliotecas (SIBI/UFBA), com os dados fornecidos pelo(a) autor(a).

Macedo, Márcio Cerqueira de Farias  
Efficient Shadow Anti-Aliasing Techniques using Silhouette  
Revectorization / Márcio Cerqueira de Farias Macedo. --  
Salvador, 2018.

159 f. : il

Orientador: Antônio Lopes Apolinário Jr..  
Tese (Doutorado - Programa de Pós-Graduação em Ciência da  
Computação) -- Universidade Federal da Bahia, Instituto de  
Matemática, 2018.

1. Cálculo de Sombras. 2. Renderização em Tempo Real. 3.  
Computação Gráfica. I. Apolinário Jr., Antônio Lopes. II. Título.

## **TERMO DE APROVAÇÃO**

**MÁRCIO CERQUEIRA DE FARIAS MACEDO**

### **EFFICIENT SHADOW ANTI-ALIASING TECHNIQUES USING SILHOUETTE REVECTORIZATION**

Esta Tese de Doutorado foi julgada adequada à obtenção do título de Doutor em Ciência da Computação e aprovada em sua forma final pelo Programa de Pós-Graduação em Ciência da Computação da Universidade Federal da Bahia.

Salvador, 28 de Maio de 2018

---

Prof. Dr. Antônio Lopes Apolinário Júnior  
Universidade Federal da Bahia

---

Prof. Dr. Karl Philips Apaza Aguero  
Universidade Federal da Bahia

---

Prof. Dr. Vinicius Moreira Mello  
Universidade Federal da Bahia

---

Prof. Dr. Esteban Walter Gonzalez Clua  
Universidade Federal Fluminense

---

Prof. Dr. Ricardo Guerra Marroquim  
Universidade Federal do Rio de Janeiro



## ACKNOWLEDGEMENTS

Here, I would like to express my gratitude to everyone who has directly supported me during my Ph.D. studies.

First, I would like to thank my advisor Prof. Dr. Antônio Lopes Apolinário Júnior for his enthusiasm, guidance and patience throughout my time at the Federal University of Bahia, supporting my ideas and providing insightful suggestions that greatly helped me in these last years.

Next, I owe a special thanks to Prof. Dr. Karl Apaza Agüero for being a reviewer of some papers related to this project, sharing his opinions with respect to the work being developed. Also, I wish to express my gratitude to my former advisor and also good friend Prof. Dr. Antonio Carlos dos Santos Souza, for introducing me to the field of Computer Graphics and initiating my passion in all the aspects related to real-time rendering.

I am grateful to all my colleagues from the Computer Graphics Laboratory at the Federal University of Bahia and the Labrasoft at the Federal Institute of Bahia for their help and discussion. Special thanks go to Rafaela Souza Alcantara, always ready to exchange ideas about my work, and Almir Vinicius Teixeira, who helped me to implement a shadow algorithm in a well-known game engine.

I am thankful to Vladimir Bondarev for helping me to understand the theoretical principles of the shadow silhouette revectorization in the beginning of my Ph.D. work.

With respect to the financial support, I would like to thank Coordenação de Aperfeiçoamento de Pessoal do Nível Superior (CAPES) for the scholarship program. Furthermore, I would like to thank the NVIDIA Corporation, who provided the hardware used in the experimental setup through the GPU Education Center Program.

Finally, I would like to dedicate this work to my friends and my family. In special, I would like to thank my mother Vilma for the good advices that help me to keep the focus to achieve my goals. Next, I would like to thank my grandmother Lucidalva and my father Edson for always estimulating me to study. I would like to thank my brother Danilo, for sharing the fun times with me during these last years. Last, but not least, I would like to thank my girlfriend Verônica, for her love, support and patience with me and my long hours of study and dedication. Looking at me with her beautiful smile, she was always ready to share her optimistic view of the life with me, mainly when I got frustrated or confused about my work.

Thank you very much!



## RESUMO

A renderização em tempo real de sombras de alta qualidade é um problema desafiador na área de computação gráfica. A técnica de mapeamento de sombras é a mais adotada para resolver tal problema, porém ela introduz artefatos de serrilhamento ao longo da silhueta das sombras e não é capaz de simular o efeito de penumbra. As técnicas capazes de simular penumbra são computacionalmente muito custosas, provendo desempenho muito mais lento do que o necessário para o tempo real. Nesta tese, é apresentada a técnica de mapeamento de sombras baseada em revetorização, uma técnica que leva em consideração a resolução do ponto de vista da câmera e a forma da silhueta da sombra para prover anti-serrilhamento com um baixo custo adicional de processamento. Levando em consideração a melhoria na qualidade visual obtida com a técnica de revetorização de sombras, a função de visibilidade baseada em revetorização é estendida para a proposição de um conjunto de técnicas que proveem anti-serrilhamento de alta qualidade para sombras com ou sem penumbra. A transformada de distância Euclidiana também é integrada com a função de visibilidade baseada em revetorização para prover escalabilidade e desempenho em tempo real para a simulação de penumbra. Os resultados, avaliados em termos de qualidade visual e tempo de renderização, mostram que as técnicas propostas produzem menos artefatos visuais do que os trabalhos relacionados, enquanto mantém o desempenho em tempo real, principalmente para o cálculo de sombras sem penumbra.

**Palavras-chave:** Renderização, Tempo Real, Anti-Serrilhamento, Sombras, Revetorização, Transformada de Distância.



# ABSTRACT

Real-time rendering of high-quality shadows is a challenging problem in computer graphics. Shadow mapping is widely adopted for real-time shadow rendering, but introduces aliasing artifacts along the shadow silhouette and is not able to simulate the penumbra effect. Techniques that simulate penumbra are computationally expensive, providing performance far from real time. In this thesis, we present the revectorization-based shadow mapping, a technique that takes advantage of the camera-view resolution and the shadow silhouette shape to suppress shadow aliasing artifacts at little additional cost. Inspired by the superior visual quality obtained with the shadow silhouette revectorization, we extend the revectorization-based visibility function to propose a set of techniques that provide high-quality anti-aliasing for both shadow rendering and penumbra simulation. We further integrate the Euclidean distance transform into the revectorization-based visibility function to provide scalability and real-time performance for the penumbra simulation. The results, evaluated in terms of visual quality and rendering time, show that the proposed techniques produce less visual artifacts than related work, while keeping the real-time performance, mainly for the shadow rendering without the penumbra simulation.

**Keywords:** Rendering, Real Time, Anti-Aliasing, Shadows, Revectorization, Distance Transform.



# CONTENTS

<b>Chapter 1—Introduction</b>	1
1.1 Motivation . . . . .	1
1.2 Hypothesis . . . . .	6
1.3 Contributions . . . . .	6
1.4 Organization . . . . .	7
<b>Chapter 2—Background and State-of-the-Art Review</b>	9
2.1 Rendering Equation . . . . .	9
2.2 Shadow Rendering . . . . .	12
2.3 Hard Shadows . . . . .	16
2.3.1 Warping . . . . .	16
2.3.2 Partitioning . . . . .	17
2.3.3 Silhouette Recovery . . . . .	18
2.4 Filtered Hard Shadows . . . . .	20
2.5 Visually Plausible Soft Shadows . . . . .	22
2.5.1 Percentage-Closer Soft Shadows . . . . .	22
2.5.2 Back-Projection . . . . .	24
2.5.3 Pre-Filtering . . . . .	25
2.5.4 Screen-Space Filtering . . . . .	26
2.6 Accurate Soft Shadows . . . . .	27
2.7 Discussion . . . . .	29
2.8 Summary . . . . .	30
<b>Chapter 3—Revectorization-Based Shadow Mapping</b>	31
3.1 Revectorization-Based Conservative Shadow Silhouette Recovery . . . . .	32
3.1.1 Overview . . . . .	32
3.1.2 Shadow Silhouette Localization . . . . .	33
3.1.3 Shadow Silhouette Traversal . . . . .	35
3.1.4 Shadow Silhouette Normalization . . . . .	37
3.1.5 Hard Shadow Anti-Aliasing Visibility Function . . . . .	38
3.2 Revectorization-Based Non-Conservative Shadow Silhouette Recovery . . . . .	39
3.2.1 Overview . . . . .	40
3.2.2 Shadow Silhouette Localization . . . . .	40
3.2.3 Shadow Silhouette Traversal . . . . .	41
3.2.4 Shadow Silhouette Normalization . . . . .	42

3.2.5 Hard Shadow Anti-Aliasing Visibility Function . . . . .	43
3.3 Results and Discussion . . . . .	44
3.3.1 Experimental Setup . . . . .	44
3.3.2 Visual Quality Evaluation . . . . .	45
3.3.3 Rendering Time Evaluation . . . . .	53
3.3.4 Limitations . . . . .	55
3.4 Summary . . . . .	55
<b>Chapter 4—Revectorization-Based Filtered Shadow Mapping</b>	57
4.1 Revectorization-based Percentage-Closer Filtering . . . . .	57
4.1.1 Filtered Hard Shadow Anti-Aliasing Visibility Function . . . . .	58
4.1.2 Revectorization-Based Filtering . . . . .	59
4.2 Euclidean Distance Transform Shadow Mapping . . . . .	63
4.2.1 Overview . . . . .	63
4.2.2 Euclidean Distance Transform Shadowing . . . . .	63
4.2.3 Euclidean Distance Transform Filtering . . . . .	65
4.3 Results and Discussion . . . . .	66
4.3.1 Experimental Setup . . . . .	67
4.3.2 Visual Quality Evaluation . . . . .	67
4.3.3 Rendering Time Evaluation . . . . .	70
4.3.4 Limitations . . . . .	74
4.4 Summary . . . . .	75
<b>Chapter 5—Revectorization-Based Soft Shadow Mapping</b>	77
5.1 Variable-Size Penumbra Estimation . . . . .	77
5.2 Euclidean Distance Transform Soft Shadow Mapping . . . . .	78
5.3 Revectorization-Based Soft Shadow Mapping . . . . .	80
5.4 Screen-Space Revectorization-Based Soft Shadow Mapping . . . . .	82
5.5 Results and Discussion . . . . .	83
5.5.1 Experimental Setup . . . . .	83
5.5.2 Visual Quality Evaluation . . . . .	83
5.5.3 Rendering Time Evaluation . . . . .	87
5.5.4 Discussion . . . . .	88
5.5.5 Limitations . . . . .	90
5.6 Summary . . . . .	91
<b>Chapter 6—Revectorization-Based Accurate Soft Shadow Mapping</b>	93
6.1 Revectorization-Based Accurate Soft Shadow Rendering . . . . .	93
6.1.1 Adaptive Light Source Sampling . . . . .	93
6.1.2 Final Rendering . . . . .	97
6.1.3 Temporally Coherent Soft Shadow Computation . . . . .	98
6.2 Results and Discussion . . . . .	99

CONTENTS	xiii
6.2.1 Experimental Setup . . . . .	99
6.2.2 Visual Quality Evaluation . . . . .	100
6.2.3 Rendering Time Evaluation . . . . .	102
6.2.4 Limitations . . . . .	105
6.3 Summary . . . . .	108
<b>Chapter 7—Concluding Remarks</b>	109
7.1 Conclusion . . . . .	109
7.2 Future Work . . . . .	110
<b>Appendix A—Revectorization-Based Shadow Mapping Source Code for GLSL</b>	125
A.1 Overview . . . . .	125
A.2 Shadow Silhouette Localization . . . . .	126
A.3 Shadow Silhouette Traversal . . . . .	126
A.4 Shadow Silhouette Normalization . . . . .	128
A.5 Conservative Revectorization-based Shadow Mapping (RBSM) Visibility Function . . . . .	128
A.6 Summary . . . . .	128
<b>Appendix B—Revectorization-Based Shadow Mapping Source Code for Unity</b>	131
B.1 Shadows in Game Engines . . . . .	131
B.2 Shadows in Unity . . . . .	132
B.3 Revectorization-Based Shadow Mapping in Unity . . . . .	134
B.4 Summary . . . . .	137



## LIST OF FIGURES

1.1	An illustration of umbra, penumbra and lit effects. . . . .	1
1.2	Shadows enhancing the visual understanding of the scene. . . . .	2
1.3	Examples of applications that make use of shadows. . . . .	3
1.4	Factors that influence the size of a penumbra. . . . .	4
1.5	Shadows produced with aliasing artifacts in different game titles. . . . .	5
1.6	Shadows in Tom Clancy's The Division. . . . .	6
2.1	An overview of ray tracing. . . . .	12
2.2	An overview of shadow volume. . . . .	13
2.3	An overview of shadow mapping. . . . .	14
2.4	Aliasing artifacts produced by shadow mapping. . . . .	15
2.5	False self-shadowing produced by shadow mapping. . . . .	15
2.6	Shadow anti-aliasing by warping. . . . .	16
2.7	Shadow anti-aliasing by partitioning. . . . .	17
2.8	Shadow anti-aliasing by silhouette recovery. . . . .	19
2.9	Shadow anti-aliasing by hard shadow filtering. . . . .	20
2.10	Visually plausible soft shadow rendering with PCSS. . . . .	23
2.11	Visually plausible soft shadow rendering with back-projection. . . . .	24
2.12	Visually plausible soft shadow rendering with screen-space filtering. . . . .	26
2.13	Accurate soft shadows produced by different techniques. . . . .	28
3.1	Normalized relative position of a pixel in a shadow map texel. . . . .	32
3.2	An overview of RBSM for conservative hard shadow anti-aliasing. . . . .	33
3.3	Orientation of a lit fragment inside an aliased shadow silhouette. . . . .	35
3.4	Artifacts generated by RBSM in the shadows produced by sloped surfaces. . . . .	36
3.5	Shadow silhouette shapes handled by conservative RBSM. . . . .	37
3.6	RBSM conservative anti-aliasing for three different shadow silhouette shapes. . . . .	39
3.7	An overview of RBSM for non-conservative hard shadow anti-aliasing. . . . .	40
3.8	Orientation of a shadowed fragment inside an aliased shadow silhouette. . . . .	41
3.9	Additional shadow silhouette shapes handled by non-conservative RBSM. . . . .	42
3.10	RBSM non-conservative anti-aliasing for distinct shadow silhouette shapes. . . . .	43
3.11	Visual comparison of hard shadow techniques for a $1024^2$ shadow map. . . . .	45
3.12	Visual comparison of hard shadow techniques for a $2048^2$ shadow map. . . . .	46
3.13	Visual comparison of hard shadow techniques for a $4096^2$ shadow map. . . . .	47
3.14	Visual comparison of shadow mapping and RBSM for simple scenarios. . . . .	48
3.15	Visual comparison of shadow mapping and RBSM for a $1024^2$ shadow map. . . . .	49
3.16	Visual comparison of shadow mapping and RBSM for a $2048^2$ shadow map. . . . .	49

3.17	Visual comparison of shadow mapping and RBSM for a $2048^2$ shadow map.	50
3.18	Visual comparison of shadow mapping and RBSM for a $2048^2$ shadow map.	51
3.19	Visual comparison of hard shadow techniques for a $512^2$ shadow map. . . . .	54
4.1	An overview of RBSM for filtered hard shadow anti-aliasing. . . . .	58
4.2	Filtered hard shadow rendering of RBSM for a U-shaped shadow silhouette.	59
4.3	The penumbra effect produced by RPCF for different penumbra sizes. . . . .	59
4.4	An overview of the optimized implementation of RPCF. . . . .	60
4.5	An overview of Euclidean Distance Transform Shadow Mapping (EDTSM).	62
4.6	A more in-depth overview of EDTSM. . . . .	64
4.7	Skeleton artifacts generated by EDT and their suppression by mean filtering.	65
4.8	Visual comparison of filtered hard shadow techniques for YeahRight. . . . .	68
4.9	Visual comparison of filtered hard shadow techniques for Bunny. . . . .	69
4.10	Visual comparison of filtered hard shadow techniques for SanMiguel. . . . .	70
4.11	Visual comparison of filtered hard shadow techniques for a noisy surface.	71
4.12	Visual comparison between EDTSM and ground-truth. . . . .	74
5.1	An overview of Euclidean Distance Transform Soft Shadow Mapping (EDTSSM).	78
5.2	An overview of Revectorization-based Soft Shadow Mapping (RBSSM). .	80
5.3	Visual comparison of soft shadow techniques for YeahRight. . . . .	84
5.4	Visual comparison of soft shadow techniques for SanMiguel. . . . .	85
5.5	Visual comparison between soft shadow techniques for SanMiguel. . . . .	86
5.6	Time usage of soft shadow techniques for YeahRight. . . . .	87
5.7	Time usage of soft shadow techniques for SanMiguel. . . . .	88
5.8	Time usage of soft shadow techniques for YeahRight. . . . .	89
5.9	Time usage of soft shadow techniques for SanMiguel. . . . .	89
5.10	Visual comparison between soft shadow techniques for a large penumbra.	91
6.1	An overview of the revectorization-based accurate soft shadow mapping.	94
6.2	Accurate soft shadow rendering by RBSM and RPCF. . . . .	98
6.3	Accurate soft shadows produced by different techniques for Armadillo. . . .	100
6.4	Accurate soft shadows produced by different techniques for YeahRight. .	101
6.5	Accurate soft shadows produced by different techniques for QuadBot. .	102
6.6	Comparison between soft shadow techniques under distinct penumbra sizes.	103
6.7	Temporal coherency provided by accurate adaptive sampling approaches.	104
6.8	Limitation of the proposed approach. . . . .	108

## **LIST OF TABLES**

2.1	A brief comparison between filtered hard shadow mapping techniques. . . . .	22
2.2	A brief comparison between visually plausible soft shadow techniques. . . . .	27
3.1	Processing time of hard shadow techniques for a $720p$ window size. . . . .	50
3.2	Processing time of hard shadow techniques for a $1024^2$ shadow map. . . . .	51
3.3	Processing time of shadow mapping and RBSM for an $1080p$ window size.	52
3.4	Processing time of shadow mapping and RBSM for a $1024^2$ shadow map.	53
4.1	Processing time of filtered hard shadow techniques for a $720p$ window size.	71
4.2	Processing time of filtered hard shadow techniques for a $1024^2$ shadow map.	72
4.3	Processing time of filtered hard shadow techniques for a $720p$ window size.	72
4.4	Processing time of each individual step of EDTSM for a $1024^2$ shadow map.	73
6.1	Processing time of different sampling strategies for a $720p$ window size. . . . .	104
6.2	Processing time of different sampling strategies for a $1024^2$ shadow map. . . . .	105
6.3	Processing time per step of the proposed approach for a $720p$ window size.	106
6.4	Processing time per step of the proposed approach for a $1024^2$ shadow map.	107
B.1	List of variables available in Unity for shadow mapping with spot lights.	132
B.2	List of functions available in Unity for shadow mapping with spot lights.	133



## LIST OF ACRONYMS

- PCSS** Percentage Closer Soft Shadows
- PCF** Percentage-Closer Filtering
- VSM** Variance Shadow Mapping
- CSM** Convolution Shadow Mapping
- ESM** Exponential Shadow Mapping
- EVSM** Exponential Variance Shadow Mapping
- GSM** Gaussian Shadow Mapping
- MSM** Moment Shadow Mapping
- SAVSM** Summed-Area Variance Shadow Mapping
- CSSM** Convolution Soft Shadow Mapping
- VSSM** Variance Soft Shadow Mapping
- ESSM** Exponential Soft Shadow Mapping
- MSSM** Moment Soft Shadow Mapping
- SAT** Summed-Area Tables
- SSPCSS** Screen-Space Percentage-Closer Soft Shadows
- SSABSS** Screen-Space Anisotropic Blurred Soft Shadows
- SSSM** Separable Soft Shadow Mapping
- RBSM** Revectorization-based Shadow Mapping
- GLSL** OpenGL Shading Language
- RPCF** Revectorization-based Percentage-Closer Filtering
- EDTSM** Euclidean Distance Transform Shadow Mapping
- EDT** Euclidean Distance Transform

**PBA** Parallel Banding Algorithm

**CUDA** Compute Unified Device Architecture

**EDTSSM** Euclidean Distance Transform Soft Shadow Mapping

**RBSSM** Revectorization-based Soft Shadow Mapping

**SSRBSSM** Screen-Space Revectorization-based Soft Shadow Mapping

# Chapter

# 1

In this chapter, we present the motivation of this work, as well as the main question of research and the achieved contributions. Finally, we briefly show how the rest of this thesis is organized.

## INTRODUCTION

### 1.1 MOTIVATION

According to the level of visibility with respect to the light source, a point can be classified as being lit, in penumbra or in umbra. To understand this classification, let us visualize the scenario shown in Figure 1.1. In this scenario, the blue point (Figure 1.1-(a)) is **lit** because it is totally visible by the light source (white circle located at the top-left corner of Figure 1.1), the green point (Figure 1.1-(b)) is in **penumbra** because it is partially visible to the light source, and the red point (Figure 1.1-(c)) is in **umbra** because it is not visible to the light source, since all the light rays emitted by the light source in the direction of the red point are blocked by the cube. On the basis of this classification, we can define a **shadow** as a composition of umbra and penumbra points, or, in other words, as a composition of points that are partially or not visible by the light source.

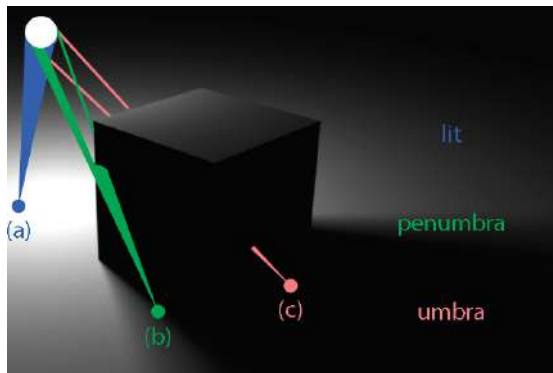


**Figure 1.1** A scene illuminated by an area light source. According to the level of occlusion of the light source, a point can be located in a lit (a), penumbra (b), or (c) umbra region. Image is courtesy of (EISEMANN et al., 2011).

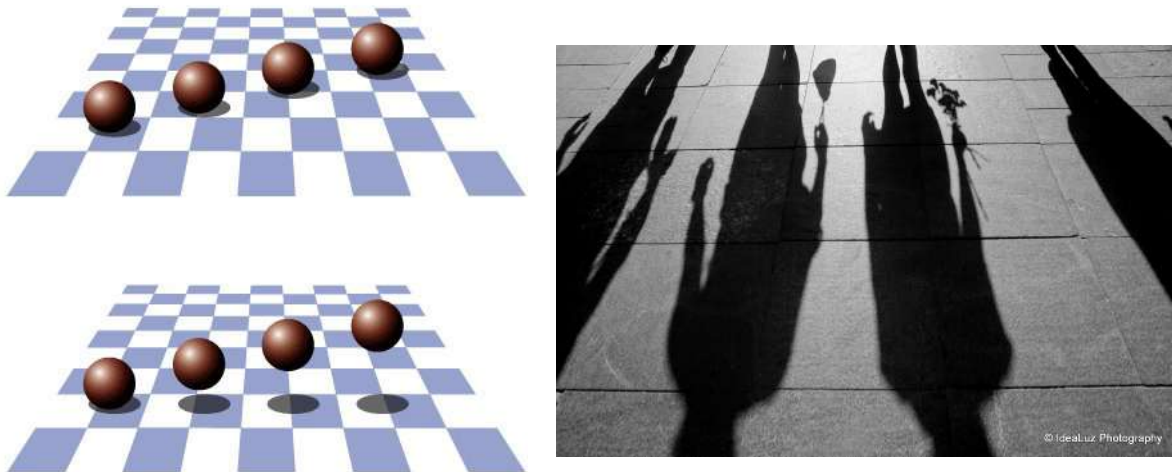


**Figure 1.2** (Left) Our visual perception of the scene changes according to the disposition of the shadows cast by the virtual spheres. (Right) Shadows provide information about the shape of the objects even if they are not visible in the scene. Left image is in the public domain. Right image is courtesy of ©IdeaLuz Photography.

In the real world, shadows are important because they enhance our understanding of the surrounding scene. As shown on the left of Figure 1.2, the presence of shadows improves our visual perception because they enhance our comprehension with respect to the spatial disposition of light blocker and shadow receiver objects. Moreover, as exemplified on the right of Figure 1.2, shadow silhouettes can provide information about the shape of the objects even if those objects cannot be visualized in the scene.

In computer graphics, shadows enhance the realism of the images rendered from virtual scenes. As shown in Figure 1.3, shadow rendering can be useful for a variety of applications, being able to:

- Enhance the visual quality of virtual animations generated during movie production, as illustrated by the movie picture shown in Figure 1.3-(a). Hence, shadow rendering is desirable for the industry of film and visual effects (CHRISTENSEN et al., 2006);
- Improve the realism of virtual players and scenarios, as well as the immersion of the user in the virtual world. Specially for games (STORY; WYMAN, 2016), whose example is shown in Figure 1.3-(b), user interactivity is the key factor that motivates the real-time rendering of shadows, with support to the presence of dynamic light sources, light blocker and shadow receiver objects;
- Simulate the influence of indoor and outdoor illumination in the interior appearance of rooms and buildings (SCHMIDT et al., 2016). This aspect is useful for architectural walk-throughs and ergonomic design of offices. An example of such an application can be seen in Figure 1.3-(c);

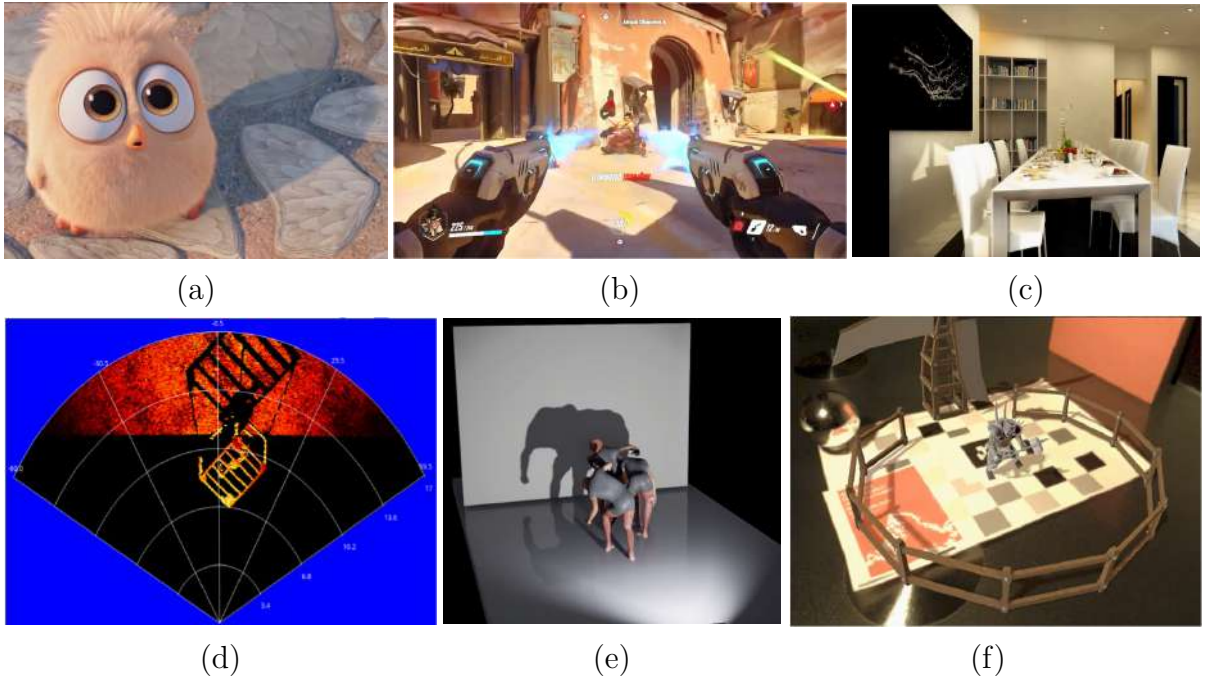


**Figure 1.3** Shadows are desirable in several applications, such as: (a) movies (©Rovio Entertainment), (b) games (©Blizzard Entertainment), (c) interior design (©3DPower), (d) simulation (CERQUEIRA et al., 2017), (e) art (WON; LEE, 2016), and (f) augmented reality (NOWROUZEZAHRAI et al., 2011).

- Increase the visual understanding, allowing the modelling of virtual scenarios to be done as accurately as possible. This feature is specially important for simulators and computer vision applications that need to establish a spatial relationship between the rendered objects and require high-quality shadow rendering (LAWSON; SALANITRI; WATERFIELD, 2016). An example of such an application is the sonar simulator shown in Figure 1.3-(d);
- Fool the audience about the shape of the shadow caster. Figure 1.3-(e), for instance, shows the shadow of an elephant, although the shadow casters are just actors with different poses. In this sense, art and sculpture can make use of shadows as a part of the work of art (MITRA; PAULY, 2009; CHEN et al., 2017) or the performance art (WON; LEE, 2016), enabling new levels of creativity for the artist and new levels of immersion for the audience;
- Allow the real-time, seamlessly integration of virtual content into an augmented reality application (FRANKE, 2014). From Figure 1.3-(f), for example, we can see that the shadow cast by the virtual warrior into the real scene enhances the realism of the scene visualization;

Specifically for games and augmented reality applications, a successful shadow ren-

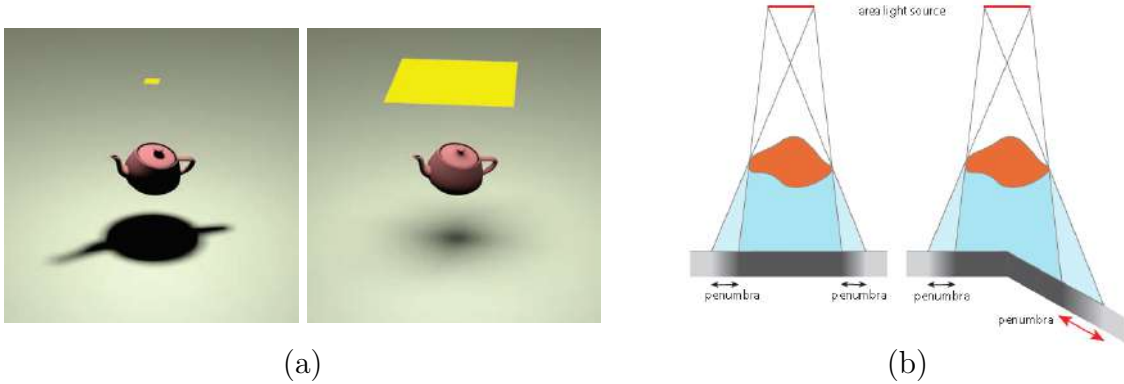


**Figure 1.4** The penumbra size varies according to (a) the size of the light source and (b) the distance between light blocker and shadow receiver objects. Image (a) courtesy of (EISEMANN et al., 2011). Image (b) courtesy of (SCHWARZLER et al., 2012).

dering algorithm must fulfill two essential requirements:

**High Visual Quality** - To improve the user's perception of the virtual scene, shadows must be accurate, temporally coherent, and free from artifacts.

**Real-Time Performance** - For applications where virtual scenes change dynamically, shadows should ideally be computed in real time, enabling the user to interact with the application and receive fast feedback (*i.e.*, without too much delay). As pointed by related work (YANG et al., 2010), shadows should ideally be computed faster than 100 frames per second, saving time for other operations of the application (*e.g.*, geometry rendering, morphing, collision detection, shading).

These requirements are also desirable for offline applications (*e.g.*, movies) that require a preview of the shadow effect before running a more costly, non-interactive accurate shadow rendering solution.

Unfortunately, the methods that compute highly accurate shadows take too much processing time to be used interactively for dynamic scenes. That happens because a real-world shadow contains the penumbra effect, that is characterized by the smooth transition located between lit and umbra regions. The main problem to simulate the penumbra effect lies in the determination of its size, that varies according to two factors: the size of the light source, where the larger is the light source, the larger is the penumbra size (Figure 1.4-(a)); the distance of the light source to both light blocker and shadow receiver objects, where a slight deformation on the receiver surface can cause the penumbra to grow in size (Figure 1.4-(b)).

The task of computing both umbra and penumbra components of the shadow makes the shadow rendering algorithm computationally expensive. In this case, the algorithm needs to perform an accurate visibility evaluation over the light source on the basis of the geometric information available in the scene. To simplify the shadow rendering problem, some methods restrict the shadow evaluation only for the fragments visible in the scene. Also, only the umbra component of the shadow is computed on the basis of an image-based representation of the light source view. These simplifications make the methods

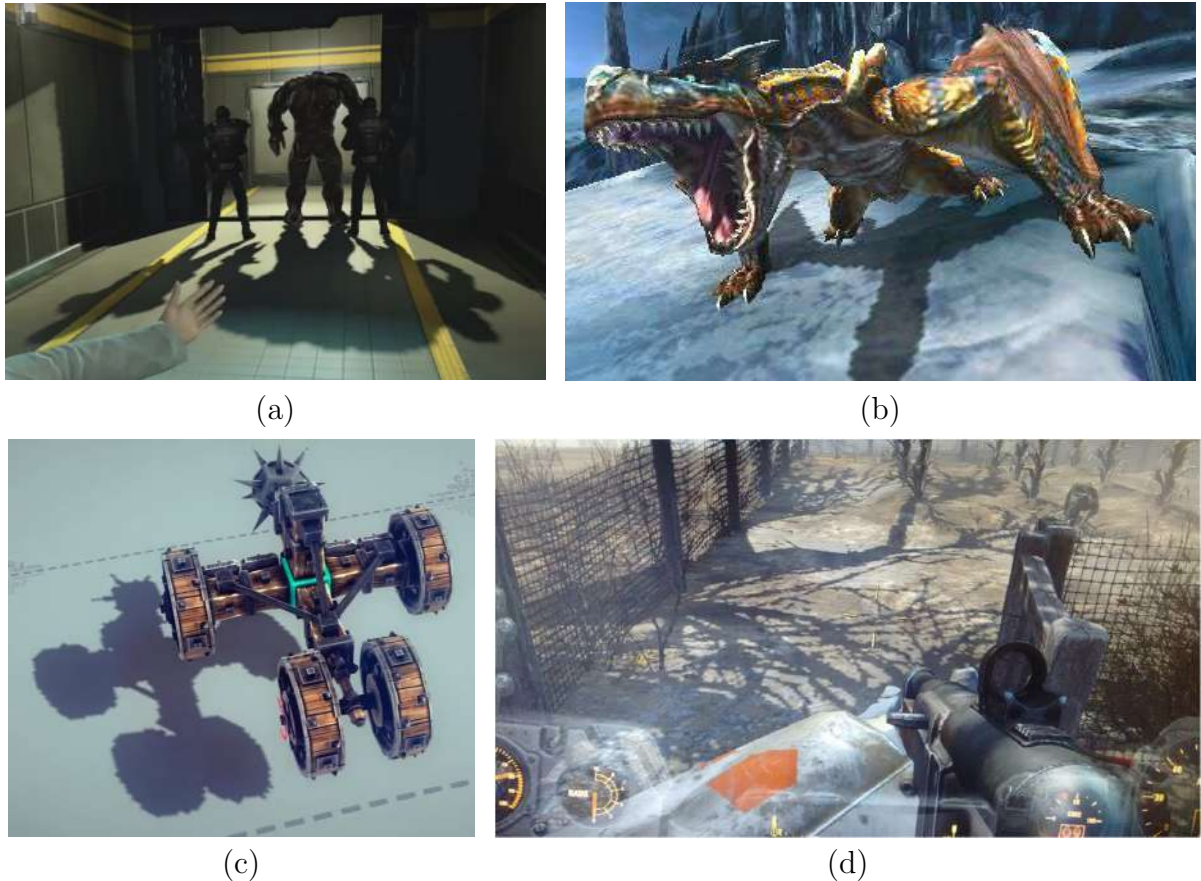


**Figure 1.5** Shadows produced with perspective aliasing artifacts in different game titles: (a) The Amazing Spider Man, 2012 (©Activision); (b) Monster Hunter 4 Ultimate, 2013 (©Capcom Co., Ltd.); (c) Besiege, 2015 (©Spiderling Studios); (d) Fallout 4, 2015 (©Bethesda Game Studios).

feasible for real-time applications, but prone to artifacts that lower the shadow visual quality. Examples of shadow artifacts are visible in the silhouette of the shadows shown in Figure 1.5 and in the close up shown in Figure 1.6.

In practice, shadows can be computed from object- or image-based approaches. Object-based approaches aim to compute accurate shadows by forming a single polygon mesh, called shadow volume, composed of all the projections between a ray emitted from a point light source and each vertex located at the object's silhouette (CROW, 1977). Because the resolution of the shadow volume is viewpoint independent, artifacts are effectively suppressed in this solution. Unfortunately, object-based approaches tend to be slower and less scalable than image-based approaches.

Image-based approaches typically store the depth buffer of the scene rendered from the light's viewpoint in a shadow map and use this information to determine, in the camera view, whether a fragment is in shadow (WILLIAMS, 1978). Despite the advantages of

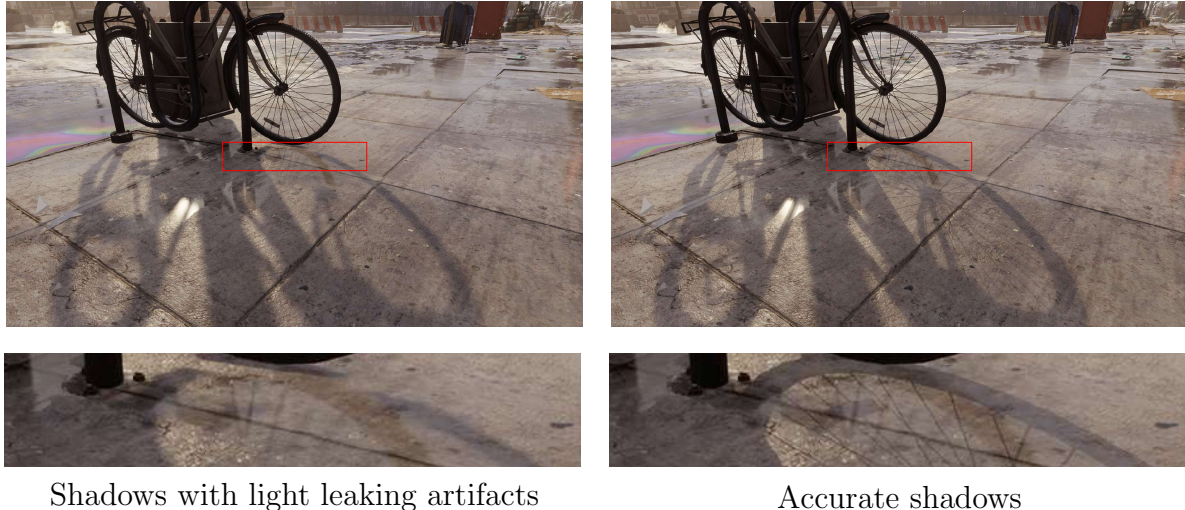


**Figure 1.6** Shadows produced with (left) and without (right) artifacts in Tom Clancy’s The Division, 2016 (©Ubisoft).

such a shadow map representation, the limited resolution of the shadow map generates aliasing (seen in the shadow silhouettes of Figure 1.5), light leaking (seen in the closeup of Figure 1.6) and temporal incoherency artifacts that still can be seen in games and other interactive applications, remaining as a challenging problem for image-based approaches.

## 1.2 HYPOTHESIS

In this work, we aim to answer the following question of research: *How can we make an efficient use of low-resolution shadow maps to achieve high-quality, anti-aliased shadow rendering in real time?*

As we show in the rest of this thesis, our investigations pointed out that the answer to this question relies on the proposal of the revectorization-based shadow mapping, a new technique that makes use of the camera-view resolution and the shadow silhouette shape to reduce the artifacts found in literature, even in the shadows generated from shadow maps with low resolution. We further extend the concept of shadow revectorization to provide anti-aliasing for shadows with both umbra and penumbra effects. Also, we make a novel use of the Euclidean distance transform for high-quality, real-time penumbra simulation with reduced light leaking artifacts and enhanced scalability in terms of penumbra size.

## 1.3 CONTRIBUTIONS

The main contributions to the field of shadow rendering are summarized, in order of importance, as follows:

1. A real-time, memory-efficient shadow anti-aliasing approach that is able to reduce the perspective aliasing artifacts commonly found in the umbra regions generated

- on the basis of an image-based approach;
2. A set of shadow rendering techniques that are able to produce real-time, high-quality shadows with fixed-, variable-size penumbra and less artifacts than related work;
  3. An anti-aliasing, screen-space shadow mapping technique that generates shadows faster than the techniques commonly found in the literature, at the cost of slightly reduced visual quality;
  4. An adaptive light source sampling approach that is able to generate temporally coherent, accurate shadows from a few light source samples, speeding up the accurate shadow computation;
  5. A practical implementation of the memory-efficient shadow anti-aliasing technique in a well-known game engine. This contribution not only shows that the proposed technique is easy to be implemented and integrated into an application, but also allows the evaluation of the proposed technique in the context of more complex environments typically found in games.

## 1.4 ORGANIZATION

The remainder of this work is organized as follows:

**Chapter 2, Background and State-of-the-Art Review.** This chapter gives an overview of relevant work in the field of shadow rendering. The basic concepts of shadow rendering as well as a review of recent related work are presented.

**Chapter 3, Revectorization-Based Shadow Mapping.** This chapter presents the technique proposed to solve the problem of real-time shadow anti-aliasing using the concept of shadow silhouette revectorization.

**Chapter 4, Revectorization-Based Filtered Shadow Mapping.** This chapter focuses on the description and evaluation of two techniques that simulate fixed-size penumbra from revectorized shadows.

**Chapter 5, Revectorization-Based Soft Shadow Mapping.** This chapter presents three techniques able to compute anti-aliased variable-size penumbra on the basis of the techniques shown in Chapters 3 and 4.

**Chapter 6, Revectorization-Based Accurate Soft Shadow Mapping.** In this chapter, we introduce the proposed technique able to compute accurate shadows interactively. The concept of shadow silhouette revectorization is used to guide a temporally coherent adaptive sampling of the area light source.

**Chapter 7, Concluding Remarks.** This chapter concludes this thesis, showing the final considerations about this work, and suggesting potential future directions.



# Chapter

# 2

In this chapter, we present the theoretical background behind the field of shadow rendering and review the most relevant and recent works proposed in the literature.

## BACKGROUND AND STATE-OF-THE-ART REVIEW

For the rest of this manuscript, we use the following mathematical notation: boldface for points and vectors, italics for scalars and non-standard functions, normal font for traditional mathematical functions (*e.g.*,  $\cos$ ,  $\sin$ ), calligraphic mathematical symbol for sets (*e.g.*,  $\mathcal{A}$ ), and sans serif for matrices (*e.g.*,  $\mathbf{S}$ ). For convenience, we assume that scalars and functions are defined in  $\mathbb{R}$ , points and vectors are defined in  $\mathbb{R}^3$ , unless stated otherwise. The subscripts  $x$ ,  $y$  and  $z$  are used to refer to the positions of the variables in the 3D space.

### 2.1 RENDERING EQUATION

The problem of shadow computation can be understood as a part of the global illumination problem, which is the reproduction of the photorealistic appearance of an object located inside a 3D scene and illuminated by an area light source. The quantity that captures the appearance of an object in a 3D scene is called radiance. Radiance expresses how much power arrives at (or leaves from) a certain point on a surface in a given direction (DUTRE et al., 2006). We refer to radiance by the function  $L(\mathbf{p}, \Theta)$ , where  $\mathbf{p}$  is the surface point and  $\Theta$  is the radiance direction. Also, we use the terms  $L(\mathbf{p} \rightarrow \Theta)$  and  $L(\mathbf{p} \leftarrow \Theta)$  to define the radiance leaving and arriving at the point  $\mathbf{p}$  in the direction  $\Theta$ , respectively.

The photorealistic appearance of an object is typically computed by the equilibrium distribution of light energy inside the scene. However, the light emitted by an area light source may interact in many ways with the objects in the scene and to model all the possible behaviours and interactions of the light in the scene is computationally impracticable. To ease this computation, global illumination methods commonly assume that light is emitted, reflected, or transmitted from a surface point. Moreover, they assume that light travels instantaneously in straight lines, without influence of external factors (DUTRE et al., 2006).

The formulation of the global illumination rendering equation relies on the principle of energy conservation. Let us define  $L_e(\mathbf{p} \rightarrow \Theta)$  as the radiance emitted by the point  $\mathbf{p}$  in the direction  $\Theta$ , and  $L(\mathbf{p} \rightarrow \Theta)$  as the total exitant radiance leaving the point  $\mathbf{p}$  in the direction  $\Theta$ .  $L(\mathbf{p} \rightarrow \Theta)$  is equivalent to the sum of the emitted and reflected radiance at the point  $\mathbf{p}$  in the direction  $\Theta$ . The reflected radiance is the result of an interaction between the incoming radiance  $L(\mathbf{p} \leftarrow \Psi)$  and the bidirectional reflectance distribution function  $f_r(\mathbf{p}, \Psi \rightarrow \Theta)$ , which defines how the light is reflected at the point  $\mathbf{p}$  according to the radiance incident in direction  $\Psi$  and reflected in direction  $\Theta$ . Hence, we can formalize the global illumination rendering equation as (KAJIYA, 1986; IMMEL; COHEN; GREENBERG, 1986)

$$L(\mathbf{p} \rightarrow \Theta) = L_e(\mathbf{p} \rightarrow \Theta) + \int_{\Omega_+} f_r(\mathbf{p}, \Psi \rightarrow \Theta) L(\mathbf{p} \leftarrow \Psi) \cos(\mathbf{n}_p, \Psi) d\omega_\Psi, \quad (2.1)$$

where the integral term denotes the total reflected radiance over the hemisphere  $\Omega_+$  above  $\mathbf{p}$  and  $\cos(\mathbf{n}_p, \Psi)$  is the cosine of the angle formed by the normal vector  $\mathbf{n}_p$  of the point  $\mathbf{p}$  and the ingoing direction  $\Psi$ . The bouncing behaviour of the reflected light is represented by the incoming radiance  $L(\mathbf{p} \leftarrow \Psi)$ , which depends on the outgoing radiance  $L(\mathbf{q} \rightarrow -\Psi)$  at a different point  $\mathbf{q}$ .

An alternative, simpler formulation of the rendering equation replaces the integration over the hemisphere around the surface point by an integration over all the surfaces visible to the surface point. In this case, a ray casting operation is used to find the closest point  $\mathbf{q}$  visible to the point  $\mathbf{p}$  at direction  $\Psi$ . Using the ray casting operation, we can define a binary visibility function  $V_{\text{ray}}(\mathbf{p}, \mathbf{q}) \in \{0, 1\}$

$$V_{\text{ray}}(\mathbf{p}, \mathbf{q}) = \begin{cases} 0 & \text{if } \mathbf{p} \text{ and } \mathbf{q} \text{ are not mutually visible,} \\ 1 & \text{otherwise.} \end{cases} \quad (2.2)$$

Using these definitions, we can reformulate the rendering equation as

$$L(\mathbf{p} \rightarrow \Theta) = L_e(\mathbf{p} \rightarrow \Theta) + \int_{\mathcal{A}} f_r(\mathbf{p}, \Psi \rightarrow \Theta) L(\mathbf{q} \rightarrow -\Psi) V_{\text{ray}}(\mathbf{p}, \mathbf{q}) G(\mathbf{p}, \mathbf{q}) d\mathcal{A}_q, \quad (2.3)$$

where the set  $\mathcal{A}$  represents all the surfaces present in the scene and

$$G(\mathbf{p}, \mathbf{q}) = \frac{\cos(\mathbf{n}_p, \Psi) \cos(\mathbf{n}_q, -\Psi)}{\|\mathbf{p} - \mathbf{q}\|^2}. \quad (2.4)$$

As the focus of our proposal relies on the shadow computation only, we are more interested in the computation of the direct illumination that arrives at the surface coming directly from the area light source. In this sense, we can assume that the integration must be calculated over all the area light source samples  $\mathbf{l}$  visible to the point  $\mathbf{p}$ . Then, the rendering equation is simplified to

$$L(\mathbf{p} \rightarrow \Theta) = \int_{\mathcal{L}} f_r(\mathbf{p}, \vec{\mathbf{pl}} \rightarrow \Theta) L_e(\mathbf{l} \rightarrow \vec{\mathbf{lp}}) V_{\text{ray}}(\mathbf{p}, \mathbf{l}) G(\mathbf{p}, \mathbf{l}) d\mathcal{L}_l, \quad (2.5)$$

where the set  $\mathcal{L}$  represents the surface area of the area light sources present in the scene, and  $L_e(\mathbf{l} \rightarrow \vec{\mathbf{l}}\mathbf{p})$  is the emitted radiance of the area light source sample  $\mathbf{l}$  visible to the point  $\mathbf{p}$  along the direction  $\vec{\mathbf{l}}\mathbf{p}$ . We have omitted the emitted radiance term  $L_e(\mathbf{p} \rightarrow \Theta)$  in (2.5) because we assume that the term is different from zero for light sources only. In this case, the term is only added to the sum when a light source is visible in the final rendered image.

If we separate the shading term from the shadow term, we obtain an alternative form of the direct lighting equation

$$L(\mathbf{p} \rightarrow \Theta) = \int_{\mathcal{L}} f_r(\mathbf{p}, \vec{\mathbf{l}} \rightarrow \Theta) G(\mathbf{p}, \mathbf{l}) d\mathcal{L}_l \cdot \frac{1}{|\mathcal{L}|} \int_{\mathcal{L}} L_e(\mathbf{l} \rightarrow \vec{\mathbf{l}}\mathbf{p}) V_{\text{ray}}(\mathbf{p}, \mathbf{l}) d\mathcal{L}_l \quad (2.6)$$

If we assume that the area light source has homogeneous directional radiation over its surface and that the area light source is uniformly colored (EISEMANN et al., 2011), we can reduce the emitted radiance  $L_e(\mathbf{l} \rightarrow \vec{\mathbf{l}}\mathbf{p})$  to a constant value  $L_e^*$ , which is taken out from the integral. This results in the equation

$$L(\mathbf{p} \rightarrow \Theta) = L_e^* \int_{\mathcal{L}} f_r(\mathbf{p}, \vec{\mathbf{l}} \rightarrow \Theta) G(\mathbf{p}, \mathbf{l}) d\mathcal{L}_l \cdot \frac{1}{|\mathcal{L}|} \int_{\mathcal{L}} V_{\text{ray}}(\mathbf{p}, \mathbf{l}) d\mathcal{L}_l \quad (2.7)$$

Although (2.7) is an approximation of the physically correct solution (2.5), this equation allows the reproduction of realistic shadows. To solve the integral (2.7) numerically, we can sample the area light source uniformly

$$L(\mathbf{p} \rightarrow \Theta) = L_e^* \sum_{i=0}^{n-1} f_r(\mathbf{p}, \vec{\mathbf{l}}_i \rightarrow \Theta) G(\mathbf{p}, \mathbf{l}_i) V_{\text{ray}}(\mathbf{p}, \mathbf{l}_i), \quad (2.8)$$

where  $n \in \mathbb{N}$  is the number of point light source samples.

In practice, by solving (2.8), we are able to produce **accurate soft** shadows that simulate both umbra and penumbra effects. However, as pointed by related work (EISEMANN et al., 2011), hundreds or thousands of area light source samples are typically required to allow the estimation of accurate soft shadows from (2.8), making this equation computationally expensive to be solved in real time.

One alternative to simplify (2.8) relies on the computation of **hard** shadows that simulate only the umbra effect. Hard shadows are extremely suitable for real-time applications because, to compute them, one just needs to replace the visibility sum over the  $n$  light source samples (2.8) to a visibility evaluation over a single point light source  $\mathbf{l}'$ . Then, the shadow term of the direct-lighting equation becomes just  $V_{\text{ray}}(\mathbf{p}, \mathbf{l}')$  in

$$L(\mathbf{p} \rightarrow \Theta) = L_e^* f_r(\mathbf{p}, \vec{\mathbf{l}}' \rightarrow \Theta) G(\mathbf{p}, \mathbf{l}') V_{\text{ray}}(\mathbf{p}, \mathbf{l}'). \quad (2.9)$$

Obviously, this alternative equation presents a trade-off between visual quality and rendering performance, since hard shadows can be easily computed in real time, but are not as accurate as soft shadows due to the lack of the penumbra simulation. A common alternative to remedy this situation is to treat  $V_{\text{ray}}(\mathbf{p}, \mathbf{l}')$  as a real-valued, continuous

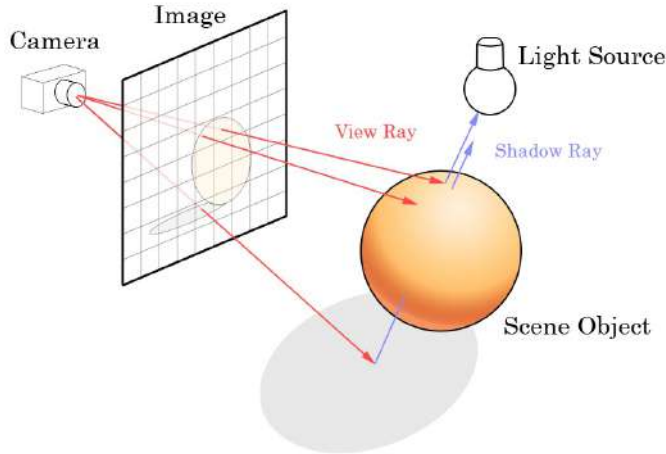


**Figure 2.1** In ray tracing, the camera sends several view rays into the scene. When these rays hit an object, they send shadow rays in the direction of the light source. Then, a point is determined to be in shadow if its corresponding shadow ray hits another point before reaching the light source. The original image is in the public domain.

visibility function. Therefore,  $\mathbf{l}'$  is considered as an approximation of the area light source, so that it could enable  $V_{\text{ray}}$  to estimate how much of the area light source is visible from a given surface point in the scene. Techniques that use this strategy typically produce **visually plausible soft** shadows, since they simulate the variable-size penumbra effect without sampling the entire area light source. Another alternative to improve the accuracy of hard shadows is to simply blur the resulting shadows with a fixed-size filter, generating **filtered hard** shadows with fixed-size penumbra.

In the next section, we present the most traditional techniques able to compute  $V_{\text{ray}}$  and solve (2.9). Next, we review the existing methods that extend these traditional techniques to compute hard and soft shadows efficiently.

## 2.2 SHADOW RENDERING

One of the main issues to solve the simplified rendering equation (2.8, 2.9) is how to compute the binary visibility function  $V_{\text{ray}}(\mathbf{p}, \mathbf{l})$  (2.2), regardless of whether  $\mathbf{l}$  is a sample of an area light source (2.8) or just a single point light source (2.9). The most traditional techniques able to accomplish this task are: ray tracing, shadow volume and shadow mapping.

**Ray tracing** (WHITTED, 1980) is a well-known object-based shadow algorithm able to compute accurate hard shadows. In this technique, a view ray (red arrows in Figure 2.1) is traced from the camera viewpoint to the virtual scene through each pixel in the image plane (gray grid in Figure 2.1). If the view ray hits a surface point in the scene, a new shadow ray is traced from the hit point to the light source. If the shadow ray hits an opaque object before reaching the light source, the surface point hit by the view ray is in shadow (see the point hit by the lower view ray in Figure 2.1). Otherwise, the

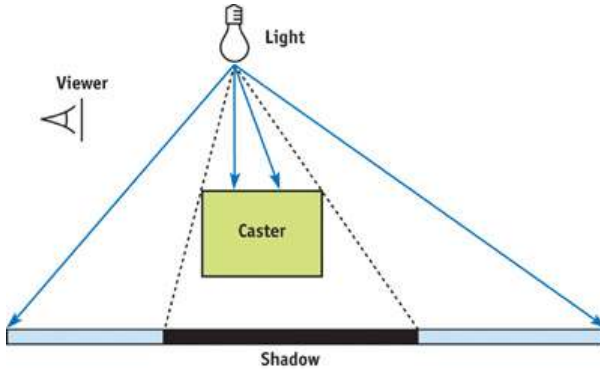


**Figure 2.2** In shadow volume, a point is in shadow if it is located inside the shadow volume formed by the extrusion of the vertices located at the silhouette of the shadow caster in the direction of the rays emitted by the light source. Image is courtesy of (MCGUIRE, 2004).

surface point is directly visible by the light source and is lit (see the point hit by the upper view ray in Figure 2.1). Ray tracing is not only able to simulate shadows, but also many other effects (*e.g.*, reflection, refraction), a property that makes this technique a powerful tool for computing some global illumination effects. Unfortunately, even with the recent advances in literature (WALD et al., 2014; FUETTERLING et al., 2015; PERARD-GAYOT; KALOJANOV; SLUSALLEK, 2017), ray tracing does not provide real-time performance for dynamic scenes. Therefore, it is mostly used for applications that use offline rendering (*e.g.*, movie production) or for the rendering of precomputed effects for static or dynamic scenes (MORGAN; PRANCKEVICIUS, 2014).

A faster alternative to ray tracing is **shadow volume** (CROW, 1977). A shadow volume consists of a set of polygons formed by an extrusion (dotted lines in Figure 2.2) of the vertices located at the silhouette of the objects presented in the scene (green caster in Figure 2.2) in the direction of the rays emitted by the light source (light in Figure 2.2). A surface point is in shadow (black rectangle in Figure 2.2) if it is located inside the shadow volume, and is lit otherwise. Shadow volume is an object-based algorithm faster than ray tracing and generates accurate hard shadows. However, despite the recent advances towards adapting the use of shadow volume to compute real-time shadows (GERHARDS et al., 2015; MORA et al., 2016), shadow volume does not provide stable frame rates, since the shadow rendering time greatly depends on the number of polygons of the shadow volume seen in the camera view. Moreover, shadow volume still demands higher memory footprints, because one needs to store the many polygons that form the shadow volume. Finally, the recent shadow volume techniques are still slow for real-time applications.

A faster, less accurate alternative than both ray tracing and shadow volume is **shadow mapping** (WILLIAMS, 1978). Shadow mapping is an image-based shadow algorithm composed of two passes, whose pipeline is depicted in Figure 2.3. In the first pass, the technique samples the 3D space viewed from the light source (an example is shown in the top-middle of Figure 2.3) and rasterizes the distance of the light source to the closest surface points of the scene into a depth texture called **shadow map**, as shown in the top-right of Figure 2.3. In the second pass, each surface point visible in the camera view

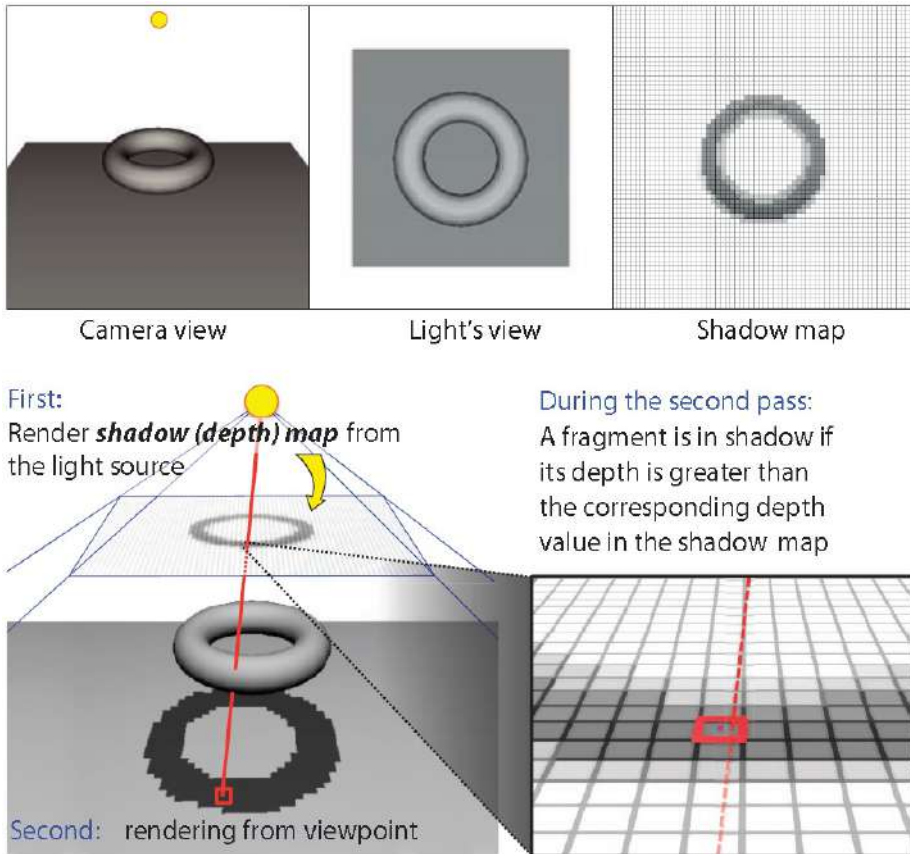


**Figure 2.3** In shadow mapping, the scene (top-left) is rendered from the viewpoint of the light source (top-middle), and its depth buffer is stored in a shadow map (top-right). Then, a point is in shadow if its distance to the light source is greater than the one stored in the shadow map (bottom). Image is courtesy of (EISEMANN et al., 2011).

is projected into the light source view and its distance to the light source is compared to the one stored in the shadow map (*i.e.*, shadow test). If the surface point is farther from the light source than its light blocker as stored in the shadow map, the surface point is in shadow. Otherwise, the surface point is lit and must be shaded accordingly. An example of the final result produced by shadow mapping is shown on the bottom of Figure 2.3.

The shadow mapping solution has several advantages, such as: simplicity, flexibility, scalability, hardware support and real-time performance. However, the finite resolution of the shadow map introduces some problems:

1. Pixels of the shadow map do not correspond to pixels in screen space, as can be seen in Figure 2.4-(a). This insufficient resolution of the shadow map (gray grid in Figure 2.4-(a)) generates aliasing artifacts, mainly along the shadow silhouette, as can be seen in the silhouette of the shadows shown in Figure 2.4-(b);
2. Due to numerical precision issues, pixels of the screen space may lie between pixels of the shadow map, generating false self-shadowing. In Figure 2.5-(a), false self-

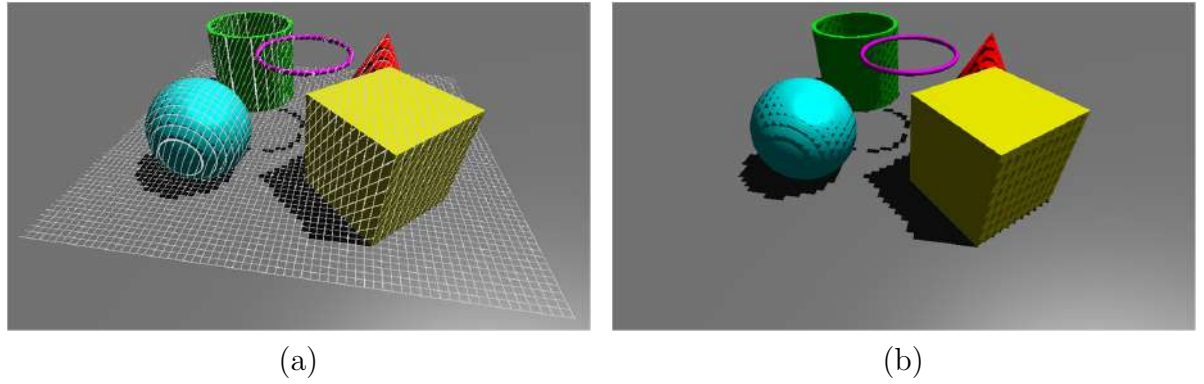


**Figure 2.4** Due to the (a) limited resolution of the shadow map (gray grid projected into the camera view), shadow mapping generates hard shadows with (b) perspective aliasing artifacts. Images are courtesy of ©Vladimir Bondarev.

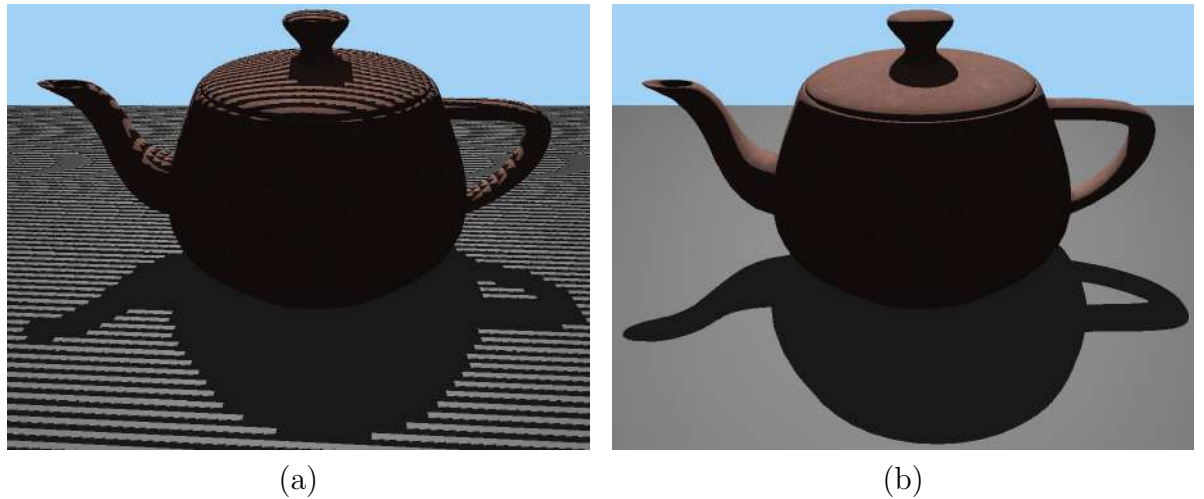


**Figure 2.5** Hard shadows (a) with false self-shadowing. (b) Accurate hard shadows.

shadowing is visible by the striped umbra artifacts present in both plane and teapot objects;

3. Because of the previous artifacts, whenever the camera or the light source moves in the scene, the shadow's shape may change in a temporally incoherent, unrealistic way (EISEMANN et al., 2011). This effect is mainly seen in videos and animations.

While false self-shadowing can be easily solved by adding a fixed (WILLIAMS, 1978) or adaptive depth bias (DOU et al., 2014) to influence the shadow test, aliasing artifacts and temporal incoherence are two of the major problems of image-based approaches, hampering the generation of accurate hard shadows, as exemplified by Figure 2.5-(b).

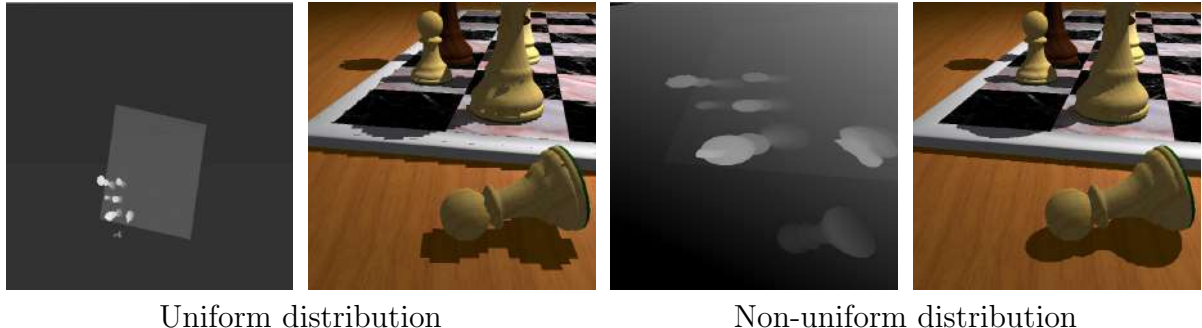


**Figure 2.6** (Left) A uniform distribution of depth values in the shadow map produces aliased artifacts along the shadow silhouette. (Right) A non-uniform, perspective distribution of depth values improves shadow visual quality. Images courtesy of (STAMMINGER; DRETTAKIS, 2002).

In the following sections, we present the different types of shadows that can be simulated on the basis of shadow mapping and we also discuss many strategies proposed to alleviate the aliasing problem of shadow mapping. We refer the reader to reference books (EISEMANN et al., 2011) (WOO; POULIN, 2012) for a more complete review of the existing shadow rendering algorithms.

## 2.3 HARD SHADOWS

Hard shadows represent only the umbra component of the shadow, in other words, the total absence of light. Shadow mapping is the most traditional technique able to solve (2.9) in real time, at the cost of generating aliased hard shadows. In this section, we discuss the different strategies that have been proposed to generate anti-aliased hard shadows in real time with shadow mapping.

### 2.3.1 Warping

Aliasing artifacts can be reduced by changing the parametrization of the shadow map generation. In other words, by changing the warping function that transforms world-space coordinates to shadow map texture coordinates, one can improve the shadow map resolution in the region near the viewpoint, while lowering the sampling density in the regions far from the viewpoint. This warping effect can be seen in Figure 2.6. In Figure 2.6-left, the shadow map generation wastes space of the shadow map due to the uniform distribution of the depth values. Then, as can be seen in Figure 2.6-right, by warping the shadow map generation with a non-uniform perspective projection, one can make a better use of the available shadow map resolution, improving the sampling density for the objects visible in the current camera viewpoint.

Different from the approaches that aim to distribute the depth values uniformly in the shadow map texture (BRABEC; ANNEN; SEIDEL, 2002), perspective shadow mapping (STAMMINGER; DRETTAKIS, 2002) is the first technique proposed to warp the shadow



**Figure 2.7** For a large scene, the use of an insufficient shadow map resolution may generate aliasing artifacts along the shadow silhouette (a). The efficient distribution of several high-resolution shadow maps per sub-units of the 3D space helps on reducing these aliasing artifacts (b). Images courtesy of (LAURITZEN; SALVI; LEFOHN, 2011).

map using non-uniform perspective projection instead of the orthographic one. While this simple changing of parametrization has hardware support and greatly improves the quality of the shadow rendering, the algorithm does not handle several special cases and restrictions, reducing the quality of the shadow map parametrization.

Approaches such as light-space perspective shadow mapping (WIMMER; SCHERZER; PURGATHOFER, 2004), trapezoidal shadow mapping (MARTIN; TAN, 2004), and perspective optimal shadow mapping (CHONG; GORTLER, 2004; CHONG; GORTLER, 2007) try to generalize the use of perspective shadow maps for different scenarios and light sources, and distribute the error equally among objects located near and far from the viewer. Logarithmic parametrization (LLOYD et al., 2008) is an alternative approach to obtain a higher accurate warping algorithm at the cost of lower frame rate.

Warping techniques minimize aliasing artifacts efficiently, but flickering artifacts still can be seen when the camera or the light source moves in the scene. These flickering artifacts are caused by the use of the non-uniform sampling strategy, that may change the warping function per frame, in a temporally incoherent way. Also, even if the warping strategies make better use of the shadow map resolution, aliasing artifacts are still generated by such techniques because the shadow map resolution, the source of the aliasing, remains finite and limited.

### 2.3.2 Partitioning

An alternative to reduce aliasing artifacts is to make use of several shadow maps generated from different locations to better sample the depth of the objects located near and far the camera viewpoint. Figure 2.7 shows shadows generated without and with partitioned shadow maps.

Approaches based on z-partitioning split the 3D space inside the view frustum into several sub-units along the z-axis and associate a separate shadow map for each sub-unit (ENGEL, 2006; ZHANG et al., 2006; ZHANG; SUN; NYMAN, 2008; LAURITZEN; SALVI; LEFOHN, 2011).

Another set of techniques evaluates the error produced by the use of a single low-resolution shadow map and try to adapt the shadow map configuration, either by generating more shadow maps or increasing the shadow map resolutions, in order to reduce the aliasing artifacts caused by the insufficient shadow map resolution (FERNANDO et al., 2001; ARVO, 2004; GIEGL; WIMMER, 2007b; GIEGL; WIMMER, 2007a; LEFOHN; SENGUPTA; OWENS, 2007).

Partitioning techniques are useful to reduce aliasing artifacts caused mainly by the use of a single shadow map in a large-scale virtual environment. To further improve the accuracy of the solution, these techniques are commonly associated with warping techniques. Thus, the several shadow maps generated from partitioning approaches are built using an improved parametrization approach. While this combination may work in some situations, for simpler scenarios in which high-quality shadows could be rendered with a single shadow map of high resolution, the use of partitioned shadow maps may only increase memory usage (although recent works, such as (SINTORN et al., 2014; KAMPE et al., 2016; SCANDOLO; BAUSZAT; EISEMANN, 2016a; SCANDOLO; BAUSZAT; EISEMANN, 2016b), have focused on the efficient compression of shadow maps) and processing time.

### 2.3.3 Silhouette Recovery

Some techniques aim to compute accurate hard shadows by minimizing the jagged shadow silhouettes produced by shadow mapping.

Hybrid approaches based on shadow mapping, shadow volume (MCCOOL, 2000; CHAN; DURAND, 2004), and ray tracing (HERTEL; HORMANN; WESTERMANN, 2009) have been proposed in the literature. As can be seen in the comparison between Figures 2.8-(a) and 2.8-(b), these methods are able to estimate accurate hard shadows. However, as shown in Figure 2.8-(c), they compute shadows faster than the reference solutions, but still much slower than shadow mapping.

To reconstruct accurate shadow silhouettes, some techniques rely on the storage of additional geometric information. In shadow silhouette mapping (SEN; CAMMARANO; HANRAHAN, 2003), the vertex that lies on the geometry silhouette is stored in the shadow map. Fast sub-pixel anti-aliased shadow mapping (PAN et al., 2009) uses pixel's position and associated face normal in addition to the shadow map. Sub-pixel shadow mapping (LECOQCQ et al., 2014) stores triangle information (*i.e.*, 3D vertex coordinates and depth derivatives) with the shadow map. Each one of these techniques has a different visibility function that uses this augmented information to reconstruct accurate shadow silhouettes. However, they also increase memory consumption and processing time to achieve such a goal.

To solve the mismatch problem of shadow mapping, the mapping of each pixel in the camera view into an exclusive texel in the shadow map, other approaches, such as (AILA;

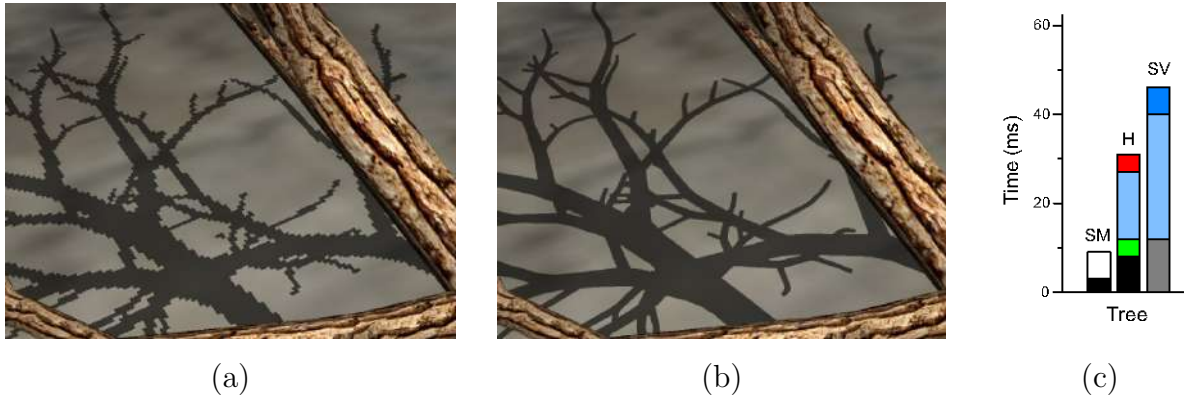


**Figure 2.8** Silhouette recovery techniques solve aliasing artifacts (a) by recovering accurate shadow silhouettes (b). These techniques guarantee high-quality anti-aliasing, however, they add a high computational overhead for shadow mapping (c). SM - Shadow mapping. H - Silhouette recovery technique. SV - Shadow volume. Images courtesy of (CHAN; DURAND, 2004).

LAINÉ, 2004; JOHNSON et al., 2005; WYMAN; HOETZLEIN; LEFOHN, 2015), treat the shadow map as an irregular data structure to correct the insufficient shadow map sampling. Unfortunately, the building and management of such data structures demand additional processing time to the shadow rendering algorithm.

To perform shadow anti-aliasing, shadow map silhouette revectorization (BONDAREV, 2014) embeds shadow silhouettes into a discontinuity space and revectorizes them according to their discontinuity directions. While the technique indeed alleviates aliasing, the method consists of two passes in the shader, increases memory consumption and does not work well for sloped surfaces, generating artifacts during revectorization. By adapting this technique to work in a single pass in the shader, revising its theory to reduce memory consumption, adding support for shadow anti-aliasing in sloped surfaces, and extending it to support penumbra simulation, we show that we can take advantage of this shadow revectorization effect to provide high-quality shadow anti-aliasing.

Techniques for reconstructing shadow silhouettes are useful because they can solve the aliasing problem in an accurate way. However, as exemplified by the performance results shown in Figure 2.8-(c), most of these techniques add a high computational overhead to shadow mapping. Also, by incorporating additional geometric information into the shadow map, these techniques typically add a large memory footprint to the hard shadow rendering.

Warping and partitioning strategies seem to be well established in industry, since the state-of-the-art techniques satisfy the requirements of games and other interactive applications (LAURITZEN; SALVI; LEFOHN, 2011). In this scenario, these strategies are typically integrated with other strategies, such as silhouette recovery and hard shadow filtering, to improve the accuracy of the latter ones. On the other hand, shadow silhouette recovery techniques solve the aliasing problem accurately, but they are not as fast and

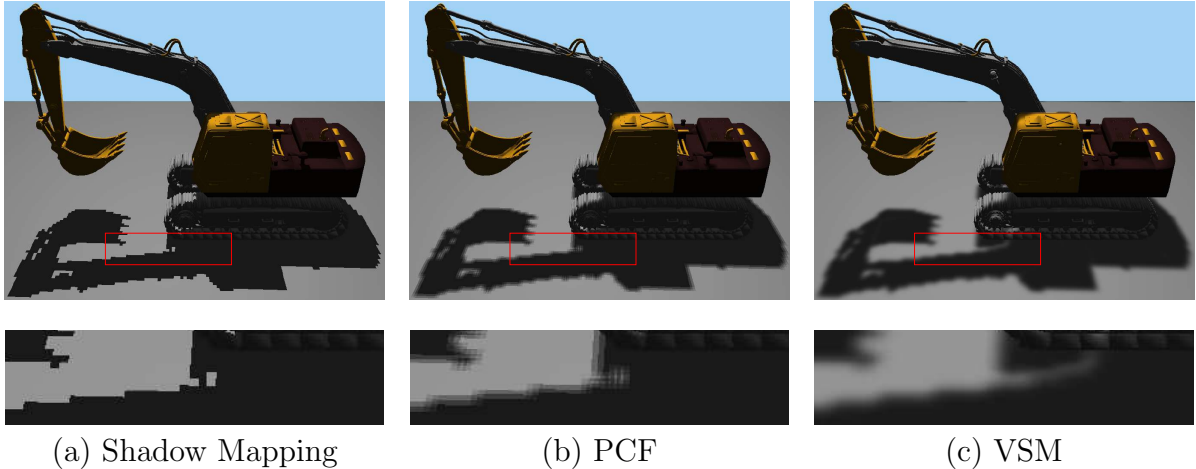


**Figure 2.9** Hard shadow filtering techniques minimize the shadow aliasing problem of shadow mapping (a) by simulating fixed-size penumbra. Unfortunately, (b) banding or (c) light leaking artifacts may affect the visual quality of the penumbra rendering.

lightweight as shadow mapping.

While the simplification of (2.9) guarantees real-time performance, hard shadows techniques are not realistic because they do not generate penumbra natively and produce shadows with visual quality far from the physically accurate solution. In the next section, we discuss alternative solutions that simulate the penumbra effect on the basis of the filtering of hard shadows.

## 2.4 FILTERED HARD SHADOWS

To simulate the penumbra effect on the basis of the hard shadows generated by shadow mapping, some techniques perform filtering over the hard shadows, or over the shadow map itself, to produce filtered hard shadows with fixed-size penumbra. This effect can be seen in Figure 2.9. By blurring the hard shadows shown in Figure 2.9-(a), we can produce fixed-size penumbra, as seen in Figures 2.9-(b) and 2.9-(c).

The most traditional algorithm for fixed-size penumbra simulation is Percentage-Closer Filtering (PCF) (REEVES; SALESIN; COOK, 1987). As an extension of shadow mapping, PCF takes the shadow test results performed over a filter region and averages them to determine the final shadow intensity. By filtering the shadow test results, rather than the shadow map itself, PCF is not prone to light leaking artifacts, and provides real-time performance, while keeping low memory consumption for the penumbra simulation. However, PCF does not support texture pre-filtering, does not provide scalability in terms of filter size, and requires a high number of samples to solve banding artifacts. An example of banding artifacts produced by PCF can be seen in Figure 2.9-(b).

To make the shadow filtering scalable, Variance Shadow Mapping (VSM) (DON-NELLY; LAURITZEN, 2006) uses Chebyshev's inequality, depth and squared depth stored in the shadow map to determine the shadow intensity of a surface point by means of a probability of whether the point is in shadow. VSM supports shadow map pre-

filtering and is scalable for the filter size, but generates light leaking artifacts in shadows. An example of light leaking artifacts produced by VSM is shown in Figure 2.9-(c).

To reduce the light leaking artifacts of VSM, Convolution Shadow Mapping (CSM) (ANNEN et al., 2007) uses Fourier series to approximate and linearize the shadow test. In CSM, the shadow map is converted into filtered basis textures that are used to determine the final shadow intensity as a weighted sum of basis functions stored in basis textures. CSM supports pre-filtering and reduces light leaking artifacts as compared to VSM, at the cost of more memory consumption and processing time than VSM.

To minimize the processing time required by CSM, Exponential Shadow Mapping (ESM) (ANNEN et al., 2008; SALVI, 2008) approximates the shadow test by an exponential function, rather than Fourier series. ESM stores exponent-transformed depth values into the shadow map, which are later used for penumbra simulation. ESM is faster and requires less memory footprint than CSM, while generating visual results similar to the ones obtained with VSM.

To improve the visual quality of both VSM and ESM, Exponential Variance Shadow Mapping (EVSM) (LAURITZEN; MCCOOL, 2008) merges both ESM and VSM theories to produce high-quality fixed-size penumbra simulation. In EVSM, light leaking only occurs at places where both ESM and VSM techniques generate such an artifact.

As an alternative to both VSM and ESM techniques, Gaussian Shadow Mapping (GSM) (GUMBAU et al., 2011; GUMBAU et al., 2013) replaces Chebyshev's inequality by a Gaussian cumulative distribution function to minimize light leaking. Also, inspired by EVSM, GSM warps its visibility function to take advantage of the exponential function proposed in ESM to further reduce light leaking.

Moment Shadow Mapping (MSM) (PETERS; KLEIN, 2015; PETERS, 2017) improves VSM by storing four powers of depth in the shadow map and treating the penumbra simulation as a Hamburger or Hausdorff moment problem. MSM reduces the light leaking artifacts of VSM, generates results similar to EVSM, while keeping nearly the same rendering time of both techniques, but consuming more memory requirements than VSM.

Filtering techniques are an efficient alternative to shadow mapping, producing shadows that mimic the appearance of the penumbra effect. In Table 2.1, we show a general classification of the filtered hard shadow techniques presented in this section with respect to the relevant attributes discussed so far.

VSM, CSM, ESM, EVSM, GSM, and MSM techniques filter the shadow map by warping the depth stored in the shadow map into another basis function, making the penumbra simulation scalable in terms of filter size. However, as shown in Figure 2.9-(c), these shadow map filtering techniques introduce noticeable light leaking artifacts that reduce the shadow visual quality. On the other hand, PCF filters the hard shadows produced with shadow mapping to avoid light leaking. However, PCF is not scalable with respect to the filter size.

Despite requiring low processing time to minimize the aliasing artifacts produced by shadow mapping, none of the filtered hard shadow techniques presented in this section can remove the aliasing artifacts caused by the use of low-resolution shadow maps, since they work over jagged shadow silhouettes (Figure 2.9-(b)). Increasing the resolution of

Method	Property			
	Anti-aliasing	Reduced Leaking	Scalability	Memory Footprint
PCF	✗	✓	✗	Low
VSM	✗	✗	✓	Medium
CSM	✗	✗	✓	High
ESM	✗	✗	✓	Medium
EVSM	✗	✗	✓	Medium
GSM	✗	✗	✓	Medium
MSM	✗	✗	✓	Medium

**Table 2.1** Classification of filtered hard shadow mapping techniques proposed in the literature according to the following attributes: anti-aliasing for shadows produced with low-resolution shadow maps, reduced light leaking artifact generation, scalability with respect to the filter size and memory consumption (**low** if the algorithm uses only the shadow map, **medium** if the algorithm uses two or more channels of the shadow map and **high** if the algorithm uses additional textures for penumbra simulation).

the shadow map may overcome this issue, at the cost of higher memory consumption and processing time. But, even in this case, any closeup on the shadow could reveal the aliasing artifacts. Larger kernel sizes may also remove the aliasing of the shadows, however, they severely blur out the shadows, losing too much detail of the shadow silhouette.

As we further state in the next section, filtered hard shadows are more realistic than hard shadows, but they also lack realism because they are able to simulate only fixed-size penumbra, meanwhile real-world shadows mostly contain variable-size penumbra.

## 2.5 VISUALLY PLAUSIBLE SOFT SHADOWS

Differently from the techniques that compute fixed-size penumbra, visually plausible soft shadow techniques take into consideration the fact that the size of the penumbra varies according to the distance of the surface point to both light source and other light blocker surface points. Shadows that are computed on the basis of a single point light source and that can simulate variable-size penumbra are called visually plausible soft shadows. Soft shadows because they simulate the variable-size penumbra effect. Visually plausible shadows because they resemble the visual quality of accurate shadows. An example of a visually plausible soft shadow is shown in Figure 2.10.

Here, we review the existing soft shadow methods that have been proposed to extend the concept of hard shadow mapping to compute soft shadows in real time.

### 2.5.1 Percentage-Closer Soft Shadows

Area light sources produce soft shadows in which the penumbra size varies along the shadow silhouette, as visible in Figure 2.10. The task of estimating this penumbra size in a general configuration is non-trivial (EISEMANN et al., 2011).

To ease the task of variable penumbra size estimation, the Percentage Closer Soft Shadows (PCSS) technique uses an assumption that both light source, light blocker and



**Figure 2.10** Visually plausible soft shadows have penumbra whose size varies according to the distance of each surface point to both light source and light blocker objects. Image courtesy of (FERNANDO, 2005).

shadow receiver objects are all planar and parallel to each other (SOLER; SILLION, 1998). Hence, by the use of similar triangles, the penumbra size can be easily estimated (FERNANDO, 2005).

The PCSS framework consists of three main steps: the average blocker depth computation, the penumbra size estimation and the soft shadow filtering. First, the shadow map is searched in a given region and the average distance of the blocker to the light source is computed. Then, this average distance is used in addition to the light source size and the receiver depth for the penumbra size estimation. Finally, the PCF is applied over the penumbra size of the soft shadow filtering. PCSS is easy to implement, provides anti-aliasing, uses only one shadow map, and requires neither pre-processing nor additional geometric information. However, PCSS produces aliased shadows for large area light sources (EISEMANN et al., 2011). Also, this technique scales poorly for large filter sizes because a large amount of texture lookups for both average blocker depth estimation and soft shadow filtering steps is required.

Temporal coherence has already been exploited to generate visually plausible soft shadows on the basis of the PCSS framework (SCHERZER et al., 2009; SCHERZER; SCHWARZLER; MATTAUSCH, 2011; SCHWARZLER et al., 2013). While these tech-

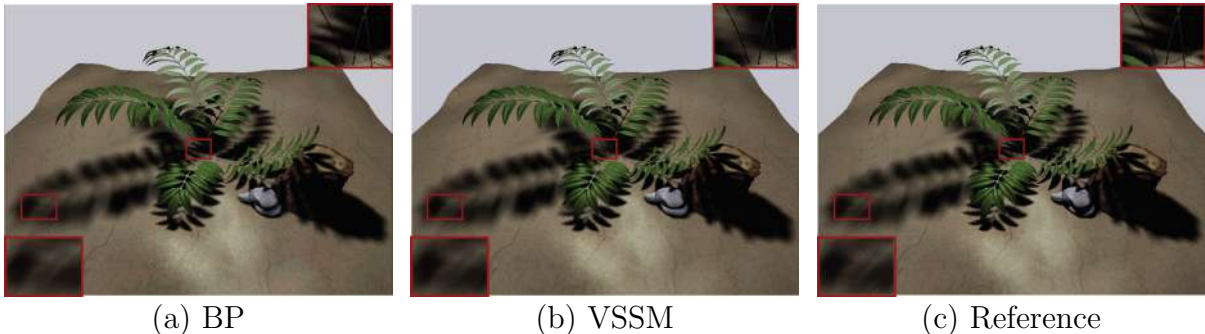


**Figure 2.11** While providing a plausible visual quality for the soft shadow rendering, back-projection (BP) approaches (such as (GUENNEBAUD; BARTHE; PAULIN, 2007) (a)) are too much slower than pre-filtering techniques (such as VSSM (b)). Images courtesy of (YANG et al., 2010).

niques are able to provide realistic soft shadows in real time, they require several frames to converge to a correct solution. Also, the frame rate may change considerably between frames for dynamic scenes with moving objects, cameras or light sources, being inadequate for applications that demand constant frame rates. Shen et al. (SHEN et al., 2011) propose an analytical filtering solution to improve the image quality of PCSS, but the algorithm is inefficient in terms of performance for large filter sizes.

To improve the performance of PCSS, Klein et al. (KLEIN; NISCHWITZ; OBERMEIER, 2012) compute the average blocker depth and estimate the penumbra size only for the fragments located at the hard shadow silhouette. Then, for each fragment outside the shadow silhouette, a gathering approach and an erosion operation are used to locate the shadow silhouette and estimate the penumbra intensity of the soft shadows. This approach is slightly faster than PCSS for large kernel sizes, but is still prone to aliasing artifacts at the penumbra location.

### 2.5.2 Back-Projection

Rather than using the PCSS framework to compute soft shadows, back-projection techniques aim to provide an accurate soft shadow solution by unprojecting a micropatch for each shadow map texel and then using this geometric representation to compute the amount of the light source occluded by the blocker objects (ATTY et al., 2006; AS-ZODI; SZIRMAY-KALOS, 2006; GUENNEBAUD; BARTHE; PAULIN, 2006; BAVOIL; CALLAHAN; SILVA, 2008). Micropatches are approximations of the blocker geometry. Thus, they may cause shadow overestimation and light leaking. To solve such problems, the authors of (SCHWARZ; STAMMINGER, 2007) propose the use of an occlusion bit-mask. In fact, they place sample points on the area light source and use a simple bit representation to track which of the samples are occluded. Unfortunately, this approach suffers from performance issues, especially for high-resolution shadow maps. Hierarchical solutions and techniques based on efficient contour detection are commonly used to

reduce the computational cost of the soft shadow mapping (GUENNEBAUD; BARTHE; PAULIN, 2007; YANG et al., 2009).

Back-projection techniques generate high-quality soft shadows using a single shadow map, as shown in Figure 2.11-(a). However, these methods are still prone to artifacts and achieve only interactive performance due to the usage and computation of multiple shadow maps required to properly track the micropatches into the area light source.

### 2.5.3 Pre-Filtering

To solve both problems of aliasing and scalability of the PCSS, pre-filtering techniques commonly use a filterable function to approximate either the average blocker depth estimation, the shadow test or both of them.

Summed-Area Variance Shadow Mapping (SAVSM) (LAURITZEN, 2008) replaces the PCF step of PCSS by VSM (DONNELLY; LAURITZEN, 2006), which makes the soft shadow filtering scalable with respect to the filter size. Unfortunately, the average blocker depth estimation remains costly and the use of VSM for shadow filtering makes SAVSM more prone to light leaking artifacts than PCSS.

Convolution Soft Shadow Mapping (CSSM) (ANNEN et al., 2008) proposes a constant-time average blocker depth estimation on the basis of a pre-filtered shadow map and pre-filtered Fourier series basis images. CSM (ANNEN et al., 2008) is used to perform soft shadow filtering over the penumbra area. Indeed, CSSM brings scalability to PCSS, however, suffers from light leaking artifacts and high memory consumption.

Variance Soft Shadow Mapping (VSSM) (DONG; YANG, 2010; YANG et al., 2010) estimates the average blocker depth efficiently on the basis of a pre-filtered shadow map and the Chebyshev's Inequality. VSSM provides performance compatible with related work, makes use of the VSM theory to estimate the average blocker depth, and generates soft shadows with reduced light leaking artifacts.

Exponential Soft Shadow Mapping (ESSM) (SHEN; FENG; YANG, 2013) uses the ESM (ANNEN et al., 2008; SALVI, 2008) theory to estimate the average blocker depth and compute the final soft shadow intensity in constant time on the basis of a pre-filtered exponential shadow map. A number of improvements are proposed to alleviate light leaking artifacts, improve the accuracy of the pre-filtering, and keep the real-time performance of the approach.

Similarly to VSSM, Moment Soft Shadow Mapping (MSSM) (PETERS et al., 2016; PETERS et al., 2017) generates a pre-filtered moment shadow map (PETERS; KLEIN, 2015), and use it to estimate the average blocker depth and perform the soft shadow filtering by solving the Hamburger moment problem. Some schemes to optimize the approach, as well as to handle numerical precision issues, are presented as well.

Different from the previous approaches, the work proposed by related work (SELGRAD et al., 2015) uses a new pre-filtering method in which a per-texel fragment list of all blockers is stored in a multi-layer shadow map (XIE; TABELLION; PEARCE, 2007). Depth and opacity of all the blocker fragments are stored in a hierarchical representation, where each level stores the average depth and the accumulated opacity of the texels involved. This shadow map representation is then used to perform shadow filtering.

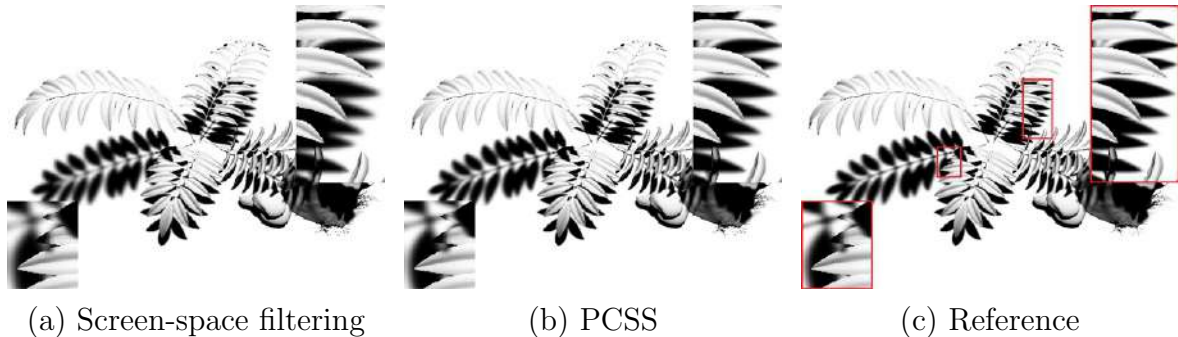


**Figure 2.12** Screen-space filtering (a) is able to generate soft shadows visually similar to the ones generated by PCSS (b) and the reference solution (c). Images courtesy of (BUADES; GUMBAU; CHOVER, 2015).

Stochastic soft shadow mapping (LIKTOR et al., 2015) samples a 4D shadow light field using a stochastic soft shadow map and converts such samples to a pre-filterable basis. The authors use EVSM to represent the visibility function, but any other pre-filterable basis could be used.

Pre-filtering techniques are a good alternative to produce real-time visually plausible soft shadows (an example is shown in Figure 2.11-(b)) with constant-time filtering. Most of them make use of Summed-Area Tables (SAT) (CROW, 1984) as their pre-filtering function to avoid the brute-force sampling proposed by the PCSS technique. However, the time to build the SAT structure increases according to the shadow map resolution used. So, pre-filtering techniques are typically scalable with respect to the average blocker depth estimation and soft shadow filtering, but do not provide scalability for high shadow map resolutions. Furthermore, the drawback shared by the pre-filtering techniques is that they are prone to light leaking or incorrect shadow computation at contact borders, making their use unsuitable for complex scenarios.

#### 2.5.4 Screen-Space Filtering

An alternative to improve the performance of the soft shadow computation is to perform some or all the soft shadow filtering in the screen space. The basic idea behind this strategy is to generate hard shadows in the camera viewpoint with traditional shadow mapping, adapt the PCSS theory to estimate a screen-space penumbra size, and blur the hard shadows by the application of a separable filter over the penumbra region.

Screen-Space Percentage-Closer Soft Shadows (SSPCSS) (MOHAMMADBAGHER et al., 2010) proposes that the PCSS framework must be fully computed in screen space. Blocker search and shadow filtering steps are filtered in screen space by the use of a separable cross bilateral filter (PHAM; VLIET, 2005). Screen-Space Anisotropic Blurred Soft Shadows (SSABSS) (ZHENG; SAITO, 2011) computes the average blocker depth in light space and performs screen-space anisotropic Gaussian blur over the penumbra size to improve the visual quality of SSPCSS. Separable Soft Shadow Mapping (SSSM) (BUADES; GUMBAU; CHOVER, 2015) proposes a separable algorithm to estimate the

Method	Property			
	Anti-aliasing	Reduced Leaking	Scalability (BD/SF)	Working space
PCSS	✗	✓	✗/✗	Light space
SAVSM	✗	✗	✗/✓	Light space
VSSM	✗	✗	✓/✓	Light space
ESSM	✗	✗	✓/✓	Light space
MSSM	✗	✗	✓/✓	Light space
SSPCSS	✗	✓	✓/✓	Screen space
SSABSS	✗	✓	✗/✓	Screen space
SSSM	✗	✓	✓/✓	Screen space

**Table 2.2** Classification of the main visually plausible soft shadow techniques proposed in the literature according to the following attributes: anti-aliasing for shadows produced with low-resolution shadow maps, reduced light leaking artifact generation, scalability with respect to the average blocker depth (BD) estimation and soft shadow filtering (SF), and working space.

average blocker depth and uses the Gaussian filtering to filter the shadows in screen space.

The main advantage of screen-space approaches over related work is that, by the use of separable filtering techniques, the soft shadow computation can be done faster. However, while this strategy may work well in scenarios such as the one shown in Figure 2.12, screen-space filtering provides just an approximation of the effect obtained by the filtering of perspectively deformed kernels in the shadow map (light) space. That is why the screen-space filtering strategy is not as accurate as the previous strategies.

In Table 2.2, we evaluate the properties of the main techniques proposed for visually plausible soft shadow rendering. Similar to the filtered hard shadow techniques, none of the visually plausible soft shadow rendering techniques is able to minimize aliasing artifacts for low-resolution shadow maps. Also, only PCSS and the screen-space techniques are able to reduce light leaking artifacts. Similar to PCF, PCSS uses a solution that does not provide scalability. In this sense, only the screen-space techniques sacrifice accuracy to achieve higher performance and scalability for the soft shadow rendering.

Visually plausible soft shadows are more accurate than hard and filtered hard shadows, but still lack realism because these shadows are computed on the basis of a single point light source. In the next section, we show the proposed techniques dedicated to solve the simplified rendering equation (2.8) by means of area light source sampling.

## 2.6 ACCURATE SOFT SHADOWS

Differently from the other techniques presented in the previous sections, accurate soft shadow techniques do not work with single point light sources. In order to evaluate the simplified rendering equation (2.8) correctly, they sample the area light source so that they can evaluate the binary visibility function  $V_{\text{ray}}$  correctly.

The most traditional version of ray tracing (WHITTED, 1980) can only reproduce hard shadows because only one shadow ray is sent to evaluate the visibility condition of the surface point. By distributing several shadow rays per area light source and

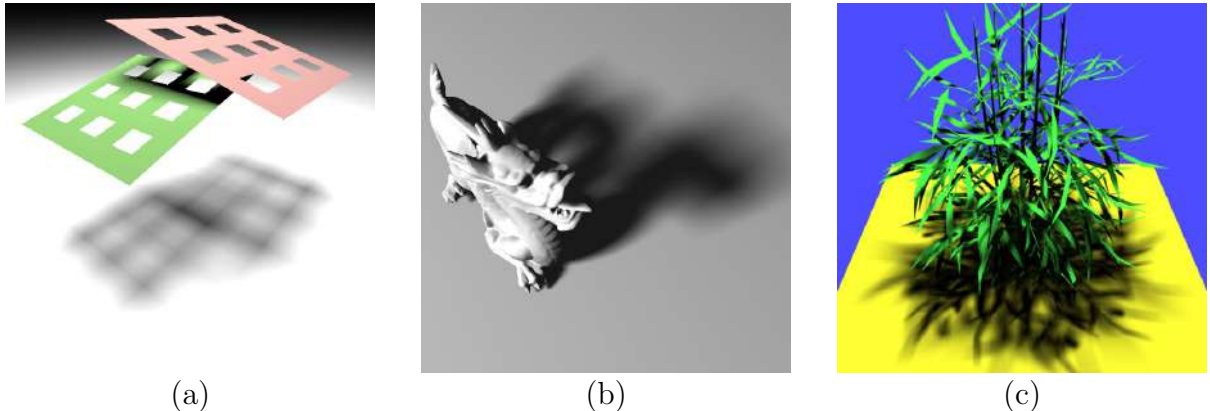


**Figure 2.13** Shadows may be computed according to the visibility function proposed by ray tracing (a), shadow volume (b) or shadow mapping (c). Images (a, b, c) are courtesy of (BILLEN; DUTRÉ, 2016; WANG et al., 2014; AGRAWALA et al., 2000) respectively.

averaging their results, one can render accurate soft shadows with ray tracing (COOK; PORTER; CARPENTER, 1984), as shown in Figure 2.13-(a). One problem with this approach is that the use of regular or random sampling patterns to evaluate the area light source generates aliasing or noise artifacts along the shadow silhouette. Since then, several sampling strategies (*e.g.*, stochastic sampling (COOK, 1986), stratified sampling (MITCHELL, 1996), uniform jitter sampling (OUELLETTE; FIUME, 2001), Poisson disc sampling (WEI, 2008), adaptive sampling (HACHISUKA et al., 2008; MEHTA; WANG; RAMAMOORTHI, 2012), line sampling (BILLEN; DUTRÉ, 2016)) have been used with ray tracing to alleviate aliasing, each one of them which its own advantages and drawbacks (RAMAMOORTHI et al., 2012; PILLEBOUE et al., 2015). However, regardless of the sampling strategy used, ray tracing demands seconds to produce accurate shadows, making this technique unsuitable to generate shadows for interactive or real-time applications.

An alternative to compute accurate shadows faster than ray tracing relies on the use of shadow volume (CROW, 1977). To compute accurate soft shadows from shadow volume, the authors of (BROTMAN; BADLER, 1984) proposed an algorithm that generates hard shadows of several shadow volumes computed for each point light source randomly positioned over the area light source and averages the hard shadow intensities to produce a single soft shadow appearance. This approach produces accurate soft shadows faster than the alternatives based on ray tracing, at the cost of prohibitively large memory footprints.

The use of penumbra wedges located in the penumbra regions is an alternative solution to compute soft shadows from shadow volume (AKENINE-MOLLER; ASSARSSON, 2002; ASSARSSON; AKENINE-MOLLER, 2003; ASSARSSON et al., 2003; LAINE et al., 2005; FOREST; BARTHE; PAULIN, 2006; LEHTINEN; LAINE; AILA, 2006), although more accurate and faster solutions do exist, such as (MORA et al., 2012; WANG et al., 2014), as shown in Figure 2.13-(b).

Since the development of the accumulation buffer (HAEBERLI; AKELEY, 1990), many algorithms have been proposed to use shadow mapping to generate hard shadows in real time and average them using the accumulation buffer.

For a linear light source, the 2D version of an area light source, only two shadow maps placed at the vertices of the linear light source are required to produce accurate soft shadows using a two-channel shadow map which stores depth and visibility (HEIDRICH; BRABEC; SEIDEL, 2000).

For static scenes, visibility precomputation is allowed and some algorithms make use of this strategy to compute interactive or real-time accurate soft shadows (HERF; HECKBERT, 1996; HECKBERT; HERF, 1997; HERF, 1997; AGRAWALA et al., 2000; ST-AMOUR; PAQUETTE; POULIN, 2005), as can be seen in Figure 2.13-(c). The clear drawback of precomputation is that, for dynamic scenes, the precomputed structures must be recalculated for every frame, decreasing the efficiency of the solution.

For dynamic scenes, alias-free shadow maps (SINTORN; EISEMANN; ASSARSSON, 2008) have been used for hard shadow estimation per light source sample. In that work, the authors could generate high-quality, accurate soft shadows at interactive frame rates, because the alias-free shadow map generation is considerably costly when compared to alternative shadow mapping approaches. The adaptive sampling solution proposed in (SCHWARZLER et al., 2012) uses a screen-space subdivision criteria to determine how many light source samples are needed to generate accurate soft shadows. Although this technique works well when the camera is far away from the scene, because a few light source samples are needed to provide visually accurate soft shadows, the subdivision step consumes too much processing time to determine the number of samples, making this approach inefficient when the camera is relatively close to penumbra regions, where a large number of light source samples are required to provide accurate soft shadows.

While the evaluation of (2.8) provides high-quality visual results, the estimation of the visibility function for several light source samples is computationally expensive (SCHWARZLER et al., 2012), preventing its use for interactive applications, such as games and augmented reality.

## 2.7 DISCUSSION

In this thesis, we aim to propose shadow rendering algorithms for real-time anti-aliasing of hard and soft shadows on the basis of the concept of shadow revectorization. To do so, we improve the theory initially proposed by related work (BONDAREV, 2014) to perform shadow anti-aliasing of higher quality, with a memory footprint as small as the one required by shadow mapping. Also, we extend the original work on shadow revectorization to support anti-aliasing of filtered hard shadows, visually plausible soft shadows, and the rendering of accurate soft shadows.

As shown in Section 2.3, shadow silhouette recovery techniques generally produce accurate hard shadows, but are inefficient in terms of processing time and memory consumption. In this thesis, we propose a new technique for efficient, accurate shadow anti-aliasing that works well for both low- and high-resolution shadow maps, while keeping performance and memory footprint as low as the ones obtained with shadow mapping.

Taking advantage of our proposed technique for silhouette recovery, we aim to present a novel technique that is able to generate anti-aliased filtered hard shadows for both low- and high-resolution shadow maps, without as much light leaking artifacts as related work, because we do not rely on shadow map pre-filtering for penumbra simulation. To achieve the desired scalability for the penumbra simulation, at the cost of higher memory consumption, we make use of Euclidean distance transform to filter the hard shadows.

On the basis of the developed filtered hard shadow techniques, we propose different techniques that take advantage of the improved hard shadow silhouette recovery strategy obtained with shadow revectorization to achieve anti-aliased soft shadow rendering. The main technique uses a screen-space approach that improves the accuracy of the existing screen-space soft shadow techniques, while providing real-time performance through the scalability for the soft shadow filtering.

Finally, our main focus of research in this thesis is the proposition of real-time techniques for efficient shadow artifact minimization. The faster existing strategy to compute accurate soft shadows relies on the evaluation of the shadow mapping visibility function over a discrete representation of the area light source. Such a discretization may occur by the uniform or adaptive sampling of the area light source. While the uniform sampling may generate several, unnecessary light source samples, which further increases the computational cost of the visibility evaluation over the area light source, the current solution for adaptive sampling is prone to aliasing, banding artifacts (due to the undersampling of the penumbra region) and consequent temporal incoherence (SCHWARZLER et al., 2012).

To improve the performance of the accurate soft shadow generation, while keeping the high visual accuracy of the solution, we propose an alternative adaptive solution strategy to generate a few, consistent light source samples to represent the area light source. By replacing the shadow mapping visibility function by a revectorization-based visibility function that already provides shadow anti-aliasing, we target to further reduce the number of light source samples required to generate accurate soft shadows.

## 2.8 SUMMARY

In this chapter, we have presented the theoretical background for shadow rendering. Moreover, we have discussed the advantages and drawbacks of the existing shadow rendering techniques with respect to the simulation of hard and soft shadows.

As we show in the next chapters, we propose a set of techniques to solve the main problem still found in both hard and soft shadow mapping techniques proposed in the literature: the aliasing artifacts. For hard shadows, we make use of the shadow revectorization to achieve the desired high visual quality of the shadow rendering. For filtered hard shadows and visually plausible soft shadows, we make use of the Euclidean distance transform to simulate penumbra with high performance and visual quality. Finally, since the main problem of the existing techniques for accurate soft shadow rendering relies on its high computational cost, we propose an adaptive solution that uses a revectorization-based visibility function to speed up the computation of accurate soft shadows.

# Chapter

# 3

*In this chapter, we present and evaluate our proposed technique that uses the concept of shadow revectorization for real-time hard shadow anti-aliasing. To further state the practical contribution of this work, we show the results of the proposed technique in the context of a game engine.*

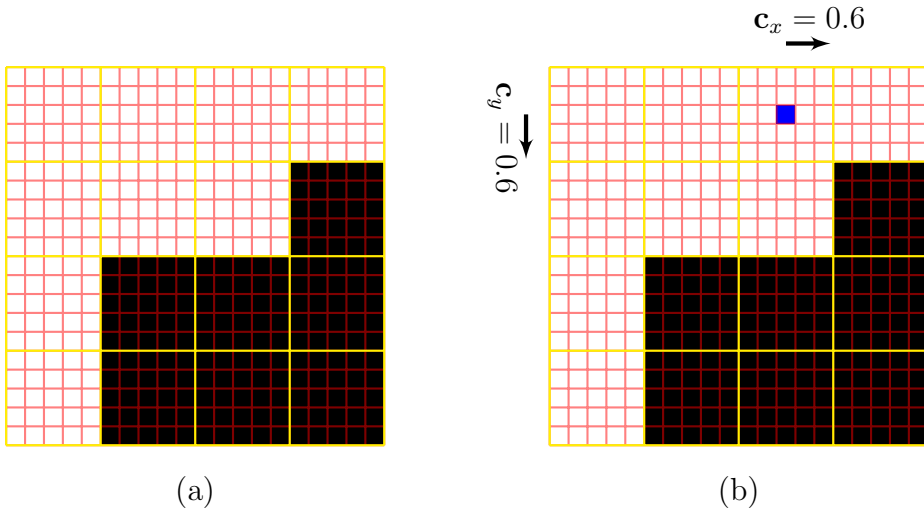
## REVECTORIZATION-BASED SHADOW MAPPING

Image revectorization may be defined as an anti-aliasing approach that uses the available image resolution to reduce the jagged pattern of an aliased region by the recovering of its approximate original color. The main advantage of such an approach is the ability to generate images of higher visual quality in real time.

In the field of real-time shadows, techniques based on shadow mapping generate aliasing artifacts along the shadow silhouette mainly when using low-resolution shadow maps for the shadow computation. In this case, the revectorization of the aliased shadow is a useful alternative to improve the shadow visual quality and its temporal coherence, while keeping the low memory consumption and real-time performance of the rendering. The first attempt for such a shadow revectorization technique (BONDAREV, 2014) considered only the aliasing present in hard shadows, required two passes on the shader, did not handle the artifacts produced by the revectorization on sloped surfaces, and required an additional texture for shadow anti-aliasing.

In this chapter, we present the Revectorization-based Shadow Mapping (RBSM), our proposed technique for hard shadow anti-aliasing that alleviates the aforementioned problems of the shadow revectorization proposed in (BONDAREV, 2014). We show how this technique can be used for conservative (Section 3.1) and non-conservative anti-aliasing (Section 3.2). This chapter covers the discussion and results mainly presented in four authored publications (MACEDO; APOLINÁRIO, 2016; MACEDO; APOLINÁRIO; AGÜERO, 2017; MACEDO et al., 2017; MACEDO; APOLINÁRIO, 2018).

To ease the explanation of the proposed approach, let us assume that each camera-view fragment (or pixel) is visually represented by a red square (as can be seen in the red grid shown in Figure 3.1-(a)), that is projected in a shadow map texel represented by a yellow square (as can be seen in the yellow grid shown in Figure 3.1-(a)). The normalized relative position (or sub-coordinates)  $\mathbf{c} \in \mathbb{R}^2$  of the camera-view fragment in the shadow map texel (Figure 3.1-(b)) is estimated by



**Figure 3.1** Shadow mapping estimates shadow intensities per projected shadow map texel (each yellow square in the yellow grid) rather than per camera-view fragment (or pixel, represented by each red square inside the red grid) (a). To help on the minimization of these aliasing artifacts, we estimate the normalized relative position  $\mathbf{c}$  of each camera-view fragment (blue square in (b)) inside the projected shadow map texel.

$$\begin{aligned} \mathbf{c}_x &= \tilde{\mathbf{p}}_x n - \lfloor \tilde{\mathbf{p}}_x n \rfloor \\ \mathbf{c}_y &= \tilde{\mathbf{p}}_y m - \lfloor \tilde{\mathbf{p}}_y m \rfloor, \end{aligned} \quad (3.1)$$

where  $\tilde{\mathbf{p}}$  represents a surface point transformed to the light source viewpoint,  $n$  and  $m$  are the shadow map width and height.

From the subtraction with the floor function in (3.1), we know that  $\mathbf{c}_x$  and  $\mathbf{c}_y$  lie in the closed unit interval  $[0, 1]$ .

### 3.1 REVECTORIZATION-BASED CONSERVATIVE SHADOW SILHOUETTE RECOVERY

### 3.1.1 Overview

RBSM is an algorithm that aims to locate shadow silhouette patterns in the scene and to use the available screen-space resolution provided by the camera view to perform shadow anti-aliasing through the revectorization of the shadow. To do that efficiently, the algorithm operates only over the lit side of the shadow silhouette, achieving what we call a conservative shadow anti-aliasing. An overview of RBSM can be seen in Figure 3.2. A pseudocode of RBSM is shown in Algorithm 1.

To minimize the shadow aliasing, RBSM defines a visibility function that works per fragment in the camera view. Much like an extension of the morphological anti-aliasing (JIMENEZ et al., 2011) for hard shadows, RBSM takes as input the shadow map (Line 2 of Algorithm 1) and the scene rendered from the camera viewpoint, with the aliased hard

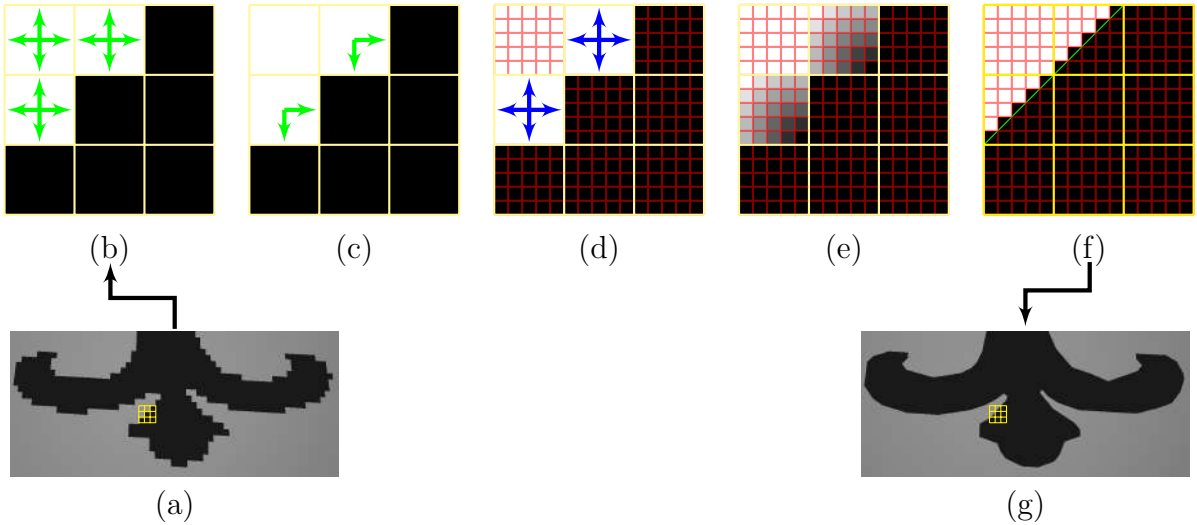


**Figure 3.2** An overview of the RBSM pipeline for conservative hard shadow anti-aliasing. Given the aliased shadow silhouettes generated by shadow mapping (a), a neighbourhood evaluation (green arrows in (b)) is conducted to detect aliased lit fragments (b) and also the directions (green arrows in (c)) of where the shadow silhouette is located (c). Then, the algorithm traverses (blue arrows in (d)) the light space (yellow grid) to determine the normalized relative distance (gray shades in (e)) of each camera-view lit fragment (each red square in the red grid) to the shadow silhouette (e). Finally, the algorithm uses a linear comparison (green line in (f)) to revectorize the shadow silhouette (f, g) in the camera space.

shadows estimated by the shadow test (Figures 3.2-(a, b) and Lines 4-5 of Algorithm 1). After the evaluation of the spatial coherency between neighbours in the shadow map (Figure 3.2-(b)), the algorithm proceeds by detecting the directions of where aliasing artifacts are located (Figure 3.2-(c), Line 6 of Algorithm 1). In RBSM, these directions (green arrows in Figure 3.2-(c)) are represented as discontinuities in the shadowing process. On the basis of the discontinuity representation, the next step of RBSM consists in the traversal of the lit side of the shadow silhouette (Figure 3.2-(d)). This traversal is performed with the goal of computing not only the size of the aliased silhouette where the fragment is located, but also the relative position of the fragment in this aliased silhouette (Line 7 of Algorithm 1). After the traversal is ended for all directions, RBSM computes the size of the aliased silhouette and the distance of each fragment to the ends of the shadow silhouette. This distance is normalized to the origin of the local coordinate system of the aliased silhouette, as shown in Figure 3.2-(e). Finally, a linear comparison between vertical and horizontal normalized distances is computed to determine whether a fragment must be revectored (put in shadow) by the algorithm (Figure 3.2-(f) and Line 8 of Algorithm 1).

### 3.1.2 Shadow Silhouette Localization

The first step of RBSM consists in the generation of the aliased hard shadows as proposed by shadow mapping. Hence, let us assume  $\mathbf{p}$  as a surface point in the camera view and

**Algorithm 1** Revectorization-based shadow mapping

---

```

1: for each frame do
2:    $S \leftarrow \text{RENDERSHADOWMAP};$ 
3:   for each surface point  $\mathbf{p}$  in camera view do
4:      $\tilde{\mathbf{p}} \leftarrow \text{TRANSFORMTOLIGHTSPACE}(\mathbf{p});$ 
5:      $V_{\text{SM}} \leftarrow \text{COMPUTESHADOWTEST}(\tilde{\mathbf{p}}, S);$ 
6:      $\mathbf{d} \leftarrow \text{COMPUTESILHOUETTEDIRECTION}(V_{\text{SM}});$ 
7:      $\mathbf{r} \leftarrow \text{ESTIMATERELATIVEPOSITION}(\mathbf{p}, \tilde{\mathbf{p}}, \mathbf{d}, S);$ 
8:      $V_{\text{RBSM}} \leftarrow \text{PERFORMANTIALIASING}(\mathbf{r}, V_{\text{SM}});$ 
9:   end for
10: end for

```

---

$\tilde{\mathbf{p}}$  is  $\mathbf{p}$  transformed into the light source view (Line 4 of Algorithm 1). Also, let  $S$  be a shadow map with  $m$  rows and  $n$  columns, where each pixel  $S(i, j) \in [0, 1]$ , with  $i \in [0, n]$  and  $j \in [0, m]$ .  $S$  stores the distance  $\tilde{\mathbf{p}}_z$  of the **closest** surface point  $\tilde{\mathbf{p}}$  seen from the light source and projected in the shadow map texture coordinates  $(i, j)$  (Line 2 of Algorithm 1). We define the binary shadow mapping test  $V_{\text{SM}}(\tilde{\mathbf{p}}_z, S(i, j)) \in \{0, 1\}$ , or simply  $V_{\text{SM}}$ , as (WILLIAMS, 1978) (Line 5 of Algorithm 1)

$$V_{\text{SM}} = \begin{cases} 0 & \text{if } \tilde{\mathbf{p}}_z > S(i, j), \\ 1 & \text{otherwise,} \end{cases} \quad (3.2)$$

which indicates that  $\mathbf{p}$  is in shadow if its distance  $\tilde{\mathbf{p}}_z$  to the light source is higher than the depth stored in the corresponding shadow map texel  $S(i, j)$ . In (3.2), the value 0 indicates that  $\mathbf{p}$  is in the umbra and 1 otherwise.

Unfortunately, the shadow test generates aliasing artifacts along the hard shadow silhouette, as shown in Figure 3.2-(a). To revectorize these aliased hard shadows, one needs to detect the directions where the aliased shadow silhouette is located. These directions can be detected according to the difference between the illumination condition of neighbour shadow map samples. So, to evaluate the coherency between neighbour shadow tests and detect shadow silhouette directions, we can define the absolute difference of neighbour shadow tests  $\mathbf{d} \in \mathbb{N}^4$  to map the 4-connected neighbourhood shadow test evaluation of  $\tilde{\mathbf{p}}$  to be

$$\begin{aligned} \mathbf{d}(V_{\text{SM}}) = & (V_{\text{SM}}(\tilde{\mathbf{p}}_z, S(i-1, j)) \oplus V_{\text{SM}}(\tilde{\mathbf{p}}_z, S(i, j))), \\ & V_{\text{SM}}(\tilde{\mathbf{p}}_z, S(i+1, j)) \oplus V_{\text{SM}}(\tilde{\mathbf{p}}_z, S(i, j)), \\ & V_{\text{SM}}(\tilde{\mathbf{p}}_z, S(i, j-1)) \oplus V_{\text{SM}}(\tilde{\mathbf{p}}_z, S(i, j)), \\ & V_{\text{SM}}(\tilde{\mathbf{p}}_z, S(i, j+1)) \oplus V_{\text{SM}}(\tilde{\mathbf{p}}_z, S(i, j))), \end{aligned} \quad (3.3)$$

where  $\oplus$  denotes the exclusive or (XOR) logical operator.

As shown in (3.3),  $\mathbf{d}$  is a 4D vector that is used to detect whether the shadow silhouette is located at the four possible directions of the 2D space (*i.e.*, left, right, top, and bottom directions). For instance,  $\mathbf{d}_x$ ,  $\mathbf{d}_y$ ,  $\mathbf{d}_z$ ,  $\mathbf{d}_w$  indicate whether the shadow silhouette is located at left ( $\mathbf{d}_x = 1$ ), right ( $\mathbf{d}_y = 1$ ), top ( $\mathbf{d}_z = 1$ ) or bottom ( $\mathbf{d}_w = 1$ ) sides of a fragment.

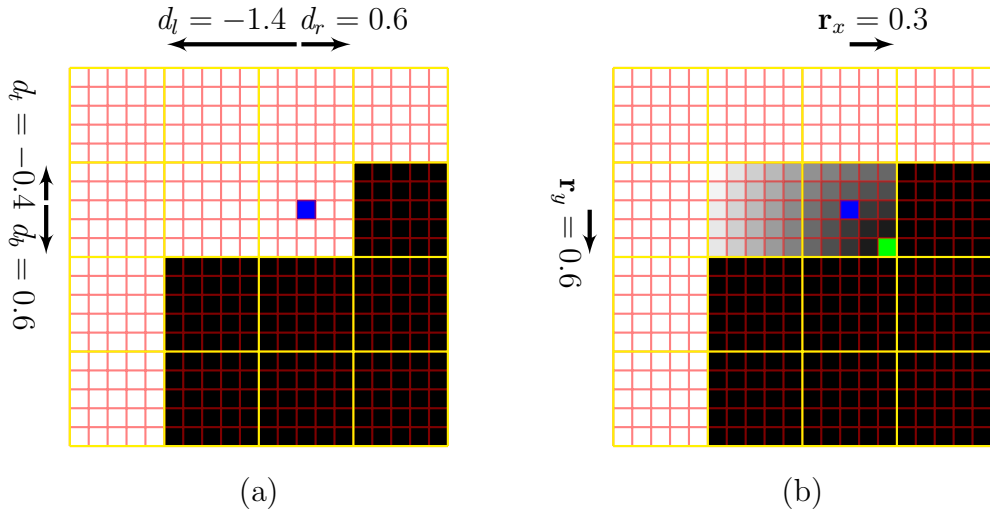


**Figure 3.3** An example of the orientation used for a fragment located in the lit side of an aliased shadow silhouette. Given a camera-view (red grid) fragment (blue square) projected in the shadow map texel (yellow grid), we may compute the distances ( $d_l, d_r, d_t, d_b$ ) of the fragment to the ends of the shadow silhouette (a). Then, we may orient and normalize these distances to the origin (green square) of the local shadow aliasing, to estimate the relative position  $\mathbf{r}$  of the fragment in the shadow silhouette (b).

In this sense, if the shadow test (3.2) states that a fragment is lit and its visibility condition is different from at least one of its neighbours in  $S$ , the vector  $\mathbf{d}$  (3.3) is able to detect where the shadow silhouettes are located and store their directions (Line 6 of Algorithm 1 and Figure 3.2-(c)).

### 3.1.3 Shadow Silhouette Traversal

Inspired by morphological anti-aliasing (JIMENEZ et al., 2011), the following step of RBSM consists in the shadow silhouette traversal, which estimates the distances of the fragments to the ends of the shadow silhouette, as shown in Figures 3.2-(d) and 3.3-(a).

On the basis of the normalized camera-view fragment position computed from (3.1), a fragment located in the lit side of a shadow silhouette can be oriented as shown in Figure 3.3. Let us denote  $d_l$ ,  $d_r$ ,  $d_t$ , and  $d_b$  to be the oriented signed distances of the fragment to the shadow silhouette computed for left, right, top, and bottom directions, respectively. In practice, each one of those distances can be computed by a sum of the integer distance between shadow map texels plus the real-valued relative position  $\mathbf{c}$  (3.1) of the fragment in the shadow map texel.

To estimate the aforementioned oriented signed distances, we need to perform, for each  $\mathbf{p}$  belonging to the lit side of the shadow silhouette, a traversal in  $S$  using  $\tilde{\mathbf{p}}$  for all the four directions of the 2D space (*i.e.*, left, right, top, and bottom directions), in order to detect the ends of the shadow silhouette. For each shadow map neighbour of a given fragment being accessed in a specific direction, RBSM computes the shadow test (3.2) for the neighbour sample and detects whether the shadow test result of the

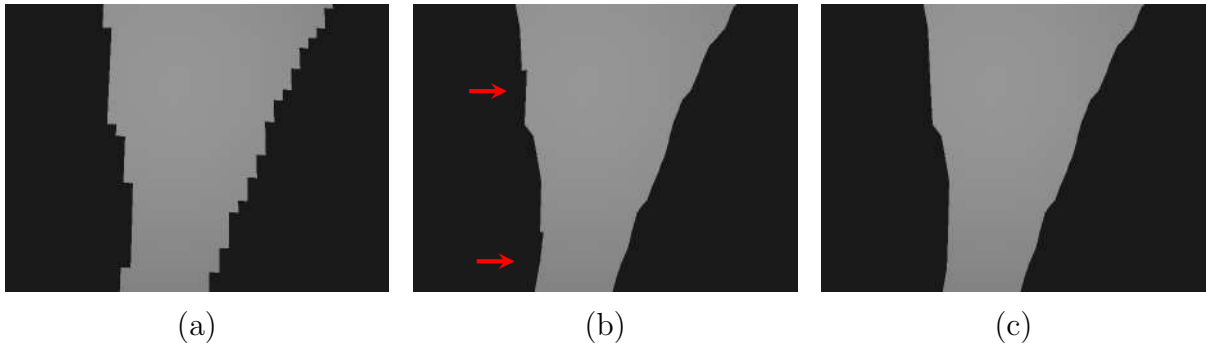


**Figure 3.4** Jagged shadow silhouettes (a) are revectorized with RBSM (b). However, artifacts (pointed by red arrows) may arise for sloped surfaces due to the depth change that affects the shadow test (b). By using our solution, we can reduce this problem (c).

neighbour is different from the one estimated for the given fragment. In this case, since the conservative RBSM operates only over lit fragments, a shadowed fragment has been detected. Therefore, we have detected the end of the shadow silhouette and we need to end the traversal in that particular direction. On the other hand, if the shadow test is the same between neighbour shadow map texels, we need to check if the neighbours share at least one discontinuity direction in common (3.3). If that is not the case, the neighbour shadow map texel accessed during traversal does not belong to the same shadow silhouette and the shadow traversal must be ended.

To better understand the shadow silhouette traversal, let us visualize the scenario shown in Figure 3.2-(d). Only for the lit fragments inside the shadow silhouette, we perform the shadow silhouette traversal (resulting in the blue arrows depicted in Figure 3.2-(d)). To the right of these fragments, there are shadowed fragments that mark the end of the shadow silhouette. To the left of these fragments, there are other lit fragments. However, since these neighbour lit fragments do not have discontinuity directions, they do not belong to the same shadow silhouette. One important note with respect to this traversal is that, while the rotation of the light source influences the visual aspect of the shadow aliasing seen from the camera viewpoint, the generated shadow map is still aligned with the light source coordinate system. Therefore, the traversal provided by RBSM over X and Y axis of the shadow map works well regardless of the orientation of the light source.

For **sloped** surfaces, the depth of the shadow map sample being accessed may change in relation to the depth accessed in the initial shadow map texel. If we use the same depth retrieved from  $\tilde{\mathbf{p}}_z$  for shadow test during traversal, artifacts may arise in the cases where the depth change in  $S(i, j)$  affects the shadow test result (Figure 3.4-(b)). To solve this problem, we use the shadow mapping assumption that  $\tilde{\mathbf{p}}_z \geq S(i, j)$  holds for every shadow map texel. Thus, to detect this depth change during traversal, we check whether  $|\tilde{\mathbf{p}}_z - S(i, j)| < \epsilon$  holds. If the condition is true, we update  $\tilde{\mathbf{p}}_z$  before the shadow test:  $\tilde{\mathbf{p}}_z = \tilde{\mathbf{p}}_z - \epsilon$ . In fact, we use an approach that ensures for fragments in shadow,  $\tilde{\mathbf{p}}_z > S(i, j)$ . Conversely, for lit fragments,  $\tilde{\mathbf{p}}_z < S(i, j)$ . As shown in Figure 3.4-(c), this

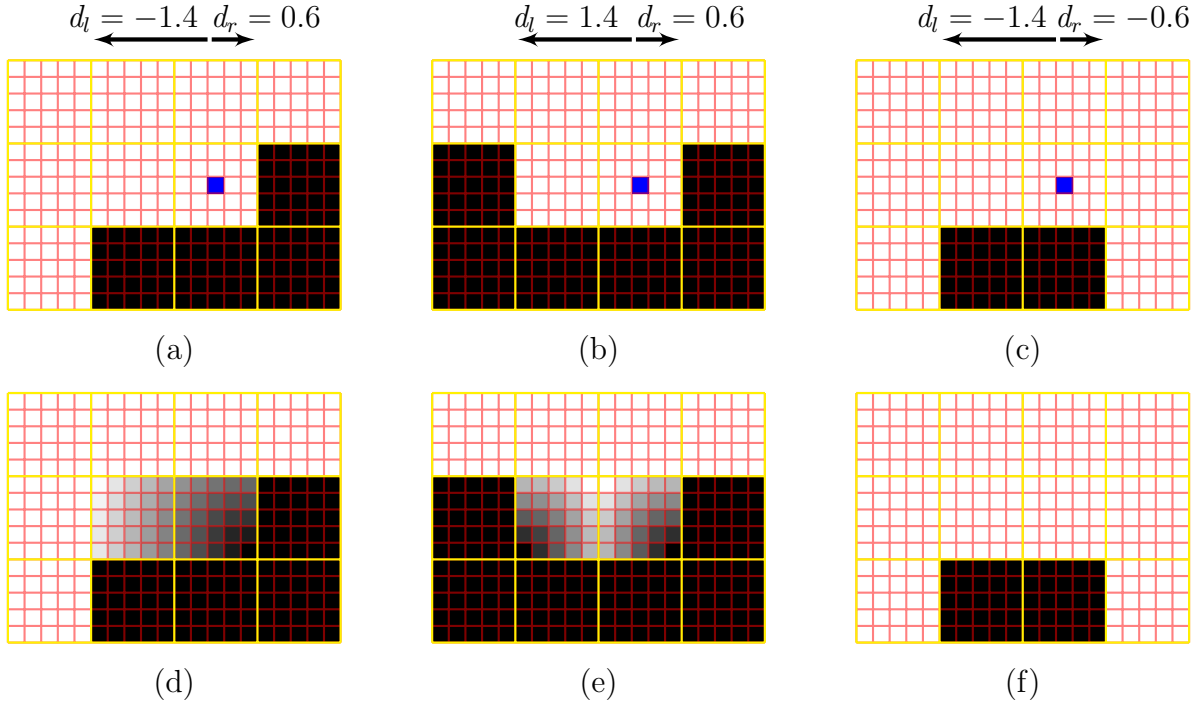


**Figure 3.5** Conservative RBSM deals basically with (a) L-shaped, (b) U-shaped and (c) I-shaped shadow silhouettes. The signed distance computed for each fragment allows the detection of the shadow silhouette shape in which the fragment is located, as well as the computation of the relative position of each fragment in the shadow silhouette (d, e, f).

solution alleviates the artifacts caused by the shadow revectorization. To detect only the cases of depth change, the value of  $\epsilon$  must be chosen carefully. In our setup, the difference between  $\tilde{\mathbf{p}}_z$  and  $\mathbf{S}(i, j)$  is relatively small. Hence, we have empirically defined  $\epsilon = 2.5 \times 10^{-5}$ , which has sufficed for all our test cases.

### 3.1.4 Shadow Silhouette Normalization

After the computation of the signed distances of the fragment to the shadow silhouette (Figure 3.3-(a)), we need to normalize such values to the unit interval, as illustrated in Figures 3.2-(e) and 3.3-(b).

As depicted in Figure 3.3-(a), each one of the oriented signed distances is positive towards the shadow silhouette and negative otherwise. On the basis of this signed distance, we can detect the type of shadow silhouette shape in which the fragment is located, as shown in Figure 3.5. Let  $T(d_1, d_2) \in \{-2, 0, 1\}$  be the following function that, for any two signed distance values  $d_1$  and  $d_2$ , is defined as

$$T(d_1, d_2) = \begin{cases} -2 & \text{if } (d_1 > 0) \wedge (d_2 > 0), \\ 0 & \text{else if } (d_1 < 0) \wedge (d_2 < 0), \\ 1 & \text{otherwise.} \end{cases} \quad (3.4)$$

As shown in Figure 3.5-(a) and Equation (3.4), an L-shaped shadow silhouette has  $T(d_1, d_2) = 1$  because both positive and negative distance values are computed for the fragment located in the shadow silhouette. As seen in Figure 3.5-(b), a lit fragment in a U-shaped shadow silhouette has  $T(d_1, d_2) = -2$  for a specific axis, because both signed distances are positive. Likewise, a lit fragment in an I-shaped shadow silhouette has  $T(d_1, d_2) = 0$  for a specific axis because both signed distances are negative, as can be seen in Figures 3.5-(c).

Assuming that  $\mathbf{r} \in \mathbb{R}^2$ , illustrated in Figure 3.3-(b), is the relative position of the fragment in the shadow silhouette,  $\mathbf{r}$  can be computed as follows

$$\begin{aligned}\mathbf{r}_x &= \max(T(d_l, d_r), 2V_{\text{SM}} - 1) \frac{|\max(T(d_l, d_r)d_l, T(d_l, d_r)d_r)|}{|d_l| + |d_r|} \\ \mathbf{r}_y &= \max(T(d_t, d_b), 2V_{\text{SM}} - 1) \frac{|\max(T(d_t, d_b)d_t, T(d_t, d_b)d_b)|}{|d_t| + |d_b|}.\end{aligned}\quad (3.5)$$

For L-shaped shadow silhouettes ( $T(d_1, d_2) = 1$ ), as illustrated in Figure 3.5-(d), Equation (3.5) computes the relative position on the basis of the positive distance values previously estimated, since they are the output of the right-handed *max* function. For fragments on the lit side of U-shaped shadow silhouettes, the function  $T(d_1, d_2)$  changes the sign of the distances computed, such that  $\mathbf{r}$  is calculated on the basis of the minimum distance value, closest to the end of the shadow silhouette, as shown in Figure 3.5-(e). Also, since  $T(d_1, d_2) = -2$ , the scale by factor 2 is used to normalize  $\mathbf{r}$  to the interval  $[0, 1]$ . For fragments located on the lit side of I-shaped shadow silhouettes, the function  $T(d_1, d_2)$  makes the relative position to be 0 since  $T(d_1, d_2)$  for any two negative distance values  $d_1$  and  $d_2$  is 0. This is illustrated in Figure 3.5-(f).

### 3.1.5 Hard Shadow Anti-Aliasing Visibility Function

To produce anti-aliased hard shadows, as depicted in Figures 3.2-(f, g), we need to take three facts into consideration: the result of the shadow test  $V_{\text{SM}}$  (3.2), the type of the shadow silhouette shape in which the fragment is located (Figure 3.6), and the normalized relative position  $\mathbf{r}$  of the fragment in the shadow silhouette (Figure 3.3).

Figure 3.6 shows the visual effect that we aim to achieve using RBSM. As shown in this figure, fragments that were estimated to be in shadow ( $V_{\text{SM}} = 0$ ) by the shadow test must remain in shadow after the shadow revectorization. On the other hand, the algorithm must not perform anti-aliasing for I-shaped shadow silhouettes (Figures 3.6-(c, f)), since the revectorization effect is best suited for L- and U-shaped shadow silhouettes (Figures 3.6-(a, b, d, e)). Fragments located at I-shaped shadow silhouettes can be easily detected by checking whether  $\mathbf{r}_x \mathbf{r}_y = 0$ , following (3.5). For lit fragments located in the L- and U-shaped shadow silhouettes, a simple linear comparison using  $\mathbf{r}$  ( $1 - \mathbf{r}_x > \mathbf{r}_y$ ) is able to determine whether the fragment must be shadowed or remain lit.

Given those circumstances, the RBSM hard shadow anti-aliasing visibility function  $V_{\text{RBSM}}(V_{\text{SM}}, \mathbf{r}) \in \{0, 1\}$  is defined as follows

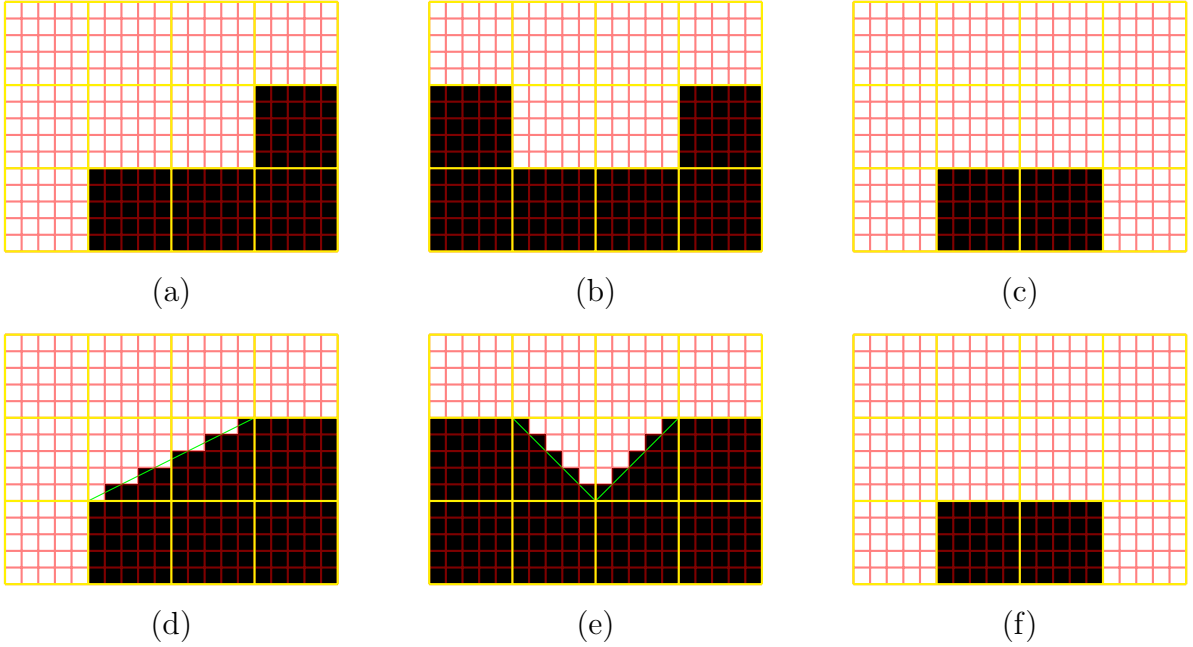


**Figure 3.6** Conservative RBSM deals with (a, d) L-shaped, (b, e) U-shaped and (c, f) I-shaped shadow silhouettes. At the top of the figure, we show the shadow silhouette produced by shadow mapping. On the bottom of the figure, we show the expected anti-aliasing produced by the conservative RBSM.

$$V_{\text{RBSM}}(V_{\text{SM}}, \mathbf{r}) = \begin{cases} 0 & \text{if } (V_{\text{SM}} = 0) \vee ((\mathbf{r}_x \mathbf{r}_y > 0) \wedge (1 - \mathbf{r}_x > \mathbf{r}_y)), \\ 1 & \text{otherwise.} \end{cases} \quad (3.6)$$

While this way of revectorizing shadow silhouettes is able to suppress aliasing artifacts with reasonable accuracy, the algorithm uses a conservative approach to perform the shadow anti-aliasing because it operates only on the lit side of the shadow silhouette, achieving a small overhead compared to shadow mapping, but introducing the overestimation of the shadow silhouette. To solve this problem, we propose an adaptation of the RBSM pipeline to reduce the overestimation of the hard shadow anti-aliasing.

### 3.2 REVECTORIZATION-BASED NON-CONSERVATIVE SHADOW SILHOUETTE RECOVERY

The main problem of the conservative anti-aliasing provided by RBSM is that, by working over the lit side of the shadow silhouette, the technique is able to recover an approximate shadow silhouette, but suffers from overestimation artifacts because the real, accurate shadow silhouette is not located only in the external part of the shadow produced by shadow mapping. By analyzing both sides (lit and shadowed), we can reduce the overestimation. In this sense, to improve the anti-aliasing provided by RBSM, we propose an extension of its pipeline to use both lit and shadowed sides of the shadow silhouette for hard shadow revectorization.

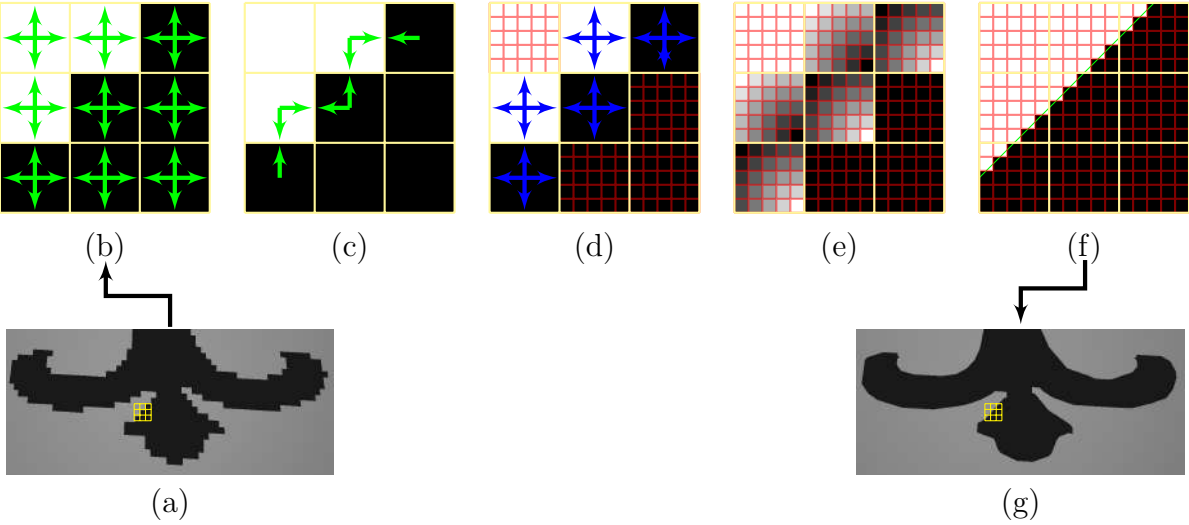


**Figure 3.7** An overview of the RBSM pipeline for non-conservative hard shadow anti-aliasing. Given the aliased shadow silhouettes generated by shadow mapping (a), a neighbourhood evaluation (green arrows in (b)) is conducted to detect aliased fragments (b) and also the directions (green arrows in (c)) of where the shadow silhouette is located (c), regardless of whether the fragment is located in the inner- or the outer-side of the shadow silhouette. Then, the algorithm traverses the light space (blue arrows in (d)) to determine the normalized relative distance (gray shades in (e)) of the camera-view fragments (red grid) located on both sides of the shadow silhouette to the shadow silhouette itself (e). Finally, taking advantage of this normalized relative distance, the algorithm computes a dilated version of the revectorized shadow, with less overestimation artifacts than the conservative approach (f, g).

### 3.2.1 Overview

An overview of the non-conservative RBSM pipeline is shown in Figure 3.7. Also, this non-conservative RBSM uses the same pseudocode shown in Algorithm 1. As can be seen in Figure 3.7-(b), after the shadow map generation, both shadow test (3.2) and neighbourhood evaluation are computed for all lit and now also shadowed fragments visible in the camera view. Then, on the basis of the neighbourhood evaluation previously computed, the algorithm detects all the fragments located in the shadow silhouette using the discontinuity representation of (3.3) for both sides of the shadow silhouette (Figure 3.7-(c)). For each fragment in the aliased shadow silhouette, a traversal is performed for both sides of the shadow silhouette (Figure 3.7-(d)) to estimate the aliasing size and the normalized relative distance of each fragment to the shadow silhouette (Figure 3.7-(e)). Then, a new visibility function is used to determine the new location of the revectorized shadow silhouette (Figures 3.7-(f, g)).

### 3.2.2 Shadow Silhouette Localization

For non-conservative anti-aliasing, we need to detect the directions where the shadow silhouette is located in both inner- and outer-sides of the shadow silhouette, because the

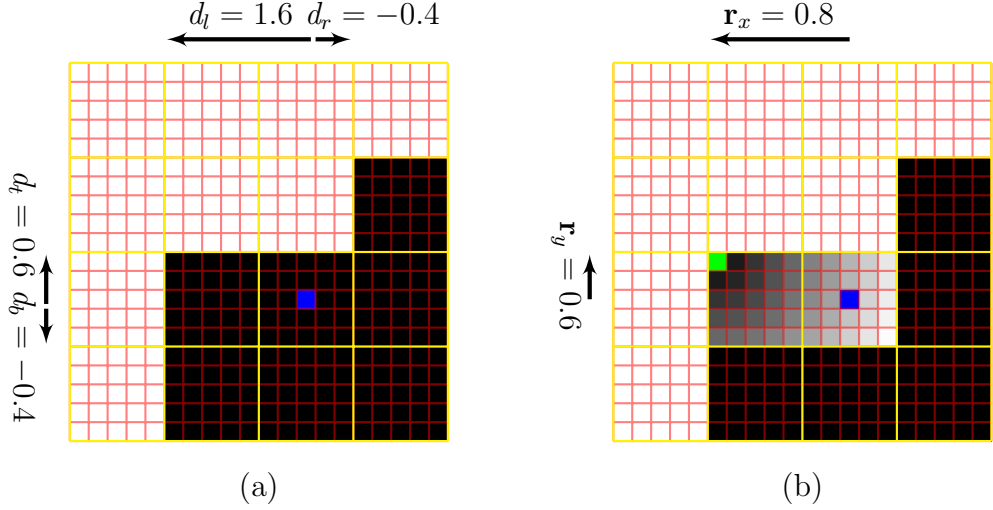


**Figure 3.8** An example of the orientation used for a fragment located in the shadowed side of an aliased shadow silhouette. Given a camera-view (red grid) fragment (blue square) projected in the shadow map texel (yellow grid), we may compute the distances ( $d_l$ ,  $d_r$ ,  $d_t$ ,  $d_b$ ) of the fragment to the ends of the shadow silhouette (a). Then, we may orient and normalize these distances to the origin (green square) of the local shadow aliasing, to estimate the relative position  $\mathbf{r}$  of the fragment in the shadow silhouette (b).

shadow anti-aliasing will cover both parts of the silhouette, as shown in Figure 3.7-(f).

For every fragment in the camera view, we compute the shadow test (3.2) and the directions of where the shadow silhouette is located (3.3). As a result of this step, we have the directions of where the shadow silhouette is located for all the fragments situated in the aliased shadow silhouette (Figure 3.7-(c)).

### 3.2.3 Shadow Silhouette Traversal

Similarly to the conservative RBSM, during the traversal of the shadow silhouette (Figure 3.7-(d)), regardless of whether the fragment is located in the lit or shadowed side of the shadow silhouette, we still need to perform the shadow test (3.2) for each neighbour shadow map texel being accessed. To detect the end of the shadow silhouette, we check if the neighbour fragment has a different visibility condition than the one estimated by the initial fragment of the traversal. In this sense, for lit fragments, the shadow silhouette ends in a shadowed fragment (Figure 3.3-(a)). On the counterpart, for shadowed fragments, the shadow silhouette ends in a lit fragment (Figure 3.8-(a)). If the visibility condition between neighbours is the same, we still compute the discontinuity directions (3.3) and check whether neighbour fragments share at least one discontinuity direction. If that is not the case, the traversal has stepped out of the lit/shadowed side of the aliased shadow silhouette.

The result of this step is the estimation of the oriented signed distance for both lit (Figure 3.3-(a)) and shadowed (Figure 3.8-(a)) fragments located in the aliased silhouette.

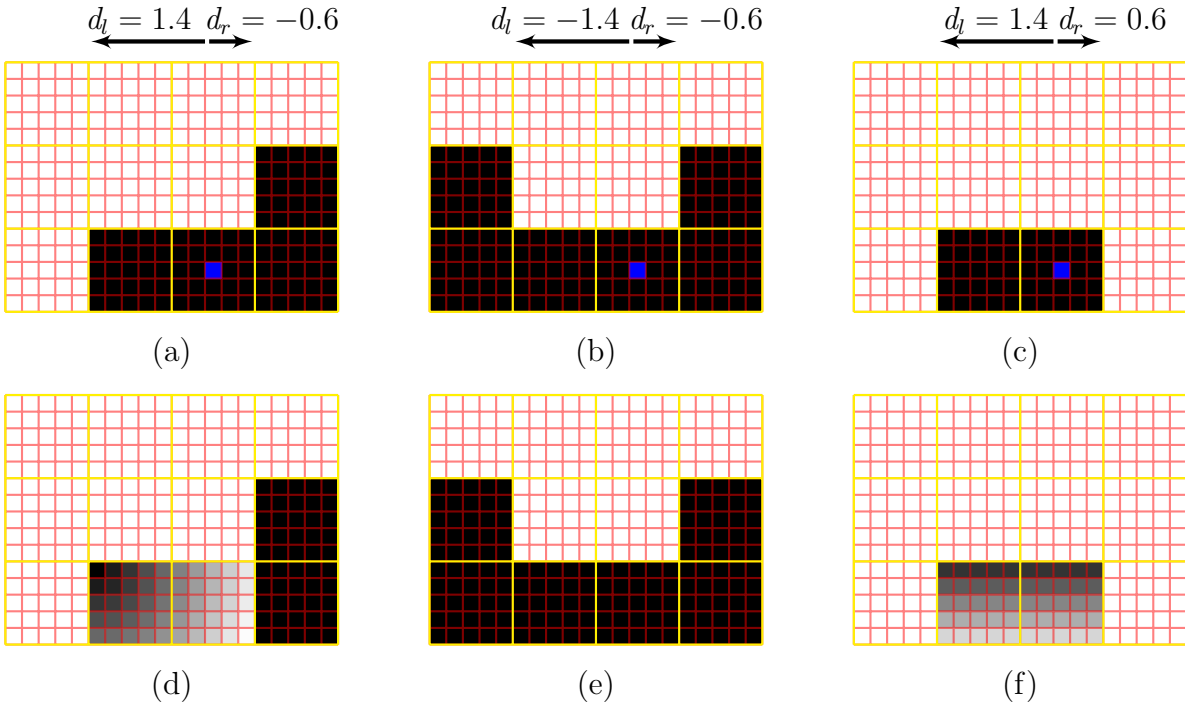


**Figure 3.9** Fragments in the shadowed side of the aliasing can be located in (a) L-shaped, (b) U-shaped and (c) I-shaped shadow silhouettes. The behaviour of the normalized relative position computation (d, e, f) is different from the one computed for lit fragments.

### 3.2.4 Shadow Silhouette Normalization

Once the shadow silhouette traversal has ended, we proceed with the computation of the normalized distance  $\mathbf{r}$  of each fragment to the corner of the aliased shadow silhouette (Figure 3.7-(e)). Depending on whether the fragment is located inside or outside the shadowed part of the silhouette, the origin of this local coordinate system (represented by the green square in Figures 3.3-(b) and 3.8-(b)) is changed. Nevertheless, the origin is still located at the corner of the aliasing.

To compute the normalized relative position of the fragment in the shadow silhouette, we use (3.4) and (3.5), following the orientation shown in Figure 3.9.

As seen in Figure 3.9-(a), an L-shaped shadow silhouette has  $T(d_1, d_2) = 1$  because we can measure positive and negative distance values for the fragment located in the shadowed part of the aliased silhouette. As depicted in Figure 3.9-(b), a shadowed fragment in a U-shaped shadow silhouette has  $T(d_1, d_2) = 0$  for a specific axis because both signed distances are negative. Finally, as shown in Figure 3.9-(c), a shadowed fragment in an I-shaped shadow silhouette has  $T(d_1, d_2) = -2$  for a specific axis, because both signed distances are positive.

For a shadow fragment located in an L-shaped shadow silhouette, Equation (3.5) computes the relative position  $\mathbf{r}$  making use of the positive distance values estimated during the shadow silhouette traversal. For fragments located on the shadowed side of both U-

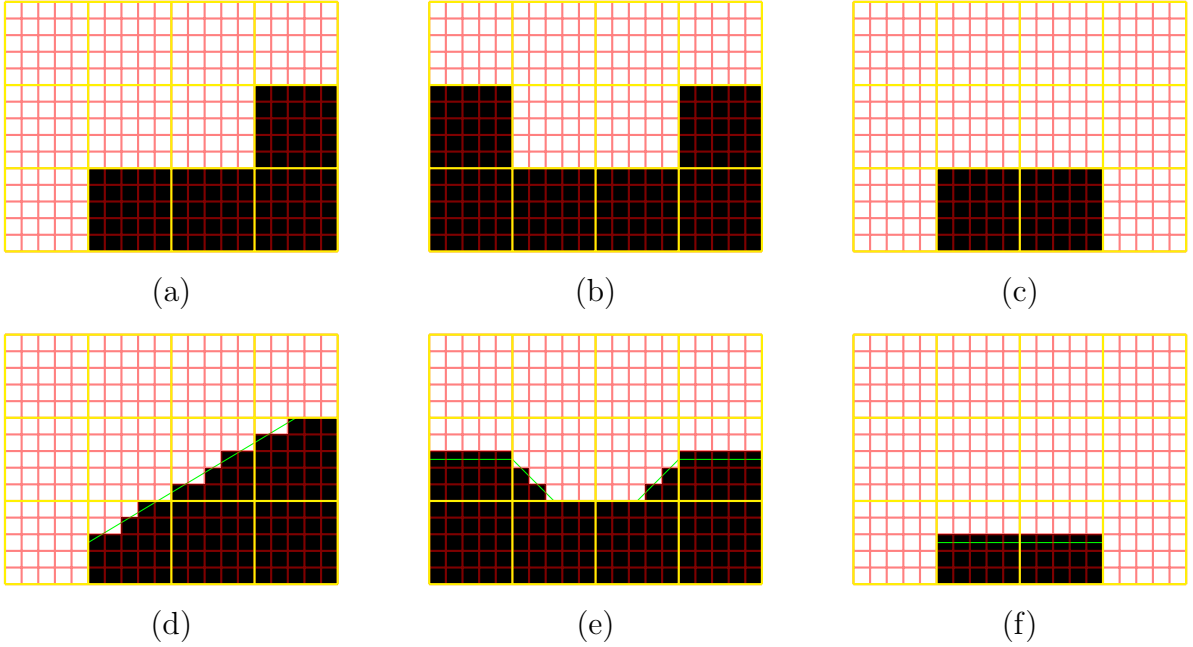


**Figure 3.10** Non-conservative RBSM for three distinct scenarios. At the top of the figure, we show the shadow silhouette produced by shadow mapping. On the bottom of the figure, we show the expected anti-aliasing produced by the non-conservative RBSM.

and I-shaped shadow silhouettes, since  $V_{SM} = 0$ , the left-handed *max* function outputs 0 for U-shaped shadow silhouettes (see Figure 3.9-(e)) and  $-1$  for I-shaped shadow silhouettes (see Figure 3.9-(f)). That scale factor makes the estimated relative positions to look like the ones illustrated in Figures 3.9-(e, f).

### 3.2.5 Hard Shadow Anti-Aliasing Visibility Function

Before proposing the non-conservative anti-aliasing, as depicted in Figures 3.7-(f, g), we first need to analyze the proposed improved visibility function  $V_{RBSM}^*(V_{SM}, \mathbf{r}) \in \{0, 1\}$  for the separate cases when the fragment is lit ( $V_{SM} = 1$ ) or is in shadow ( $V_{SM} = 0$ )

$$V_{RBSM}^*(0, \mathbf{r}) = \begin{cases} 0 & \text{if } (\mathbf{r}_x \mathbf{r}_y = 0) \vee (|\mathbf{r}_x| + |\mathbf{r}_y| > \frac{1}{2}), \\ 1 & \text{otherwise.} \end{cases} \quad (3.7)$$

$$V_{RBSM}^*(1, \mathbf{r}) = \begin{cases} 0 & \text{if } (\mathbf{r}_x \mathbf{r}_y > 0) \wedge (\mathbf{r}_x + \mathbf{r}_y < \frac{1}{2}), \\ 1 & \text{otherwise.} \end{cases} \quad (3.8)$$

As shown in Figure 3.10, for the originally shadowed part of the shadow silhouette, whenever the fragment is distant to the corner of the shadow silhouette by more than a value of  $\frac{1}{2}$  (see Figure 3.9 for a reference of the relative position computed for every shadow silhouette shape), the shadowed part is changed to be lit in (3.7). Since  $\mathbf{r}$  can be negative for shadowed fragments, according to (3.5), we use the *max* function to put this value to 0. Likewise, for the originally lit part of the shadow silhouette, whenever

the fragment is distant to the origin of the shadow silhouette by less than a value of  $\frac{1}{2}$ , the lit part is put in shadow, as shown in (3.8).

As can be seen in (3.7) and (3.8), the visibility functions are, in some way, complementary to each other. So, we can define the non-conservative visibility function as

$$V_{\text{RBSM}}^*(V_{\text{SM}}, \mathbf{r}) = \begin{cases} 0 & \text{if } (\mathbf{r}_x \mathbf{r}_y = 2V_{\text{SM}}) \vee ((|\mathbf{r}_x| |\mathbf{r}_y| > 0) \wedge ((1 - V_{\text{SM}}) \\ & \quad + (2V_{\text{SM}} - 1)(|\mathbf{r}_x| + |\mathbf{r}_y|) < \frac{1}{2})), \\ 1 & \text{otherwise.} \end{cases} \quad (3.9)$$

In the next section, we show a comparison between both implementations of RBSM, discussing in more details the advantages and drawbacks of each approach.

### 3.3 RESULTS AND DISCUSSION

In this section, we evaluate different hard shadow techniques in terms of visual quality and rendering performance. We follow related work (SEN; CAMMARANO; HANRAHAN, 2003; CHAN; DURAND, 2004) and compare both conservative and non-conservative RBSM with the traditional shadow mapping technique, as well as the stencil shadow volume (HEIDMANN, 1991) for generating ground-truth hard shadows.

We have tested our RBSM in different scenarios. For the models of Figures 3.11, 3.14 and 3.15, we evaluate how RBSM handles the aliasing artifacts generated by low-resolution shadow maps in models with low geometric complexity. In Figures 3.12 and 3.16, we evaluate how well RBSM performs anti-aliasing for shadow silhouettes that contain several intersections and fine details of the object. In Figure 3.13, we show how RBSM reduces the aliasing of the shadows generated by a complex model with fine details along its silhouette. In Figure 3.17, we test the anti-aliasing provided by RBSM in a complex scenario with trees and several overlapping objects that produce holes and aliased shadows even for high-resolution shadow maps. Finally, in Figure 3.18, we show an example of the RBSM anti-aliasing for a game-like, outdoor scenario.

#### 3.3.1 Experimental Setup

For all the tests contained in this thesis, a computer equipped with an Intel Core™ i7-3770K CPU (3.50 GHz), 8GB RAM, and an NVIDIA GeForce GTX Titan X graphics card was used to run the experimental tests. For some scenarios, OpenGL (SHREINER et al., 2013) and OpenGL Shading Language (GLSL) (ROST et al., 2009) were used to implement RBSM, shadow mapping and shadow volume. For the other scenarios, we have used the Unity Pro version 5.6.0.f3 and the Cg language (FERNANDO; KILGARD, 2003) to evaluate the performance of the conservative RBSM for distinct, game-like scenarios, typical of a game engine. Most of the figures shown in this section do not contain scenes with high-frequency textures because they could potentially mask shadow rendering irregularities. That is why we have chosen to use white textures in the ground planes and in some of the other objects.

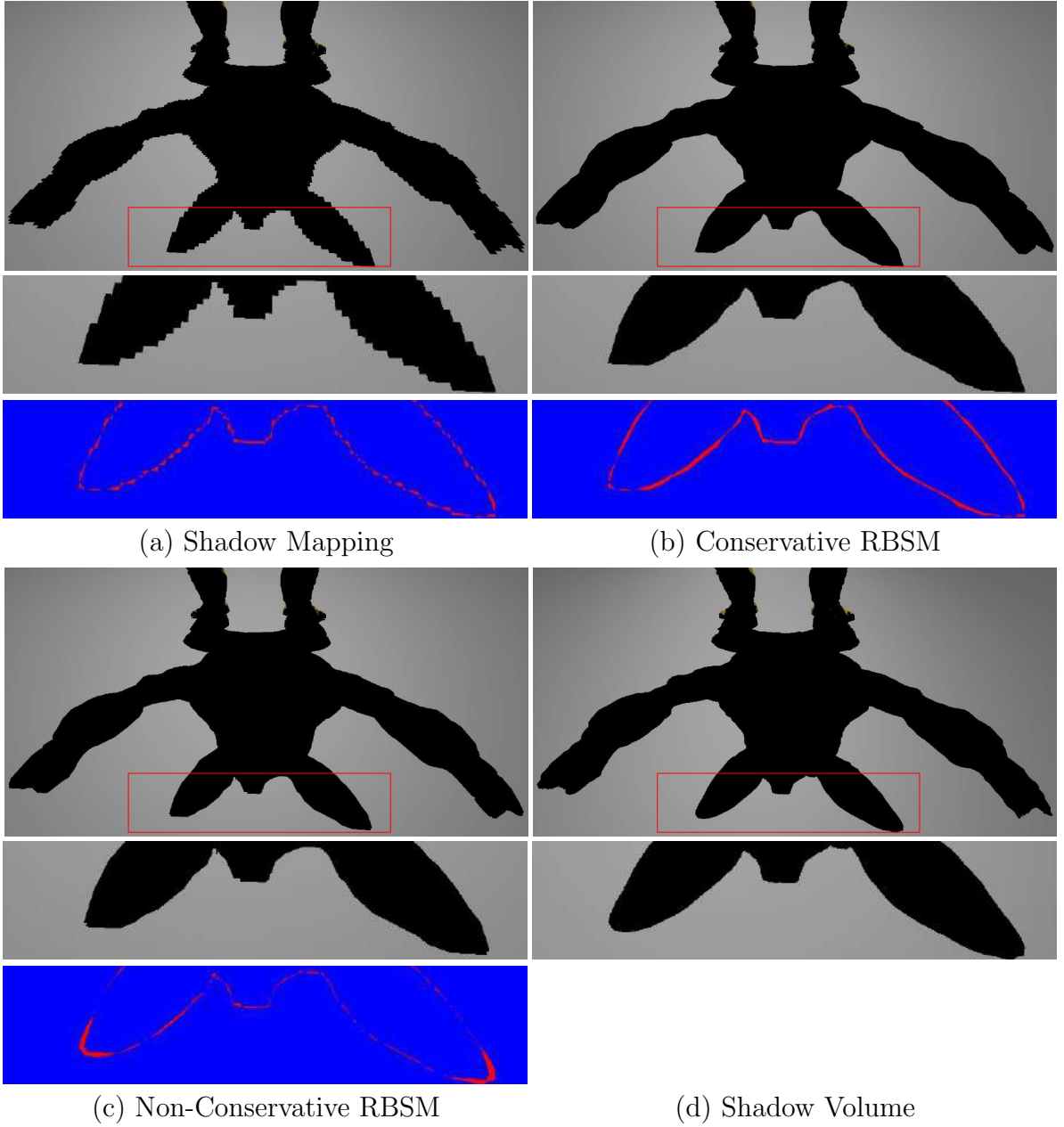


**Figure 3.11** A visual comparison between (a) shadow mapping, (b) conservative, (c) non-conservative RBSM and (d) shadow volume for the Armadillo model using a  $1024^2$  shadow map resolution. False color visualizations show the difference between the shadows generated by different hard shadow techniques (a, b, c) and the ones obtained by the reference shadow volume solution (d).

### 3.3.2 Visual Quality Evaluation

In Figures 3.11, 3.12 and 3.13, we compare both shadow mapping, RBSM and shadow volume for scenarios with different shadow map resolutions. In all the figures, it is visible

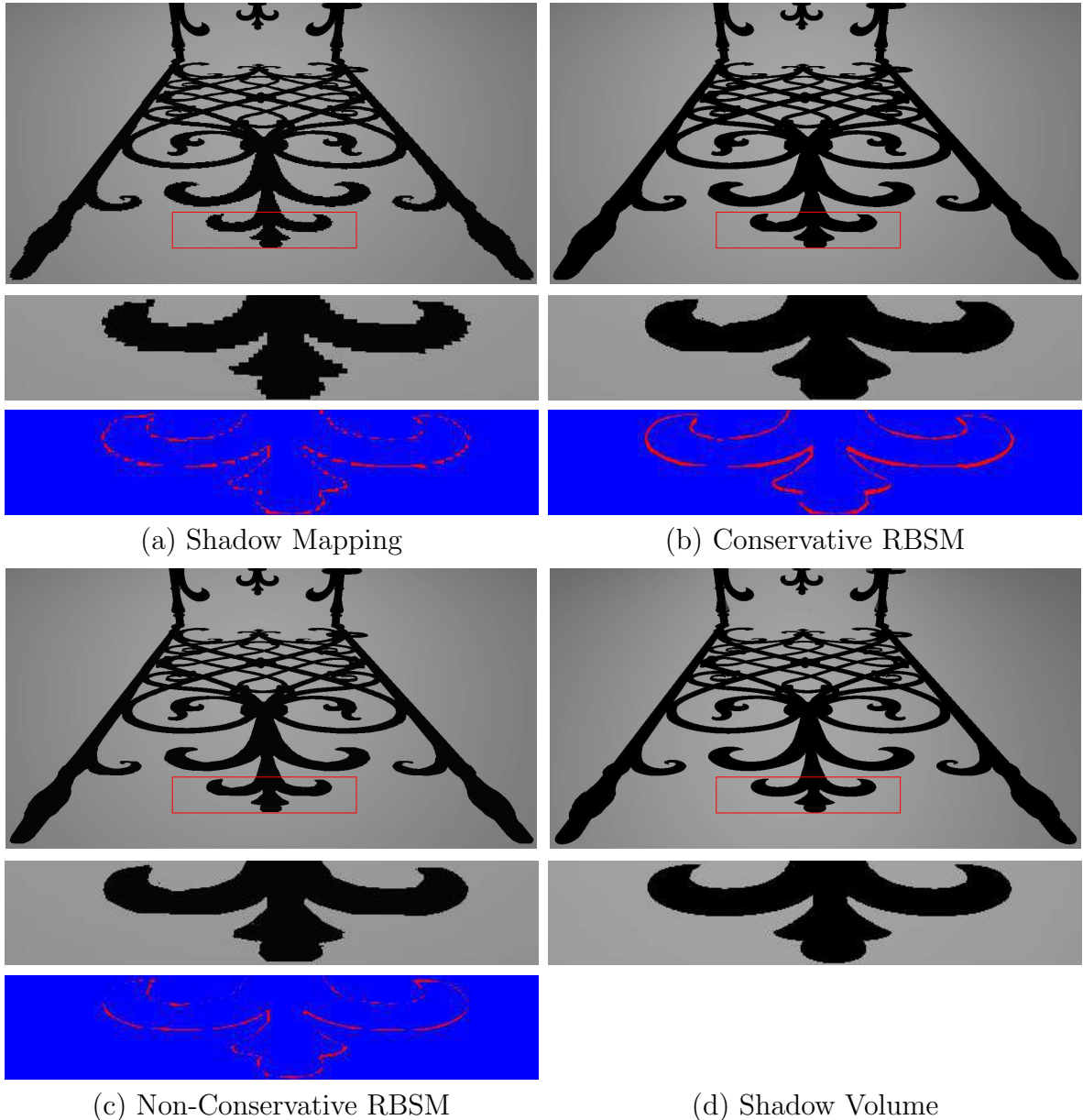


**Figure 3.12** A visual comparison between (a) shadow mapping, (b) conservative, (c) non-conservative RBSM and (d) shadow volume for the Fence model using a  $2048^2$  shadow map resolution. False color visualizations show the difference between the shadows generated by different hard shadow techniques (a, b, c) and the ones obtained by the reference shadow volume solution (d).

that RBSM improves the visual quality of the shadows generated by shadow mapping by removing the aliasing artifacts along the shadow silhouette. In all those figures, the false color visualizations also show that the non-conservative RBSM produces shadows that resemble the ones generated by shadow volume. Meanwhile, the conservative RBSM is able to successfully reduce the aliasing artifacts of shadow mapping, but causing a slight

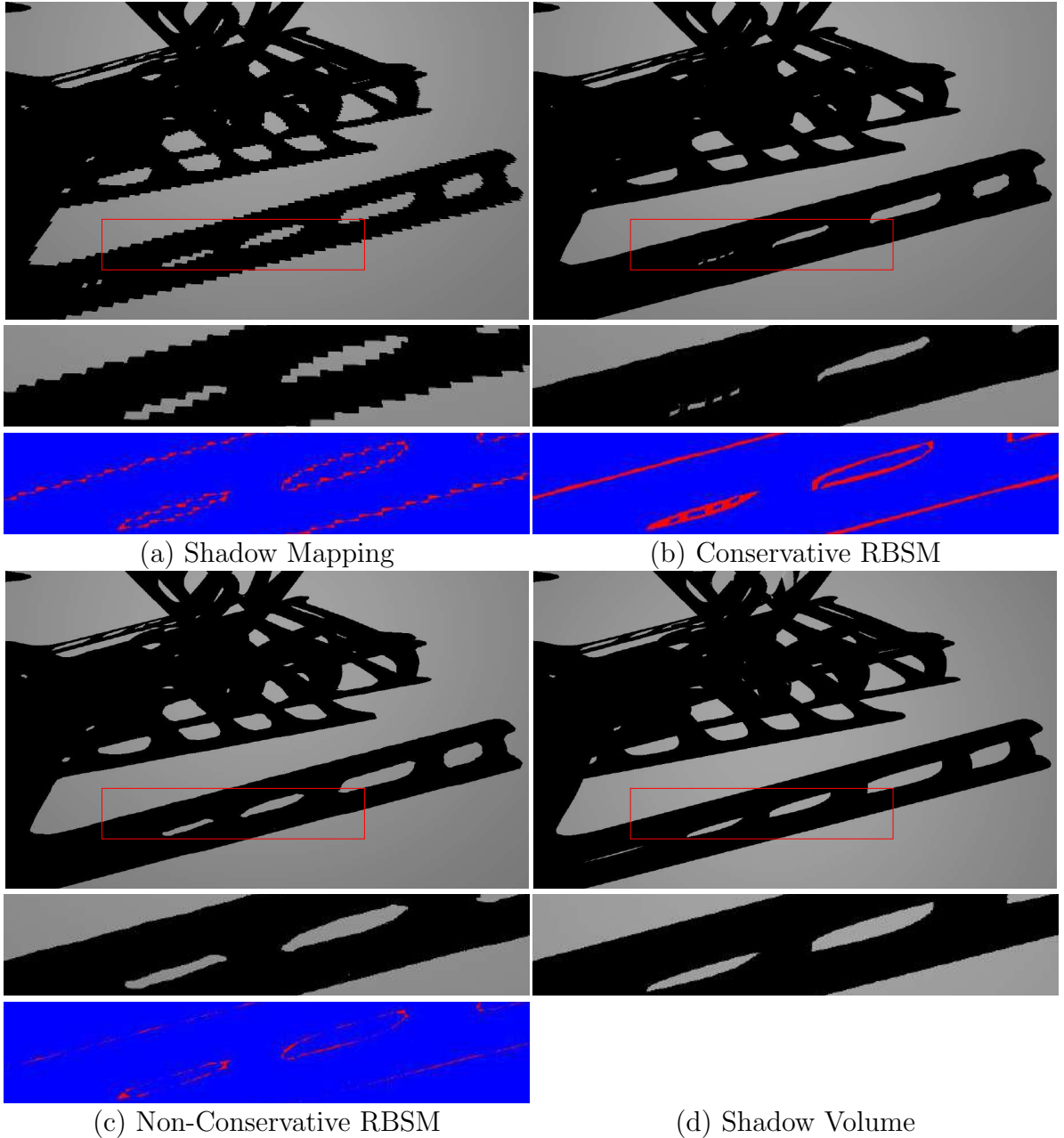


**Figure 3.13** A visual comparison between (a) shadow mapping, (b) conservative, (c) non-conservative RBSM and (d) shadow volume for the YeahRight model using a  $4096^2$  shadow map resolution. False color visualizations show the difference between the shadows generated by different hard shadow techniques (a, b, c) and the ones obtained by the reference shadow volume solution (d).

overestimation in the shadow.

In Figures 3.14, 3.15 and 3.16, we show a visual comparison between shadow mapping and conservative RBSM for different models and shadow map resolutions. We can see

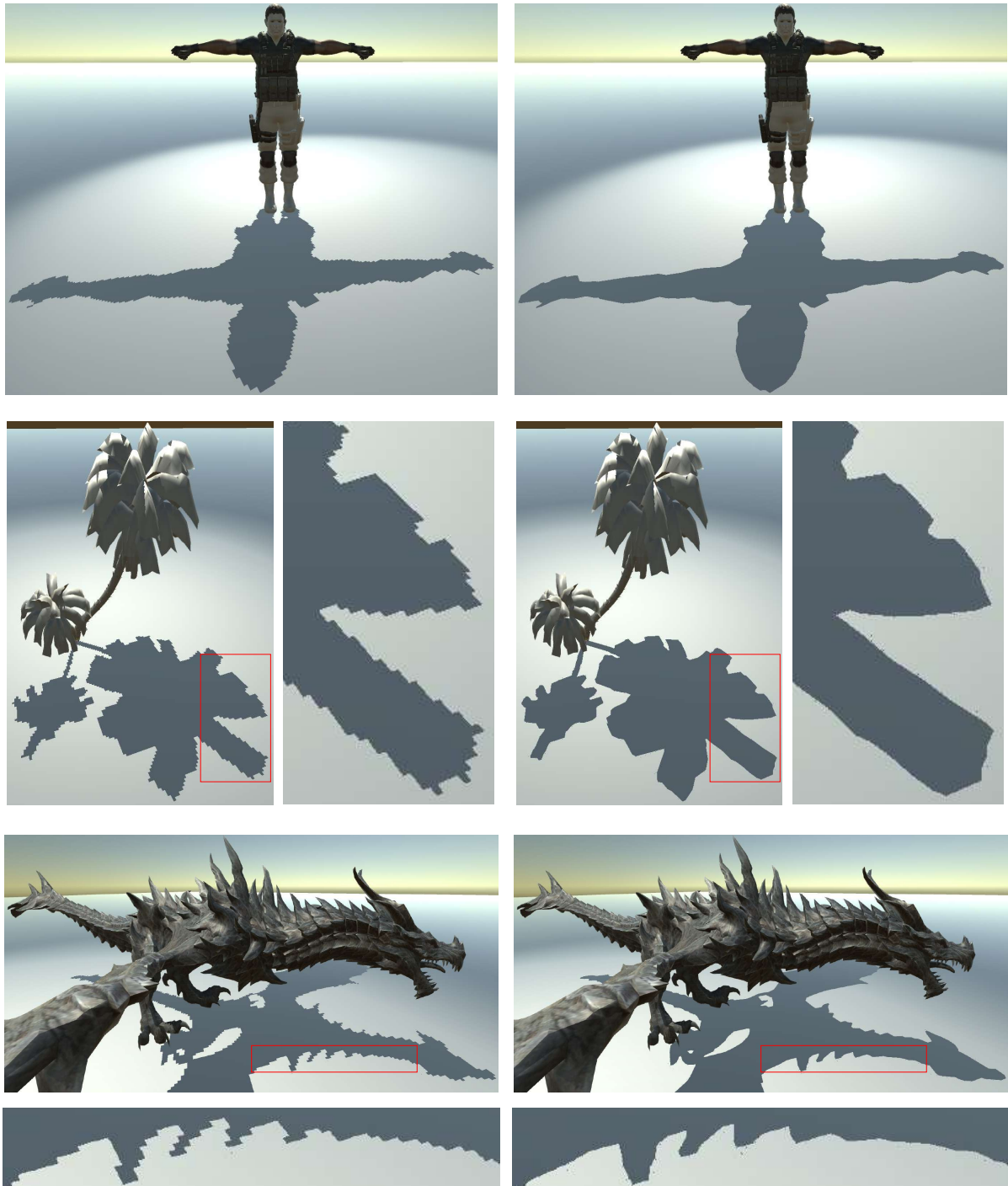


**Figure 3.14** A visual comparison between shadow mapping (left) and conservative RBSM (right) for the Chris, Coconut and Dragon models using  $256^2$ ,  $512^2$  and  $1024^2$  shadow map resolutions.

that, regardless of the shadow map resolution used, shadow mapping generates aliasing

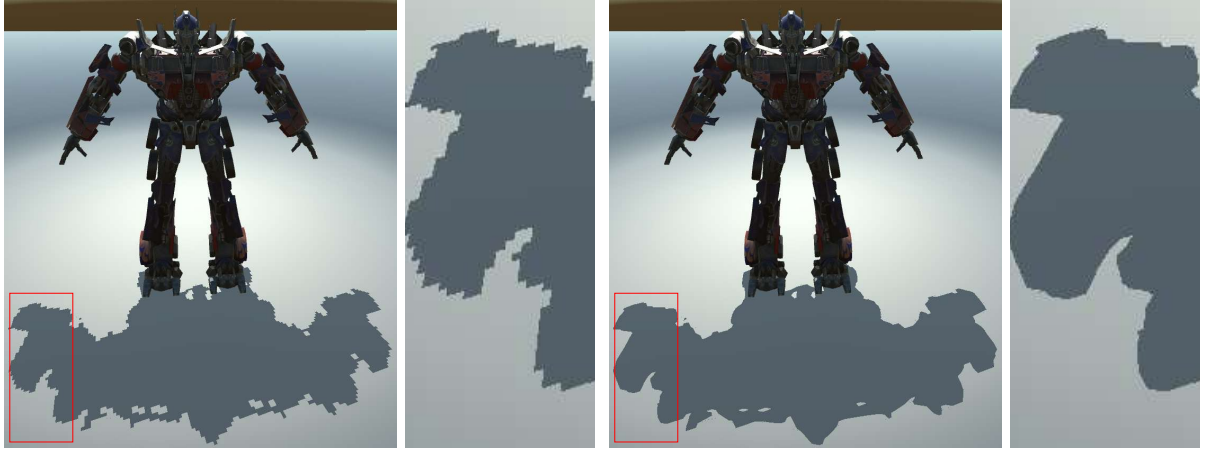


**Figure 3.15** A visual comparison between shadow mapping (left) and conservative RBSM (right) for the Robot model using a  $1024^2$  shadow map resolution.

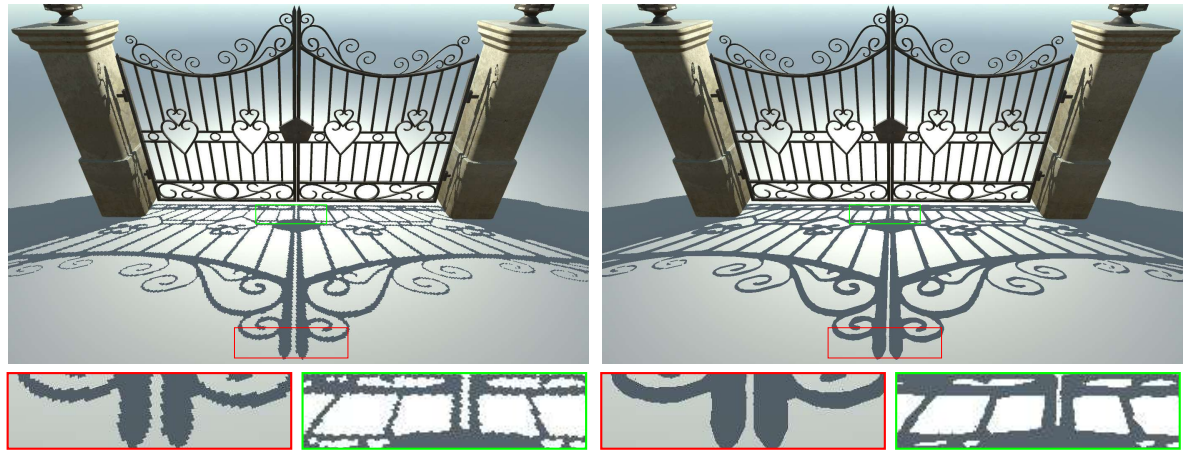


**Figure 3.16** A visual comparison between shadow mapping (left) and conservative RBSM (right) for the Gate model using a  $2048^2$  shadow map resolution.

artifacts along the shadow silhouette because the shadow map resolution is finite and does not match the pixel resolution of the camera view. Then, by traversing the shadow aliasing silhouette, RBSM is able to minimize the artifacts and improve the shadow visual quality.

The quality of the shadow revectorization is dependent on the shadow map resolution used and the quality of the aliased silhouette. RBSM works well for the scenarios shown in Figures 3.12 and 3.14 despite the use of low ( $256^2$ ) and medium ( $512^2$  and  $1024^2$ ) shadow map resolutions. In these cases, the objects and their shadows are relatively simple, since there is not much intersection between shadow silhouettes and a few fine details to be captured by the shadow map. Hence, the aliasing is the most noticeable artifact that prevents an accurate shadow rendering. So, by the use of RBSM, we can minimize these artifacts and improve the shadow visual quality efficiently. On the other hand, the

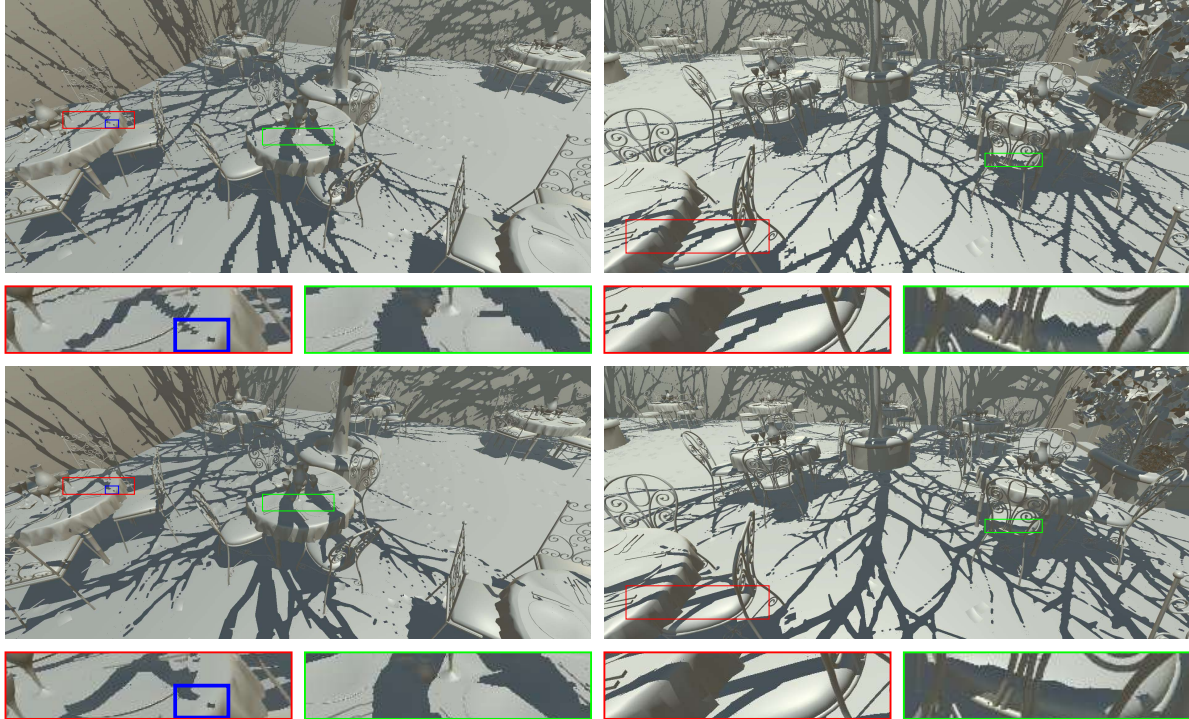


**Figure 3.17** A visual comparison between shadow mapping (top) and conservative RBSM (bottom) for the complex San Miguel model using a  $2048^2$  shadow map resolution.

<b>Scene</b>	<b>Method</b>	<b>Shadow Map Resolution</b>			
		$512^2$	$1024^2$	$2048^2$	$4096^2$
Figure 3.11	Shadow Mapping	3.28 ms	3.31 ms	3.36 ms	3.68 ms
	Conservative RBSM	3.48 ms	3.63 ms	3.82 ms	4.43 ms
	Non-conservative RBSM	3.58 ms	3.66 ms	3.86 ms	4.48 ms
	Shadow Volume	145.9 ms	145.9 ms	145.9 ms	145.9 ms
Figure 3.12	Shadow Mapping	3.02 ms	3.03 ms	3.10 ms	3.34 ms
	Conservative RBSM	3.28 ms	3.38 ms	3.52 ms	4.28 ms
	Non-conservative RBSM	3.34 ms	3.41 ms	3.62 ms	4.39 ms
	Shadow Volume	153.8 ms	153.8 ms	153.8 ms	153.8 ms
Figure 3.13	Shadow Mapping	9.14 ms	9.25 ms	9.31 ms	9.58 ms
	Conservative RBSM	9.44 ms	9.51 ms	9.64 ms	10.27 ms
	Non-conservative RBSM	9.52 ms	9.56 ms	9.72 ms	10.39 ms
	Shadow Volume	338.9 ms	338.9 ms	338.9 ms	338.9 ms

**Table 3.1** Rendering performance for different hard shadow techniques for varying shadow map resolution. Scenes were rendered at an output  $720p$  resolution.

shadows shown in the red closeups of Figures 3.13, 3.15 and in the green closeup of Figure 3.16 have a more complex shape, with several intersections in the shadow silhouette and fine details captured by the shadow map, respectively. In these cases, RBSM minimizes

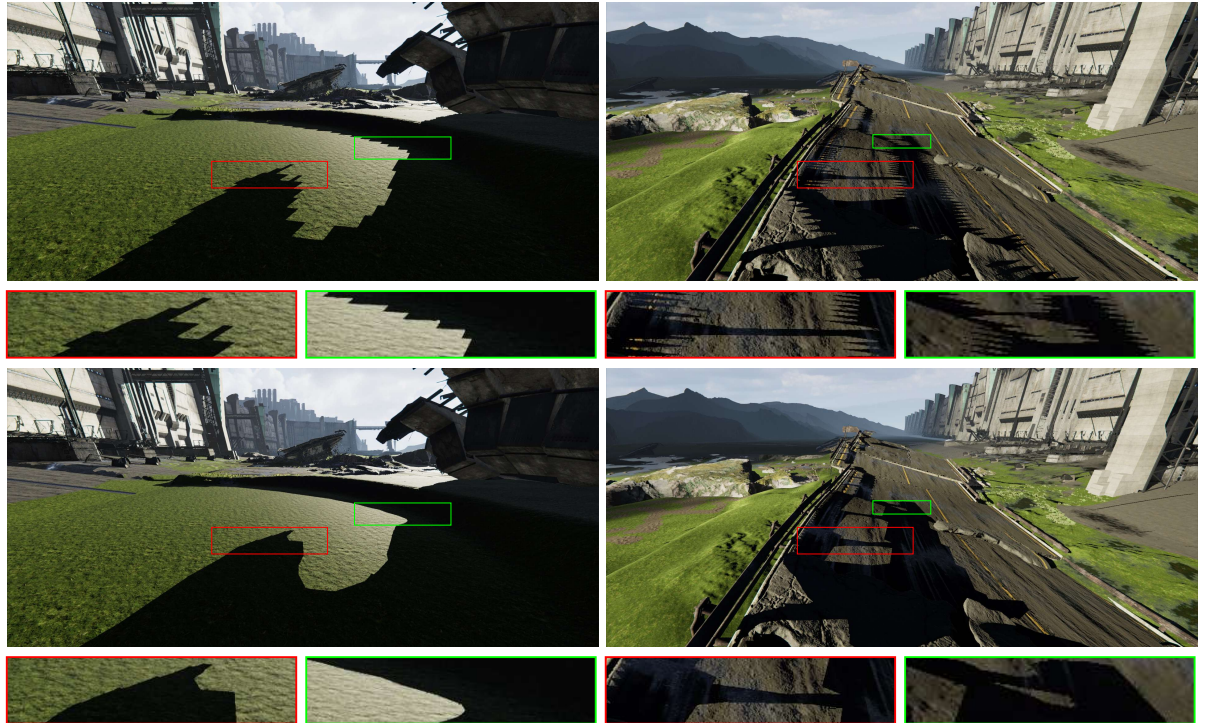


**Figure 3.18** A visual comparison between shadow mapping (top) and conservative RBSM (bottom) for the exterior environment of the Unity’s Adam model using a  $2048^2$  shadow map resolution.

<b>Scene</b>	<b>Method</b>	<b>Output Resolution</b>		
		<i>480p</i>	<i>720p</i>	<i>1080p</i>
Figure 3.11	Shadow Mapping	2.92 ms	3.31 ms	4.00 ms
	Conservative RBSM	3.17 ms	3.63 ms	4.39 ms
	Non-conservative RBSM	3.19 ms	3.66 ms	4.45 ms
	Shadow Volume	80.31 ms	145.9 ms	307.6 ms
Figure 3.12	Shadow Mapping	2.70 ms	3.03 ms	3.69 ms
	Conservative RBSM	2.95 ms	3.38 ms	4.01 ms
	Non-conservative RBSM	3.01 ms	3.41 ms	4.24 ms
	Shadow Volume	81.43 ms	153.8 ms	333.3 ms
Figure 3.13	Shadow Mapping	8.91 ms	9.25 ms	9.94 ms
	Conservative RBSM	9.15 ms	9.51 ms	10.2 ms
	Non-conservative RBSM	9.19 ms	9.56 ms	10.3 ms
	Shadow Volume	190.1 ms	338.9 ms	713.9 ms

**Table 3.2** Rendering performance for different hard shadow techniques for varying output resolution. Scenes were rendered at a  $1024^2$  shadow map resolution.

the aliasing artifacts at the cost of causing a shadow overestimation, suppressing some details of the original shadow silhouette.

<b>Scene</b>	<b>Method</b>	<b>Shadow Map Resolution</b>			
		Low ( $256^2$ )	Medium ( $512^2$ )	High ( $1024^2$ )	Very High ( $2048^2$ )
Figure 3.14-top	Shadow Mapping	4.96 ms	4.99 ms	5.01 ms	5.03 ms
	RBSM	5.03 ms (1.41%)	5.07 ms (1.60%)	5.10 ms (1.79%)	5.12 ms (1.78%)
Figure 3.14-medium	Shadow Mapping	5.14 ms	5.16 ms	5.17 ms	5.20 ms
	RBSM	5.14 ms (0.00%)	5.19 ms (0.58%)	5.20 ms (0.58%)	5.21 ms (0.19%)
Figure 3.14-bottom	Shadow Mapping	5.06 ms	5.09 ms	5.11 ms	5.12 ms
	RBSM	5.14 ms (1.58%)	5.16 ms (1.37%)	5.20 ms (1.76%)	5.22 ms (1.95%)
Figure 3.15	Shadow Mapping	5.08 ms	5.11 ms	5.12 ms	5.14 ms
	RBSM	5.14 ms (1.18%)	5.16 ms (0.97%)	5.18 ms (1.17%)	5.22 ms (1.55%)
Figure 3.16	Shadow Mapping	5.07 ms	5.08 ms	5.14 ms	5.16 ms
	RBSM	5.12 ms (0.98%)	5.14 ms (1.18%)	5.15 ms (0.19%)	5.18 ms (0.38%)
Figure 3.17	Shadow Mapping	5.02 ms	5.03 ms	5.04 ms	5.04 ms
	RBSM	5.08 ms (1.19%)	5.10 ms (1.39%)	5.11 ms (1.38%)	5.13 ms (1.78%)
Figure 3.18	Shadow Mapping	7.43 ms	7.46 ms	7.48 ms	7.69 ms
	RBSM	7.46 ms (0.40%)	7.51 ms (0.67%)	7.57 ms (1.20%)	7.74 ms (0.65%)

**Table 3.3** Rendering performance (including percentual of overhead) for shadow mapping and RBSM for varying shadow map resolution. Scenes were rendered at an output  $1080p$  resolution.

In Figure 3.17, we show a more complex scenario that contains many structures with fine details (trees), non-planar shadow receivers (chairs on the floor) and multiple objects that overlap each other. In this case, shadow mapping not only generates the aliasing artifacts, but is also not able to capture the fine details of the light blocker objects, causing the appearance of holes along the shadow silhouette (see the blue rectangles in Figure 3.17). RBSM helps on the minimization of shadow aliasing artifacts (see the closeups of Figure 3.17), but is not able to solve the problem of the shadow holes caused by the insufficient shadow map resolution used.

In Figure 3.18, we show that our shadow anti-aliasing implementation works not only for indoor environments, but also for large outdoor environments with high-detailed structures, such as vegetations, streets and buildings. The closeups in Figure 3.18 show that a shadow map with insufficient resolution for outdoor scenes clearly generates shadow aliasing artifacts that can be effectively suppressed by RBSM. Hence, we can see that RBSM is an algorithm able to provide shadow anti-aliasing for planar (*e.g.*, shadows seen in the white ground planes of Figures 3.11, 3.12 and 3.13) and non-planar shadow receivers (Figure 3.17), simple (Figures 3.11, 3.14 and 3.15) and complex scenarios in

<b>Scene</b>	<b>Method</b>	<b>Output Resolution</b>		
		<i>720p</i>	<i>1080p</i>	<i>2160p</i>
Figure 3.14-top	Shadow Mapping	5.01 ms	5.03 ms	5.04 ms
	RBSM	5.11 ms (1.99%)	5.12 ms (1.78%)	5.12 ms (1.58%)
Figure 3.14-medium	Shadow Mapping	5.19 ms	5.20 ms	5.20 ms
	RBSM	5.19 ms (0.00%)	5.21 ms (0.19%)	5.22 ms (0.38%)
Figure 3.14-bottom	Shadow Mapping	5.11 ms	5.12 ms	5.14 ms
	RBSM	5.16 ms (0.97%)	5.22 ms (1.95%)	5.34 ms (3.89%)
Figure 3.15	Shadow Mapping	5.02 ms	5.14 ms	5.21 ms
	RBSM	5.18 ms (3.18%)	5.22 ms (1.55%)	5.24 ms (0.57%)
Figure 3.16	Shadow Mapping	5.05 ms	5.16 ms	5.17 ms
	RBSM	5.10 ms (0.99%)	5.18 ms (0.38%)	5.25 ms (1.54%)
Figure 3.17	Shadow Mapping	4.99 ms	5.04 ms	5.07 ms
	RBSM	5.03 ms (0.80%)	5.13 ms (1.78%)	5.14 ms (1.38%)
Figure 3.18	Shadow Mapping	7.49 ms	7.69 ms	15.08 ms
	RBSM	7.63 ms (1.86%)	7.74 ms (0.65%)	15.55 ms (3.11%)

**Table 3.4** Rendering performance (including percentual of overhead) for shadow mapping and RBSM for varying output resolution. Scenes were rendered at a  $1024^2$  shadow map resolution.

small (Figure 3.13), medium (Figure 3.17) and large (Figure 3.18) scale.

### 3.3.3 Rendering Time Evaluation

Tables 3.1 and 3.2 show timing results obtained from different hard shadow techniques in our developed application. Shadow mapping and RBSM techniques are almost two orders of magnitude faster than shadow volume, generating shadows in real time, regardless of the shadow map or output resolution used. It is worthy to note that RBSM is less than 1 millisecond slower than shadow mapping, while providing an improved visual quality for the hard shadow rendering. Meanwhile, to reduce the overestimation of the conservative RBSM, non-conservative RBSM demands an overhead of less than 0.3 milliseconds to provide an improved hard shadow anti-aliasing.

To corroborate the results shown in Tables 3.1 and 3.2, we measured the average processing time obtained in the Unity game engine to run the scenarios shown in Figures 3.14, 3.15, 3.16, 3.17 and 3.18. The results were reported in Tables 3.3 and 3.4, for varying shadow map and output resolutions. Similarly to the shadow mapping technique, RBSM becomes slower as long as both shadow map (Table 3.3) and output resolutions

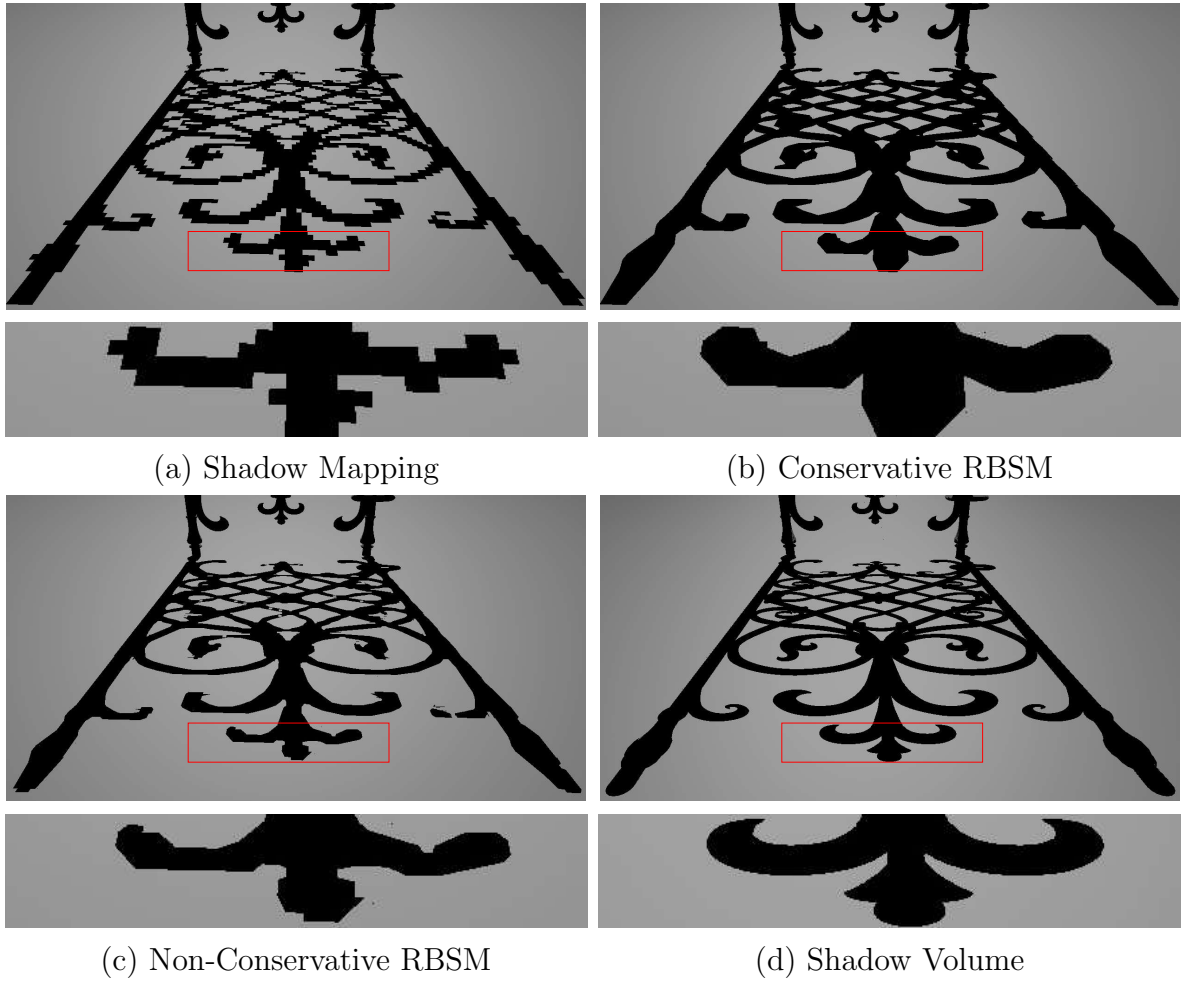


**Figure 3.19** A visual comparison between (a) shadow mapping, (b) conservative, (c) non-conservative RBSM and (d) shadow volume for the Fence model using a  $512^2$  shadow map resolution.

(Table 3.4) are increased. Fortunately, the percentage of overhead added by RBSM keeps small regardless of the shadow map or output resolution used, proving that the RBSM technique is scalable with respect to these changes in resolution and adds a small overhead of processing time to shadow mapping.

Both Table 3.3 and Table 3.4 show that the RBSM technique is about 0.01 to 0.5 milliseconds (or between 0.1% and 3.9%) slower than shadow mapping for the hardware setup used. Meanwhile, we can see from all the figures shown in this paper that RBSM greatly improves the visual quality of the shadow. Hence, we believe that RBSM proved to be an efficient hard shadow anti-aliasing technique, because it can leverage the shadow visual quality, while adding a pretty small overhead of  $\sim 1.2\%$ , in average, in the total frame time of a popular game engine.

### 3.3.4 Limitations

Similar to other image-based hard shadow techniques, the main limitation of the anti-aliasing provided by RBSM relies on its accuracy, that is highly dependent on the shadow map resolution used. For instance, as can be seen in Figure 3.19, for a low-resolution shadow map, RBSM minimizes the aliasing problem, but does not recover an accurate shadow silhouette at the shadowed region, introducing shadow overestimation (Figure 3.19-(b)) or producing shadowed shapes (Figure 3.19-(c)) that deviate from the ones obtained by accurate hard shadow techniques (Figure 3.19-(d)). By comparing Figures 3.12 and 3.19, we can see that just by increasing the shadow map resolution, we can minimize such a problem.

Because the technique does not rely on additional geometric details to perform the anti-aliasing, RBSM does not handle holes caused by the use of an insufficient shadow map resolution. Moreover, for models with fine details, the revectorization does not perform well for low-resolution shadow maps, since the shadow map is not able to capture the fine geometric details of the model.

The visibility functions of both conservative and non-conservative RBSM may introduce some small artifacts along the anti-aliased shadow silhouette due to the shadow silhouette traversal step, that may compute the oriented signed distances incorrectly due to small depth changes in the geometry. The solution proposed in Section 3.1.3 helps minimizing these artifacts.

## 3.4 SUMMARY

In this chapter, we have presented the RBSM, a hard shadow mapping technique that does not rely on an additional texture or geometric information to perform real-time hard shadow anti-aliasing. By traversing the shadow silhouette, RBSM is able to minimize aliasing by the definition of a visibility function that closes the aliased silhouette, recovering an approximate hard shadow silhouette.

Two ways to perform the shadow revectorization were presented. The first, called conservative RBSM, operates only over the lit side of the shadow silhouette, achieving real-time hard shadow anti-aliasing, but promoting shadow overestimation. The second, called non-conservative RBSM, operates over both lit and shadowed sides of the shadow silhouette to produce an anti-aliasing with higher accuracy than the one provided by conservative RBSM, at the cost of slightly increased processing time.

Compared to shadow mapping, RBSM reduces shadow aliasing in real time. Compared to shadow volume, RBSM produces high-quality shadows that resemble the ones obtained by such an accurate hard shadow technique, but RBSM is pretty much faster than shadow volume, being more adequate for real-time applications.

To show that RBSM is easy to implement, meanwhile providing a practical contribution for this thesis, an integration of RBSM into the popular Unity game engine has been done. In the Unity game engine, we could compare both shadow mapping and RBSM techniques for different scenarios, ranging from the simplest to the most complex, game-like ones. In this case, the visual quality and performance obtained by RBSM reinforced

the idea that the shadow revectorization is ready to be used for practical applications that make use of hard shadow rendering.

To further expand the theory of RBSM, in the next chapters we show how RBSM can be used to enhance the visual quality of shadows that simulate the penumbra effect.

# Chapter

# 4

*In this chapter, we present the extension of RBSM to produce filtered hard shadows, or fixed-size penumbra, in real time. To do so efficiently, we make a novel use of the concept of Euclidean distance transform to generate the penumbra effect with high quality.*

## REVECTORIZATION-BASED FILTERED SHADOW MAPPING

As discussed in the previous chapter, both conservative and non-conservative versions of Revectorization-based Shadow Mapping (RBSM) were originally designed to provide anti-aliasing for hard shadows. In this chapter, we present two new techniques that extend the RBSM theory to provide anti-aliasing for filtered hard shadows, or fixed-size penumbra. The first technique, called Revectorization-based Percentage-Closer Filtering (RPCF), is a direct extension of RBSM for filtered hard shadow rendering. RPCF generates fixed-size penumbra with higher quality than Percentage-Closer Filtering (PCF) at the cost of being slower than PCF because of the use of the shadow revectorization as a basis for the hard shadow filtering. To minimize the overhead of RPCF, keeping its high visual quality results, we developed another technique, called Euclidean Distance Transform Shadow Mapping (EDTSM). In this chapter, we present and evaluate both techniques with respect to the state-of-the-art. This chapter covers the discussion and results mainly presented in the four following authored publications (MACEDO; APOLINÁRIO, 2016; MACEDO; APOLINÁRIO; AGÜERO, 2017; MACEDO; APOLINÁRIO JR., 2017a; MACEDO; APOLINÁRIO, 2018).

### 4.1 REVECTORIZATION-BASED PERCENTAGE-CLOSER FILTERING

An overview of the pipeline to produce filtered hard shadows can be seen in Figure 4.1. While the pipeline is pretty much similar to the one proposed for non-conservative RBSM (see Section 3.2), to introduce filtering for the anti-aliased hard shadows, we need to change the RBSM visibility function such that the algorithm outputs penumbra intensities, rather than whether a fragment is in shadow.

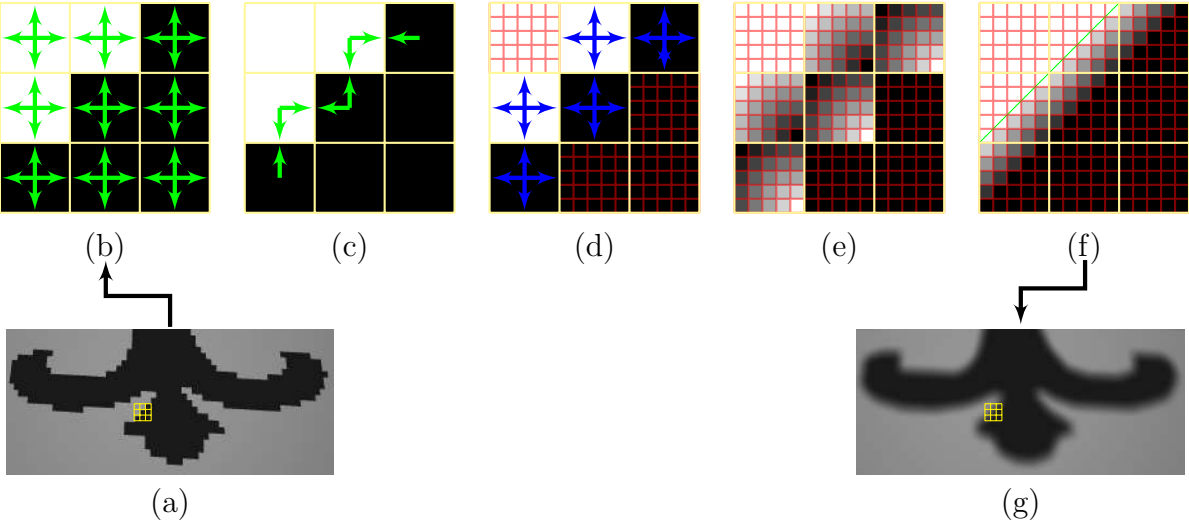


**Figure 4.1** An overview of the pipeline for filtered hard shadow anti-aliasing. Similar to non-conservative RBSM, a neighbourhood evaluation (green arrows in (b)) detects aliased fragments (b) and shadow silhouette directions (green arrows in (c)) for both shadowed and lit fragments. Afterwards, the algorithm traverses the light space (blue arrows in (d)) to estimate the normalized relative distance of the camera-view fragments (red grid) to the shadow silhouette itself (e). Finally, the normalized distance values are used as input for a visibility function that outputs the distance of each fragment to a revectorization line (green line in (f)).

#### 4.1.1 Filtered Hard Shadow Anti-Aliasing Visibility Function

To produce filtered hard shadows, as shown in Figure 4.1-(f), we need to first change the way that the relative position  $\mathbf{r}$  of the fragment inside the shadow silhouette is computed. For a U-shaped shadow silhouette, as illustrated in Figure 4.2, the revectorization effect produced by RBSM changes according to the visibility function used. To be clearly able to detect the shadow silhouette shape in which the fragment is located just by checking the sign of  $\mathbf{r}$ , let us compute  $\mathbf{r}$  as

$$\begin{aligned} \mathbf{r}_x &= T(d_l, d_r) \frac{\max(T(d_l, d_r)d_l, T(d_l, d_r)d_r)}{|d_l| + |d_r|} \\ \mathbf{r}_y &= T(d_t, d_b) \frac{\max(T(d_t, d_b)d_t, T(d_t, d_b)d_b)}{|d_t| + |d_b|}. \end{aligned} \quad (4.1)$$

From (4.1), a lit fragment is located in an L-shaped shadow silhouette if both  $\mathbf{r}_x$  and  $\mathbf{r}_y$  are positive. A lit fragment is located in a U-shaped shadow silhouette if  $\mathbf{r}_x$  or  $\mathbf{r}_y$  is negative, because the  $T$  function (3.4) outputs a negative value in this case. Likewise, a lit fragment is located in an I-shaped shadow silhouette if  $\mathbf{r}_x$  or  $\mathbf{r}_y$  is 0.

Let us define a modified version of the non-conservative RBSM visibility function  $V_{\text{RBSM}}^{**}(V_{\text{SM}}, \mathbf{r}) \in [0, 1]$  for fixed-size penumbra simulation as

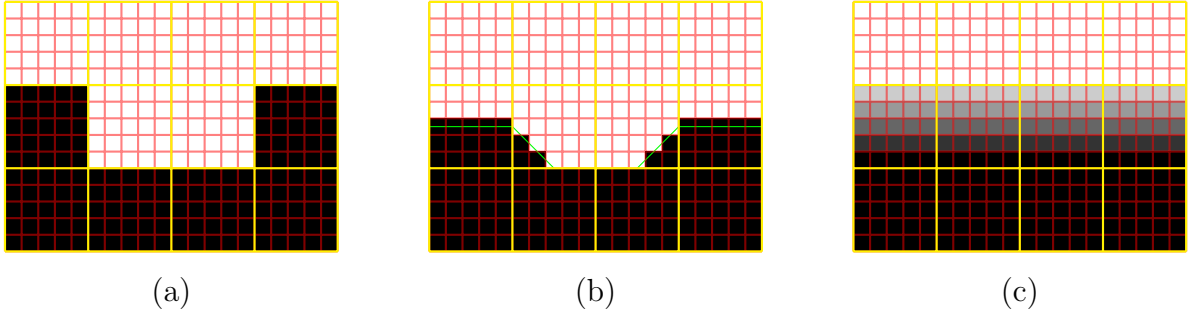


**Figure 4.2** For a U-shaped shadow silhouette (a), the revectorization effect provided by non-conservative RBSM (b) is different from the one produced by RBSM when aiming filtered hard shadow rendering (c).

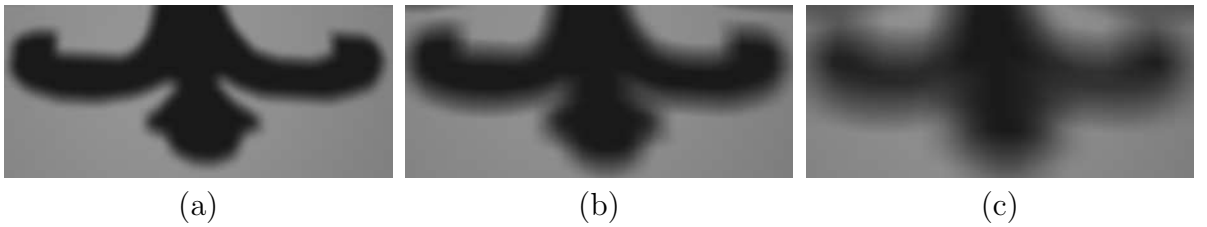


**Figure 4.3** The penumbra effect produced by RPCF for different penumbra sizes.

$$V_{\text{RBSM}}^{**}(V_{\text{SM}}, \mathbf{r}) = \begin{cases} 1 - V_{\text{SM}} + (2V_{\text{SM}} - 1)\max(\mathbf{r}_x, \mathbf{r}_y) & \text{if } \mathbf{r}_x \mathbf{r}_y < 0, \\ V_{\text{SM}} & \text{else if } \mathbf{r}_x \mathbf{r}_y = 0, \\ \min(\max(1 - V_{\text{SM}} + (2V_{\text{SM}} - 1)(\mathbf{r}_x + \mathbf{r}_y), 0), 1) & \text{otherwise.} \end{cases} \quad (4.2)$$

In (4.2), we basically modified Equation (3.9), such that, rather than clamping  $V_{\text{RBSM}}^*$  to be 0 or 1, we use the addition and subtraction operations over  $\mathbf{r}$  and  $V_{\text{SM}}$  to determine the smooth transition that characterizes the filtered hard shadow intensities. With such a modification, we are able to produce fixed-size penumbra such as the one shown in Figure 4.1-(g).

#### 4.1.2 Revectorization-Based Filtering

One problem with the use of (4.2) is that the penumbra size is fixed and limited, proportional to the size of the shadow silhouette, which depends on the shadow map resolution. To enable control over the filter size, we simply incorporate PCF into the revectorization pipeline, giving name to the RPCF technique (Figure 4.3). For each sample of RPCF, we set its visibility condition to be the shadow test (3.2) if the sample is located in a place outside the shadow silhouette. Otherwise, if the sample is located in the lit or shadowed side of the shadow silhouette, we assume its visibility as the result of Equation (4.2). Then, the final intensity of a given fragment is computed by the average of shadow

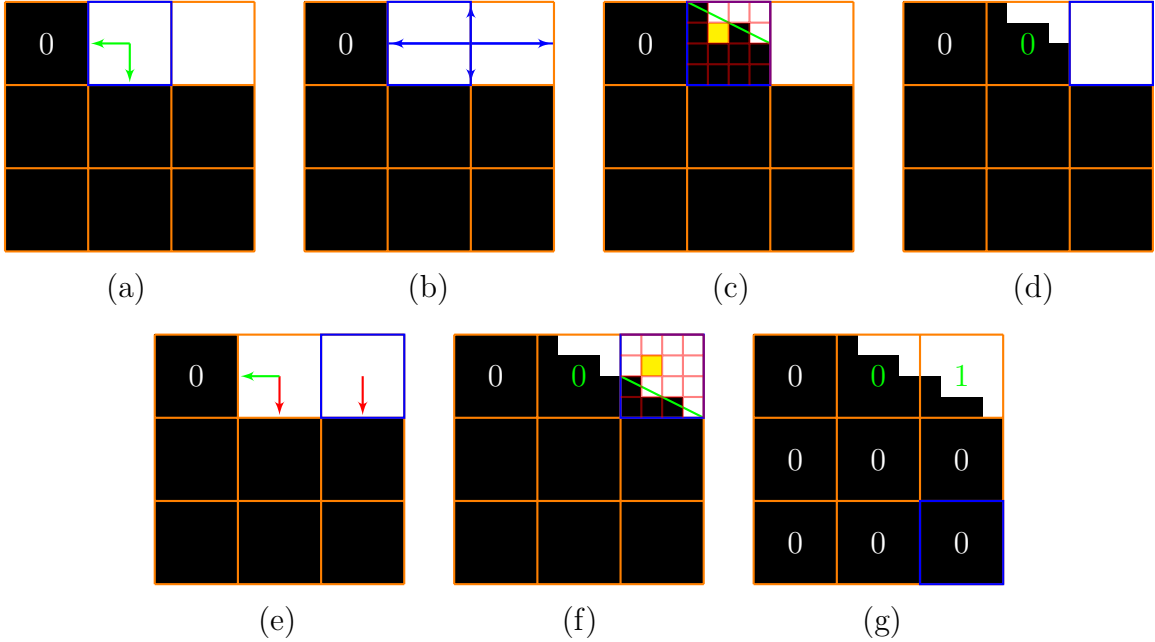


**Figure 4.4** An illustration of the optimized implementation of RPCF listed in Algorithm 2. For each shadow map sample (blue rectangle) inside the filter kernel (orange grid) we compute its shadow intensity and locate the direction of the shadow silhouette (a). Then, we estimate the shadow silhouette size (b) and perform the shadow revectorization in the camera-space (red grid) sample (yellow rectangle) (c). For the next sample (d), the algorithm checks whether silhouette is located at the same direction of the previous sample (red arrows in (e)), to reuse the relative position previously estimated for the shadow revectorization (f). In (g), we show the filter result. This figure shows the filter kernel aligned with the light space, and each shadow map texel equivalent to a  $4 \times 4$  grid in the camera space only for visualization purposes.

intensities computed for every sample located in the RPCF kernel.

In terms of performance, the RBSM step with the most computational cost is the shadow silhouette size estimation. In a naïve implementation, one would need to traverse the shadow map several times to locate the ends of the shadow silhouette for every shadow map sample inside the RPCF kernel. To reduce the computational cost of the revectorization, we take advantage of the fact that, once we have computed the shadow silhouette size, we may reuse such an information to define the visibility of neighbor shadow map samples. This prevents the algorithm from a new traversal over the shadow map, saving costly shadow map texture lookups. The steps of this revectorization are given in Algorithm 2 and shown in Figure 4.4.

Given the kernel size for shadow filtering  $w_{\text{filter}} \in \mathbb{N}$  (Line 2 of Algorithm 2), we sample the neighbourhood of size  $P$  of each fragment  $\tilde{\mathbf{p}}$  projected in the shadow map  $\mathbf{S}$  (Line 10 of Algorithm 2, Figure 4.4-(a)). Then, for each sample  $\tilde{\mathbf{s}}$ , we proceed as proposed in the RBSM algorithm (Algorithm 1), by computing the shadow test (3.2), the silhouette directions (3.3) (Lines 11-12 of Algorithm 2), estimating the relative position of  $\tilde{\mathbf{s}}$  in the aliased silhouette (Lines 16-17 of Algorithm 2 and Figure 4.4-(b)) and

**Algorithm 2** Revectorization-based shadow filtering

---

```

1:  $P \leftarrow$  penumbra size;
2:  $w_{\text{filter}} \leftarrow$  shadow filter size;
3:  $V_{\text{RBSSM}}^{**} \leftarrow 0$ ;
4:  $\mathbf{d}^{\text{prev}} \leftarrow \text{null}$ ;
5:  $\mathbf{r}^{\text{prev}} \leftarrow \text{null}$ ;
6: for each frame do
7:    $S \leftarrow \text{RENDERSHADOWMAP}$ ;
8:   for each surface point  $\mathbf{p}$  in camera view do
9:      $\tilde{\mathbf{p}} \leftarrow \text{TRANSFORMTOLIGHTSPACE}(\mathbf{p})$ ;
10:    for each sample  $\tilde{\mathbf{s}}$  of  $S$  in  $w_{\text{filter}}$ , neighbour of  $\tilde{\mathbf{p}}$  in  $P$  do
11:       $V_{\text{SM}} \leftarrow \text{COMPUTESHADOWTEST}(\tilde{\mathbf{s}}, S)$ ;
12:       $\mathbf{d} \leftarrow \text{COMPUTESILHOUETTEDIRECTION}(V_{\text{SM}})$ ;
13:      if HASSAME DIRECTION( $\mathbf{d}, \mathbf{d}^{\text{prev}}$ ) then
14:         $\mathbf{r} \leftarrow \text{UPDATERELATIVEPOSITION}(\mathbf{r}_{\text{prev}})$ ;
15:      else
16:         $\mathbf{s} \leftarrow \text{TRANSFORMTOCAMERASPACE}(\tilde{\mathbf{s}})$ ;
17:         $\mathbf{r} \leftarrow \text{ESTIMATERELATIVEPOSITION}(\mathbf{s}, \tilde{\mathbf{s}}, \mathbf{d}, S)$ ;
18:      end if
19:       $V_{\text{RBSSM}}^{**} \leftarrow V_{\text{RBSSM}}^{**} + \text{PERFORMANTI ALIASING}(\mathbf{r}, V_{\text{SM}})$ ;
20:    end for
21:     $\mathbf{d}^{\text{prev}} \leftarrow \mathbf{d}$ ;
22:     $\mathbf{r}^{\text{prev}} \leftarrow \mathbf{r}$ ;
23:  end for
24:  return  $V_{\text{RBSSM}}^{**}/w_{\text{filter}}$ ;
25: end for
26:
27: procedure HASSAME DIRECTION( $\mathbf{d}, \mathbf{d}^{\text{prev}}$ )
28:   for each coordinate  $c$  of  $\mathbf{d}$  do
29:     if  $\mathbf{d}_c == \mathbf{d}_c^{\text{prev}}$  and  $\mathbf{d}_c == 1$  then
30:       return true;
31:     end if
32:   end for
33:   return false;
34: end procedure

```

---

performing the revectorization of the fragment using (4.2) (Line 19 of Algorithm 2 and Figure 4.4-(c)). If the next sample inside the RPCF kernel (Figure 4.4-(d)) is located in the same silhouette of the previous sample (Line 13 of Algorithm 2 and Figure 4.4-(e)), we update the relative position previously computed (Line 14 of Algorithm 2) by taking into consideration the distance between previous and current samples. Then, we use the updated relative position to perform the revectorization of the current sample (Line 19 of Algorithm 2 and Figure 4.4-(f)). To detect whether the current sample is located in the

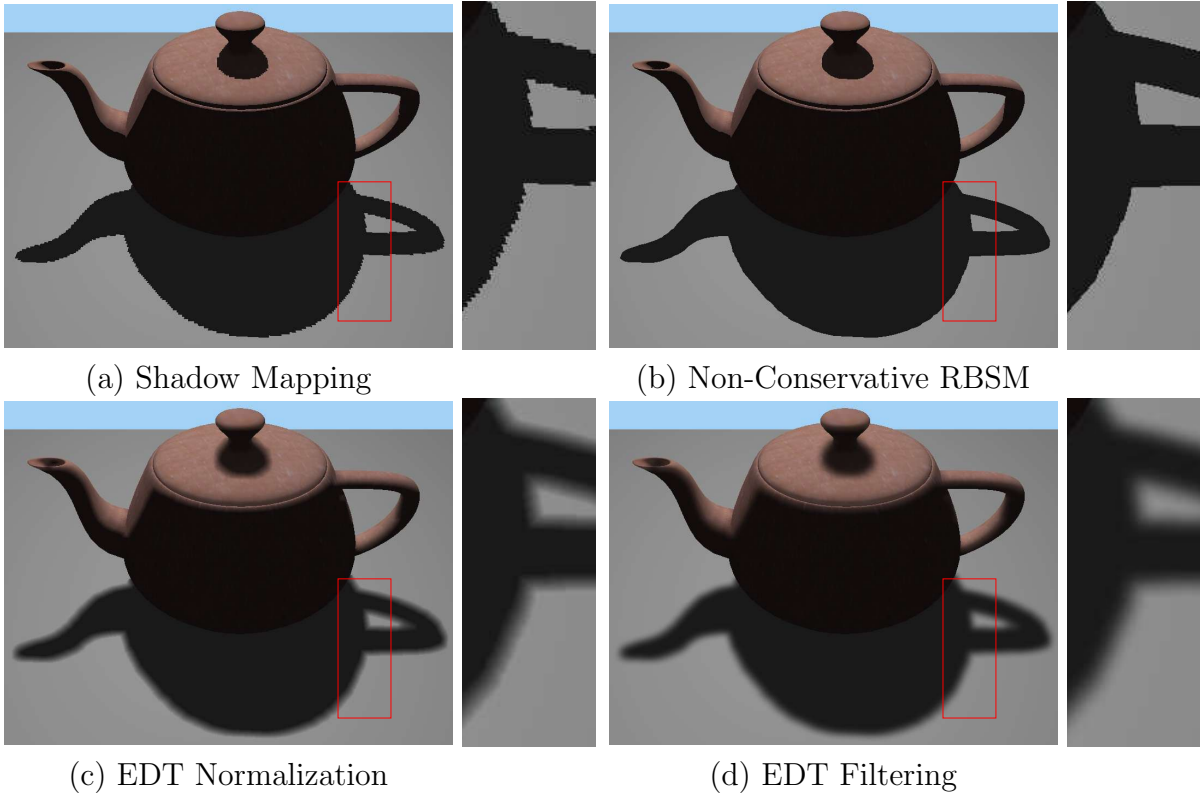


**Figure 4.5** An overview of EDTS defense. Given the aliased hard shadows obtained with the traditional shadow mapping (a), non-conservative RBSM is applied to generate anti-aliased hard shadows (b). Then, penumbra intensities are computed on the basis of a normalized EDT over the penumbra region (c). Finally, a mean filter (d) is applied over the normalized EDT to reduce skeleton artifacts generated by the EDT computation.

same silhouette of the previous sample, we check whether the current sample is located in a shadow silhouette (*i.e.*, if a single coordinate of  $\mathbf{d}$  is equal to 1) and whether both samples share, at least, a single silhouette direction in common (*i.e.*, if both samples have the same coordinate of  $\mathbf{d}$  equals to 1) (Lines 27-34 of Algorithm 2). Finally, the final penumbra intensity of  $\mathbf{p}$  is computed as an average of the shadow intensities computed inside the RPCF kernel (Line 24 of Algorithm 2 and Figure 4.4-(g)).

While RPCF is able to suppress the aliasing artifacts commonly generated by PCF, the technique inherits one of the problems of PCF: non-scalability with respect to the filter size. To minimize such a problem, we propose another technique that computes shadows on the basis of separable Euclidean Distance Transform (EDT).

**Algorithm 3** Euclidean distance transform shadow mapping

---

```

1:  $P \leftarrow$  penumbra size;
2:  $w_{\text{filter}} \leftarrow$  mean filter size;
3: for each frame do
4:    $S \leftarrow \text{RENDERSHADOWMAP};$ 
5:    $G \leftarrow \text{RENDERGBUFFER};$ 
6:    $R \leftarrow \text{REVECTORIZESHADOW}(S, G);$ 
7:    $\text{EDT} \leftarrow \text{PERFORMEDTSHADOWING}(R, G, P);$ 
8:    $F \leftarrow \text{FILTERSHADOW}(\text{EDT}, G, w_{\text{filter}});$ 
9:    $\text{RENDERSHADOWEDSCENE}(F, G);$ 
10: end for

```

---

## 4.2 EUCLIDEAN DISTANCE TRANSFORM SHADOW MAPPING

### 4.2.1 Overview

EDTS is a technique that uses EDT to simulate the penumbra effect over anti-aliased hard shadows. In Figure 4.5, we show the steps that are required to simulate fixed-size penumbra using EDT on the basis of the hard shadows generated by shadow mapping. The full process is listed in Algorithm 3.

The main assumption of EDTS is that the penumbra intensity of a fragment can be approximated by the Euclidean distance of the fragment to the nearest fragment located in the hard shadow silhouette. Therefore, the first step of EDTS consists in the generation of the shadow map texture (Line 4 of Algorithm 3) for real-time hard shadow rendering. To avoid shadow aliasing (Figure 4.5-(a)), this technique requires the use of a hard shadow anti-aliasing technique before the fixed-size penumbra simulation. Hence, we make use of non-conservative RBSM (Figure 4.5-(b) and Line 6 of Algorithm 3) to generate anti-aliased hard shadows in real time. Also, to restrict shadow and shading computations to the fragments visible to the camera, as suggested by the deferred rendering pipeline, we use a G-buffer  $G$  (SAITO; TAKAHASHI, 1990) of viewport width  $w$  and height  $h$  that stores, for each pixel  $G(i, j) \in \mathbb{R}^6$ , the world-space position  $\mathbf{p}$  and normal  $\mathbf{n}$  of the visible surface points in the camera viewpoint. (Line 5 of Algorithm 3). Afterward, to simulate the penumbra effect, the EDT is computed over the image with the hard shadows previously estimated. Then, the Euclidean distance is normalized (Figure 4.5-(c) and Line 7 of Algorithm 3) and filtered (Figure 4.5-(d) and Line 8 of Algorithm 3) inside a user-defined fixed-size penumbra region, because the penumbra intensity of a fragment must lie in the interval of intensities between the umbra and lit regions.

### 4.2.2 Euclidean Distance Transform Shadowing

Let us call *seed* a fragment that lies in the hard shadow silhouette (green rectangles in Figure 4.6) and that will be used as a basis for the EDT computation. Even if it is located in a thin aliased shadow, a seed fragment can be easily located in the screen space of the camera view by the application of a  $3 \times 3$  rectangular filter over the shadows

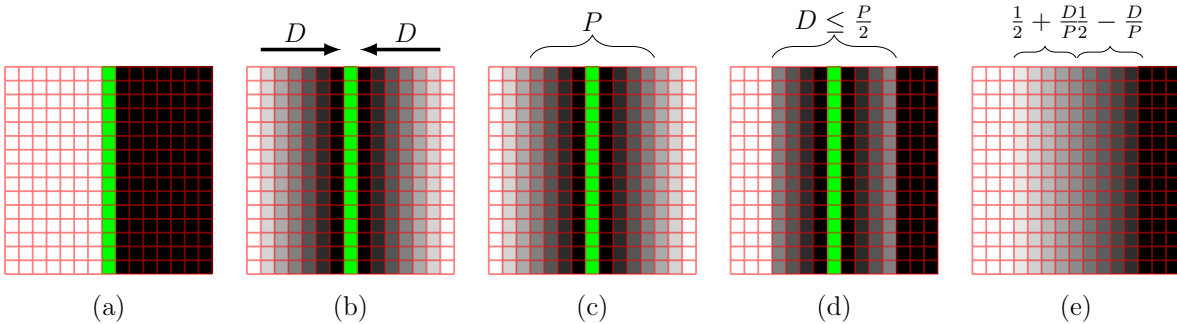


**Figure 4.6** A more in-depth overview of EDTSM. First, non-conservative RBSM is used (a) to generate anti-aliased shadow silhouettes (green rectangles) in the camera view (red grid). Then, for every fragment in the screen space, the world-space position is retrieved from the G-buffer, and the world-space distance  $D$  to closest fragment located in the shadow silhouette is computed (b). Given a user-defined penumbra size  $P$  (c), the algorithm restricts the penumbra computation for fragments located in the penumbra region (d). Finally, the EDT previously computed is normalized to simulate the smooth transition between lit and umbra regions that characterize the penumbra effect (e).

produced with non-conservative RBSM. In this case, a fragment is a seed if the hard shadow intensity of the fragment differs from the hard shadow intensity of one of its neighbours located in the 8-connected neighbourhood of the fragment in the screen space (Figure 4.6-(a)).

Once the seed fragments have been detected in the image, the EDT can be computed. So, for each non-seed fragment, the world-space Euclidean distance  $D$  of the fragment to the nearest seed located in the shadow silhouette is computed (Figure 4.6-(b)),  $D$  being a world-space distance computed on the basis of the world-space position retrieved from a G-buffer (SAITO; TAKAHASHI, 1990) previously computed. Just by applying the EDT in the world space, the user does not have control over the desired penumbra size. To solve this problem, let us assume  $P$  as a user-defined parameter which controls the size of the penumbra that will be simulated. As shown in Figure 4.6-(c), each half of the penumbra size belongs to one side of the shadow silhouette. Therefore, one can easily detect whether a fragment belongs to the desired penumbra region by checking if the distance of the fragment to the shadow silhouette is lower or equal than half of the penumbra size (i.e.,  $D \leq P/2$ ) (Figure 4.6-(d)). For the fragments located outside of the penumbra region, the shadow intensity is given by the shadow test (umbra and lit regions in Figure 4.6-(d)). Meanwhile, for fragments in the penumbra region, we keep the result of the EDT as shadow intensity.

As can be seen in Figure 4.6-(d), EDT does not resemble a penumbra mostly because it is not normalized. The transition between umbra and lit regions in the desired penumbra is not smooth as it should be to characterize a penumbra. To solve this problem, the Euclidean distance is normalized to the closed unit interval  $[0, 1]$ , assuming that umbra and lit fragments have intensities 0 and 1, respectively. Hence, the final intensity  $I \in [0, 1]$  of the fragments located in the penumbra region is

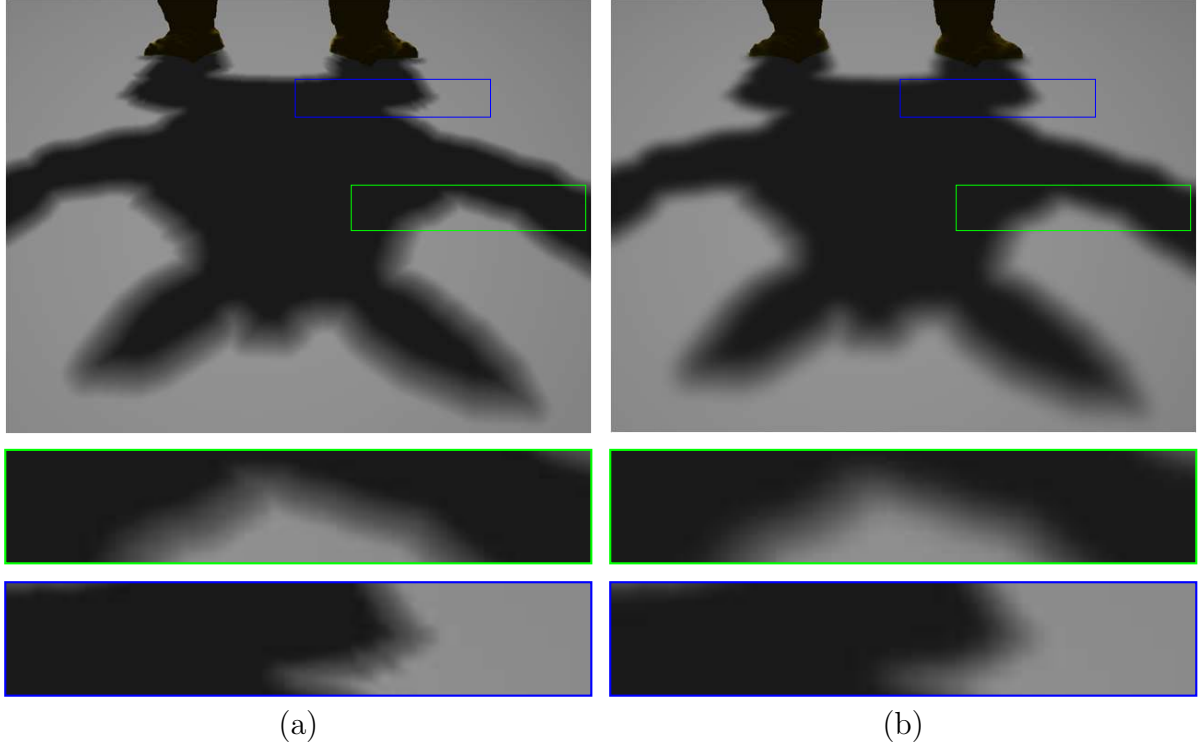


**Figure 4.7** After the EDT computation, skeleton artifacts may arise along gradient discontinuities (green closeup of (a)). Also, aliasing artifacts may still remain even after the shadow revectorization (blue closeup of (a)). By applying a simple mean filter, those artifacts can be suppressed (b).

$$I = \begin{cases} \frac{1}{2} - \frac{D}{P} & \text{if the fragment was in shadow,} \\ \frac{1}{2} + \frac{D}{P} & \text{otherwise.} \end{cases} \quad (4.3)$$

As shown in (4.3), the final intensity of each fragment depends on the previous visibility condition given by RBSM. For instance, knowing that the maximum distance of each fragment belonging to the penumbra region to the nearest seed is  $P/2$  (Figure 4.6-(d)), if the fragment was in shadow, as computed by RBSM, the new penumbra intensity of the fragment must lie in the interval  $[0, \frac{1}{2}]$ , because 0 is the intensity of the fragments located in shadow and  $\frac{1}{2}$  is the intensity of the fragments located in the middle of the penumbra region. Accordingly, lit fragments, as computed by RBSM, must have their penumbra intensities lying in the interval  $[\frac{1}{2}, 1]$ . By the use of (4.3), EDTSM is able to satisfy these constraints and simulate the penumbra effect (Figure 4.6-(e)).

#### 4.2.3 Euclidean Distance Transform Filtering

A well-known feature of EDT is the generation of skeletons along gradient discontinuities (WRIGHT; CIPOLLA; GIBLIN, 1995). This property of EDT is desirable in several

applications, such as integer medial axis estimation (HESSELINK; ROERDINK, 2008). However, these skeletons generated by EDT, when visualized inside a penumbra, constitute an artifact because a penumbra does not have skeletons along its silhouette (green closeup of Figure 4.7-(a)). Moreover, RBSM is able to minimize aliasing artifacts generated by shadow mapping, but is not able to remove all of them (blue closeup of Figure 4.7-(a)). To minimize both skeleton and aliasing artifacts simultaneously, a simple screen-space separable mean filter is applied over the shadow silhouette (Figure 4.7-(b)). The mean filtering was chosen to solve these problems because of its simplicity, low processing time, separability and effectiveness to suppress the skeleton artifacts even for low-order filter sizes.

The EDT algorithm is performed in screen space, taking as input the image of the shadowed scene rendered from the camera viewpoint. In this sense, special care must be taken to make this process edge aware and viewpoint invariant. Edge awareness is important because different objects cannot influence on the penumbra computation of each other. Viewpoint invariance is desirable because the penumbra size must be kept constant, regardless of the distance of the viewer to the shadowed region. EDTSM solves both problems by the use of the depth value and world-space position stored in the G-buffer. Depth information is used to detect edges, which separate different objects in the scene. In this sense, for instance, a fragment is only considered to be in penumbra if the depth difference between the fragment and its nearest seed is below a user-defined threshold (empirically, we have set this depth threshold as  $2.5 \times 10^{-3}$ ). Also, only neighbours with similar depth difference are taken into account for mean filtering. In counterpart, to make the EDT viewpoint invariant, world-space position is used to compute the Euclidean distance values  $D$  in the EDT. Inspired by screen-space soft shadow algorithms, the viewpoint invariance of the mean filtering is solved by estimating the mean filter size  $w_{\text{filter}}^{\text{screen}}$  that varies according to the distance of the camera to the scene. Here,  $w_{\text{filter}}^{\text{screen}}$  is measured as (MOHAMMADBAGHER et al., 2010)

$$w_{\text{filter}}^{\text{screen}} = \frac{w_{\text{filter}} z_{\text{screen}}}{\mathbf{p}_{z_{\text{eye}}}}, \quad (4.4)$$

$$z_{\text{screen}} = \frac{1}{2 \tan \frac{fov_y}{2}}, \quad (4.5)$$

where  $w_{\text{filter}}$  is the mean filter size defined by the user,  $\mathbf{p}_{z_{\text{eye}}}$  is the distance of the fragment  $\mathbf{p}$  to the center of the camera,  $fov_y$  specifies the vertical field of view angle and  $z_{\text{screen}}$  is the inverse of the viewport scale, in terms of field of view.

### 4.3 RESULTS AND DISCUSSION

In this section, we compare our EDTSM and RPCF techniques with traditional filtered hard shadow mapping techniques, such as PCF (REEVES; SALESIN; COOK, 1987), Variance Shadow Mapping (VSM) (DONNELLY; LAURITZEN, 2006), and Exponential Variance Shadow Mapping (EVSM) (LAURITZEN; MCCOOL, 2008), as well as the state-of-the-art fixed-size penumbra simulation technique, Moment Shadow Mapping (MSM) (PETERS; KLEIN, 2015). These techniques were chosen for evaluation because

they produce fixed-size penumbra, lying in the scope of this chapter. Therefore, techniques that simulate variable-size penumbra (*i.e.*, soft shadows) on the basis of point or area light sources are not evaluated in this section.

We have tested different penumbra simulation techniques in three distinct scenarios. Figure 4.8 shows a model with fine detailed structures along its silhouette. Figure 4.9 shows shadows cast on a non-planar model. Figure 4.10 shows a scenario with several light blocker and shadow receiver objects positioned over each other.

### 4.3.1 Experimental Setup

For EDT computation, we have used the open-source implementation of the Parallel Banding Algorithm (PBA) (CAO et al., 2010) implemented in Compute Unified Device Architecture (CUDA) (KIRK; HWU, 2013). Although many other works have attempted to compute EDT efficiently (RONG; TAN, 2006; SCHNEIDER; KRAUS; WESTERMANN, 2009; WANG; TAN, 2013), in our tests, PBA delivered the fastest and most accurate EDT computation.

CUDA/OpenGL interoperability was used to optimize resource management and processing time. A filter of order  $15 \times 15$  was applied to suppress skeleton and banding artifacts. Specifically for RPCF, we have used a filter of order  $7 \times 7$ , since the technique demands less samples to suppress banding artifacts. In the results, we have tested filters of higher orders only to determine whether the techniques are scalable in terms of the filter size.

### 4.3.2 Visual Quality Evaluation

In the **blue** closeups of Figures 4.8 and 4.9, we show whether the different shadowing techniques are able to suppress aliasing artifacts. For small penumbra sizes, the blur provided by PCF is insufficient to suppress aliasing artifacts (Figures 4.8-(a) and 4.9-(a)). The same effect is visible for the shadow map filtering techniques (Figures 4.8-(b, c, d) and 4.9-(b, c, d)), which simulate penumbra with blurred jagged silhouettes along the shadow. Techniques that use shadow revectorization as basis for penumbra simulation (RPCF and EDTSM) are able to minimize this artifact efficiently (Figures 4.8-(e, f) and 4.9-(e, f)).

In the **red** closeups of Figures 4.8, 4.9 and 4.10, we show whether each technique generates light leaking artifacts inside the shadow. All shadow map filtering techniques are prone to light leaking artifacts. In this sense, VSM (Figures 4.8-(b), 4.9-(b) and 4.10-(b)) is more susceptible to light leaking than EVSM (Figures 4.8-(c), 4.9-(c) and 4.10-(c)). In terms of visual quality, MSM is better than both VSM and EVSM, greatly reducing the light leaking artifacts (the effectiveness of MSM is mainly visible in Figure 4.9-(d)). The techniques that filter shadows to simulate penumbra (PCF, RPCF and EDTSM) are not prone to light leaking artifacts (Figures 4.8-(a, e, f), 4.9-(a, e, f) and 4.10-(a, e, f)).

RPCF and EDTSM support shadow rendering for planar (Figures 4.8-(e, f)) and non-planar receivers (Figures 4.9-(e, f)). Moreover, both techniques support penumbra simulation not only for simple scenarios, but also for more complex, game-like scenarios,

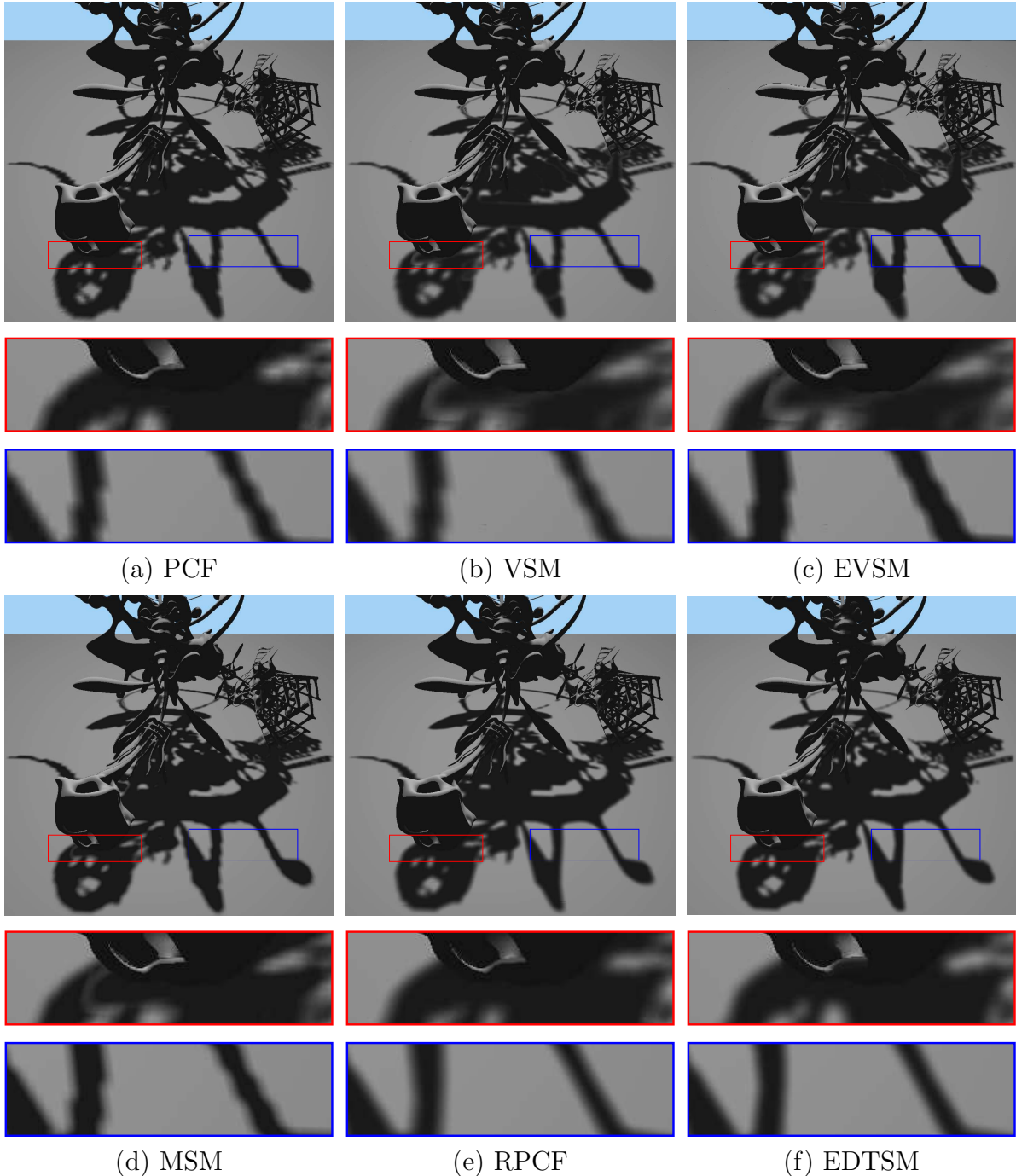


**Figure 4.8** Fixed-size penumbra produced by different techniques. Each closeup shows whether the technique handles light leaking (red) and aliasing (blue) artifacts. Images were generated for the YeahRight model using a  $1024^2$  shadow map resolution.

such as the one shown in Figures 4.10-(e, f), where several light blocker and shadow receiver objects with fine detailed structures (*e.g.*, trees) are located in the same scene.

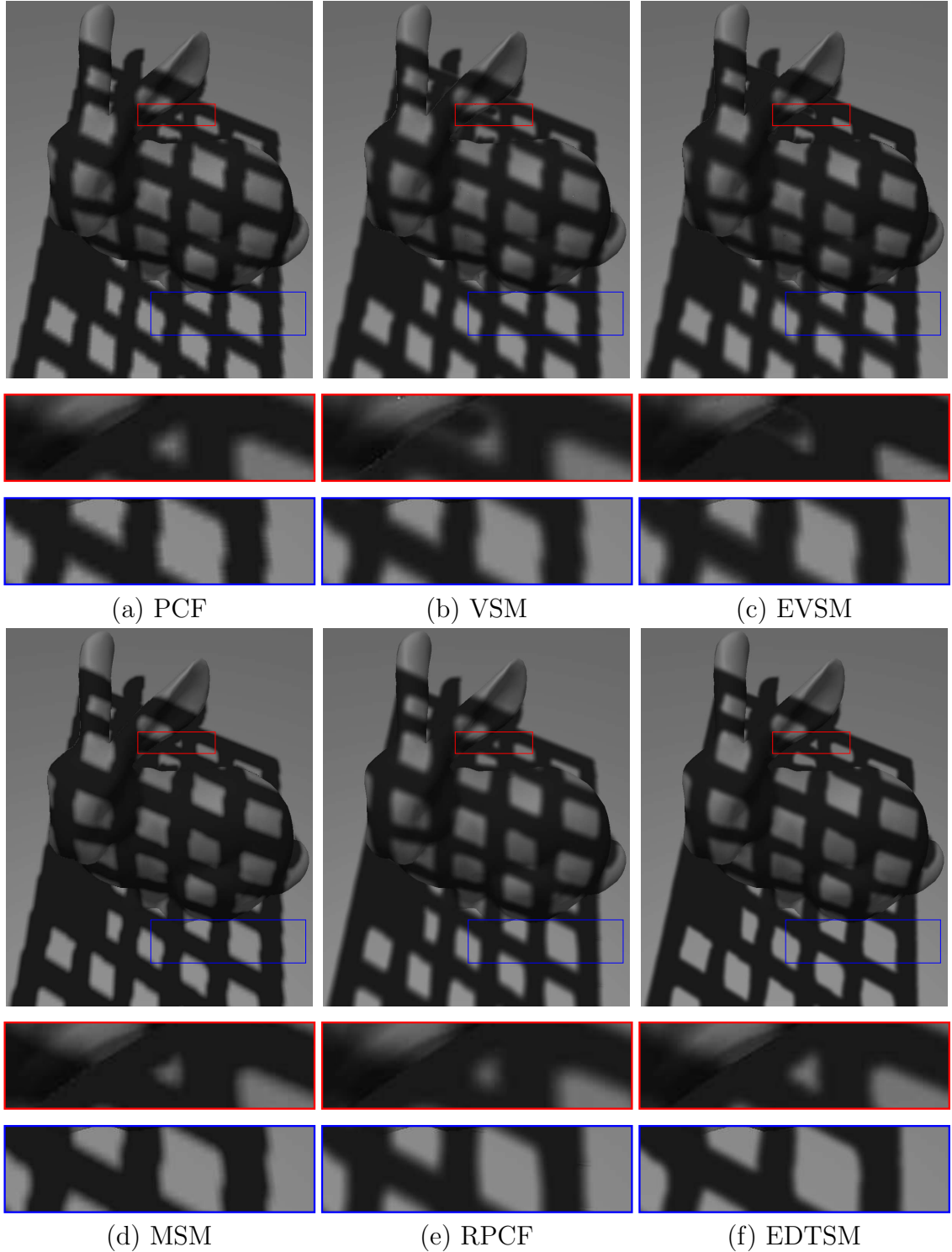


**Figure 4.9** Fixed-size penumbra produced by different techniques. Each closeup shows whether the technique light leaking (red) and aliasing (blue) artifacts. Images were generated for the Bunny model using a  $1024^2$  shadow map resolution.

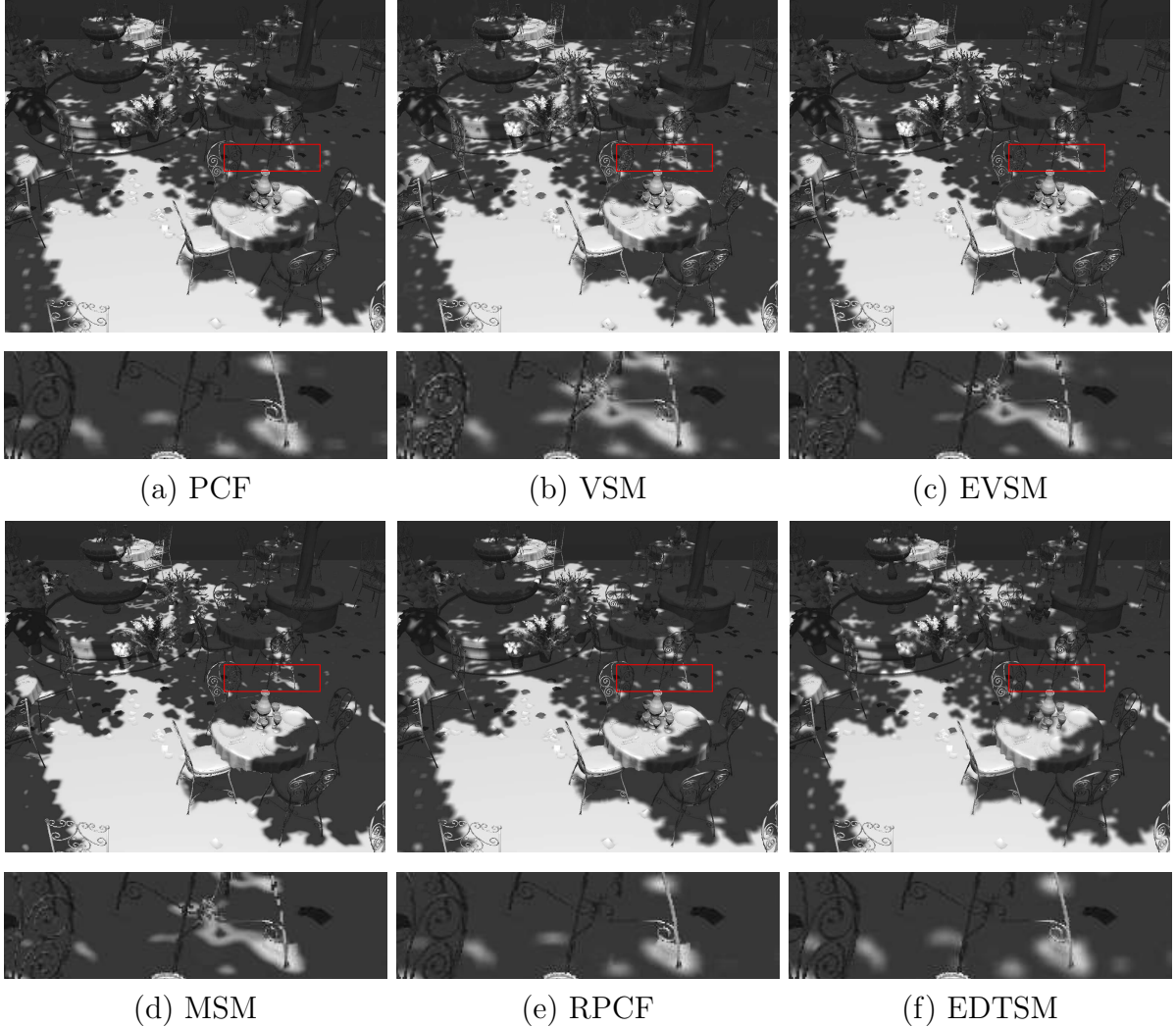


**Figure 4.10** Fixed-size penumbra produced by different techniques. Each closeup shows whether the technique handles light leaking artifacts. Images were generated for the SanMiguel model using a  $1024^2$  shadow map resolution.

Also, despite being an image-based technique, EDTSM supports penumbra simulation on noisy surfaces with high-frequency details, as shown in Figure 4.11. In this figure, we reinforce that EDTSM is able to separate penumbra simulation from self-shadowing, while properly handling the noisy depth differences distributed over the surface. Hence, the gamut of scenes shown in this section reveals that both EDTSM and RPCF are able to generate fixed-size penumbra, with less aliasing and light leaking than related work.

### 4.3.3 Rendering Time Evaluation

As shown in Tables 4.1 and 4.2, shadow map filtering is an efficient way to simulate penumbra, being relatively scalable with respect to the shadow map (Table 4.1), view-

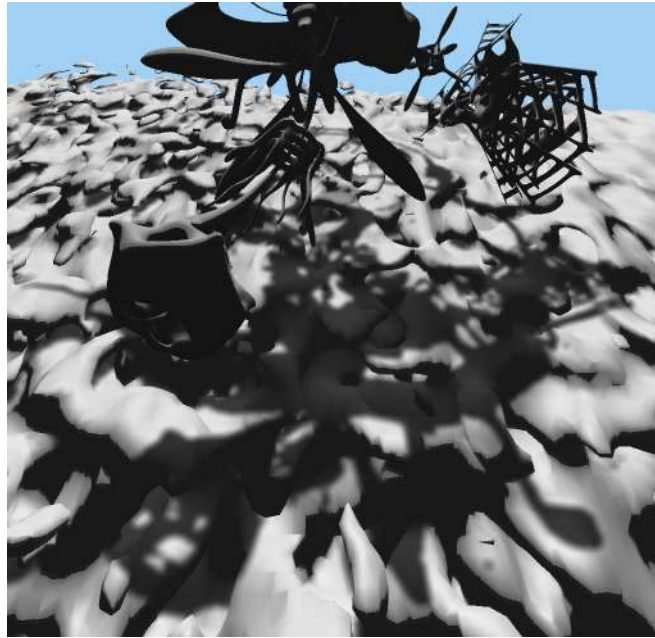


**Figure 4.11** Fixed-size penumbra simulation on a noisy surface with laterally increasing frequency. Image was generated for the YeahRight model using a  $1024^2$  shadow map resolution.

<b>Scene</b>	<b>Method</b>	<b>Shadow Map Resolution (ms)</b>			
		$512^2$	$1024^2$	$2048^2$	$4096^2$
Figure 4.8	PF	10.5	10.6	10.8	12.0
	PCF	11.3	11.4	11.4	11.7
	EDTSM	12.9	13.0	13.2	13.8
	RPCF	26.2	27.3	27.8	30.0
Figure 4.9	PF	1.9	2.1	2.4	3.6
	PCF	2.9	3.0	3.1	3.5
	EDTSM	4.5	4.6	4.8	5.7
	RPCF	10.4	11.0	11.5	12.0
Figure 4.10	PF	126.9	128.2	129.8	133.8
	PCF	126.7	129.0	130.3	133.5
	EDTSM	129.5	130.9	132.8	136.3
	RPCF	138.8	141.2	145.7	148.1

**Table 4.1** Processing time for several hard shadow filtering techniques and different scenes rendered at an output  $720p$  resolution. Measurements include varying shadow map resolution. PF - Pre-filtering techniques that produce nearly the same processing time results (namely VSM, EVSM and MSM).

port (Table 4.2) and kernel resolutions (Table 4.3). Moreover, the different shadow map filtering techniques that we have tested in this chapter provide nearly the same low rendering times, that is why they are refereed by a single row in each table. However, all this efficiency comes at the price of light leaking artifacts generation inside shadows (Figures

Scene	Method	Output Resolution (ms)		
		480p	720p	1080p
Figure 4.8	PF	9.9	10.6	11.3
	PCF	9.8	11.4	11.9
	EDTSM	10.8	13.0	14.9
	RPCF	16.4	27.3	30.3
Figure 4.9	PF	0.9	2.1	3.1
	PCF	0.9	3.0	4.0
	EDTSM	2.3	4.6	6.9
	RPCF	4.3	11.0	12.5
Figure 4.10	PF	127.8	128.2	128.8
	PCF	127.8	129.0	129.5
	EDTSM	129.3	130.9	133.5
	RPCF	132.9	141.2	143.7

**Table 4.2** Processing time for several hard shadow filtering techniques and different scenes rendered at a  $1024^2$  shadow map resolution. Measurements include varying output image resolution. PF - Pre-filtering techniques that produce nearly the same processing time results (namely VSM, EVSM and MSM).

Scene	Method	Kernel Size (ms)			
		$7^2$	$15^2$	$23^2$	$31^2$
Figure 4.8	PF	10.3	10.6	10.8	11.1
	PCF	9.8	11.4	13.5	17.0
	EDTSM	12.4	13.0	13.5	14.3
	RPCF	27.3	77.5	166.6	285.7
Figure 4.9	PF	1.8	2.1	2.4	2.7
	PCF	1.2	3.0	5.6	9.3
	EDTSM	4.1	4.6	5.3	6.1
	RPCF	11.0	65.7	145.3	255.7
Figure 4.10	PF	127.9	128.2	128.4	128.6
	PCF	128.3	129.0	130.2	133.5
	EDTSM	130.3	130.9	131.6	132.6
	RPCF	141.2	200.2	366.3	552.2

**Table 4.3** Processing time for several hard shadow filtering techniques and different scenes rendered at an output  $1280 \times 720$  resolution and using a  $1024^2$  shadow map resolution. Measurements include varying kernel size. PF - Pre-filtering techniques that produce nearly the same processing time results (namely VSM, EVSM and MSM).

4.8-(b, c, d), 4.9-(b, c, d) and 4.10-(b, c, d)). PCF is more scalable to the shadow map resolution than the shadow map filtering techniques (Table 4.1), but is one of the slowest techniques for high-order filter sizes (Table 4.3) and is prone to aliasing artifacts along the shadow silhouette (Figures 4.8-(a) and 4.9-(a)). RPCF is able to suppress aliasing artifacts (Figures 4.8-(e), 4.9-(e) and 4.10-(e)), but is the slowest penumbra simulation

Scene	Step	Output Resolution (ms)		
		480p	720p	1080p
Figure 4.8	G-buffer	4.1	4.5	4.7
	Shadow Map	4.3	4.3	4.3
	RBSM	0.2	0.4	0.6
	EDT	1.3	2.3	2.9
	Mean Filter	0.7	1.2	2.0
	Shading	0.2	0.3	0.4
	<b>Total</b>	<b>10.8</b>	<b>13.0</b>	<b>14.9</b>
Figure 4.9	G-buffer	0.1	0.3	0.4
	Shadow Map	0.2	0.2	0.2
	RBSM	0.1	0.4	0.7
	EDT	1.1	2.3	3.1
	Mean Filter	0.7	1.2	2.2
	Shading	0.1	0.2	0.3
	<b>Total</b>	<b>2.3</b>	<b>4.6</b>	<b>6.9</b>
Figure 4.10	G-buffer	63.4	63.5	63.6
	Shadow Map	63.0	63.0	63.0
	RBSM	0.6	0.7	1.0
	EDT	1.3	2.3	3.3
	Mean Filter	0.7	1.1	2.2
	Shading	0.3	0.3	0.4
	<b>Total</b>	<b>129.3</b>	<b>130.9</b>	<b>133.5</b>

**Table 4.4** Processing time of each individual step of the proposed EDTSM (including G-buffer and shadow map rendering) for different scenes rendered using a  $1024^2$  shadow map resolution. Measurements include varying output image resolution.

technique, regardless of shadow map (Table 4.1), viewport (Table 4.2) and kernel resolution (Table 4.3). EDTSM is slightly slower than the majority of previous work (Table 4.1) and is not scalable with respect to the output image resolution (Table 4.2), because EDT is an image-based operation. Finally, EDTSM is more scalable to the filter size than PCF and RPCF techniques, becoming even faster than these two related work for high-order filter sizes (Table 4.3).

In Table 4.4, we show the processing time obtained for each step of EDTSM for varying output resolution. We have not conducted the same analysis for other parameters because a variation in the shadow map resolution (Table 4.1) affects mainly the shadow map rendering and RBSM computation steps. Meanwhile, the variation of the kernel size (Table 4.3) affects only the mean filtering step.

From Table 4.4, we can see that, as expected, the processing times demanded by G-buffer and shadow map rendering steps vary according to the number of triangles present in the scene. With respect to the **shadowing** step of the algorithm, the EDT computation is the bottleneck of EDTSM. We recall that, to the best of our knowledge, the algorithm that we use to compute the EDT in real time, the PBA (CAO et al., 2010),

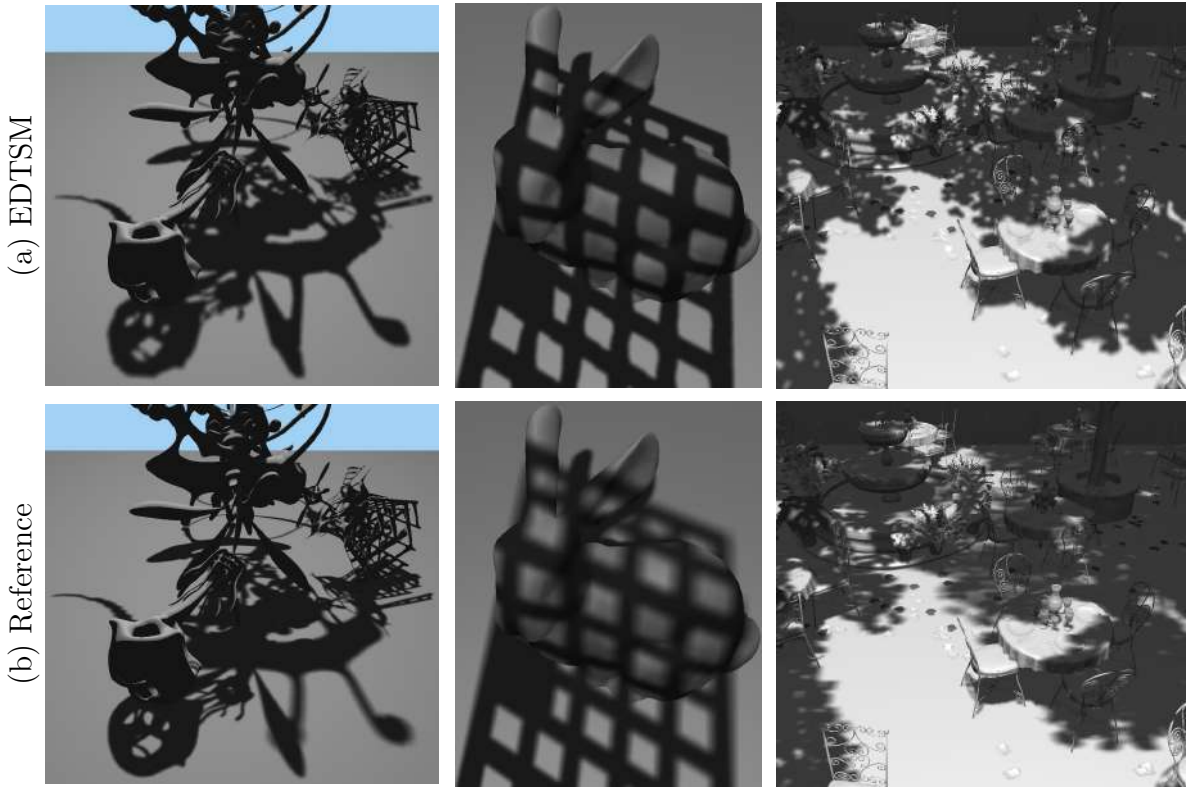


**Figure 4.12** A comparison between shadows generated by EDTSM (top) and the ground-truth technique (bottom) for three scenes shown in this section. Ground-truth images were computed using the average of 1024 samples from an area light source.

is the fastest algorithm able to compute exact EDT. Even in this case, the algorithm still demands more than 2 milliseconds to compute the EDT in  $720p$  or higher output resolutions.

#### 4.3.4 Limitations

In terms of visual quality, both RPCF and EDTSM techniques are based on shadow mapping and non-conservative RBSM. Hence, similarly to all the techniques evaluated in this section, the quality of the penumbra simulated with the proposed techniques is dependent on the resolution of the shadow map used, although the use of RBSM as a basis for the penumbra simulation increases the quality of the penumbra rendering. Also, both RPCF and EDTSM techniques lie in the category of shadow mapping techniques that simulate fixed-size penumbra on the basis of a point light source to achieve real-time performance (Figure 4.12-(a)). Unfortunately, both RPCF and EDTSM techniques, similarly to the other fixed penumbra shadowing techniques existing in the literature, are not able to capture the realism of ground-truth soft shadows (Figure 4.12-(b)), mainly because real-world penumbra has a variable size that varies according to the distance of each shadow receiver fragment to both light blocker fragments and the area light source.

In terms of rendering performance, RPCF is not scalable to the kernel size, similarly to PCF, although the technique requires a small kernel size to generate penumbra free from banding artifacts. As for EDTSM, the costly step of the technique is the EDT computation, making EDTSM slightly slower than the majority of related work for the same scene configurations. Despite these facts, the quality of the penumbra simulated stimulates the use of EDTSM for anti-aliased fixed-size penumbra rendering.

#### 4.4 SUMMARY

In this chapter, we have presented two techniques for fixed-size penumbra simulation: RPCF, a filtered hard shadow mapping technique that extends the non-conservative RBSM to output penumbra intensities rather than hard shadow intensities; EDTSM, a technique that simulates penumbra by computing a normalized EDT over the hard shadows generated by non-conservative RBSM.

Compared to other filtered hard shadow techniques, both RPCF and EDTSM technique are able to reduce shadow aliasing and light leaking, keeping real-time frame rates and high-quality penumbra simulation for planar and non-planar receivers, simple and complex scenarios. By performing the filtering over the light space, RPCF is slightly more accurate than EDTSM, meanwhile EDTSM is faster than RPCF due to the use of a separable implementation of EDT to speed up the hard shadow filtering.

Both RPCF and EDTSM share the same limitation of other fixed-size penumbra simulation techniques that are based on shadow mapping: the quality of the simulation depends on the accuracy of the shadow map rendered, and fixed-size penumbra is not much realistic, because real-world penumbra has a variable size along its silhouette.

In the next chapters, we show how to extend both RPCF and EDTSM techniques to simulate variable-size penumbra on the basis of a single point light source, enhancing the quality of the shadow rendering, at the cost of a lower frame rate.



# Chapter

# 5

*In this chapter, we present the extension of RBSM to provide anti-aliasing for visually plausible soft shadow rendering. A novel solution that computes soft shadows almost entirely on the screen space is designed to keep high-quality anti-aliasing, while improving the performance of the revectorization-based soft shadow rendering.*

## REVECTORIZATION-BASED SOFT SHADOW MAPPING

As shown in the previous chapter, Revectorization-based Shadow Mapping (RBSM) can be adapted for fixed-size penumbra simulation, but this kind of shadow rendering lacks realism because real-world shadows contain variable-size penumbra along its silhouette. In this chapter, we present three new techniques that use the concepts of shadow revectorization and Euclidean distance transform to provide visually plausible soft shadow rendering. The first technique, named Euclidean Distance Transform Soft Shadow Mapping (EDTSSM), is an extension of Euclidean Distance Transform Shadow Mapping (EDTSM) for soft shadow rendering. The second technique, named Revectorization-based Soft Shadow Mapping (RBSSM), improves the accuracy of EDTSSM, at the cost of loss in performance. The third technique, called Screen-Space Revectorization-based Soft Shadow Mapping (SSRBSSM), provides a balance between accuracy and performance, keeping visual quality as accurate as RBSSM, while generating soft shadows faster than EDTSSM. In this chapter, we present and evaluate all these techniques with respect to the state-of-the-art in the field of visually plausible soft shadow mapping. This chapter covers the discussion and results mainly presented in an authored publication (MACEDO; APOLINÁRIO, 2017).

### 5.1 VARIABLE-SIZE PENUMBRA ESTIMATION

To estimate the penumbra size of a given region, Percentage Closer Soft Shadows (PCSS) proposes that one needs to first approximate the scene by objects that are planar and parallel to each other. The depth of such a planar approximation is given by the average blocker depth  $z_{\text{avg}}(w_k^{\text{avg}}, \tilde{p}_z, S)$ , or simply  $z_{\text{avg}}$ , for a kernel with size  $w_k^{\text{avg}} \in \mathbb{N}$  (FER-NANDO, 2005)

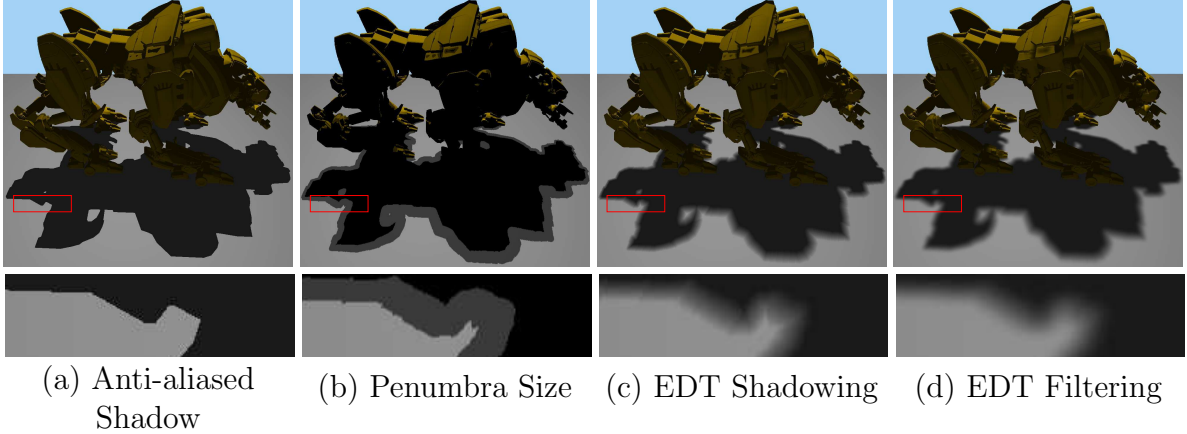


**Figure 5.1** An overview of EDTSSM. We estimate anti-aliased hard shadows in the camera view with non-conservative RBSM (a). On the basis of PCSS, we estimate the penumbra size of the fragments located at the hard shadow silhouette (b), and use it to normalize the EDT that is computed to measure the distance of each fragment to the closest hard shadow silhouette, simulating the penumbra effect (c). To suppress the skeleton artifacts generated by the EDT, an edge-aware viewpoint-invariant filtering algorithm is applied over the shadow (d).

$$z_{\text{avg}} = \frac{\sum_{i=0}^{w_k^{\text{avg}}} \sum_{j=0}^{w_k^{\text{avg}}} (1 - V_{\text{SM}}) S(i, j)}{\epsilon + \sum_{i=0}^{w_k^{\text{avg}}} \sum_{j=0}^{w_k^{\text{avg}}} (1 - V_{\text{SM}})}, \quad (5.1)$$

where  $\epsilon = 0.001$  is a small constant value to avoid the division by zero.

Then, on the basis of the parallel-planar assumption of PCSS, the variable penumbra size  $w_p(w_1, z_{\text{avg}}, \tilde{\mathbf{p}}_z)$ , or simply  $w_p$ , can be estimated according to the light source size  $w_1$  as (FERNANDO, 2005)

$$w_p = w_1 \frac{\tilde{\mathbf{p}}_z - z_{\text{avg}}}{z_{\text{avg}}} \quad (5.2)$$

In the next sections, we show each one of the proposed techniques make use of those equations to generate visually plausible soft shadows.

## 5.2 EUCLIDEAN DISTANCE TRANSFORM SOFT SHADOW MAPPING

In Algorithm 4, we present a high-level overview of the proposed approach to compute soft shadows on the basis of a normalized EDT. The steps of this approach are depicted in Figure 5.1. We render the scene from the light source and camera viewpoints (Lines 3 and 4 of Algorithm 4) to produce anti-aliased hard shadows with non-conservative RBSM (Figure 5.1-(a), Line 5 of Algorithm 4). Then, we estimate the penumbra size of the fragments located in the hard shadow silhouette (Figure 5.1-(b), Line 6 of Algorithm 4), such that we can apply the normalized EDT to compute the soft shadow (Figure

**Algorithm 4** Euclidean distance transform soft shadow mapping

---

```

1:  $w_{\text{filter}} \leftarrow$  soft shadow filter size;
2: for each frame do
3:    $S \leftarrow \text{RENDERSHADOWMAP};$ 
4:    $G \leftarrow \text{RENDERGBUFFER};$ 
5:    $R \leftarrow \text{REVECTORIZESHADOW}(S, G);$ 
6:    $P \leftarrow \text{ESTIMATEPENUMBRA SIZE}(R, S);$ 
7:    $\text{EDT} \leftarrow \text{PERFORMEDTSHADOWING}(R, G, P);$ 
8:    $F \leftarrow \text{FILTERSHADOW}(\text{EDT}, G, w_{\text{filter}});$ 
9:    $\text{RENDERSHADOWEDSCENE}(F, G);$ 
10:  end for

```

---

5.1-(c), Line 7 of Algorithm 4) and filter it to suppress the skeleton artifacts generated by the application of the EDT (Figure 5.1-(d), Line 8 of Algorithm 4).

The key difference between EDTSM and EDTSSM is that the penumbra size is no longer fixed, determined by the user. Now, for each fragment in the camera view, we must determine whether the fragment is located in a penumbra region, and what is the entire variable-sized penumbra region in the world space, such that we can compute the soft shadows on the basis of an EDT. The PCSS framework proposes that the penumbra size must be computed for every fragment in the camera view, since this size determines the area of the shadow map that must be filtered by the algorithm (FERNANDO, 2005). Similarly to (KLEIN; NISCHWITZ; OBERMEIER, 2012), we optimize such approach by computing the penumbra size only for the fragments located at the hard shadow silhouette and propagating such a data for the remaining fragments outside the shadow silhouette. Differently from (KLEIN; NISCHWITZ; OBERMEIER, 2012), we compute the penumbra size of the fragments located at the revectorized, anti-aliased hard shadow silhouette. Also, we propagate the penumbra size in real time using the nearest neighbour search provided by the EDT algorithm.

Similarly to EDTSM, to determine whether a fragment is located in the shadow silhouette in the image with the revectorized hard shadows (Figure 5.1-(a)), we check whether the visibility condition of the current fragment is different from at least one of the neighbours located inside a  $3 \times 3$  rectangular filter. Then, for each fragment in the shadow silhouette, we take advantage of the planar-parallel assumption of PCSS to estimate the penumbra size in real time (Figure 5.1-(b)), following Equations (5.1) and (5.2).

Once we have the penumbra size  $w_p$  computed for every fragment located in the revectorized hard shadow silhouette, we need to propagate this data for the fragments located outside the shadow silhouette. To do so, for each fragment outside the hard shadow silhouette, we compute the EDT, that returns exactly the location of the closest fragment located in the hard shadow silhouette. In this case, since  $w_p$  was estimated with respect to the light space, it cannot be directly used to define the size of the penumbra in the world space, since this task is non-trivial (FERNANDO et al., 2001). Hence, we multiply  $w_p$  by a user-defined parameter  $\beta$ , which helps with the definition of the

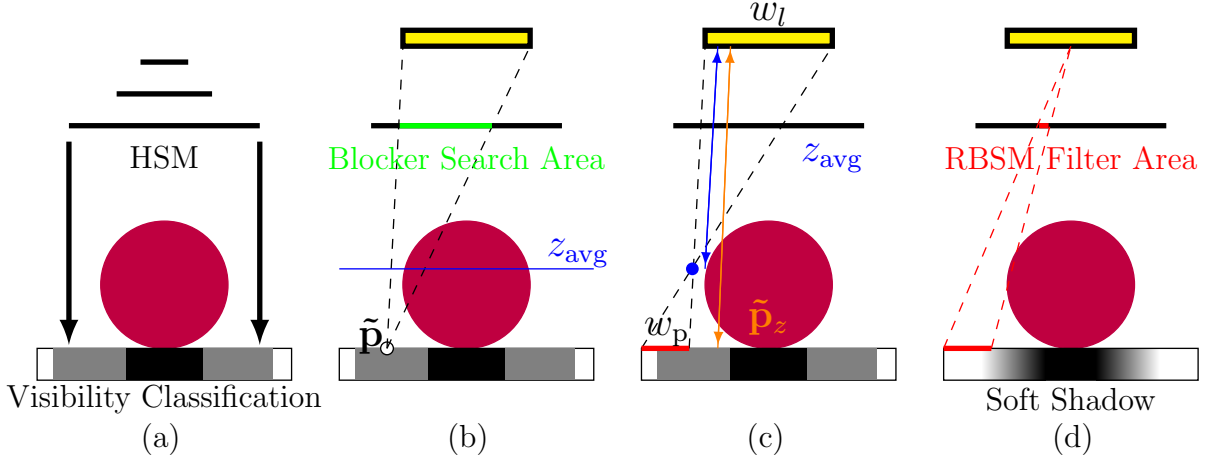


**Figure 5.2** An overview of RBSSM. After shadow map and G-buffer rendering, a hierarchical shadow map (HSM) is built to locate potential penumbra fragments in the camera view (a). For these fragments, the average blocker depth ( $z_{\text{avg}}$  in (b)) is computed, then the penumbra size ( $w_p$  in (c)) is estimated and filtered using RBSM to generate the soft shadows (d).

penumbra size in the world space. In our experimental tests, we have verified that  $\beta = 750$  keeps the penumbra size similar to the one found in the most common soft shadow mapping algorithm, such as PCSS.

Then, to compute the penumbra intensity of each fragment located in  $w_p$ , we have slightly changed (4.3) to take into account the variable-size penumbra

$$I = \begin{cases} \frac{1}{2} - \frac{D}{\beta w_p} & \text{if the fragment was in the hard shadow,} \\ \frac{1}{2} + \frac{D}{\beta w_p} & \text{otherwise.} \end{cases} \quad (5.3)$$

With (5.3), we are able to compute soft shadows such as the one shown in Figure 5.1-(c). To suppress the skeleton artifacts commonly produced by the use of EDT, we apply the same mean filtering step shown in Section 4.2.3, using (4.4).

### 5.3 REVECTORIZATION-BASED SOFT SHADOW MAPPING

Another alternative to compute anti-aliased soft shadows in real time consists in the direct integration of RBSM into the PCSS pipeline. Hence, RBSSM computes anti-aliased shadows based on PCSS and RBSM frameworks. Two steps are added into RBSM to perform penumbra size estimation and soft shadow filtering. To identify potential fragments located in the penumbra, improving the performance of the approach, we make use of a hierarchical shadow map (HSM) (GUENNEBAUD; BARTHE; PAULIN, 2006)  $H$ . In this case,  $H$  is a two-channel pyramidal-like min-max texture, that, at level  $l$ , has  $\frac{m}{2^l}$  rows and  $\frac{n}{2^l}$  columns. Each pixel in the first level ( $l = 0$ ) of  $H$  is defined by the shadow map itself. Then, the subsequent levels of  $H$  can be iteratively built by computing both minimal and maximal values of the depths stored in a  $2 \times 2$  region of the previous level.

**Algorithm 5** Revectorization-based soft shadow mapping

---

```

1:  $w_l \leftarrow$  light source size;
2:  $w_k^{\text{avg}} \leftarrow$  kernel size for average blocker depth estimation;
3: for each frame do
4:    $S \leftarrow \text{RENDERSHADOWMAP};$ 
5:    $G \leftarrow \text{RENDERGBUFFER};$ 
6:    $H \leftarrow \text{BUILDHIERARCHICALSHADOWMAP};$ 
7:   for each surface point  $\mathbf{p}$  visible in camera view from  $G$  do
8:      $\tilde{\mathbf{p}} \leftarrow \text{TRANSFORMTOLIGHTSPACE}(\mathbf{p});$ 
9:      $V_{\text{HSM}} \leftarrow \text{ESTIMATEVISIBILITYFROMHSM}(\tilde{\mathbf{p}}, H);$ 
10:    if  $V_{\text{HSM}} = \text{umbra}$  or  $V_{\text{HSM}} = \text{lit}$  then
11:       $V_{\text{RBSSM}} \leftarrow \text{COMPUTESHADOWTEST}(\tilde{\mathbf{p}}, S);$ 
12:    else
13:       $z_{\text{avg}} \leftarrow \text{COMPUTEAVGBLOCKDEPTH}(w_k^{\text{avg}}, \tilde{\mathbf{p}}, S);$ 
14:       $w_p \leftarrow \text{ESTIMATEPENUMBRA SIZE}(w_l, z_{\text{avg}}, \tilde{\mathbf{p}}_z);$ 
15:       $V_{\text{RBSSM}} \leftarrow \text{COMPUTESOFTSHADOW}(w_p, \tilde{\mathbf{p}}, S);$ 
16:    end if
17:   end for
18: end for

```

---

Indeed, the process of computing  $H$  works like mip-mapping, but we compute minimal and maximal values over a region rather than the average of the depth values.

With the map  $H$ , given the shadow map region intersected by the frustum formed by the light source area and the surface point  $\tilde{\mathbf{p}}$ , the depth values  $z_{\min} \in [0, 1]$  and  $z_{\max} \in [0, 1]$  of the corresponding hierarchical shadow map level must be retrieved to allow the evaluation of the illumination condition of the surface point by the visibility function  $V_{\text{HSM}}(\tilde{\mathbf{p}}_z, z_{\min}, z_{\max})$

$$V_{\text{HSM}}(\tilde{\mathbf{p}}_z, z_{\min}, z_{\max}) = \begin{cases} \text{lit} & \text{if } \tilde{\mathbf{p}}_z \leq z_{\min}, \\ \text{in umbra} & \text{else if } \tilde{\mathbf{p}}_z \geq z_{\max}, \\ \text{in penumbra} & \text{otherwise.} \end{cases} \quad (5.4)$$

An overview of RBSSM is shown in Figure 5.2 and is listed in Algorithm 5. First, we generate the shadow map  $S$  from the light source viewpoint (WILLIAMS, 1978) (Line 4 of Algorithm 5), the G-buffer  $G$  to avoid calculations on hidden fragments, evaluating the illumination only for the fragments visible to the camera (Line 5 of Algorithm 5), and the hierarchical shadow map  $H$ , to quickly classify the penumbra surface points in the scene and discard the non-penumbra surface points from the soft shadow calculation (Line 6 of Algorithm 5 and Figure 5.2-(a)).

Afterwards, we transform each visible surface point  $\mathbf{p}$  to the light source viewpoint (Lines 7 and 8 of Algorithm 5) and use  $H$  to identify the potential fragments located in the penumbra using (5.4) (Line 9 of Algorithm 5, Figure 5.2-(a)). The visibility of the surface points located outside the penumbra is given by the shadow test (3.2) (Lines 10-11 of Algorithm 5). Meanwhile, for the surface points located in the penumbra, we

proceed as proposed in the PCSS, computing average blocker depth (5.1) and penumbra size (5.2) (Lines 13-14 of Algorithm 5).

Rather than using the typical Percentage-Closer Filtering (PCF) for soft shadow filtering in the penumbra size  $w_p$ , we replace the PCF technique by Revectorization-based Percentage-Closer Filtering (RPCF) (Line 15 of Algorithm 5 and Figure 5.2-(d)).

RBSSM is able to generate soft shadows with high visual quality and real-time performance. An alternative to reduce its visual quality and improve its rendering performance consists on the realization of the soft shadow filtering in the screen space, as we show in the next section.

#### 5.4 SCREEN-SPACE REVECTORIZATION-BASED SOFT SHADOW MAPPING

SSRBSSM is an alternative approach to compute soft shadows on the basis of RBSM and PCSS frameworks that favors rendering performance rather than visual quality. The algorithm is much similar to RBSSM, except for the soft shadow filtering step, that is computed in the screen space.

SSRBSSM computes a shadow map and a G-buffer (Figure 5.2-(a)). Then, the average blocker depth and penumbra size are estimated in the shadow map space as well (Figures 5.2-(b, c)). However, the penumbra size estimated by RBSSM works well for filtering in the shadow map space. Since we aim to filter the soft shadows in the screen space, we estimate a screen-space penumbra size using (4.4).

To produce anti-aliased screen-space soft shadows, we must obtain the information about the anti-aliased hard shadows in the screen space. To do so, we produce filtered hard shadows in the screen-space using the RBSM technique (4.2) and save the filtered hard shadow intensity of each visible fragment. Next, we separate the soft shadow filtering in two steps: horizontal and vertical filtering in the screen space. In the horizontal pass, filtering is performed over the filtered hard shadow on the screen-sized penumbra area. In the vertical pass, filtering is done over the horizontally filtered hard shadows. In this step, the filtering must be edge-aware, since we lose information about the edge location in screen space. Hence, we use the separable cross-bilateral filter technique proposed in (PHAM; VLIET, 2005) for this purpose. Because the bilateral filter is not separable in essence, striped artifacts may appear during the filtering. We reduce such artifacts by increasing the bilateral filter sampling rate. Even in this case, since the number of increased samples is still smaller than the number of samples required for a non-separable implementation of the bilateral filter, separable bilateral filter is better suited, in terms of performance requirements, to our solution than the non-separable version of the bilateral filter.

As we show in the next section, the computation of the screen-space soft shadow filtering together with the high-quality revectorization-effect makes SSRBSSM an efficient alternative for simpler scenarios, where high performance is desirable for soft shadow rendering.

## 5.5 RESULTS AND DISCUSSION

In this section, we evaluate the techniques in terms of visual quality and performance. We compare the proposed approaches (EDTSSM, RBSSM and SSRBSSM) with the most traditional real-time soft shadow technique (PCSS), well-known shadow map pre-filtering techniques (Variance Soft Shadow Mapping (VSSM) and Moment Soft Shadow Mapping (MSSM)) and one of the most recent screen-space soft shadow techniques (Screen-Space Anisotropic Blurred Soft Shadows (SSABSS)). The visual quality is evaluated for the same shadow map and viewport resolutions and for different scenarios. Performance is evaluated for different shadow map and viewport resolutions and for different scenarios. Hard shadow techniques are not evaluated in this section because they are out of the scope of this chapter.

### 5.5.1 Experimental Setup

Following related work (PETERS et al., 2016), we fixed the filter size of  $9 \times 9$  for the blocker search step, and  $15 \times 15$  for the soft shadow filtering step of PCSS, VSSM, MSSM and EDTSSM techniques. For RBSSM, we have used a kernel size of  $7 \times 7$  since the filtering variant (Equation (4.2)) of RBSM requires less samples to effectively minimize banding artifacts. For the screen-space techniques, namely SSABSS and SSRBSSM, we have used a kernel size of  $31 \times 31$ , similarly to related work (BUADES; GUMBAU; CHOVER, 2015).

### 5.5.2 Visual Quality Evaluation

In Figures 5.3, 5.4 and 5.5, we show a comparison between the proposed approaches for different scenarios. In Figure 5.3, we evaluate the techniques for a complex object, with fine, detailed structures along its silhouette. In Figures 5.4 and 5.5, we show how different techniques handle the soft shadow computation for a more complex scenario, with multiple objects in different scales distributed all over the scene. Not only the scalability of the methods are evaluated for such a scenario with increased geometry complexity, but also the accuracy of the methods are evaluated due to the presence of multiple overlapping objects affecting the appearance of the shadow.

An equal low shadow map resolution comparison between different soft shadow techniques is depicted in Figure 5.3. For the limited  $1024^2$  shadow map resolution, PCSS generates aliasing artifacts along the soft shadow silhouette (Figure 5.3-(a)). VSSM and MSSM suffer from aliasing and light leaking artifacts (Figures 5.3-(b, d)). SSABSS provides similar visual quality than PCSS in this scenario (Figure 5.3-(c)). EDTSSM is not prone to aliasing artifacts, but promotes an overblurring of the shadow (Figure 5.3-(e)). Both RBSSM and SSRBSSM are able to effectively minimize the aliasing artifacts without the shadow overblurring (Figures 5.3-(f, g)), producing anti-aliased soft shadows comparable with ground-truth shadows (Figure 5.3-(h)).

A comparison between different soft shadow techniques for a more complex (game-like) scenario, due to the presence of several overlapping objects distributed along the scene and with different geometry complexity, is shown in Figures 5.4 and 5.5. As pointed

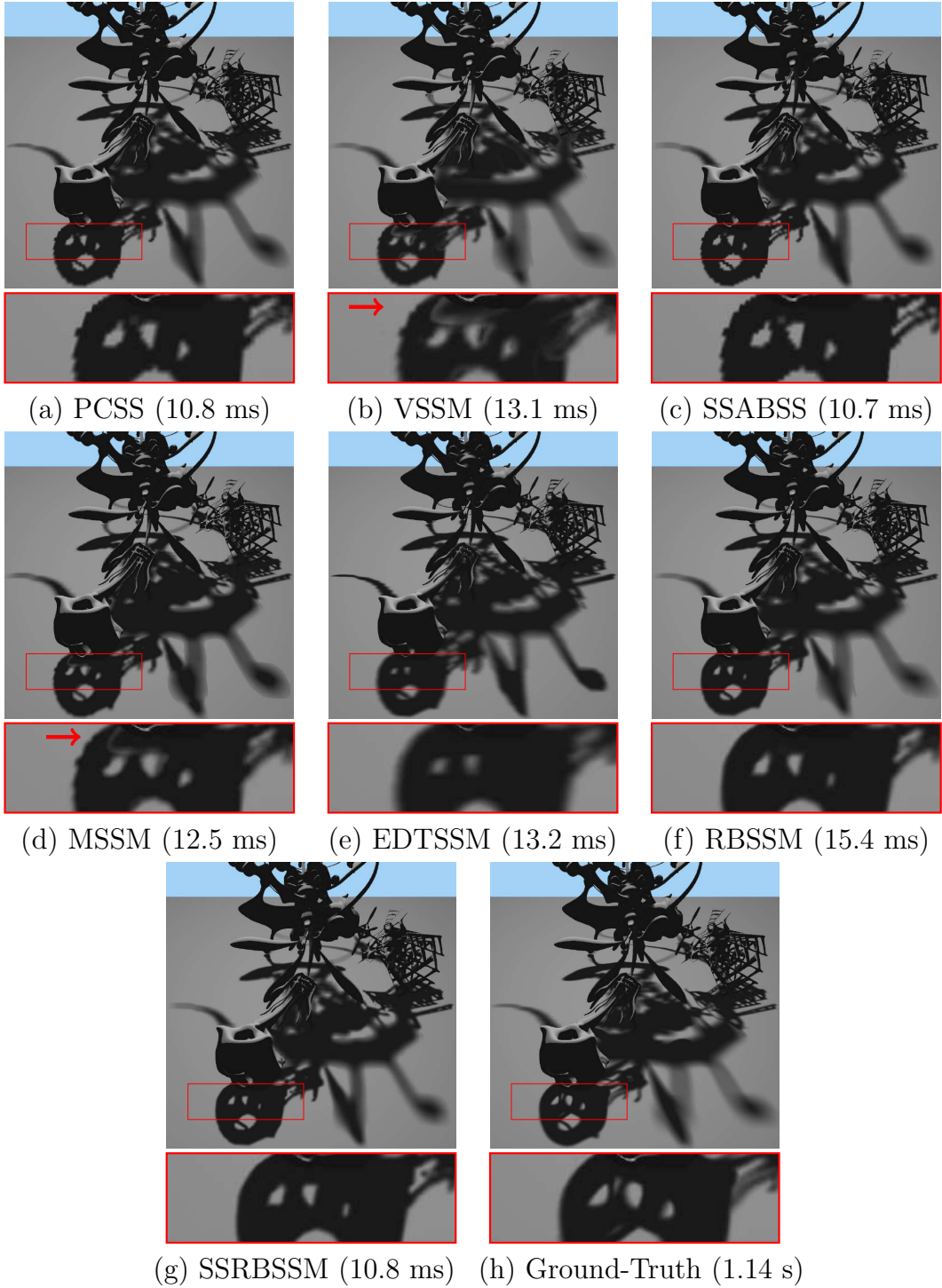


**Figure 5.3** A visual comparison between distinct soft shadow techniques. Shadow map pre-filtering techniques produce soft shadows with light leaking artifacts (pointed by red arrows). Images were generated for the YeahRight model using a  $1024^2$  shadow map resolution. The ground-truth image was computed using the average of 1024 area light source samples.

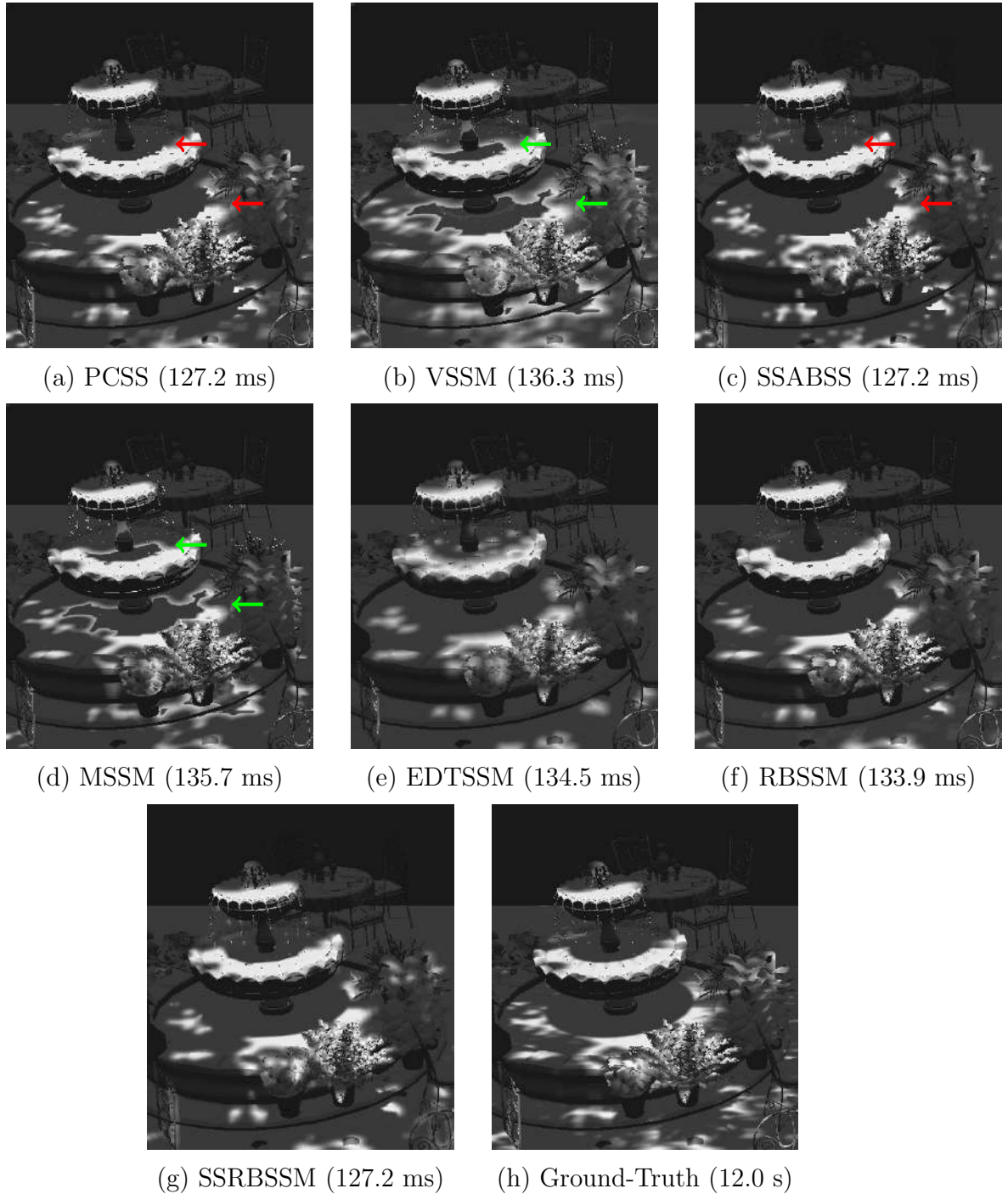


**Figure 5.4** An equal low shadow map resolution comparison between soft shadow techniques for a complex scenario. Aliasing and light leaking artifacts are pointed by red and green arrows. Images were generated for the San Miguel model using a  $1024^2$  shadow map resolution. The ground-truth image was computed using the average of 1024 area light source samples.

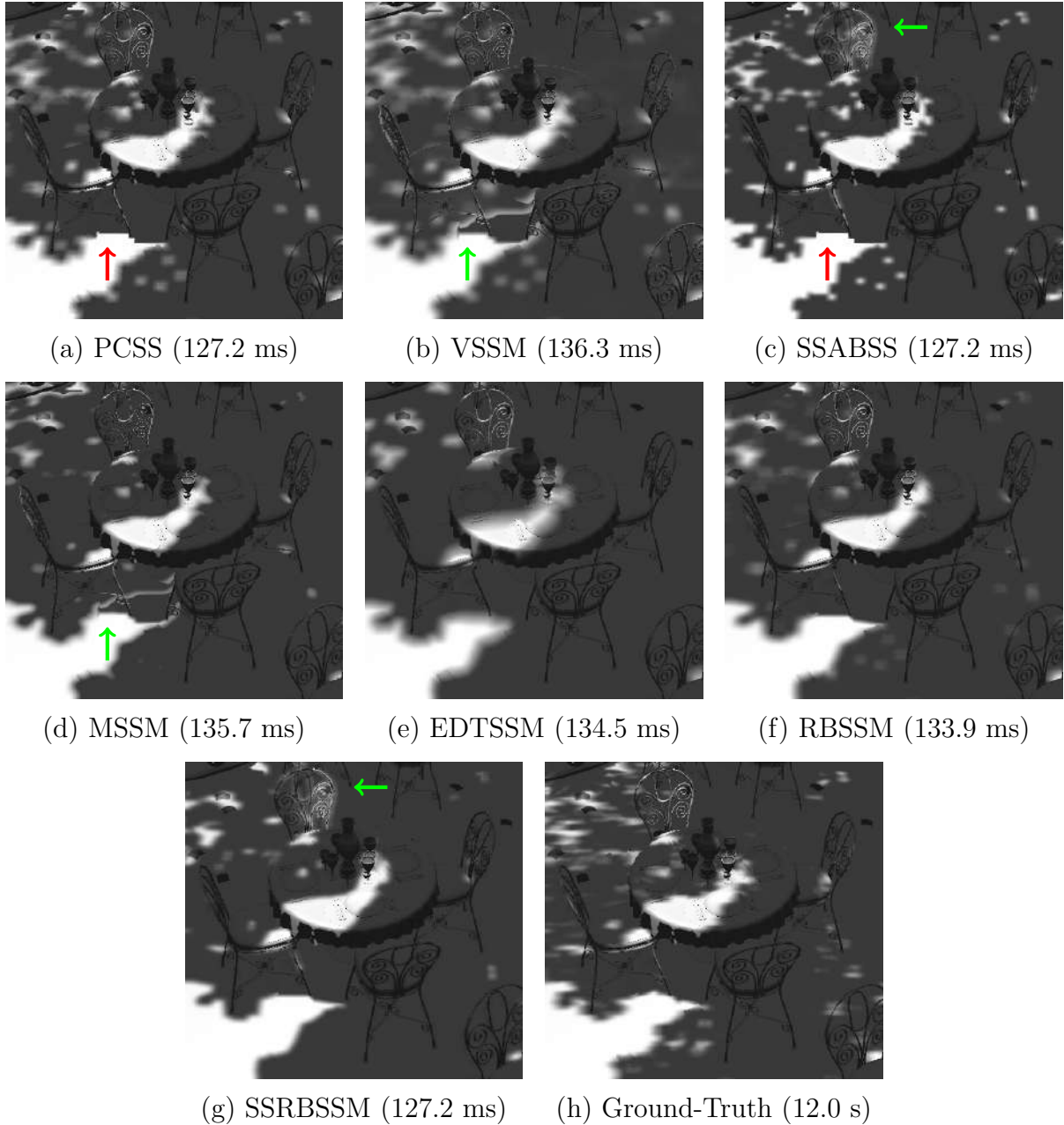


**Figure 5.5** An equal low shadow map resolution comparison between soft shadow techniques for a complex scenario. Aliasing and light leaking artifacts are pointed by red and green arrows. Images were generated for the San Miguel model using a  $1024^2$  shadow map resolution. The ground-truth image was computed using the average of 1024 area light source samples.

by red arrows, PCSS and SSABSS suffer from aliasing artifacts (Figures 5.4-(a, c) and 5.5-(a, c)). VSSM and MSSM suffer from light leaking artifacts (Figures 5.4-(b, d) and 5.5-(b, d)). Again, we can see that EDTSSM does not suffer from aliasing artifacts, but

overblurs the shadow (Figures 5.4-(e) and 5.5-(e)). RBSSM and SSRBSSM produces shadows that are more similar to the ground-truth than the other evaluated techniques (Figures 5.4-(f, g) and 5.5-(f, g)). Unfortunately, screen-space techniques are prone to light leaking artifacts near the silhouette of the objects if the depth difference of distinct objects in the scene is too small (see the region pointed by green arrows in Figures 5.5-(c, g)). In this sense, SSRBSSM is better than related work because it minimizes the aliasing artifacts (Figure 5.4-(g)).

### 5.5.3 Rendering Time Evaluation

In Figures 5.6, 5.7, 5.8 and 5.9, we show the performance of the several soft shadow techniques evaluated in this section under varying shadow map and output resolutions for the different scenarios evaluated in the previous subsection.

PCSS, SSABSS and SSRBSSM are generally the fastest techniques, regardless of the scene configuration. PCSS is relatively scalable with respect to the shadow map resolution (Figures 5.6 and 5.7) and is not scalable in terms of output resolution (Figures 5.8 and 5.9). RBSSM has the same performance characteristics of PCSS, but the additional cost demanded by the shadow revectorization makes RBSSM slower than PCSS. In this case, PCSS is faster than RBSSM, meanwhile RBSSM provides better visual quality than PCSS. On the other hand, VSSM and MSSM techniques handle well varying output resolution (Figures 5.8 and 5.9), but are not scalable with respect to the shadow map resolution, becoming two of the slowest techniques for higher shadow map resolutions (Figures 5.6 and 5.7). This happens because of the time needed to compute the summed-area table, required for the shadow map pre-filtering, increases as much as the shadow map resolution is increased. EDTSSM is scalable with respect to the shadow map resolution

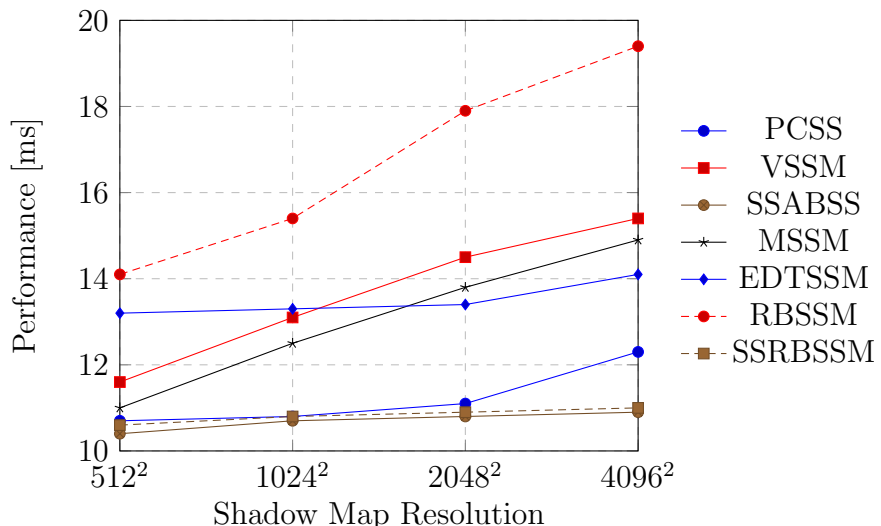


**Figure 5.6** Time usage (in milliseconds) for several soft shadow techniques. Rendering times were measured for the YeahRight model shown in Figure 5.3 at an output  $1280 \times 720$  resolution. Measurements include varying shadow map resolution.

(Figures 5.6 and 5.7), but is not scalable in terms of viewport resolution (Figures 5.8 and 5.9), because the Euclidean Distance Transform, the costly step of EDTSSM, is computed in the screen space. The screen-space techniques (SSABSS and SSRBSSM) are not that scalable in terms of viewport resolution (Figures 5.8 and 5.9), but they are generally faster than related work regardless of scene configuration.

#### 5.5.4 Discussion

Comparing solely the results obtained with EDTSSM, RBSSM and SSRBSSM, the screen-space variant is able to successfully compute soft shadows visually similar to the ones obtained with RBSSM, while being faster than EDTSSM. This fact can be mainly seen in Figures 5.3 and 5.4. The greatest advantage of SSRBSSM is that, by performing most of the computation in the screen space, the technique is faster than both revectorization-based techniques in all the scenes tested in this chapter. In this sense, RBSSM is suitable for applications that demand **high quality** shadow rendering, EDTSSM is desirable for applications that demand a balance between **quality** and **performance**, meanwhile SSRBSSM is desirable for applications that demand visually plausible soft shadow rendering with **high performance**.

Compared to related work, all the revectorization-based techniques provide the best visual quality results and are able to minimize aliasing and light leaking artifacts even for low-resolution shadow maps (Figures 5.3-(f, g), 5.4-(f, g) and 5.5-(f, g)). Also, RBSSM is the technique that produces shadows most similar to the ones generated by a dense uniform sampling of the area light source. In terms of performance, as can be seen in Figures 5.6, 5.7, 5.8 and 5.9, we clearly have three distinct groups that represent different behaviours of the soft shadow techniques. The first group composed of the screen-space

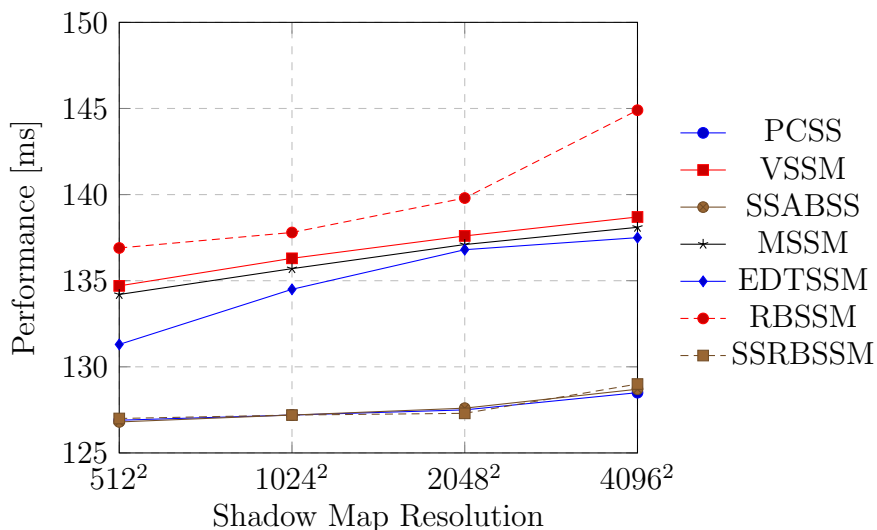


**Figure 5.7** Time usage (in milliseconds) for several soft shadow techniques. Rendering times were measured for the San Miguel model shown in Figures 5.4 and 5.5 at an output  $1280 \times 720$  resolution. Measurements include varying shadow map resolution.

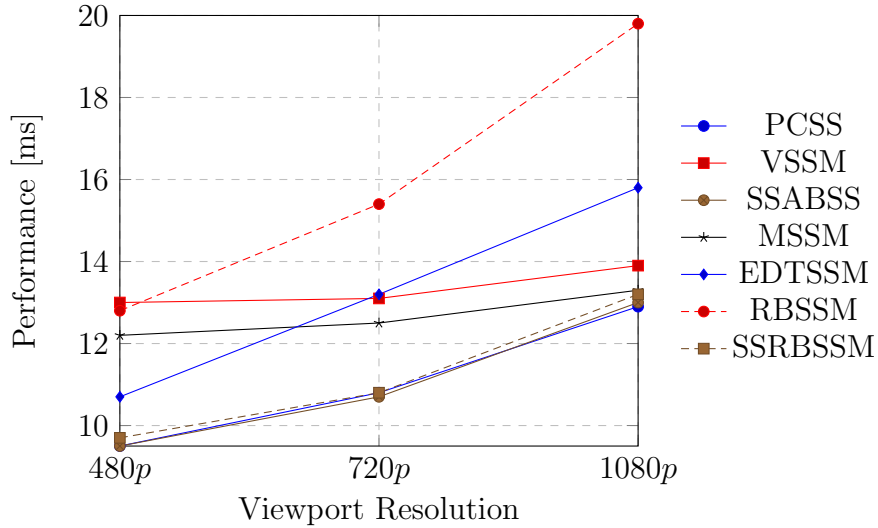


**Figure 5.8** Time usage (in milliseconds) for several soft shadow techniques. Rendering times were measured for the YeahRight model shown in Figure 5.3 at an  $1024^2$  shadow map resolution. Measurements include varying output resolution.

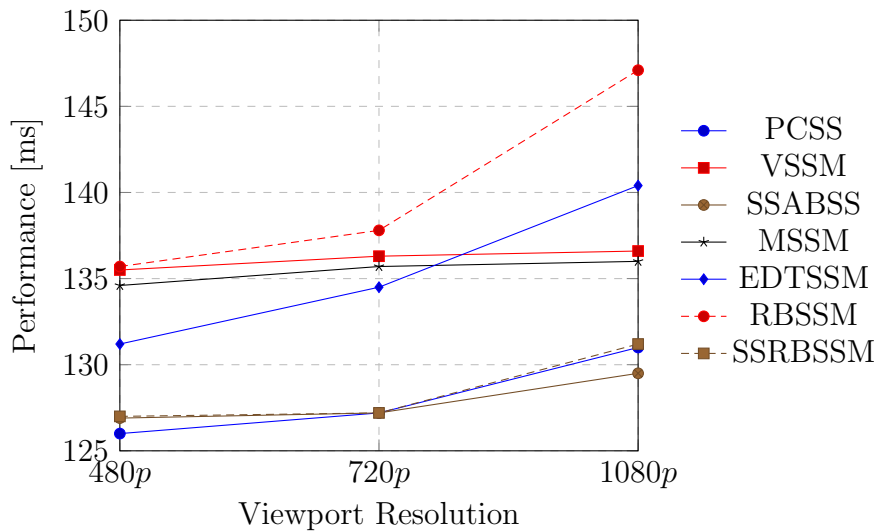


**Figure 5.9** Time usage (in milliseconds) for several soft shadow techniques. Rendering times were measured for the San Miguel model shown in Figures 5.4 and 5.5 at an  $1024^2$  shadow map resolution. Measurements include varying output resolution.

techniques and PCSS is the group of the fastest soft shadow techniques, that are scalable in terms of shadow map resolution, are not scalable with respect to viewport resolution, and achieve such a low running time by generating shadows prone to aliasing and light leaking artifacts, except for the SSRBSSM, that uses the revectorization to minimize aliasing. The second group is composed of the pre-filtering techniques, that are less sensitive to viewport variation than the screen-space techniques, but have increased pro-

cessing time and generates light leaking artifacts for simple and complex scenarios. The third group is composed of the other revectorization-based techniques, namely EDTSSM and RBSSM, whose cost increases according to both shadow map and viewport resolutions. It is worthy to note that the rate of increase in the processing time of RBSSM for higher viewport resolution is similar to the rate produced by PCSS and EDTSSM. Moreover, although RBSSM is, in average, 20% slower than the pre-filtering techniques and 50% slower than the screen-space techniques for the scenario shown in Figure 5.3, for a more complex scenario (Figures 5.4 and 5.5), in which the overall processing time of the solution is dominated by the geometry rendering, the technique becomes less than  $\approx 5\%$  more costly than the pre-filtering techniques and less than  $\approx 10\%$  more costly than the screen-space techniques. Given these facts, we can state that SSRBSSM is desirable for **simple scenarios**, since the technique is less prone to aliasing and light leaking artifacts than related work and provides one of the fastest processing times. RBSSM is desirable for **complex scenarios**, since even SSRBSSM suffers from light leaking artifacts (Figure 5.5-(g)) and RBSSM is able to provide an improved visual quality with less than 10% of processing time overhead, as compared to related work. Finally, EDTSSM provides a balance between SSRBSSM and RBSSM, obtaining competitive performance for both **simple** and **complex scenarios**.

### 5.5.5 Limitations

One of the limitations shared by all techniques evaluated in this chapter is that the quality of the generated soft shadow is highly dependent on the resolution of the shadow map. In this sense, we reinforce that the revectorization-based soft shadow techniques are able to minimize such a problem efficiently.

As a screen-space technique, SSRBSSM suffers from the same problem of the other screen-space soft shadow techniques: the screen-space filtering does not approximate the filtering produced from perspectively deformed kernels used for soft shadow filtering in the light space, nor takes into account the shadows located outside the view, while it is still prone to light leaking artifacts if the depth difference between different objects is too small (Figure 5.5-(g)). That is why the RBSSM technique, by performing the soft shadow filtering in the light space, has higher accuracy than SSRBSSM.

By using the mean filtering step as an alternative to minimize the skeleton artifacts generated by EDT, EDTSSM promotes an overblurring of the soft shadows that decreases the visual quality of the shadow rendering.

In terms of performance, RBSSM generates shadows with higher accuracy than related work, but is one of the slowest soft shadow mapping techniques.

Finally, all the techniques compared in this chapter compute soft shadows using only one shadow map, located at the center of the area light source, and assuming that both light source and blocker objects are planar and parallel to each other. This simplifying assumption makes the algorithms fast enough to run in real time and to generate visually plausible soft shadows. However, physical accuracy is lost because that assumption brings incorrect penumbra size and visibility estimations (EISEMANN et al., 2011). An example of such a problem is visible in Figure 5.10, where the PCSS algorithm fails to estimate

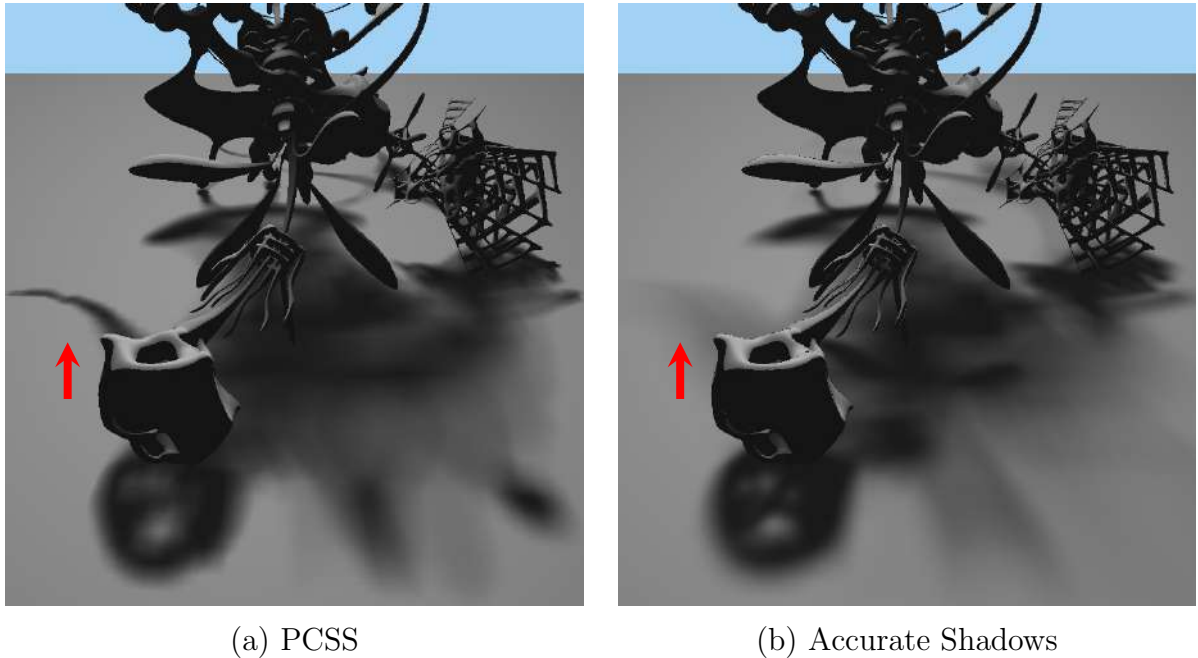


**Figure 5.10** For complex, large penumbra sizes, common real-time soft shadow techniques (a) fail to produce near accurate soft shadows (b) (see the region pointed by the red arrows). Images were generated for the YeahRight model using  $1024^2$  shadow map resolution.

the large penumbra size correctly.

## 5.6 SUMMARY

In this chapter, we have shown three techniques for visually plausible soft shadow rendering: EDTSSM, a technique that computes soft shadows on the basis of a normalized EDT, RBSSM, a technique that extends the RBSM approach to compute soft shadows, and SSRBSSM, a technique that computes soft shadows in the screen space, on the basis of the filtered hard shadow visibility function of RBSM.

Due to the revectorization effect provided by RBSM, all the proposed techniques are able to provide anti-aliasing for the soft shadow rendering. EDTSSM and RBSSM reduce the light leaking artifacts commonly generated by shadow map pre-filtering techniques, at the cost of more processing time for the shadow rendering. On the other hand, despite the limitations caused by performing the shadow filtering in the screen space, the SSRBSSM technique has shown promising results with respect to visual quality, while being one of the fastest soft shadow techniques compared to the other evaluated works.

None of the techniques proposed for visually plausible soft shadow rendering can compute accurate soft shadows because they approximate an area light source by a single point light source in order to simplify the shadow rendering problem. In the next chapter, we show how the revectorization effect can benefit the reproduction of accurate soft shadows computed on the basis of an adaptive area light source sampling.



In this chapter, we present an algorithm that takes advantage of the improved accuracy obtained with RBSM to generate accurate soft shadows from a few light source samples, while producing temporally coherent soft shadows at interactive frame rates.

## REVECTORIZATION-BASED ACCURATE SOFT SHADOW MAPPING

The problem of the techniques discussed in the previous chapter is that they are computed on the basis of a single point light source, typically located at the center of an area light source. Such an approximation decreases the quality of the shadow rendering, but makes the shadowing process real time. In this chapter, we present a new technique that uses the concepts of shadow revectorization and adaptive sampling to speed up the accurate rendering of soft shadows. The content of this chapter is based on an authored publication (MACEDO; APOLINÁRIO JR., 2017b).

### 6.1 REVECTORIZATION-BASED ACCURATE SOFT SHADOW RENDERING

An overview of the proposed algorithm is presented in Figure 6.1 and a high-level pseudocode is listed in Algorithm 6. Similarly to the solution proposed by related work (SCHWARZLER et al., 2012), we adaptively sample quads of four point light sources from the area light source (Figure 6.1-(a), Line 3 of Algorithm 6) and use them to evaluate whether banding artifacts are generated by the algorithm (Figures 6.1-(b, c, d, e, f), Lines 4-9 and 11 of Algorithm 6). In this case, we take advantage of the improved accuracy provided by the Revectorization-based Shadow Mapping (RBSM) visibility function to select less light source samples than related work (SCHWARZLER et al., 2012), while keeping its same visual quality. We further present a novel strategy to speedup the accurate soft shadow rendering on the basis of a visibility map (Figure 6.1-(g), Line 10 of Algorithm 6).

#### 6.1.1 Adaptive Light Source Sampling

Let us define the area light source  $\mathcal{L}$  as an adaptive structure where each node consists of a quad  $\mathcal{Q}$  formed by four neighbour point light sources. The main goal of the adap-

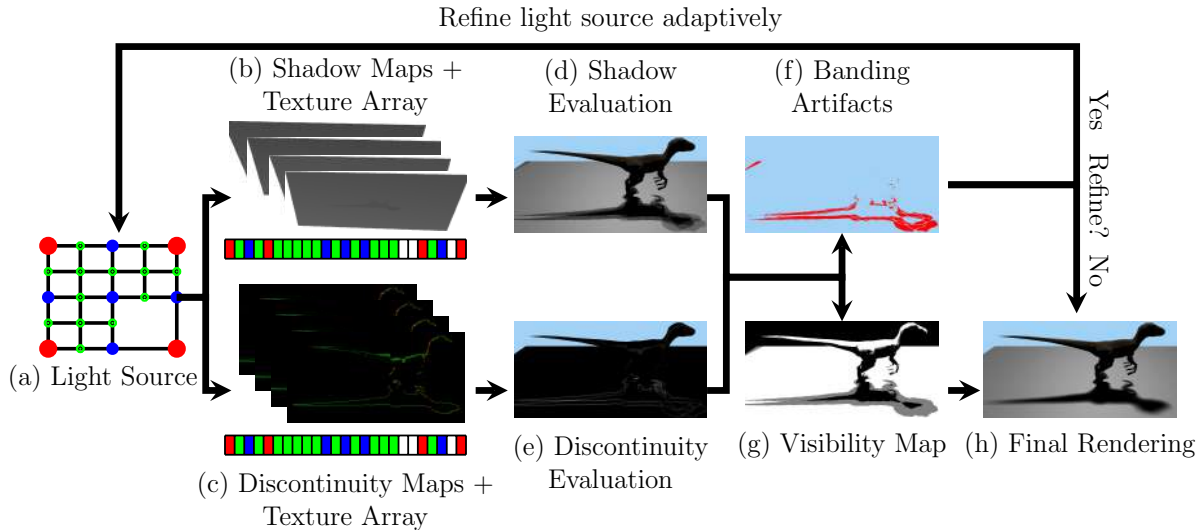


**Figure 6.1** An overview of the revectorization-based accurate soft shadow mapping. Given an area light source (a), we first generate four shadow (b) and discontinuity maps (c) for the neighbours point light sources located at the light source corners and store those maps into separate texture arrays. Then, the set of shadow and discontinuity maps (b, c) are evaluated (d, e) to detect the presence of banding artifacts (f) and build a visibility map (g) in the camera view. According to a refinement criteria, we determine whether the area light source must be adaptively refined and the algorithm reiterated for each four new neighbour samples. Otherwise, the accurate soft shadow is computed (h) on the penumbra fragments detected with the visibility map. The light source in (a) is refined to the third level of the adaptive structure, where each sample color represents a different level in the adaptive structure. As can be seen in (b, c), shadow and discontinuity maps are stored in the texture arrays according to the position of the sample (indicated by the colors) in the light source.

tive sampling is to generate only the light source samples  $\mathbf{l} \in \mathcal{L}$  that will contribute significantly to the final soft shadow appearance, generating visually accurate soft shadows. Hence, the light source refinement criteria must be view-dependent, considering whether the neighbour samples produce artifact-free soft shadows in the final rendering (SCHWARZLER et al., 2012).

We start the light source sampling by building the first level of the adaptive structure, where a single leaf node represents the quad formed by the light source samples located at the corners of the area light source (red circles in Figure 6.1-(a)).

To use RBSM in our refinement criteria, we need to compute the shadow test (3.2) and detect the discontinuity directions by the absolute difference of neighbour shadow tests  $\mathbf{d}$  (3.3) for each new point light source sample  $\mathbf{l} \in \mathcal{Q}$ . To do so, we render the scene from the viewpoint of  $\mathbf{l}$  and store the depth buffer as a shadow map (WILLIAMS, 1978) (Figure 6.1-(b)). Also, we render the scene from the camera viewpoint, compute the discontinuity and store it in a discontinuity map  $D$  of viewport width  $w$  and height  $h$  that stores, for each pixel  $D(i, j) \in \mathbb{N}^4$ , the vector  $\mathbf{d}$  (Figure 6.1-(c)). As shown in Figure

**Algorithm 6** Revectorization-based accurate soft shadowing

---

```

1: for each frame do
2:    $G \leftarrow \text{RENDERGBUFFER};$ 
3:   for each new quad  $\mathcal{Q}$  of light source  $\mathcal{L}$  with index  $q$  do
4:     for each new light source sample  $\mathbf{l}_i$  of  $\mathcal{Q}$  do
5:        $S_i \leftarrow \text{RENDERSHADOWMAP}(\mathbf{l}_i);$ 
6:        $D_i \leftarrow \text{RENDERDISCONTINUITYMAP}(S_i, G);$ 
7:     end for
8:      $ss \leftarrow \text{COMPUTESHADOWSUM}(S, G);$ 
9:      $sd \leftarrow \text{ISSOFTDISCONTINUITY}(D, G);$ 
10:     $\text{VM}_q \leftarrow \text{UPDATEVISIBILITYMAP}(ss, sd, \text{VM}_{q-1}, G);$ 
11:    if HASBANDINGARTIFACT( $ss, sd, G$ ) then
12:       $\text{REFINEADAPTIVESTRUCTURE}(\mathcal{L});$ 
13:    end if
14:  end for
15:   $\text{RENDERACCURATESOFTSHADOW}(S, D, \text{VM}, \mathcal{L}, G);$ 
16: end for

```

---

6.1, both maps are stored in separate texture arrays, whose sizes are equivalent to the maximum number of samples that can be selected from  $\mathcal{L}$  (Lines 3-7 of Algorithm 6). To optimize the discontinuity map rendering, we use a G-buffer (SAITO; TAKAHASHI, 1990) to guarantee that (3.3) is computed for visible fragments only (Lines 2 and 6 of Algorithm 6).

After the shadow and discontinuity map rendering, we need to determine whether the samples located in the same quad are sufficient for accurate soft shadow rendering. To do so, we project both shadow and discontinuity maps of the four neighbour samples into the same camera view and compare them (Figure 6.1-(d, e)) to detect whether banding artifacts are produced by the use of those samples (Figure 6.1-(f)). This comparison is done in a two-pass strategy with the scene rendered from the camera viewpoint.

In the first pass, for each fragment  $\mathbf{p}$  projected in a pixel with coordinates  $(i, j)$  in the camera view, we estimate the shadow sum  $ss(V_{\text{SM}}, \mathcal{Q}, i, j) \in [0, 4]$ , or simply  $ss$ , that is the sum of the four shadow test values of  $\tilde{\mathbf{p}}$  computed from the neighbour four shadow maps in the light quad  $\mathcal{Q}$  (Figure 6.1-(d) and Line 8 of Algorithm 6)

$$ss(V_{\text{SM}}, \mathcal{Q}, i, j) = \sum_{k=1, S_k \in \mathcal{Q}}^4 V_{\text{SM}}(\tilde{\mathbf{p}}_z, S_k(i, j)). \quad (6.1)$$

Additionally, we label a fragment as *soft discontinuity* if the fragment is in the shadow silhouette (*i.e.*,  $\mathbf{d} \neq 0$ ) for at least  $sd$  point light source samples (Figure 6.1-(e) and Line 9 of Algorithm 6). Considering  $sd \in [0, 4]$ ,  $sd = 1$  generates a really small number of samples for rendering, making the approach susceptible to banding artifacts. On the other hand,  $sd = 4$  generates several samples, as a few fragments are classified as lying in the shadow silhouette for all the four neighbour light source samples.  $sd = 2$  or  $3$  generates a moderate number of samples. We have used  $sd = 2$  for all the scenarios

shown in this chapter because this value generates less samples than  $sd = 3$ , while being much less susceptible to banding artifacts than  $sd = 1$ .

In the next pass, both shadow sum and fragment classification (Figure 6.1-(d, e)) are used to locate the fragments that potentially produce banding artifacts in the camera view (Figure 6.1-(f), Line 11 of Algorithm 6). Based on the previously computed shadow sum (6.1), fully lit (*i.e.*,  $ss = 4$ ) and fully shadowed fragments (*i.e.*,  $ss = 0$ ) are discarded from rendering because they are not located in the penumbra and cannot cause banding artifacts. Fragments classified as *soft discontinuity* are discarded from rendering as well, because RBSM will guarantee high-quality anti-aliasing for them. The remaining fragments (whose shadow sum lies between 1 and 3) are compared against their 8-connected neighbour fragments in the camera view. If the fragment has at least one neighbour fragment that has a different shadow sum or that is a *soft discontinuity*, the fragment is discarded. The only fragments rendered in the scene are the ones whose shadow sums state that the fragments are in the penumbra and the shadow sums are the same for all the 8-connected neighbours. That is the case of the fragments located in penumbra regions that are not sufficiently smooth, due to the high distance between light source samples (and their shadow maps). As shown in Figure 6.1-(f), those fragments produce banding artifacts in the final rendering, rather than a single, smooth penumbra region (SCHWARZLER et al., 2012).

Hardware occlusion query (BARTZ; MEIBNER; HUTTNER, 1998) is used to check if a single pixel was rendered on the screen. If this condition is true, the area light source is further refined according to the adaptive structure (Line 12 of Algorithm 6). Then, the algorithm is iterated for the new light quads (Figure 6.1).

To optimize the performance of our solution, while we perform the light source sampling, we build and update a visibility map  $\text{VM}$ . This map is a texture that stores the final illumination condition of each fragment (*i.e.*, whether the fragment is lit, penumbra or umbra) (Figure 6.1-(g)). With such a map, we are able to restrict the costly accurate soft shadow rendering for penumbra fragments only.

The algorithm to compute the visibility map is fairly simple, yet effective. First, we clear  $\text{VM}$ , indicating that no classification has been assigned to any visible fragment. Then, we use the estimated shadow sum to update the stored visibility condition of the fragment. Let us redefine the shadow sum as  $ss_q$  and the visibility map as  $\text{VM}_q$ , where  $q$  refers to a index of  $\mathcal{Q}$ . For the first quad of the adaptive structure, the visibility classification  $\text{VM}_0(i, j)$  of the fragment  $\mathbf{p}$  located at the pixel  $(i, j)$  is computed on the basis of the shadow sum estimated at that pixel  $ss_0(i, j)$

$$\text{VM}_0(i, j) = \begin{cases} \text{umbra} & \text{if } ss_0(i, j) = 0, \\ \text{penumbra} & \text{else if } 1 \leq ss_0(i, j) \leq 3, \\ \text{lit} & \text{otherwise.} \end{cases} \quad (6.2)$$

Additionally, we define  $\text{VM}_0$  as penumbra for the fragments classified as *soft discontinuity*.

For the next quad, assuming that the adaptive structure has more than one level, we update the visibility map by classifying the fragment as penumbra if there is a difference between the illumination condition previously estimated in the visibility map and the one

given by the current shadow sum. In other words

$$\text{VM}_q(i, j) = \begin{cases} \text{penumbra} & \text{if } \text{VM}_{q-1}(i, j) = \text{lit} \text{ and } ss_q(i, j) = 0, \\ & \text{or } \text{VM}_{q-1}(i, j) = \text{umbra} \text{ and } ss_q(i, j) = 4. \end{cases} \quad (6.3)$$

Finally, in the final rendering step (Figure 6.1-(h)), after the refinement criteria has been satisfied, we access the visibility map to determine the visibility condition of the fragment in the camera view. Lit and umbra fragments are illuminated accordingly, and for penumbra fragments only, we proceed with the computation of the final soft shadow intensity.

### 6.1.2 Final Rendering

Given the  $n$  light source samples  $\mathbf{l}$  distributed over the surface of the area light source  $\mathcal{L}$ , the final soft shadow intensity of a point  $\mathbf{p}$  (Figure 6.1-(h), Line 15 of Algorithm 6) can be computed according to the visibility function  $V \in [0, 1]$

$$V = \frac{\sum_{i=1}^n \omega_i V_{\text{RBSM}}^{**}(\mathbf{l}_i)}{\sum_{i=1}^n \omega_i}. \quad (6.4)$$

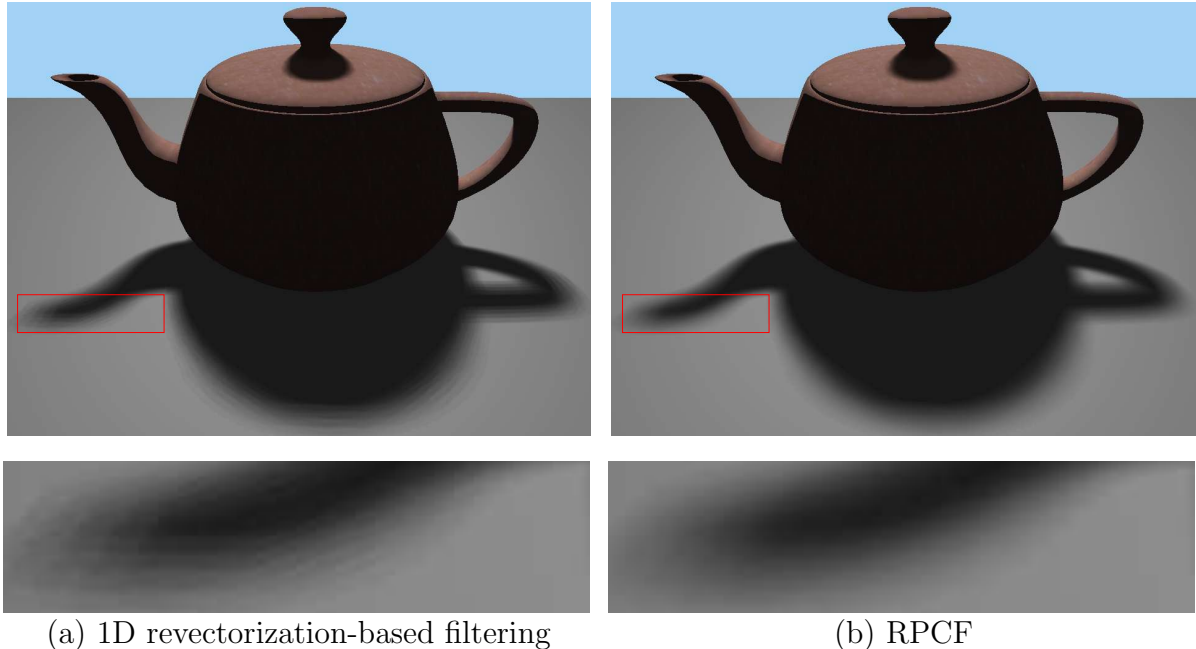
where  $V_{\text{RBSM}}^{**}(\mathbf{l}_i)$  denotes the visibility function of the filtered version of the RBSM technique (4.2) with respect to the point light source  $\mathbf{l}_i$ , and  $V$  estimates how much of the area light source is visible to the point  $\mathbf{p}$ . Therefore,  $V = 0$  indicates that the entire area light source is not visible to a given surface point  $\mathbf{p}$ , and  $V = 1$  indicates the full visibility of the area light source to  $\mathbf{p}$ .  $\omega_i$  is the weight assigned to the point light source  $\mathbf{l}_i$  that compensates for the irregular distribution of samples, computed as (SCHWARZLER et al., 2012)

$$\omega = \frac{1}{(2^\alpha + 1)^2}, \quad (6.5)$$

where  $\alpha$  is the level of the adaptive structure.

RBSM is the basis of three distinct techniques that produce different shadow outputs: conservative, non-conservative and filtered RBSM. In (6.4), we use the filtered version of RBSM because the use of filtering for shadow revectorization is efficient to solve banding artifacts.

We could compute (6.4) in  $n$  shader passes, evaluating  $V$  per sample in each pass, and using the accumulation buffer (HAEBERLI; AKELEY, 1990) to store the accumulated soft shadow intensity. Since we store the  $n$  shadow and discontinuity maps into two texture arrays (Figure 6.1-(b, c)), we are able to compute (6.4) and evaluate the filtered RBSM visibility function for all the light source samples in a single pass on the shader, further saving many read/write operations that would be needed by the accumulation buffer.



(a) 1D revectorization-based filtering

(b) RPCF

**Figure 6.2** (a) For a relatively large penumbra size, the use of the revectorization-based filtering visibility function generates banding artifacts for a few light source samples. (b) The control over the filter size provided by RPCF allows the generation of artifact-free soft shadows, at the cost of increased processing time.

### 6.1.3 Temporally Coherent Soft Shadow Computation

One alternative to further reduce processing time and the number of selected light source samples relies on the reduction of the viewport size used for occlusion query during the adaptive refinement. Unfortunately, the algorithm becomes prone to banding artifacts due to the insufficient number of samples. Rather than using the 1D filtering technique as a visibility function in (6.4), RPCF can be used to solve this problem, but the performance drops considerably when using this technique. Another problem with the viewport size reduction is that a fixed reduction factor produces incoherent soft shadows as the camera moves in the scene. In this way, we can use an adaptive approach to estimate this reduction factor to produce temporally coherent soft shadows. Also, we need to determine whether RPCF is useful to solve the banding artifacts generated from the viewport size reduction.

In general, the 1D revectorization-based filtering is well suited for scenarios with small penumbra sizes because it adds filtering for a limited extension of the anti-aliased shadow. However, for large penumbra sizes, several light source samples are still required to generate artifact-free soft shadows, because the small filter size of the filtering technique does not solve the banding artifacts in the penumbra (Figure 6.2-(a)). A more appropriate alternative for large penumbra sizes is RPCF, that requires a few light source samples to provide high-quality soft shadows (Figure 6.2-(b)). In this sense, according to the area

light source and the penumbra size, each one of the revectorization-based techniques is more adequate for accurate soft shadow rendering.

To compute the appropriate window size for occlusion query automatically, we estimate such value according to the RBSM technique used and the current level of the adaptive structure. We draw this approach from the observation that the window size reduction may change from adaptive structure level because, as long as the structure is refined, we can relax the criteria to guarantee that a small number of samples will be used for rendering. Let us assume  $ws$  the original window size,  $ws_{RBSM}(ws, \alpha)$  and  $ws_{RPCF}(ws, \alpha)$  the window sizes used for the 1D revectorization-based filtering and RPCF techniques, respectively. In this work, we have used the following window sizes

$$ws_{RBSM}(ws, \alpha) = \begin{cases} ws & \text{if } 0 \leq \alpha \leq 1, \\ \frac{ws}{2} & \text{else if } 2 \leq \alpha \leq 3, \\ \frac{ws}{4} & \text{otherwise.} \end{cases} \quad (6.6)$$

$$ws_{RPCF}(ws, \alpha) = \begin{cases} \frac{ws}{4} & \text{if } 0 \leq \alpha \leq 1, \\ \frac{ws}{6} & \text{else if } 2 \leq \alpha \leq 3, \\ \frac{ws}{8} & \text{otherwise.} \end{cases} \quad (6.7)$$

As we aim to generate a few light source samples, the idea of keeping the adaptive structure built from the previous frame and refining or condensing it in the next frame did not improve the performance of the algorithm.

## 6.2 RESULTS AND DISCUSSION

In this section, we evaluate the soft shadow techniques in terms of visual quality and performance. We compare our revectorization-based (RB) adaptive sampling with other sampling strategies, namely the uniform sampling of the area light source (using 289 samples, as suggested in (SCHWARZLER et al., 2012)) and the adaptive sampling solution proposed in (SCHWARZLER et al., 2012). Also, we compare our approach with a traditional technique from the field of real-time soft shadow mapping: Percentage Closer Soft Shadows (PCSS) (FERNANDO, 2005).

### 6.2.1 Experimental Setup

To provide a fair comparison between the adaptive sampling of (SCHWARZLER et al., 2012) and ours, we have used their solution with a reduction over the window size for occlusion query by a factor of 4 and Percentage-Closer Filtering (PCF) (REEVES; SALESIN; COOK, 1987) to compensate the banding artifacts. Their solution is always slower than ours when using the same window size for both occlusion query (during adaptive sampling) and output resolution (during final rendering). All images were generated by a rectangular area light source. Both PCF and RPCF techniques use the same kernel size of  $2 \times 2$ .

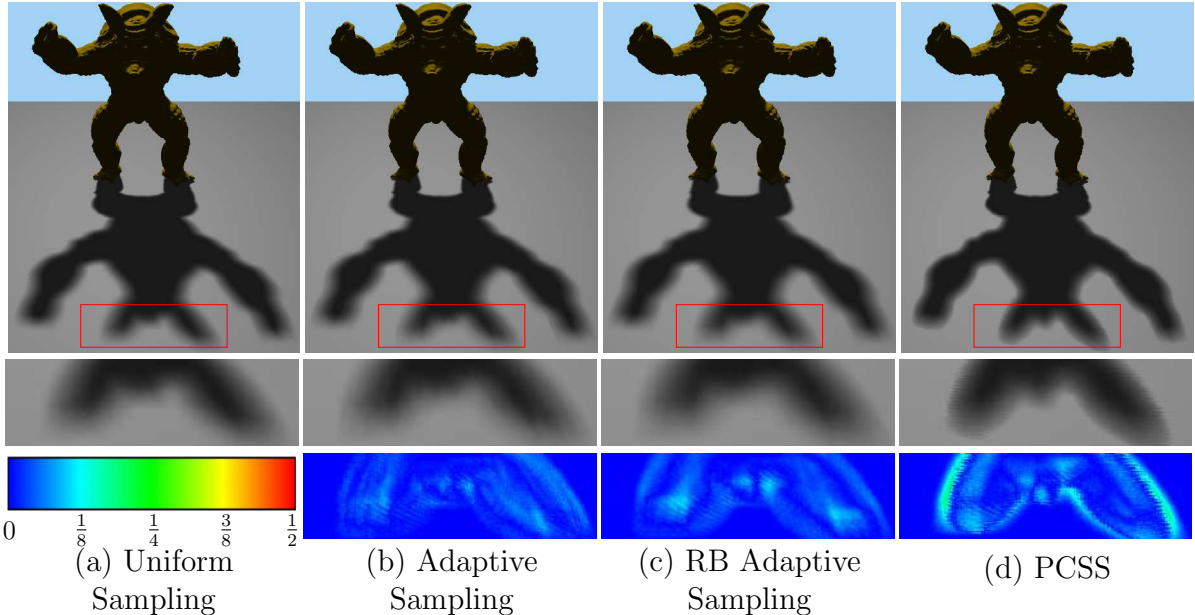


**Figure 6.3** Accurate soft shadows produced by different techniques. In this scenario, 289 light source samples were used for uniform sampling (a), 47 light source samples were used for adaptive sampling (b), and only 25 light source samples were used for our RB adaptive sampling (c). PCSS (d) uses a single point light source sample. False color visualizations show the difference between the normalized shadow intensities generated by uniform sampling, which uses the largest number of samples, and the other techniques. Images were generated for the Armadillo model using a  $1024^2$  shadow map resolution.

### 6.2.2 Visual Quality Evaluation

As shown in Figures 6.3, 6.4, 6.5, our revectorization-based adaptive sampling provides high-quality, accurate soft shadows (Figures 6.3-(c), 6.4-(c), 6.5-(c)), needing a few light source samples to achieve such a visual quality. We require about 4-11 times less samples than the uniform sampling approach (Figures 6.3-(a), 6.4-(a), 6.5-(a)) and 2-4 times less samples than the adaptive sampling approach proposed in (SCHWARZLER et al., 2012) (Figures 6.3-(b), 6.4-(b), 6.5-(b)) to achieve high visual quality. Although the real-time soft shadow technique (Figures 6.3-(d), 6.4-(d), 6.5-(d))) generates visually plausible soft shadows, the penumbra size is estimated incorrectly and some details of the shadow are lost due to the approximation of the area light source by a single point light source.

An analysis of the influence of the penumbra size over the proposed adaptive sampling algorithm can be seen in Figure 6.6. For small penumbra sizes (Figure 6.6-(a)), our approach is faster than the uniform sampling approach, while generating accurate soft shadows from a few light source samples. Real-time soft shadow algorithms, in this case, tend to produce visually plausible soft shadows (Figure 6.6-(a)). As the penumbra size increases (Figures 6.6-(b, c)), more light source samples are needed to effectively suppress banding artifacts. In this scenario, while being able to generate accurate soft shadows,

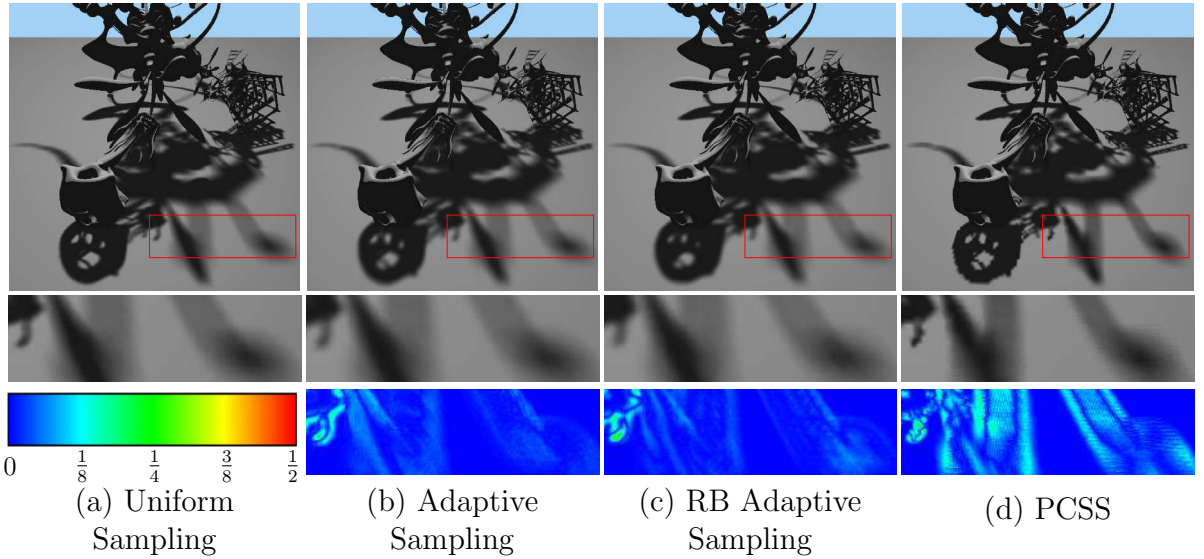


**Figure 6.4** Accurate soft shadows produced by different techniques. In this scenario, 289 light source samples were used for uniform sampling (a), 134 light source samples were used for adaptive sampling (b), and only 62 light source samples were used for our RB adaptive sampling (c). PCSS (d) uses a single point light source sample. False color visualizations show the difference between the normalized shadow intensities generated by uniform sampling, which uses the largest number of samples, and the other techniques. Images were generated for the YeahRight model using a  $1024^2$  shadow map resolution.

our approach may be slower than the uniform sampling approach mainly because of three factors: 1. RBSM is slower than the traditional shadow mapping, although it provides improved visual quality, 2. the adaptive refinement provides an additional cost to the final rendering time, while the uniform approach does not have such a step, 3. in the case where the penumbra fills much of the screen-space available, the use of the visibility map does not discard a high number of fragments from the final rendering evaluation. As shown in Figure 6.6-(b, c), for large penumbra sizes, real-time soft shadow algorithms are able to generate soft shadows with low processing time, but cannot generate accurate soft shadows (as pointed by the red arrows in Figure 6.6-(b, c)). Indeed, such a difference is mainly visible for situations such as the one shown in Figure 5.10, where the umbra region disappears entirely in penumbra. In these cases, the approximation of the area light source by a single point light source does not provide enough information for the sampling and rendering of those fine details of the penumbra.

The improved temporal coherency obtained with our solution can be seen in Figure 6.7. The adaptive sampling approach of (SCHWARZLER et al., 2012) greatly varies the number of selected light source samples according to the distance of the camera to the penumbra region. While a high number of samples is selected when a large amount of the screen space is occupied by the penumbra, a really small number of samples are selected when the camera is far away. In this case, one can see the shadows as a composition

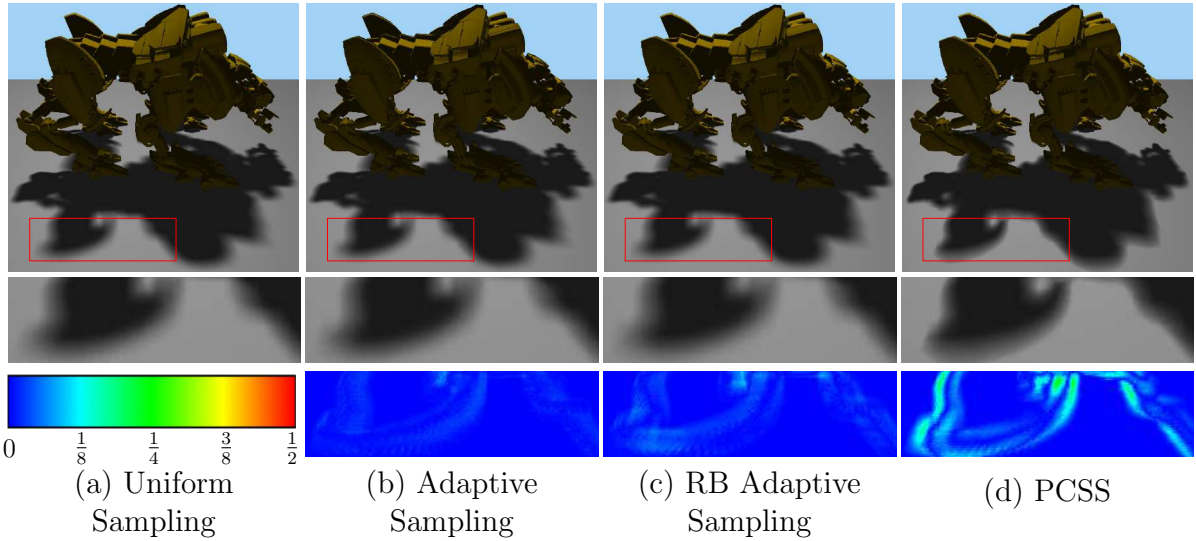


**Figure 6.5** Accurate soft shadows produced by different techniques. In this scenario, 289 light source samples were used for uniform sampling (a), 246 light source samples were used for adaptive sampling (b), and only 63 light source samples were used for our RB adaptive sampling (c). PCSS (d) uses a single point light source sample. False color visualizations show the difference between the normalized shadow intensities generated by uniform sampling, which uses the largest number of samples, and the other techniques. Images were generated for the QuadBot model using a  $1024^2$  shadow map resolution.

of several hard shadows rather than a single soft shadow (SCHWARZLER et al., 2012). Our approach keeps the number of samples selected from the area light source consistent, generating high-quality soft shadows regardless of the distance from the viewer to the penumbra region.

### 6.2.3 Rendering Time Evaluation

A performance comparison between the techniques evaluated in this section can be seen in Tables 6.1 and 6.2. The uniform sampling of the area light source provides stable frame rates under different parameters, but provides the worst performance, due to the large number of samples used for every frame. The adaptive sampling strategy proposed in (SCHWARZLER et al., 2012) becomes faster as long as the shadow map resolution increases, because less samples are required to generate high-quality accurate soft shadows when high resolution shadow maps are used. On the other hand, such a sampling strategy is sensitive to high output resolutions due to the use of a screen-space criteria. For a 1080p output resolution, the adaptive sampling strategy provides performance similar to uniform sampling. Our revectorization-based sampling strategy provides the best performance among the evaluated accurate soft shadow techniques, regardless of the shadow map and output resolutions used. Obviously, PCSS obtains better performance since the technique uses only one sample of the light source to compute the soft shadows. However, as shown

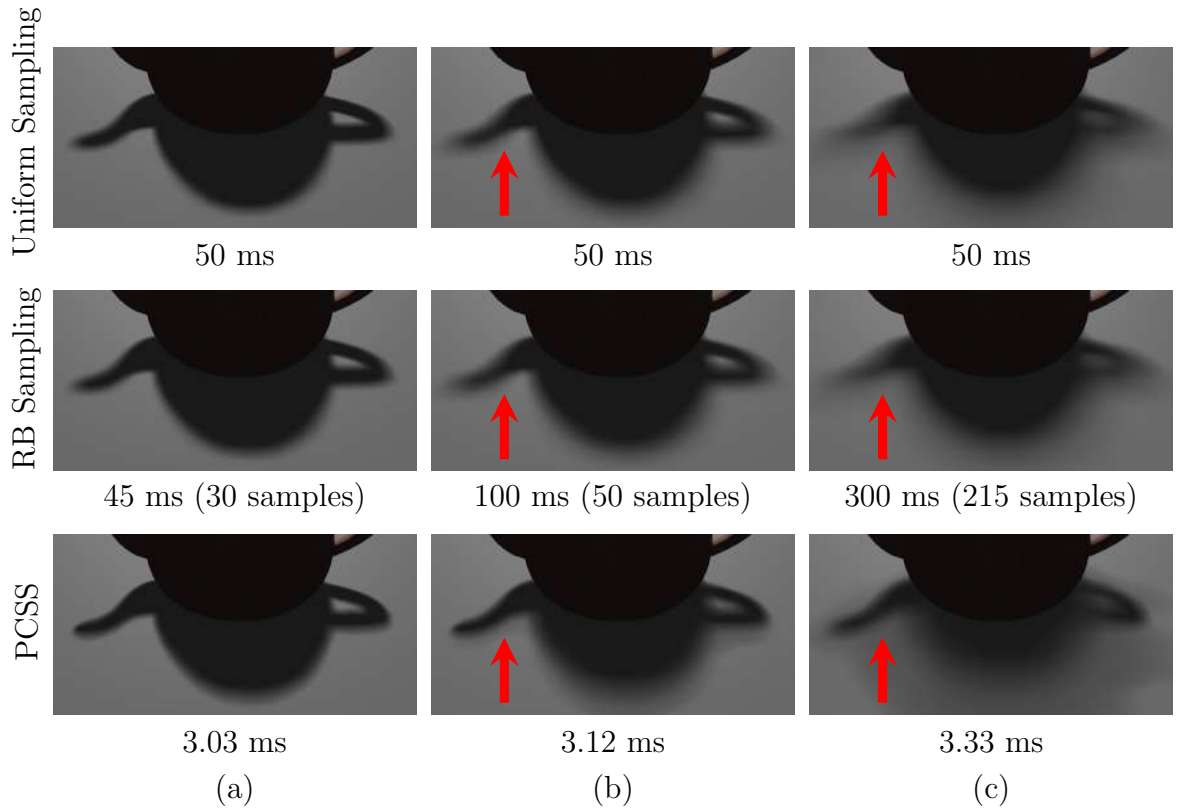


**Figure 6.6** A performance/visual quality comparison between different soft shadow techniques under distinct penumbra sizes. For small penumbra sizes (a), our approach is generally faster than the uniform sampling approach. The opposite occurs for large penumbra sizes (b, c), which demands an increased number of samples to minimize the banding artifacts. A real-time soft shadow approach is able to render visually plausible soft shadows for small penumbra sizes (a), but deviates from the accurate soft shadow under large penumbra sizes (see the region pointed by the red arrows in b, c). Images were generated for the Teapot model using a  $1024^2$  shadow map resolution.

in Figures 6.3, 6.4 and 6.5, PCSS also provides the worst soft shadows in terms of visual quality.

An in-depth evaluation of the rendering times obtained for each step of our algorithm is shown in Tables 6.3 and 6.4. It is visible that the bottlenecks of our approach are the shadow map rendering and the accurate soft shadow rendering. The shadow map rendering is costly because, different from the discontinuity map rendering and other steps, this one cannot take advantage of a G-buffer rendering to optimize the performance of the scene rendering. So, the entire scene must be rendered several times, according to the number of samples selected from the area light source. On the other hand, the accurate soft shadow rendering is costly because of the shadow revectorization visibility function that must be computed for every light source sample. The other steps of our

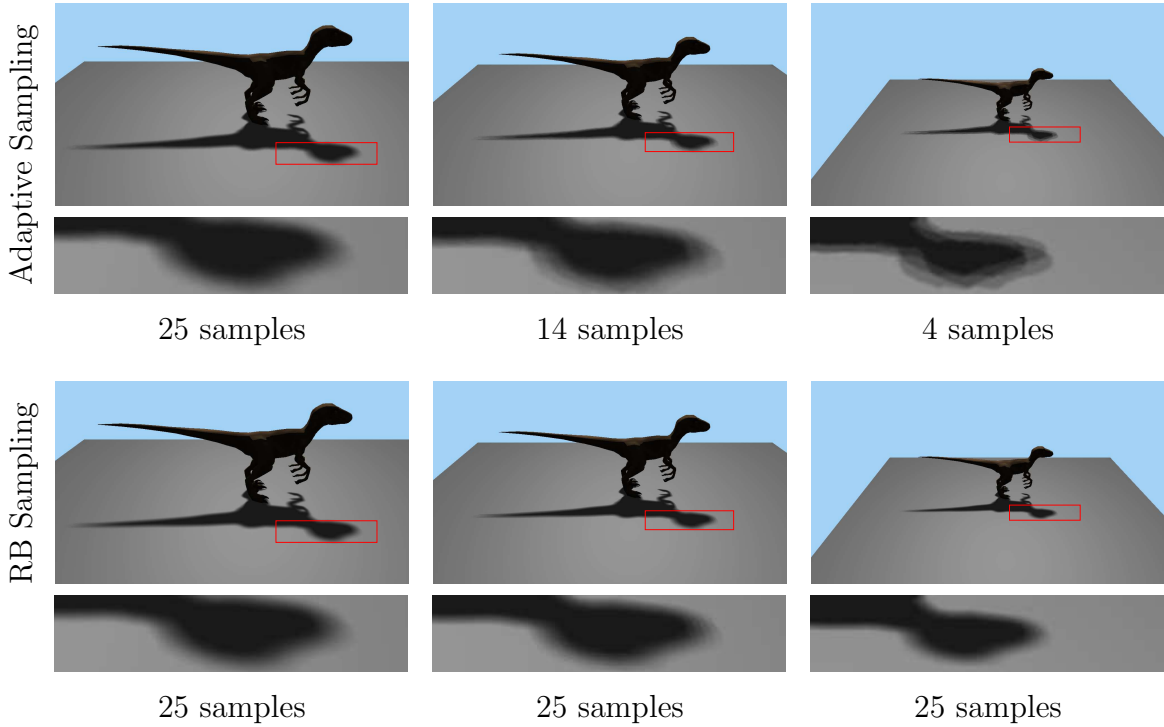


**Figure 6.7** The temporal coherency provided by both adaptive sampling and revectorization-based (RB) adaptive sampling approaches. Our approach works well independently of the camera position, while keeping consistent the number of samples selected from the area light source. Images were generated for the Raptor model using a  $1024^2$  shadow map resolution.

<b>Model</b>	<b>Method</b>	<b>Shadow Map Resolution</b>		
		$512^2$	$1024^2$	$2048^2$
Armadillo (Figure 6.3)	Uniform Sampling	350 ms	360 ms	380 ms
	Adaptive Sampling	175 ms	100 ms	95 ms
	RB Adaptive Sampling	95 ms	80 ms	80 ms
	PCSS	5.3 ms	5.4 ms	5.5 ms
YeahRight (Figure 6.4)	Uniform Sampling	1.4s	1.4 s	1.4 s
	Adaptive Sampling	1.5 s	770 ms	950 ms
	RB Adaptive Sampling	340 ms	495 ms	620 ms
	PCSS	11.2 ms	11.3 ms	11.7 ms
QuadBot (Figure 6.5)	Uniform Sampling	800 ms	820 ms	830 ms
	Adaptive Sampling	950 ms	840 ms	610 ms
	RB Adaptive Sampling	380 ms	385 ms	400 ms
	PCSS	7.4 ms	7.5 ms	7.6 ms

**Table 6.1** Rendering times for different sampling strategies measured for different scenes rendered at an output  $720p$  resolution. Measurements include varying shadow map resolution.

<b>Model</b>	<b>Method</b>	<b>Output Resolution</b>		
		<i>480p</i>	<i>720p</i>	<i>1080p</i>
Armadillo (Figure 6.3)	Uniform Sampling	360 ms	360 ms	360 ms
	Adaptive Sampling	50 ms	100 ms	270 ms
	RB Adaptive Sampling	70 ms	80 ms	250 ms
	PCSS	3.7 ms	5.4 ms	8.1 ms
YeahRight (Figure 6.4)	Uniform Sampling	1.4 s	1.4 s	1.4 s
	Adaptive Sampling	280 ms	770 ms	1.6 s
	RB Adaptive Sampling	180 ms	495 ms	850 ms
	PCSS	10 ms	11.3 ms	14.4 ms
QuadBot (Figure 6.5)	Uniform Sampling	800 ms	820 ms	830 ms
	Adaptive Sampling	220 ms	840 ms	1 s
	RB Adaptive Sampling	130 ms	385 ms	680 ms
	PCSS	6 ms	7.5 ms	10.2 ms

**Table 6.2** Rendering times for different sampling strategies measured for different scenes rendered at an  $1024^2$  shadow map resolution. Measurements include varying output resolution.

approach (*e.g.*, discontinuity map rendering, light source refinement) are more sensitive to output resolution changes, since the calculations are done for even more fragments in the camera view.

#### 6.2.4 Limitations

Since we compute accurate soft shadows on the basis of shadow maps, we may suffer from subsampling artifacts if a low-resolution shadow map is used to generate the soft shadows. An example of those artifacts can be seen in Figure 6.8-(a), in the region pointed by the red arrows. As shown in Figure 6.8-(b), these artifacts can be minimized by increasing the shadow map resolution.

Subsampling artifacts may be caused not only because of the shadow map resolution, but also because of the light source sampling itself. If a few samples have inadequately been selected from the light source, fine details of the shadow silhouette may be lost because of the shadow overestimation caused by the blurring of the shadow silhouette. This kind of blurring happens when RPCF (Figure 6.2-(b)) is used as a visibility function to compute the soft shadows. As we discuss in Section 6.1.1, we reduce this problem by defining a refinement criteria that generate the appropriate number of samples according to the presence of banding artifacts in the final rendering.

The proposed adaptive approach can be extended for colored textured area light sources as well. Rather than using the samples located at the corners of the area light source, one must rearrange the samples to the center of the sub-quads, and use those samples to access the colored texture. Also, since an adaptive, sparse representation of the area light source may be sampled by the algorithm, one must take this fact into consideration when sampling the colored information of the light source. Indeed, instead of retrieving the actual color of the texture for the sample position, the level of the

Model	Step	Shadow Map Resolution		
		512 <sup>2</sup>	1024 <sup>2</sup>	2048 <sup>2</sup>
Armadillo (Figure 6.3)	G-Buffer Rendering	2.9 ms	2.9 ms	2.9 ms
	Shadow Map Rendering	49.6 ms	42.2 ms	42.5 ms
	Discontinuity Map Rendering	8.3 ms	6.1 ms	6.1 ms
	Light Source Refinement (First Pass)	7.7 ms	7.0 ms	7.0 ms
	Light Source Refinement (Second Pass)	2.5 ms	1.9 ms	1.6 ms
	Final Rendering	24.0 ms	19.9 ms	19.9 ms
	<b>Total</b>	<b>95 ms</b>	<b>80 ms</b>	<b>80 ms</b>
YeahRight (Figure 6.4)	G-Buffer Rendering	5.9 ms	5.9 ms	5.9 ms
	Shadow Map Rendering	243 ms	351 ms	443 ms
	Discontinuity Map Rendering	12.3 ms	17.9 ms	21.0 ms
	Light Source Refinement (First Pass)	12.3 ms	18.9 ms	21.0 ms
	Light Source Refinement (Second Pass)	3.4 ms	5.7 ms	6.5 ms
	Final Rendering	63.1 ms	95.6 ms	122.6 ms
	<b>Total</b>	<b>340 ms</b>	<b>495 ms</b>	<b>620 ms</b>
QuadBot (Figure 6.5)	G-Buffer Rendering	4.5 ms	4.5 ms	4.5 ms
	Shadow Map Rendering	234 ms	243 ms	256 ms
	Discontinuity Map Rendering	17.8 ms	18.8 ms	18.2 ms
	Light Source Refinement (First Pass)	18.4 ms	18.8 ms	19.9 ms
	Light Source Refinement (Second Pass)	5.0 ms	6.0 ms	5.1 ms
	Final Rendering	100.3 ms	93.9 ms	96.3 ms
	<b>Total</b>	<b>380 ms</b>	<b>385 ms</b>	<b>400 ms</b>

**Table 6.3** Rendering times for each step of the proposed approach, namely G-buffer, shadow map and discontinuity map rendering, first and second passes of the light source refinement, and the final accurate soft shadow rendering. Times were measured for some scenes shown in the chapter rendered at a 720p output resolution. Times include varying shadow map resolution.

sample in the adaptive structure can be used as an index to access the appropriate level of a mip-mapped version of the texture. Unfortunately, since the light source refinement criteria do not take into account the color information of the light source to generate new samples, one can lose the details of the texture if a few samples are selected from the light source.

In this work, we have proposed an adaptive sampling approach assuming that the area light source consists of a rectangular, planar shape. Therefore, the use of an adaptive structure where the light source is subdivided into quads is well suited for our purposes. To use our approach for more complex, non-rectangular, planar area light source shapes, one would need to fit a bounding box over the area of the light source, and then proceed with the light source refinement, testing whether the select samples are in the area light source surface.

As already stated in Section 6.2.2, our approach is slower than the uniform sampling strategy when using the same number of light source samples for accurate shadow rendering. Since our approach is view dependent, this scenario may occur if a large part of

Model	Step	Output Resolution		
		480p	720p	1080p
Armadillo (Figure 6.3)	G-Buffer Rendering	2.1 ms	2.9 ms	3 ms
	Shadow Map Rendering	41.4 ms	42.2 ms	141.1 ms
	Discontinuity Map Rendering	4.7 ms	6.1 ms	34.5 ms
	Light Source Refinement (First Pass)	4.2 ms	7.0 ms	36.6 ms
	Light Source Refinement (Second Pass)	1.5 ms	1.9 ms	9.6 ms
	Final Rendering	16.1 ms	19.9 ms	25.2 ms
<b>Total</b>		<b>70 ms</b>	<b>80 ms</b>	<b>250 ms</b>
YeahRight (Figure 6.4)	G-Buffer Rendering	5.9 ms	5.9 ms	5.9 ms
	Shadow Map Rendering	136.5 ms	351 ms	460 ms
	Discontinuity Map Rendering	5.6 ms	17.9 ms	35.6 ms
	Light Source Refinement (First Pass)	4.6 ms	18.9 ms	46.2 ms
	Light Source Refinement (Second Pass)	1.8 ms	5.7 ms	9.1 ms
	Final Rendering	25.6 ms	95.6 ms	293.2 ms
<b>Total</b>		<b>180 ms</b>	<b>495 ms</b>	<b>850 ms</b>
QuadBot (Figure 6.5)	G-Buffer Rendering	4.1 ms	4.5 ms	5.1 ms
	Shadow Map Rendering	86.6 ms	243 ms	311.5 ms
	Discontinuity Map Rendering	5.3 ms	18.8 ms	36.8 ms
	Light Source Refinement (First Pass)	4.5 ms	18.8 ms	44.2 ms
	Light Source Refinement (Second Pass)	1.6 ms	6.0 ms	9.4 ms
	Final Rendering	27.9 ms	93.9 ms	273 ms
<b>Total</b>		<b>130 ms</b>	<b>385 ms</b>	<b>680 ms</b>

**Table 6.4** Rendering times for each step of the proposed approach, namely G-buffer, shadow map and discontinuity map rendering, first and second passes of the light source refinement, and the final accurate soft shadow rendering. Times were measured for some scenes shown in the chapter rendered at an  $1024^2$  shadow map resolution. Times include varying output resolution.

the penumbra fills the camera view. On the other hand, as we show in Section 6.2.3, our approach is able to generate shadows visually similar to the ones obtained by uniform sampling, using much less samples if the camera is relatively distant to the penumbra region.

In terms of performance, although we have proposed a temporally coherent solution for adaptive sampling, we still cannot guarantee constant, stable frame rate because the number of samples may vary between frames, according to camera and light source movements. Such a limitation is common for adaptive sampling strategies (SCHWARZLER et al., 2012). Even in this case, as shown in Figure 6.7, we provide results more stable than related work. Also, we could not achieve real-time frame rates with our adaptive sampling approach, obtaining at least interactive frame rates for most of the scene configurations evaluated.

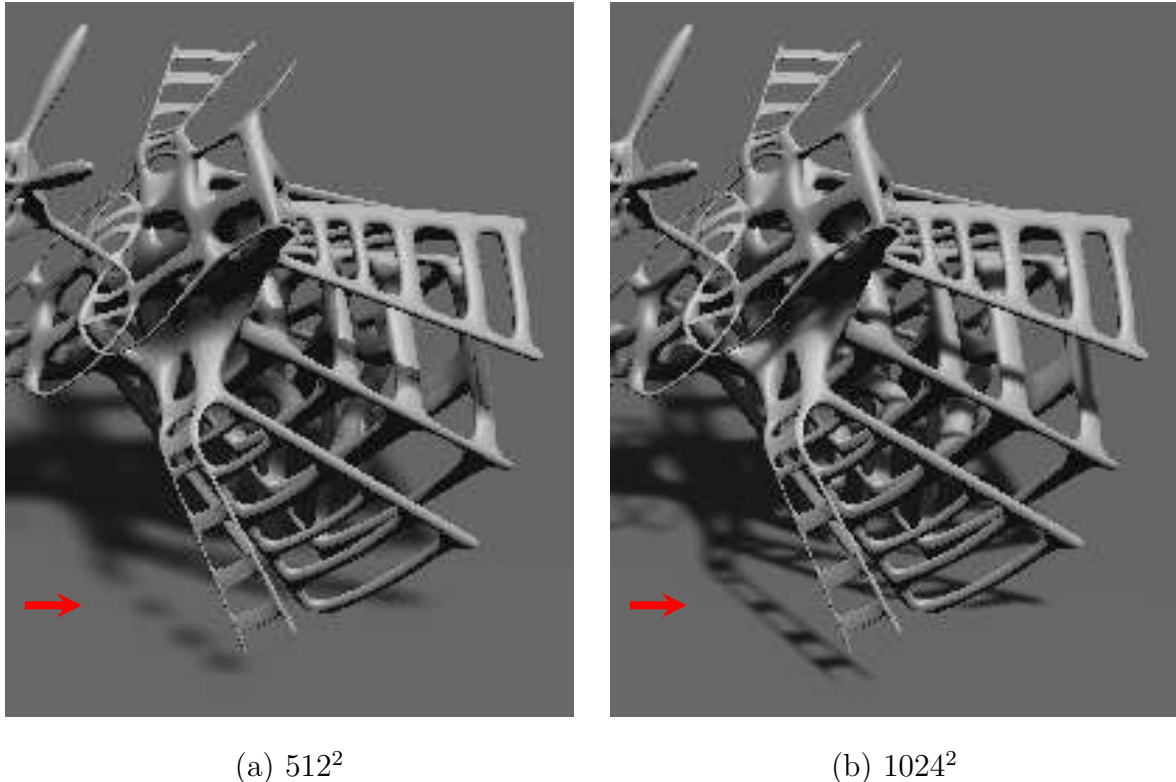


**Figure 6.8** For a low-resolution shadow map (a), fine details (pointed by red arrows) of the shadow silhouette (b) may not be captured by our algorithm. Images were generated for the YeahRight model using  $512^2$  (a) and  $1024^2$  (b) shadow map resolutions.

### 6.3 SUMMARY

In this chapter, we have presented a new soft shadow technique that uses the theory behind RBSM to guide the adaptive sampling of an area light source. By computing shadow and discontinuity maps for every point light source sampled from the area light source, we could define a view-dependent refinement criteria that detect whether the selected samples are sufficient for the generation of visually accurate soft shadows, free from banding artifacts. Also, we could define an optimization strategy by means of a visibility map to restrict the costly shadow computation for penumbra fragments only.

By using dozens or hundreds of point light sources for shadow rendering, we produced accurate soft shadows at interactive frame rates, being generally faster than other sampling strategies.

Nevertheless, to simplify the validation of the proposed technique, we have restricted our experimental setup to handle rectangular, single-colored area light sources. We believe that the theory shown in this chapter can be extended for non-rectangular, multi-colored area light sources as well.

*In this chapter, we present our final considerations about the developed work.*

## CONCLUDING REMARKS

### 7.1 CONCLUSION

In this thesis, we have extensively shown the practical uses of the concept of shadow revectorization to provide anti-aliasing for four types of shadows, namely hard shadows, filtered hard shadows, visually plausible soft shadows, and accurate soft shadows.

The main advantage that makes the shadow revectorization highly attractive for games and other interactive applications is that it adds a really small overhead (of less than one millisecond for the hardware setup used) to the shadow mapping technique, while providing a superior visual quality by the reduction of the aliasing artifacts. Another practical advantage that may increase the interest of developers in this technique relies on its easiness of implementation. We could see that in practice, when implementing it on the Unity 3D, a game engine that provides a limited source code access for developers. Without relying on the use of additional textures or modified shadow map representations, Revectorization-based Shadow Mapping (RBSM) requires the very same inputs as shadow mapping, being easier to be integrated into existing game engines and industrial applications than related work.

Another practical outcome of this thesis is the proposition of shadow rendering techniques that simulate the penumbra effect on the basis of an Euclidean Distance Transform (EDT). Although real-world, accurate soft shadows cannot be easily modelled in terms of EDT, we have shown that the integration of this kind of distance transform into the shadow revectorization pipeline allows the simulation of the smooth intensity transition present in fixed- and variable-size penumbra, while providing scalability in terms of shadow filtering and achieving processing time compatible with previous work.

Not only hard and filtered hard shadows, but also visually plausible soft shadows are prone to aliasing artifacts, mainly at contact borders and low-sized penumbra. In this case, by integrating the shadow revectorization into the popular framework of the Percentage Closer Soft Shadows (PCSS) technique, we could minimize this problem efficiently. Moreover, to further improve the performance of the proposed solution, we have

shown that this technique can take advantage of the screen space to achieve scalability in terms of shadow filtering, while keeping almost the same visual quality of the original approach. In this sense, we have proposed novel techniques that can replace the widely used PCSS, generating shadows with improved performance, reduced aliasing and light leaking artifacts.

Finally, we showed that even the field of accurate soft shadow rendering can benefit from the use of the shadow revectorization to guide the adaptive sampling of the area light source. We could see that, since the shadow revectorization technique provides improved accuracy than shadow mapping, one could select about two times less point light source samples of the area light source to produce a soft shadow that resembles the one obtained with shadow mapping. The use of a visibility map allowed us to further improve the performance of our proposal by restricting the hard shadow revectorization to the fragments located in penumbra, hence generating accurate soft shadows at interactive speed.

We have shown that the shadow revectorization provides high-quality anti-aliasing in real time, reducing light leaking artifacts and producing shadows that outperform state-of-the-art methods in terms of visual quality and/or processing time mainly for low-resolution shadow maps. By providing consistent, real-time frame rates, we believe that shadow revectorization is useful for every application in which perspective aliasing is still visible due to the use of insufficient shadow map resolution or inadequate kernel sizes for filtering.

## 7.2 FUTURE WORK

In terms of hard shadow rendering, hybrid approaches that incorporate the use of additional geometric information (such as (LECOCQ et al., 2014)) into the shadow revectorization visibility function may be useful to improve the robustness of both techniques, at the cost of more memory consumption for the final solution. Also, we have not tested our approach with partitioning strategies, such as cascaded shadow mapping (ENGEL, 2006). We believe that the integration and evaluation of the shadow revectorization pipeline into a partitioning technique is useful to further leverage the benefits and drawbacks of the anti-aliasing provided by shadow revectorization for large-scale scenarios.

With respect to filtered hard shadow rendering, Euclidean Distance Transform Shadow Mapping (EDTSM) is faster than Revectorization-based Percentage-Closer Filtering (RPCF), but is slightly slower than previous work because the EDT computation is the costly step of EDTSM, even though we make use of the fastest solution proposed so far for EDT computation. Hence, a suggestion for future work is the proposition of a faster, less accurate EDT computation to speed up EDTSM. Another option for future work is the extension of EDTSM to compute accurate soft shadows.

In the field of visually plausible soft shadow rendering, inspired by the solution proposed in (SCHWARZLER et al., 2013), temporal coherence could be exploited to reuse some soft shadow calculations per frame, further improving the performance of the revectorization-based soft shadow techniques. Another possibility for future work is the proposition of a hybrid approach that uses Revectorization-based Soft Shadow Mapping

(RBSSM) whenever visual quality is the priority for the scene rendering, and Euclidean Distance Transform Soft Shadow Mapping (EDTSSM) or Screen-Space Revectorization-based Soft Shadow Mapping (SSRBSSM) whenever performance is a priority or RBSSM would be too costly to perform soft shadow rendering. Finally, the integration of the proposed soft shadow techniques in the context of a game engine would allow the evaluation of all revectorization-based approaches in industrial applications, such as games.

For accurate soft shadow rendering, one could investigate more efficient ways to solve the problem of accurate soft shadow computation for textured and non-planar area light sources. Also, inspired by the solution proposed in (MARRS; WATSON; HEALEY, 2017), one could propose a hybrid approach that uses optimized multi-view rendering to reduce the computational cost of the shadow map rendering and adaptive area light source sampling to reduce the cost of the soft shadow rendering.

We have not tested the accuracy of the proposed techniques for a scenario with multiple light sources. In this topic, one could investigate, for instance, whether the use of Euclidean distance transform produces visually plausible results when simulating penumbra regions generated by multiple light sources.



## BIBLIOGRAPHY

- AGRAWALA, M. et al. Efficient Image-based Methods for Rendering Soft Shadows. In: *Proceedings of the ACM SIGGRAPH*. New York, NY, USA: ACM Press/Addison-Wesley Publishing Co., 2000. p. 375–384. ISBN 1-58113-208-5.
- AILA, T.; LAINE, S. Alias-Free Shadow Maps. In: *Proceedings of the EGSR*. Aire-la-Ville, Switzerland, Switzerland: Eurographics Association, 2004. p. 161–166. ISBN 3-905673-12-6.
- AKENINE-MOLLER, T.; ASSARSSON, U. Approximate Soft Shadows on Arbitrary Surfaces Using Penumbra Wedges. In: *Proceedings of the EGRW*. Aire-la-Ville, Switzerland, Switzerland: Eurographics Association, 2002. p. 297–306. ISBN 1-58113-534-3.
- ANNEN, T. et al. Real-time, All-frequency Shadows in Dynamic Scenes. *ACM Trans. Graph.*, ACM, New York, NY, USA, v. 27, n. 3, p. 1–8, ago. 2008. ISSN 0730-0301.
- ANNEN, T. et al. Convolution Shadow Maps. In: KAUTZ, J.; PATTANAIK, S. (Ed.). *Proceedings of the EGSR*. Aire-la-Ville, Switzerland: The Eurographics Association, 2007. p. 51–60. ISBN 978-3-905673-52-4. ISSN 1727-3463.
- ANNEN, T. et al. Exponential Shadow Maps. In: *Proceedings of GI*. Toronto, Ont., Canada: Canadian Information Processing Society, 2008. p. 155–161. ISBN 978-1-56881-423-0.
- ARVO, J. Tiled Shadow Maps. In: *Proceedings of the CGI*. Washington, DC, USA: IEEE Computer Society, 2004. p. 240–247. ISBN 0-7695-2171-1.
- ASSARSSON, U.; AKENINE-MOLLER, T. A Geometry-based Soft Shadow Volume Algorithm Using Graphics Hardware. *ACM Trans. Graph.*, ACM, New York, NY, USA, v. 22, n. 3, p. 511–520, jul. 2003. ISSN 0730-0301.
- ASSARSSON, U. et al. An Optimized Soft Shadow Volume Algorithm with Real-time Performance. In: *Proceedings of the ACM HWWS*. Aire-la-Ville, Switzerland, Switzerland: Eurographics Association, 2003. p. 33–40. ISBN 1-58113-739-7.
- ASZODI, B.; SZIRMAY-KALOS, L. Real-time Soft Shadows with Shadow Accumulation. In: FELLNER, D.; HANSEN, C. (Ed.). *Eurographics Short Papers*. Aire-la-Ville, Switzerland: The Eurographics Association, 2006. p. 53–56.
- ATTY, L. et al. Soft Shadow Maps: Efficient Sampling of Light Source Visibility. *Computer Graphics Forum*, v. 25, n. 4, p. 725–741, dec 2006.

- BARTZ, D.; MEIBNER, M.; HUTTNER, T. Extending Graphics Hardware For Occlusion Queries In OpenGL. In: SPENCER, S. N. (Ed.). *Proceedings of the EGCGH*. Aire-la-Ville, Switzerland: The Eurographics Association, 1998. ISBN 0-89791-097-X. ISSN 1727-3471.
- BAVOIL, L.; CALLAHAN, S. P.; SILVA, C. T. Robust Soft Shadow Mapping with Backprojection and Depth Peeling. *J. Graphics Tools*, v. 13, n. 1, p. 19–30, 2008.
- BILLEN, N.; DUTRÉ, P. Line Sampling for Direct Illumination. *Computer Graphics Forum*, Wiley-Blackwell, v. 35, n. 4, July 2016.
- BONDAREV, V. Shadow Map Silhouette Revectorization. In: *Proceedings of the ACM I3D*. New York, NY, USA: ACM, 2014. p. 162–162.
- BRABEC, S.; ANNEN, T.; SEIDEL, H.-P. Practical Shadow Mapping. *Journal of Graphics Tools*, v. 7, n. 4, p. 9–18, 2002.
- BROTMAN, L. S.; BADLER, N. I. Generating Soft Shadows with a Depth Buffer Algorithm. *IEEE Computer Graphics and Applications*, v. 4, n. 10, p. 5–14, Oct 1984. ISSN 0272-1716.
- BUADES, J. M.; GUMBAU, J.; CHOVER, M. Separable Soft Shadow Mapping. *The Visual Computer*, v. 32, n. 2, p. 167–178, 2015. ISSN 1432-2315.
- CAO, T.-T. et al. Parallel Banding Algorithm to Compute Exact Distance Transform with the GPU. In: *Proceedings of the ACM I3D*. New York, NY, USA: ACM, 2010. p. 83–90. ISBN 978-1-60558-939-8.
- CERQUEIRA, R. et al. A Novel GPU-based Sonar Simulator for Real-time Applications. *Computers & Graphics*, v. 68, n. Supplement C, p. 66 – 76, 2017. ISSN 0097-8493.
- CHAN, E.; DURAND, F. An Efficient Hybrid Shadow Rendering Algorithm. In: *Proceedings of the EGSR*. Aire-la-Ville, Switzerland: Eurographics Association, 2004. p. 185–195.
- CHEN, X. et al. Ballistic Shadow Art. In: *Proceedings of the GI*. Waterloo, Ontario, Canada: Canadian Human-Computer Communications Society, 2017. p. 190–198. ISBN 978-0-9947868-2-1.
- CHI, J.; SUN, T. Development drivers: Third-party engines and mobile gaming. *McKinsey & Company*, February 2015.
- CHONG, H. Y.; GORTLER, S. J. A Lixel for Every Pixel. In: *Proceedings of the EGSR*. Aire-la-Ville, Switzerland: Eurographics Association, 2004. p. 167–172. ISBN 3-905673-12-6.
- CHONG, H. Y.; GORTLER, S. J. *Scene Optimized Shadow Mapping*. Harvard Computer Science Technical Report: TR-07-07. Cambridge, MA, USA, 2007. 1-8 p.

- CHRISTENSEN, P. H. et al. Ray Tracing for the Movie ‘Cars’. In: *Proceedings of the IEEE Symposium on Interactive Ray Tracing*. [S.l.: s.n.], 2006. p. 1–6.
- COOK, R. L. Stochastic Sampling in Computer Graphics. *ACM Trans. Graph.*, ACM, New York, NY, USA, v. 5, n. 1, p. 51–72, jan. 1986. ISSN 0730-0301.
- COOK, R. L.; PORTER, T.; CARPENTER, L. Distributed Ray Tracing. In: *Proceedings of the ACM SIGGRAPH*. New York, NY, USA: ACM, 1984. p. 137–145. ISBN 0-89791-138-5.
- CROW, F. C. Shadow Algorithms for Computer Graphics. In: *Proceedings of the ACM SIGGRAPH*. New York, NY, USA: ACM, 1977. p. 242–248.
- CROW, F. C. Summed-area Tables for Texture Mapping. In: *Proceedings of the ACM SIGGRAPH*. New York, NY, USA: ACM, 1984. p. 207–212. ISBN 0-89791-138-5.
- DONG, Z.; YANG, B. Variance Soft Shadow Mapping. In: *Proceedings of the ACM I3D*. New York, NY, USA: ACM, 2010. p. 1–1. ISBN 978-1-60558-939-8.
- DONNELLY, W.; LAURITZEN, A. Variance Shadow Maps. In: *Proceedings of the ACM I3D*. New York, NY, USA: ACM, 2006. p. 161–165. ISBN 1-59593-295-X.
- DOU, H. et al. Adaptive Depth Bias for Shadow Maps. In: *Proceedings of the ACM I3D*. New York, NY, USA: ACM, 2014. p. 97–102. ISBN 978-1-4503-2717-6.
- DUTRE, P. et al. *Advanced Global Illumination*. Natick, MA, USA: AK Peters Ltd, 2006. ISBN 1568813074.
- EISEMANN, E. et al. *Real-Time Shadows*. Natick, MA, USA: A.K. Peters, 2011. 398 p. ISBN 978-1568814384.
- ENGEL, W. Cascaded Shadow Maps. In: *ShaderX 5.0 Advanced Rendering Techniques*. Hingham (Mass.): Charles River Media, 2006. p. 197–206.
- FERNANDO, R. Percentage-closer Soft Shadows. In: *ACM SIGGRAPH 2005 Sketches*. New York, NY, USA: ACM, 2005.
- FERNANDO, R. et al. Adaptive Shadow Maps. In: *Proceedings of the ACM SIGGRAPH*. New York, NY, USA: ACM, 2001. p. 387–390. ISBN 1-58113-374-X.
- FERNANDO, R.; KILGARD, M. J. *The Cg Tutorial: The Definitive Guide to Programmable Real-Time Graphics*. Boston, MA, USA: Addison-Wesley Longman Publishing Co., Inc., 2003. ISBN 0321194969.
- FOREST, V.; BARTHE, L.; PAULIN, M. Realistic Soft Shadows by Penumbra-wedges Blending. In: *Proceedings of the ACM Symposium on Graphics Hardware*. New York, NY, USA: ACM, 2006. p. 39–46. ISBN 3-905673-37-1.

- FRANKE, T. A. Delta Voxel Cone Tracing. In: *Proceedings of the IEEE ISMAR*. [S.l.: s.n.], 2014. p. 39–44.
- FRENCH, M. et al. The tech list. *Develop 100*, 2014.
- FUETTERLING, V. et al. Efficient Ray Tracing Kernels for Modern CPU Architectures. *Journal of Computer Graphics Techniques (JCGT)*, v. 4, n. 5, p. 90–111, December 2015. ISSN 2331-7418.
- GERHARDS, J. et al. Partitioned Shadow Volumes. *Computer Graphics Forum*, Blackwell Publishing Ltd, v. 34, n. 2, p. 549–559, 2015. ISSN 1467-8659.
- GIEGL, M.; WIMMER, M. Fitted Virtual Shadow Maps. In: *Proceedings of the GI*. New York, NY, USA: ACM, 2007. p. 159–168. ISBN 978-1-56881-337-0.
- GIEGL, M.; WIMMER, M. Queried Virtual Shadow Maps. In: *Proceedings of the ACM I3D*. New York, NY, USA: ACM, 2007. p. 65–72. ISBN 978-1-59593-628-8.
- GUENNEBAUD, G.; BARTHE, L.; PAULIN, M. Real-time Soft Shadow Mapping by Backprojection. In: *Proceedings of the EGSR*. Aire-la-Ville, Switzerland: Eurographics Association, 2006. p. 227–234. ISBN 3-905673-35-5.
- GUENNEBAUD, G.; BARTHE, L.; PAULIN, M. High-Quality Adaptive Soft Shadow Mapping. *Computer Graphics Forum*, Blackwell Publishing Ltd, v. 26, n. 3, p. 525–533, 2007. ISSN 1467-8659.
- GUMBAU, J. et al. Shadow Map Filtering with Gaussian Shadow Maps. In: *Proceedings of the ACM VRCAI*. New York, NY, USA: ACM, 2011. p. 75–82. ISBN 978-1-4503-1060-4.
- GUMBAU, J. et al. Smooth Shadow Boundaries with Exponentially Warped Gaussian Filtering. *Computers & Graphics*, v. 37, n. 3, p. 214 – 224, 2013. ISSN 0097-8493.
- HACHISUKA, T. et al. Multidimensional Adaptive Sampling and Reconstruction for Ray Tracing. *ACM Trans. Graph.*, ACM, New York, NY, USA, v. 27, n. 3, p. 33:1–33:10, ago. 2008. ISSN 0730-0301.
- HAEBERLI, P.; AKEYEY, K. The Accumulation Buffer: Hardware Support for High-quality Rendering. In: *Proceedings of the ACM SIGGRAPH*. New York, NY, USA: ACM, 1990. p. 309–318. ISBN 0-89791-344-2.
- HECKBERT, P. S.; HERF, M. *Simulating Soft Shadows with Graphics Hardware*. Pittsburgh, PA, USA, 1997.
- HEIDMANN, T. Real shadows, real time. *Iris Universe*, v. 18, p. 28–31, 1991.
- HEIDRICH, W.; BRABEC, S.; SEIDEL, H.-P. Soft Shadow Maps for Linear Lights. In: PÉROCHE, B.; RUSHMEIER, H. (Ed.). *Proceedings of the Workshop on Rendering Techniques*. Vienna: Springer Vienna, 2000. p. 269–280. ISBN 978-3-7091-6303-0.

- HERF, M. *Efficient Generation of Soft Shadow Textures*. Pittsburgh, PA, USA, 1997.
- HERF, M.; HECKBERT, P. S. Fast Soft Shadows. In: *Proceedings of the ACM SIGGRAPH*. New York, NY, USA: ACM, 1996. p. 145.
- HERTEL, S.; HORMANN, K.; WESTERMANN, R. A Hybrid GPU Rendering Pipeline for Alias-Free Hard Shadows. In: *Proceedings of Eurographics*. München, Germany: Eurographics Association, 2009. p. 59–66.
- HESSELINK, W. H.; ROERDINK, J. B. T. M. Euclidean Skeletons of Digital Image and Volume Data in Linear Time by the Integer Medial Axis Transform. *IEEE Transactions on Pattern Analysis and Machine Intelligence*, v. 30, n. 12, p. 2204–2217, 2008.
- IMMEL, D. S.; COHEN, M. F.; GREENBERG, D. P. A Radiosity Method for Non-diffuse Environments. In: *Proceedings of the ACM SIGGRAPH*. New York, NY, USA: ACM, 1986. p. 133–142. ISBN 0-89791-196-2.
- JIMENEZ, J. et al. Practical morphological anti-aliasing. In: ENGEL, W. (Ed.). *GPU Pro 2*. Natick, MA, USA: AK Peters Ltd., 2011. p. 95–113.
- JOHNSON, G. S. et al. The Irregular Z-buffer: Hardware Acceleration for Irregular Data Structures. *ACM Trans. Graph.*, v. 24, n. 4, p. 1462–1482, 2005.
- KAJIYA, J. T. The Rendering Equation. In: *Proceedings of the ACM SIGGRAPH*. New York, NY, USA: ACM, 1986. p. 143–150. ISBN 0-89791-196-2.
- KAMPE, V. et al. Fast, Memory-Efficient Construction of Voxelized Shadows. *IEEE Transactions on Visualization and Computer Graphics*, v. 22, n. 10, p. 2239–2248, 2016.
- KIRK, D. B.; HWU, W.-m. W. *Programming Massively Parallel Processors: A Hands-on Approach*. 2. ed. San Francisco, CA, USA: Morgan Kaufmann Publishers Inc., 2013. ISBN 9780123914187.
- KLEIN, A.; NISCHWITZ, A.; OBERMEIER, P. Contact Hardening Soft Shadows using Erosion. In: *Proceedings of the WSCG*. Pilsen: [s.n.], 2012.
- LAINÉ, S. et al. Soft Shadow Volumes for Ray Tracing. *ACM Transactions on Graphics*, ACM, New York, NY, USA, v. 24, n. 3, 2005.
- LAURITZEN, A. Summed-Area Variance Shadow Maps. In: NGUYEN, H. (Ed.). *GPU Gems 3*. [S.l.]: Addison-Wesley, 2008. p. 157–182.
- LAURITZEN, A.; MCCOOL, M. Layered Variance Shadow Maps. In: *Proceedings of the GI*. Toronto, Ont., Canada: Canadian Information Processing Society, 2008. p. 139–146. ISBN 978-1-56881-423-0.
- LAURITZEN, A.; SALVI, M.; LEFOHN, A. Sample Distribution Shadow Maps. In: *Proceedings of the ACM I3D*. New York, NY, USA: ACM, 2011. p. 97–102. ISBN 978-1-4503-0565-5.

- LAWSON, G.; SALANITRI, D.; WATERFIELD, B. Future directions for the development of virtual reality within an automotive manufacturer. *Applied Ergonomics*, v. 53, Part B, p. 323 – 330, 2016. ISSN 0003-6870.
- LECOQCQ, P. et al. Sub-pixel Shadow Mapping. In: *Proceedings of the ACM I3D*. New York, NY, USA: ACM, 2014. p. 103–110. ISBN 978-1-4503-2717-6.
- LEFOHN, A. E.; SENGUPTA, S.; OWENS, J. D. Resolution-matched Shadow Maps. *ACM Trans. Graph.*, ACM, New York, NY, USA, v. 26, n. 4, out. 2007. ISSN 0730-0301.
- LEHTINEN, J.; LAINE, S.; AILA, T. An Improved Physically-Based Soft Shadow Volume Algorithm. *Computer Graphics Forum*, Blackwell Publishing, Inc, v. 25, n. 3, p. 303–312, 2006.
- LIKTOR, G. et al. Stochastic Soft Shadow Mapping. In: *Proceedings of the EGSR*. Aire-la-Ville, Switzerland: Eurographics Association, 2015. p. 1–11.
- LLOYD, D. B. et al. Logarithmic Perspective Shadow Maps. *ACM Trans. Graph.*, ACM, New York, NY, USA, v. 27, n. 4, p. 106:1–106:32, nov. 2008. ISSN 0730-0301.
- MACEDO, M.; APOLINÁRIO, A. Revectorization-Based Shadow Mapping. In: *Proceedings of the GI*. School of Computer Science, University of Waterloo, Waterloo, Ontario, Canada: Canadian Human-Computer Communications Society, 2016. p. 75–83. ISBN 978-0-9947868-1-4.
- MACEDO, M.; APOLINÁRIO, A. Improved anti-aliasing for euclidean distance transform shadow mapping. *Computers & Graphics*, v. 71, p. 166 – 179, 2018. ISSN 0097-8493.
- MACEDO, M. C. F.; APOLINÁRIO, A. L. Euclidean Distance Transform Soft Shadow Mapping. In: *Proceedings of the SIBGRAPI*. [S.l.: s.n.], 2017. p. 238–245.
- MACEDO, M. C. F.; APOLINÁRIO, A. L.; AGÜERO, K. A. Optimized Visibility Functions for Revectorization-Based Shadow Mapping. *ArXiv e-prints*, nov. 2017.
- MACEDO, M. C. F.; APOLINÁRIO JR., A. L. Euclidean Distance Transform Shadow Mapping. In: *Proceedings of the GI*. School of Computer Science, University of Waterloo, Waterloo, Ontario, Canada: Canadian Human-Computer Communications Society, 2017. p. 171–180. ISBN 978-0-9947868-2-1.
- MACEDO, M. C. F.; APOLINÁRIO JR., A. L. Revectorization-Based Accurate Soft Shadow Using Adaptive Area Light Source Sampling. In: *Proceedings of the GI*. School of Computer Science, University of Waterloo, Waterloo, Ontario, Canada: Canadian Human-Computer Communications Society, 2017. p. 181–189. ISBN 978-0-9947868-2-1.
- MACEDO, M. C. F. et al. Hard Shadow Anti-Aliasing for Spot Lights in a Game Engine. In: *Proceedings of the SBGAMES*. [S.l.: s.n.], 2017.

- MARRS, A.; WATSON, B.; HEALEY, C. G. Real-Time View Independent Rasterization for Multi-View Rendering. In: *Proceedings of the EUROGRAPHICS*. Lyon, France: Eurographics Association, 2017. v. 36, n. 2, p. 17–20.
- MARTIN, T.; TAN, T.-S. Anti-aliasing and Continuity with Trapezoidal Shadow Maps. In: *Proceedings of the EGSR*. Aire-la-Ville, Switzerland: Eurographics Association, 2004. p. 153–160. ISBN 3-905673-12-6.
- MCCOOL, M. D. Shadow Volume Reconstruction from Depth Maps. *ACM Trans. Graph.*, ACM, New York, NY, USA, v. 19, n. 1, p. 1–26, jan. 2000. ISSN 0730-0301.
- MCGUIRE, M. Efficient Shadow Volume Rendering. In: FERNANDO, R. (Ed.). *GPU Gems*. [S.l.]: Addison-Wesley, 2004. p. 137–166.
- MEHTA, S. U.; WANG, B.; RAMAMOORTHI, R. Axis-aligned Filtering for Interactive Sampled Soft Shadows. *ACM Trans. Graph.*, ACM, New York, NY, USA, v. 31, n. 6, p. 163:1–163:10, nov. 2012. ISSN 0730-0301.
- MITCHELL, D. P. Consequences of Stratified Sampling in Graphics. In: *Proceedings of the ACM SIGGRAPH*. New York, NY, USA: ACM, 1996. p. 277–280. ISBN 0-89791-746-4.
- MITRA, N. J.; PAULY, M. Shadow Art. *ACM Trans. Graph.*, ACM, New York, NY, USA, v. 28, n. 5, p. 156:1–156:7, dez. 2009. ISSN 0730-0301.
- MOHAMMADBAGHER, M. et al. Screen-space Percentage-Closer Soft Shadows. In: *ACM SIGGRAPH 2010 Posters*. New York, NY, USA: ACM, 2010. p. 133–133. ISBN 978-1-4503-0393-4.
- MORA, F. et al. Lazy Visibility Evaluation for Exact Soft Shadows. *Computer Graphics Forum*, Blackwell Publishing Ltd, v. 31, n. 1, p. 132–145, 2012. ISSN 1467-8659.
- MORA, F. et al. Deep Partitioned Shadow Volumes using Stackless and Hybrid Traversals. In: *Proceedings of the EGSR*. Goslar Germany, Germany: The Eurographics Association, 2016. p. 73–83. ISBN 978-3-03868-019-2.
- MORGAN, G.; PRANKEVICIUS, A. Practical Techniques for Ray Tracing in Games. In: *GDC Vault*. [S.l.: s.n.], 2014.
- NOWROUZEZAHRAI, D. et al. Light Factorization for Mixed-frequency Shadows in Augmented Reality. In: *Proceedings of the IEEE ISMAR*. [S.l.: s.n.], 2011. p. 173–179.
- OUELLETTE, M. J.; FIUME, E. On Numerical Solutions to One-dimensional Integration Problems with Applications to Linear Light Sources. *ACM Trans. Graph.*, ACM, New York, NY, USA, v. 20, n. 4, p. 232–279, out. 2001. ISSN 0730-0301.
- PAN, M. et al. Fast, Sub-pixel Antialiased Shadow Maps. *Computer Graphics Forum*, Blackwell Publishing Ltd, v. 28, n. 7, p. 1927–1934, 2009. ISSN 1467-8659.

- PARKER, S. G. et al. OptiX: A General Purpose Ray Tracing Engine. *ACM Trans. Graph.*, ACM, New York, NY, USA, v. 29, n. 4, p. 66:1–66:13, jul. 2010. ISSN 0730-0301.
- PERARD-GAYOT, A.; KALOJANOV, J.; SLUSALLEK, P. GPU Ray Tracing using Irregular Grids. *Computer Graphics Forum*, The Eurographics Association and John Wiley & Sons Ltd., v. 36, n. 2, 2017. ISSN 1467-8659.
- PETERS, C. Non-linearly Quantized Moment Shadow Maps. In: *Proceedings of the HPG*. New York, NY, USA: ACM, 2017. p. 15:1–15:11. ISBN 978-1-4503-5101-0.
- PETERS, C.; KLEIN, R. Moment Shadow Mapping. In: *Proceedings of the ACM I3D*. New York, NY, USA: ACM, 2015. p. 7–14. ISBN 978-1-4503-3392-4.
- PETERS, C. et al. Beyond Hard Shadows: Moment Shadow Maps for Single Scattering, Soft Shadows and Translucent Occluders. In: *Proceedings of the ACM I3D*. New York, NY, USA: ACM, 2016. p. 159–170. ISBN 978-1-4503-4043-4/16/03.
- PETERS, C. et al. Improved Moment Shadow Maps for Translucent Occluders, Soft Shadows and Single Scattering. *Journal of Computer Graphics Techniques (JCGT)*, v. 6, n. 1, p. 17–67, March 2017.
- PHAM, T.; VLIET, L. van. Separable Bilateral Filtering for Fast Video Preprocessing. In: *Proceedings of the IEEE ICME*. [S.l.: s.n.], 2005.
- PILLEBOUE, A. et al. Variance Analysis for Monte Carlo Integration. *ACM Trans. Graph.*, ACM, New York, NY, USA, v. 34, n. 4, p. 124:1–124:14, 2015.
- RAMAMOORTHI, R. et al. A Theory of Monte Carlo Visibility Sampling. *ACM Trans. Graph.*, ACM, New York, NY, USA, v. 31, n. 5, p. 121:1–121:16, set. 2012. ISSN 0730-0301.
- REEVES, W. T.; SALESIN, D. H.; COOK, R. L. Rendering Antialiased Shadows with Depth Maps. In: *Proceedings of the ACM SIGGRAPH*. New York, NY, USA: ACM, 1987. p. 283–291. ISBN 0-89791-227-6.
- RONG, G.; TAN, T.-S. Jump Flooding in GPU with Applications to Voronoi Diagram and Distance Transform. In: *Proceedings of the ACM I3D*. New York, NY, USA: ACM, 2006. p. 109–116. ISBN 1-59593-295-X.
- ROST, R. J. et al. *OpenGL Shading Language*. 3rd. ed. [S.l.]: Addison-Wesley Professional, 2009. ISBN 0321637631, 9780321637635.
- SAITO, T.; TAKAHASHI, T. Comprehensible Rendering of 3-D Shapes. In: *Proceedings of the ACM SIGGRAPH*. New York, NY, USA: ACM, 1990. p. 197–206. ISBN 0-89791-344-2.
- SALVI, M. Rendering Filtered Shadows With Exponential Shadow Maps. In: *ShaderX 6.0 Advanced Rendering Techniques*. Hingham (Mass.): Charles River Media, 2008. p. 257–274.

- SCANDOLO, L.; BAUSZAT, P.; EISEMANN, E. Compressed Multiresolution Hierarchies for High-quality Precomputed Shadows. In: *Proceedings of the EUROGRAPHICS*. Goslar Germany, Germany: Eurographics Association, 2016. p. 331–340.
- SCANDOLO, L.; BAUSZAT, P.; EISEMANN, E. Merged Multiresolution Hierarchies for Shadow Map Compression. *Computer Graphics Forum*, v. 35, n. 7, p. 383–390, 2016.
- SCHERZER, D.; SCHWARZLER, M.; MATTAUSCH, O. Fast Soft Shadows with Temporal Coherence. In: ENGEL, W. (Ed.). *GPU Pro 2*. [S.l.]: A.K. Peters, 2011. ISBN 978-1568817187.
- SCHERZER, D. et al. Real-Time Soft Shadows Using Temporal Coherence. In: *Proceedings of the ISVC*. [S.l.: s.n.], 2009. (Lecture Notes in Computer Science), p. 13–24.
- SCHMIDT, T.-W. et al. State of the Art in Artistic Editing of Appearance, Lighting and Material. *Computer Graphics Forum*, v. 35, n. 1, p. 216–233, 2016. ISSN 1467-8659.
- SCHNEIDER, J.; KRAUS, M.; WESTERMANN, R. GPU-based real-time discrete euclidean distance transforms with precise error bounds. In: *Proceedings of the VISAPP*. [S.l.: s.n.], 2009. p. 435–442.
- SCHWARZ, M.; STAMMINGER, M. Bitmask Soft Shadows. *Computer Graphics Forum*, Blackwell Publishing Ltd, v. 26, n. 3, p. 515–524, 2007. ISSN 1467-8659.
- SCHWARZLER, M. et al. Fast Percentage Closer Soft Shadows Using Temporal Coherence. In: *Proceedings of the ACM I3D*. New York, NY, USA: ACM, 2013. p. 79–86. ISBN 978-1-4503-1956-0.
- SCHWARZLER, M. et al. Fast Accurate Soft Shadows with Adaptive Light Source Sampling. In: *Proceedings of the VMV*. Aire-la-Ville, Switzerland: Eurographics Association, 2012. p. 39–46. ISBN 978-3-905673-95-1.
- SELGRAD, K. et al. Filtering Multi-Layer Shadow Maps for Accurate Soft Shadows. *Computer Graphics Forum*, v. 34, n. 1, p. 205–215, 2015. ISSN 1467-8659.
- SEN, P.; CAMMARANO, M.; HANRAHAN, P. Shadow Silhouette Maps. *ACM Trans. Graph.*, v. 22, n. 3, p. 521–526, jul. 2003.
- SHEN, L.; FENG, J.; YANG, B. Exponential Soft Shadow Mapping. *Computer Graphics Forum*, Blackwell Publishing Ltd, v. 32, n. 4, p. 107–116, 2013. ISSN 1467-8659.
- SHEN, L. et al. Predicted Virtual Soft Shadow Maps with High Quality Filtering. *Computer Graphics Forum*, Blackwell Publishing Ltd, v. 30, n. 2, p. 493–502, 2011. ISSN 1467-8659.
- SHREINER, D. et al. *OpenGL Programming Guide: The Official Guide to Learning OpenGL, Version 4.3*. 8th. ed. [S.l.]: Addison-Wesley Professional, 2013. ISBN 0321773039, 9780321773036.

- SINTORN, E.; EISEMANN, E.; ASSARSSON, U. Sample Based Visibility for Soft Shadows Using Alias-free Shadow Maps. In: *Proceedings of the EGSR*. Aire-la-Ville, Switzerland, Switzerland: Eurographics Association, 2008. p. 1285–1292.
- SINTORN, E. et al. Compact Precomputed Voxelized Shadows. *ACM Trans. Graph.*, v. 33, n. 4, p. 150:1–150:8, 2014.
- SOLER, C.; SILLION, F. X. Fast Calculation of Soft Shadow Textures Using Convolution. In: *Proceedings of the ACM SIGGRAPH*. New York, NY, USA: ACM, 1998. p. 321–332. ISBN 0-89791-999-8.
- ST-AMOUR, J.-F.; PAQUETTE, E.; POULIN, P. Soft Shadows from Extended Light Sources with Penumbra Deep Shadow Maps. In: *Proceedings of the GI*. Toronto, Ont., Canada: Canadian Information Processing Society, 2005. p. 105–112.
- STAMMINGER, M.; DRETTAKIS, G. Perspective Shadow Maps. *ACM Trans. Graph.*, ACM, New York, NY, USA, v. 21, n. 3, p. 557–562, jul. 2002. ISSN 0730-0301.
- STORY, J.; WYMAN, C. HFTS: Hybrid Frustum-traced Shadows in "the Division". In: *Proceedings of the ACM SIGGRAPH Talks*. New York, NY, USA: ACM, 2016. p. 13:1–13:2. ISBN 978-1-4503-4282-7.
- WALD, I. et al. Embree: A Kernel Framework for Efficient CPU Ray Tracing. *ACM Trans. Graph.*, ACM, New York, NY, USA, v. 33, n. 4, p. 143:1–143:8, jul. 2014. ISSN 0730-0301.
- WANG, J.; TAN, Y. Efficient euclidean distance transform algorithm of binary images in arbitrary dimensions. *Pattern Recognition*, v. 46, n. 1, p. 230 – 242, 2013.
- WANG, L. et al. GEARS: A General and Efficient Algorithm for Rendering Shadows. *Computer Graphics Forum*, v. 33, n. 6, p. 264–275, 2014. ISSN 1467-8659.
- WEI, L.-Y. Parallel Poisson Disk Sampling. *ACM Trans. Graph.*, ACM, New York, NY, USA, v. 27, n. 3, p. 1–9, ago. 2008. ISSN 0730-0301.
- WHITTED, T. An Improved Illumination Model for Shaded Display. *Commun. ACM*, ACM, New York, NY, USA, v. 23, n. 6, p. 343–349, jun. 1980. ISSN 0001-0782.
- WILLIAMS, L. Casting Curved Shadows on Curved Surfaces. In: *Proceedings of the ACM SIGGRAPH*. New York, NY, USA: ACM, 1978. p. 270–274.
- WIMMER, M.; SCHERZER, D.; PURGATHOFER, W. Light Space Perspective Shadow Maps. In: KELLER, A.; JENSEN, H. W. (Ed.). *Proceedings of the EGSR*. Aire-la-Ville, Switzerland: Eurographics Association, 2004. p. 143–151. ISBN 3-905673-12-6.
- WON, J.; LEE, J. Shadow Theatre: Discovering Human Motion from a Sequence of Silhouettes. *ACM Trans. Graph.*, ACM, New York, NY, USA, 2016.

- WOO, A.; POULIN, P. *Shadow Algorithms Data Miner*. Natick, MA, USA: CRC Press, 2012. 268 p. ISBN 978-1439880234.
- WRIGHT, M. W.; CIPOLLA, R.; GIBLIN, P. J. Skeletonization using an extended Euclidean distance transform. *Image and Vision Computing*, v. 13, n. 5, p. 367 – 375, 1995.
- WYMAN, C.; HOETZLEIN, R.; LEFOHN, A. Frustum-traced Raster Shadows: Revisiting Irregular Z-buffers. In: *Proceedings of the ACM I3D*. New York, NY, USA: ACM, 2015. p. 15–23. ISBN 978-1-4503-3392-4.
- XIE, F.; TABELLION, E.; PEARCE, A. Soft Shadows by Ray Tracing Multilayer Transparent Shadow Maps. In: *Proceedings of the EGSR*. Aire-la-Ville, Switzerland: Eurographics Association, 2007. p. 265–276. ISBN 978-3-905673-52-4.
- YANG, B. et al. Variance Soft Shadow Mapping. *Computer Graphics Forum*, Blackwell Publishing Ltd, v. 29, n. 7, p. 2127–2134, 2010.
- YANG, B. et al. Packet-based Hierarchical Soft Shadow Mapping. In: *Proceedings of the EGSR*. Aire-la-Ville, Switzerland: Eurographics Association, 2009. p. 1121–1130.
- ZHANG, F.; SUN, H.; NYMAN, O. Parallel-Split Shadow Maps on Programmable GPUs. In: NGUYEN, H. (Ed.). *GPU Gems 3*. [S.l.]: Addison-Wesley, 2008. p. 203–237.
- ZHANG, F. et al. Parallel-split Shadow Maps for Large-scale Virtual Environments. In: *Proceedings of the ACM VRCIA*. New York, NY, USA: ACM, 2006. p. 311–318. ISBN 1-59593-324-7.
- ZHENG, Z.; SAITO, S. Screen Space Anisotropic Blurred Soft Shadows. In: *ACM SIGGRAPH 2011 Posters*. New York, NY, USA: ACM, 2011. p. 75–75. ISBN 978-1-4503-0971-4.



## Appendix

# A

*In this appendix, an implementation of the conservative RBSM for OpenGL Shading Language (GLSL) is shown.*

## REVECTORIZATION-BASED SHADOW MAPPING SOURCE CODE FOR GLSL

### A.1 OVERVIEW

Conservative Revectorization-based Shadow Mapping (RBSM) aims to locate shadow silhouette patterns in the scene and to use the available screen-space resolution provided by the camera view to perform shadow anti-aliasing through the revectorization effect.

The first step of RBSM consists in an evaluation of the shadow test (3.2) (Lines 9-12 of Listing A.1) for each fragment  $\tilde{p}$  projected in the **light space**. Then, the technique evaluates the difference of shadow test results between neighbour shadow map texels (3.3) (Lines 16-17 of Listing A.1). The goal of this step is to detect where the shadow aliasing is located. This step is performed only for lit fragments (Lines 13-14 of Listing A.1) because the conservative RBSM aims to minimize shadow aliasing by working over the lit-side of the shadow silhouette. Hence, since shadowed fragments will remain in shadow after the revectorization, they are discarded from the additional computation required by RBSM. After the evaluation of the spatial coherency between neighbour shadow tests, the algorithm is able to detect the directions of where the shadow aliasing is located.

For each fragment inside a shadow silhouette (Lines 18-19 of Listing A.1), the algorithm performs a traversal over the shadow silhouette in order to compute the size of the shadow silhouette, as well as the relative distance and position of each fragment with respect to the end of the shadow silhouette (Lines 23-24 of Listing A.1). To do so, the sub-coordinates of each fragment in the corresponding shadow map texels (3.1) must be computed beforehand (Lines 21-22 of Listing A.1). Next, the algorithm normalizes the relative distance of each fragment to the shadow silhouette (3.5) (Lines 25-26 of Listing A.1) and determines whether a fragment must be shadowed by RBSM (3.6) (Lines 27-28 of Listing A.1).

```

1 uniform sampler2D shadowMap; //Shadow map texture
2 uniform int shadowMapWidth; //Shadow map width
3 uniform int shadowMapHeight; //Shadow map height
4 uniform int shadowIntensity; //Shadow intensity
5
6 float RBSM(vec4 p)
7 {
8
9     //Retrieve the depth of the blocker of p
10    float z = texture2D(shadowMap, p.xy).z;
11    //Compute the shadow test
12    float shadow = (p.z <= z) ? 1.0 : 0.0;
13    //Discard p if it is in shadow
14    if(shadow == 0.0) return shadowIntensity;
15
16    //Compute the discontinuity
17    vec4 d = computeDiscontinuity(p);
18    //Discard p if it is lit and out of the shadow silhouette
19    if((d.r + d.g + d.b + d.a) == 0.0) return 1.0;
20
21    //Estimate p's sub-coordinates in light space
22    vec2 c = fract(vec2(p.x * shadowMapWidth, p.y * shadowMapHeight));
23    //Compute the relative distance of p to the shadow silhouette
24    vec4 dist = computeRelativeDistance(p, c);
25    //Normalize the relative distance to the unit interval
26    vec2 r = normalizeRelativeDistance(dist);
27    //Revectorize the shadow silhouette
28    return revectorizeShadow(r);
29
30 }

```

**Listing A.1** GLSL code for conservative RBSM implementation.

## A.2 SHADOW SILHOUETTE LOCALIZATION

Shadow silhouettes are detected according to the difference between the illumination condition of neighbour shadow map texels (Listing A.2).

Given the shadow test defined in (3.2), the first step to detect shadow silhouettes consists on the computation of (3.2) to determine the illumination condition of each fragment visible in the scene (Lines 9-10 of Listing A.1). Then, the difference between shadow tests of the current fragment and its 4-connected neighbours in the shadow map is estimated as defined in (3.3) (Lines 3-28 of Listing A.2). With the computation of (3.3), we are able to detect where the shadow silhouettes are located and discard non-silhouette fragments from further shadow computations (Lines 18-19 of Listing A.1).

## A.3 SHADOW SILHOUETTE TRAVERSAL

For every fragment inside a shadow silhouette, we need to search the ends of the shadow silhouette in order to estimate the size of the aliased shadow silhouette, as well as the

```

1 uniform vec2 shadowMapStep; //Shadow map step size
2
3 vec4 computeDiscontinuity(vec4 p)
4 {
5
6     vec4 dir = vec4(0.0, 0.0, 0.0, 0.0);
7     //x = left; y = right; z = bottom; w = top
8
9     //Perform the shadow test for the 4-connected neighbourhood
10    p.x -= shadowMapStep.x;
11    float z = texture2D(shadowMap, p.xy).z;
12    dir.x = (p.z <= z) ? 1.0 : 0.0;
13
14    p.x += 2.0 * shadowMapStep.x;
15    z = texture2D(shadowMap, p.xy).z;
16    dir.y = (p.z <= z) ? 1.0 : 0.0;
17
18    p.x -= shadowMapStep.x;
19    p.y += shadowMapStep.y;
20    z = texture2D(shadowMap, p.xy).z;
21    dir.z = (p.z <= z) ? 1.0 : 0.0;
22
23    p.y -= 2.0 * shadowMapStep.y;
24    z = texture2D(shadowMap, p.xy).z;
25    dir.w = (p.z <= z) ? 1.0 : 0.0;
26
27     //Return the absolute difference of neighbour shadow tests
28     return abs(dir - 1.0);
29
30 }
```

**Listing A.2** GLSL code for discontinuity computation.

relative distance of the fragment to the end of the shadow silhouette. This search is done in all the four directions of the 2D space (*i.e.*, left, right, top and bottom directions), such that we can estimate the 2D relative position of the fragment in the shadow silhouette (Lines 3-12 of Listing A.3). The shadow silhouette traversal algorithm for each direction of the 2D space is implemented in Lines 14-54 of Listing A.3.

For each shadow map neighbour of a given fragment (Lines 17, 26-27 of Listing A.3), RBSM computes the shadow test for the neighbour (Lines 28-32 of Listing A.3) and detects whether the shadow test result of the neighbour is different from the one estimated for the given fragment (Lines 33-34 of Listing A.3). In this case, since conservative RBSM operates over lit fragments, a shadowed fragment has been detected. Therefore, we have detected the end of the shadow silhouette and we end the traversal in the particular direction (Lines 35-37 of Listing A.3). On the other hand, if the shadow test is the same between neighbour shadow map texels (Lines 38-39 of Listing A.3), we need to check if the neighbour shadow map texel is still located in the shadow silhouette (Lines 40-41 of Listing A.3). If that is not the case, the traversal must be ended (Lines 42-44 of Listing

A.3).

To limit the extent of the shadow silhouette traversal, we define a variable **maxSize** that defines the maximum size of the shadow silhouette (Line 1 of Listing A.3). This variable is only used to improve the temporal consistency of the algorithm. Using **maxSize** = 16 was sufficient for our tests.

As a result of the shadow silhouette traversal, the algorithm returns the distance of the fragment to the end of the shadow silhouette (Lines 50-54 of Listing A.3).

## A.4 SHADOW SILHOUETTE NORMALIZATION

After the computation of the distance of each fragment to the shadow silhouette, we need to normalize such value to the unit interval, as already described in Chapter 3.

As can be seen in Listing A.4, we compute both (3.4) and (3.5) in the function **computeRelativeDistance** (Lines 1-10 of Listing A.4).

## A.5 CONSERVATIVE RBSM VISIBILITY FUNCTION

As we show in Listing A.5, a few lines of GLSL are required to implement the visibility function proposed for conservative RBSM.

In practice, the function takes as input the normalized relative position previously estimated and performs two linear comparisons to determine whether a fragment must be put in the shadowed region of the new revectorized shadow.

## A.6 SUMMARY

In this appendix, we have shown a practical implementation of conservative RBSM using the popular GLSL. By providing the implementation details of conservative RBSM, we believe that one can easily implement the other techniques shown in this thesis, such as non-conservative RBSM, Revectorization-based Percentage-Closer Filtering (RPCF) and the others. The reference full implementation of RBSM for GLSL is available in a public repository<sup>1</sup>

---

<sup>1</sup><https://github.com/MarcioCerqueira/GlobalIllumination/tree/master/ShadowMapping>

```

1 uniform int maxSize; //Maximum shadow silhouette size
2
3 vec4 computeRelativeDistance(vec4 p, vec2 c)
4 {
5
6     float dl = computeRelativeDistance(p, vec2(-1, 0), (1.0 - c.x));
7     float dr = computeRelativeDistance(p, vec2(1, 0), c.x);
8     float db = computeRelativeDistance(p, vec2(0, -1), (1.0 - c.y));
9     float dt = computeRelativeDistance(p, vec2(0, 1), c.y);
10    return vec4(dl, dr, db, dt);
11
12 }
13
14 float computeRelativeDistance(vec4 p, vec2 dir, float c)
15 {
16
17     vec4 np = p;
18     float foundSilhouetteEnd = 0.0;
19     float distance = 0.0;
20     //Compute the step of traversal for current direction
21     vec2 step = dir * shadowMapStep;
22
23     //Iteratively traverse the shadow silhouette
24     for(int it = 0; it < maxSize; it++) {
25
26         //Access the neighbour of p
27         np.xy += step;
28         //Retrieve the depth of the blocker of np
29         float z = texture2D(shadowMap, np.xy).z;
30         //Determine the visibility of np
31         float center = (np.z <= z) ? 1.0 : 0.0;
32         bool isCenterUmbra = !bool(center);
33         //When the visibility of p and np is different
34         if(isCenterUmbra) {
35             //End the traversal
36             foundSilhouetteEnd = 1.0;
37             break;
38         //When the visibility of p and np is equal
39         } else {
40             //Check if np has any discontinuity direction
41             vec4 d = computeDiscontinuity(np);
42             //Else, end the traversal
43             if((d.r + d.g + d.b + d.a) == 0.0) break;
44         }
45         //Increase the distance
46         distance++;
47     }
48
49     //Take into account p's sub-coordinates for distance estimation
50     distance = distance + (1.0 - c);
51     return mix(-distance, distance, foundSilhouetteEnd);
52
53 }
54

```

Listing A.3 GLSL code for shadow silhouette traversal.

```

1 float normalizeRelativeDistance(vec2 dist) {
2
3     float T = 1;
4     if(dist.x < 0.0 && dist.y < 0.0) T = 0;
5     if(dist.x > 0.0 && dist.y > 0.0) T = -2;
6
7     float length = min(abs(dist.x) + abs(dist.y), float(maxSize));
8     return abs(max(T * dist.x, T * dist.y))/length;
9
10 }
11
12 vec2 normalizeRelativeDistance(vec4 dist)
13 {
14
15     vec2 r;
16     r.x = normalizeRelativeDistance(vec2(dist.x, dist.y));
17     r.y = normalizeRelativeDistance(vec2(dist.z, dist.w));
18     return r;
19
20 }
```

**Listing A.4** GLSL code for relative position normalization.

```

1 float revectorizeShadow(vec2 r)
2 {
3
4     if((r.x * r.y > 0) && (1.0 - r.x > r.y)) return shadowIntensity;
5     else return 1.0;
6
7 }
```

**Listing A.5** GLSL code for conservative revectorization.

## Appendix

# B

*In this appendix, we discuss how popular game engines give support to shadow rendering and present a practical implementation of conservative RBSM into one of them.*

## REVECTORIZATION-BASED SHADOW MAPPING SOURCE CODE FOR UNITY

Real-time shadow rendering is desirable in several computer graphics applications, such as games. The most popular game engines typically provide support to this feature through the traditional shadow mapping algorithm. Unfortunately, shadow mapping is well known to generate aliasing artifacts along the shadow silhouette, decreasing the realism of the rendered virtual scenes. In this appendix, we present an implementation of the most basic conservative Revectorization-based Shadow Mapping (RBSM) for hard shadow anti-aliasing in a game engine. Even with the limited source code access provided by some game engines, we demonstrate how to implement an improvement of the shadow mapping technique for shadow anti-aliasing. We have chosen to implement our approach for spot lights in a commercial and popular game engine, the Unity 3D.

### B.1 SHADOWS IN GAME ENGINES

Unity 3D Engine<sup>1</sup> uses shadow mapping to generate shadows for spot and point light sources. For directional light sources, cascaded shadow maps (ENGEL, 2006) take advantage of the partitioning strategy (Section 2.3.2) to reduce aliasing artifacts. Area light sources are supported for the Unity Pro version and require precomputed lighting conditions of the scene. Although not natively supported, shadow volumes are available as a free plugin for older versions of Unity in the Unity Asset Store<sup>2</sup>. While these techniques may work well for some scenarios, the main problem with Unity is that both free and professional versions of the engine give limited source code access for developers (the entire source code is available through an additional payment for Unity Pro users). Hence, it is difficult for one to implement its own improvements in the shadow algorithms using the available source code.

---

<sup>1</sup><https://unity3d.com>

<sup>2</sup><https://www.assetstore.unity3d.com/en/content/1861>

Name	Type	Description
<code>_ShadowMapTexture</code>	internal	Shadow map
<code>_ShadowMapTexture_TexelSize</code>	float4	Shadow map texel size / Shadow map resolution
<code>shadowCoord</code>	float4	Coordinates to access the shadow map for a given fragment
<code>_LightShadowData</code>	float4	Shadow intensity (or shadow strength, in Unity)

**Table B.1** List of variables available in Unity for shadow mapping with spot lights.

Similarly to Unity, CryEngine<sup>3</sup> and Unreal Engine<sup>4</sup> support shadow mapping for point and spot light sources, cascaded shadow maps for directional lights and ray tracing for static scenes. Additionally, Unreal Engine supports an original technique called ray traced distance field soft shadows, which improves the visual quality of the cascaded shadow maps, further reducing the aliasing artifacts, but increasing processing time.

Although it is not formally defined as a game engine, NVIDIA GameWorks<sup>5</sup> is a sample development kit that provides support for several real-time shadow techniques into the NVIDIA ShadowWorks<sup>6</sup> and advanced ray tracing solutions via NVIDIA OptiX (PARKER et al., 2010). NVIDIA GameWorks is open-source, has already been integrated into the Unreal Engine<sup>7</sup> and is extensible to work with Unity Pro<sup>8</sup>.

Unity is the most used game engine for mobile gaming (CHI; SUN, 2015), is the second game engine most recommended by industry experts (FRENCH et al., 2014) and is also one the most popular game engines for general game production, having more than 770 millions of users over the world<sup>9</sup>. However, even with this huge popularity, Unity still produces shadows with aliasing artifacts that are mostly visible in shadows rendered from point or spot light sources. Therefore, we present an implementation of conservative RBSM that uses the available source code access in the popular Unity game engine to improve the visual quality of the hard shadows generated from spot lights.

## B.2 SHADOWS IN UNITY

Unity uses the shadow mapping as a basis to compute shadows generated from directional, point and spot light sources.

Directional light sources try to mimic the behaviour of distant light sources (*e.g.*, the sun) by emitting parallel light rays in a single, dominant direction to illuminate large outdoor scenes. Since these light sources are defined by their directions, rather than their positions, a shadow map is rendered using orthographic projection to keep the light rays

---

<sup>3</sup><https://www.cryengine.com/>

<sup>4</sup><https://www.unrealengine.com/>

<sup>5</sup><https://developer.nvidia.com/gameworks>

<sup>6</sup><https://developer.nvidia.com/shadowworks>

<sup>7</sup><https://developer.nvidia.com/nvidia-gameworks-and-ue4>

<sup>8</sup><https://developer.nvidia.com/content/gameworks-unity>

<sup>9</sup><https://unity3d.com/pt/public-relations>

Name	Input	Output	Description
<b>UNITY_DECLARE_SHADOWMAP</b>	internal _ShadowMapTexture	void	Declares the shadow map as _ShadowMapTexture
<b>SAMPLE_DEPTH_TEXTURE_PROJ</b>	internal _ShadowMapTexture and float2 shadowCoord	float	Returns the depth stored in the shadow map for a given texel
<b>UNITY_SAMPLE_SHADOW_PROJ</b>	internal _ShadowMapTexture and float4 shadowCoord	float	Returns the shadow test for a given fragment

**Table B.2** List of functions available in Unity for shadow mapping with spot lights.

parallel to each other. For large-scale scenes, a single shadow map is mostly insufficient to compute accurate shadows. To solve this problem, Unity uses a variant of the shadow mapping, the cascaded shadow mapping (ENGEL, 2006), to partition the 3D space into several parts, and associate a shadow map for each one of them<sup>10</sup>. Cascaded shadow mapping enables high-quality shadow rendering for large scenarios, at the cost of more processing time. However, even when using this technique, aliasing artifacts still can be seen in the final rendering, due to the limited resolution of the multiple shadow maps rendered.

Differently from a directional light source, a point light source has a position and works like an infinitesimal sphere that emits light rays in all directions. From a lookup on the source code, we could see that Unity builds a cube map of shadow maps to compute the shadows generated by the occlusion of the light rays. To do so, the engine renders six shadow maps, one per face of the cube, and stores the shadow maps into the cube map. While being able to compute shadows for large scenes, shadow rendering with this type of light source is relatively expensive, since six shadow maps need to be generated by the algorithm.

Spot light sources have a position, a dominant direction and are able to simulate shadows for a limited extension of the scene. Hence, a single shadow map rendered using perspective projection is able to cover the part of the scene that is illuminated by the light source. While spot light sources are not well suited for outdoor illumination and produces aliasing artifacts along the shadow silhouette, they are able to simulate shadows efficiently, since only one shadow map must be rendered per light source.

In Unity, the source code that contains where the shadow maps are generated is private. Therefore, the techniques (*e.g.*, (SEN; CAMMARANO; HANRAHAN, 2003; DONNELLY; LAURITZEN, 2006; ANNEN et al., 2008; PAN et al., 2009; LECOCQ et al., 2014; PETERS; KLEIN, 2015)) that require a modification of the structure of the shadow map to provide shadow anti-aliasing cannot be implemented in the game engine without source code access. Also, directional and point light sources use an additional

---

<sup>10</sup><https://docs.unity3d.com/Manual/DirLightShadows.html>

```

1 fixed UnitySampleShadowmap (float4 shadowCoord)
2 {
3
4     half shadow = UNITY_SAMPLE_SHADOW_PROJ(_ShadowMapTexture,
5         shadowCoord);
6
7     if(shadow > 0.0) return 1.0;
8     else return _LightShadowData.r;
9
10 }
```

**Listing B.1** Shadow mapping for spot lights in Unity.

structure (a list of shadow maps for directional light sources, and a cube map for point light sources) to store the multiple shadow maps rendered. However, Unity does not give access to the individual shadow maps generated with those light sources. Instead, the engine encapsulates these structures into a variable named **\_ShadowMapTexture**, that simply returns whether a given fragment in the camera viewpoint is located in shadow, or the depth of the blocker of a given fragment. This imposes another restriction on the implementation of a shadow anti-aliasing technique, since most of the techniques proposed in the literature require the access per shadow map to provide shadow anti-aliasing. Fortunately, spot lights produce a single shadow map, that corresponds exactly to the **\_ShadowMapTexture** variable. That is why we have chosen to focus on the implementation of a shadow anti-aliasing technique for spot lights.

A list of the variables and functions provided by Unity for shadow mapping with spot lights is shown in Tables B.1 and B.2. An example of their usage to compute the aliased hard shadows is presented in Listing B.1. The source code for shadow rendering using spot lights is available in the **UnitySampleShadowmap** method in the shader file **UnityShadowLibrary.cginc** of Unity. Basically, the **UnitySampleShadowmap** method receives as input the coordinates of the fragment rendered from the camera viewpoint, but projected on the shadow map (Line 1), uses that coordinates to access the shadow map texture **\_ShadowMapTexture** and compute the shadow test using the **UNITY\_SAMPLE\_SHADOW\_PROJ** method (Lines 4-5). Then, depending on whether the fragment is in shadow, the method returns 1.0, indicating full visibility of the fragment (Line 7) or **\_LightShadowData.r**, an intensity value accounting that the fragment is shadowed (Line 8).

### B.3 REVECTORIZATION-BASED SHADOW MAPPING IN UNITY

In Listing B.2, we show the main pipeline of the conservative RBSM implementation. First, we evaluate the shadow test for a given fragment to detect whether the fragment is shadowed or lit (Line 4-5). Conservative RBSM operates only on the lit fragments located in the aliased shadow silhouette (Line 6). Hence, for each lit fragment, we compute the offset value to access the next shadow map sample, that is equivalent to a product between **shadowCoord.w** and the value stored in the first two coordinates of

```

1 fixed UnitySampleShadowmap (float4 shadowCoord)
2 {
3
4     half shadow = UNITY_SAMPLE_SHADOW_PROJ(_ShadowMapTexture ,
5         shadowCoord);
6     if(shadow == 0) return _LightShadowData.r;
7
8     float2 shadowMapStep = float2(_ShadowMapTexture_TexelSize.x,
9         _ShadowMapTexture_TexelSize.y) * shadowCoord.w;
10    float4 d = computeDiscontinuity(shadowCoord, shadowMapStep);
11    if((d.r + d.g + d.b + d.a) == 0.0) return 1.0;
12
13    float maxSize = 16;
14    float2 c = computeSubCoordinates(shadowCoord);
15    float4 dist = computeRelativeDistance(shadowCoord, c,
16        shadowMapStep, maxSize);
17    float2 r = normalizeRelativeDistance(dist, maxSize);
18    return revectorizeShadow(r);
19
20 }
```

**Listing B.2** RBSM for spot lights in Unity.

**\_ShadowMapTexture\_TexelSize**, variable that returns the shadow map texel size in terms of width and height (Lines 8-9). Then, we evaluate the neighbour shadow map texels to compute the discontinuity directions where the aliased silhouette is located (Line 10). If an aliased silhouette has been detected (Line 11), we compute the sub-coordinates of the camera-view fragment into the shadow map (Line 14) and traverse the shadow silhouette to compute the size of the aliasing, as well as the relative distance of the fragment to the origin of the local aliasing (Lines 15-16). Next, we normalize such relative distance (Line 17) and define a visibility function to determine whether a fragment must be revectorized (Line 18). It is noteworthy that we use the variable **maxSize** to define the maximum aliasing size that we will consider for revectorization (Line 13). We define **maxSize** equals to 16 to keep the frame rate more constant.

In Listing B.3, we show how we detect whether a fragment is located in the aliased shadow silhouette. We compute the shadow test of the neighbours of each shadow map texel (3.2) by means of the **UNITY\_SAMPLE\_SHADOW\_PROJ** function (Lines 4-22). Then, in Line 24, we finally estimate the absolute difference of neighbour shadow tests (3.3). From Listing B.2 and (3.3), we know that a fragment is in the aliased shadow silhouette if at least one of the coordinates of the 4D vector **d** is greater than 0 (Line 11 in Listing B.2).

For each fragment located in the aliased shadow silhouette, we need to perform the shadow silhouette traversal to be able to revectorize the shadow silhouette. Before starting the shadow silhouette traversal, we need to compute the sub-coordinates of the fragment in the shadow map texel, as shown in Listing B.4. In this case, since the window size orientation of Unity is different from the one used by OpenGL Shading Language (GLSL), we had to change the way we computed (3.1) to keep both Unity and GLSL implemen-

```

1 float4 computeDiscontinuity(float4 shadowCoord, float2 shadowMapStep)
2 {
3
4     float4 dir = float4(0.0, 0.0, 0.0, 0.0);
5     //x = left; y = right; z = bottom; w = top
6
7     shadowCoord.x += shadowMapStep.x;
8     dir.x = UNITY_SAMPLE_SHADOW_PROJ(_ShadowMapTexture, shadowCoord);
9     dir.x = (dir.x > 0.0) ? 1.0 : 0.0;
10
11    shadowCoord.x -= 2.0 * shadowMapStep.x;
12    dir.y = UNITY_SAMPLE_SHADOW_PROJ(_ShadowMapTexture, shadowCoord);
13    dir.y = (dir.y > 0.0) ? 1.0 : 0.0;
14
15    shadowCoord.x += shadowMapStep.x;
16    shadowCoord.y -= shadowMapStep.y;
17    dir.z = UNITY_SAMPLE_SHADOW_PROJ(_ShadowMapTexture, shadowCoord);
18    dir.z = (dir.z > 0.0) ? 1.0 : 0.0;
19
20    shadowCoord.y += 2.0 * shadowMapStep.y;
21    dir.w = UNITY_SAMPLE_SHADOW_PROJ(_ShadowMapTexture, shadowCoord);
22    dir.w = (dir.w > 0.0) ? 1.0 : 0.0;
23
24    return abs(dir - 1.0);
25
26 }

```

**Listing B.3** Discontinuity direction estimation in Unity.

```

1 float2 computeSubCoordinates(float4 shadowCoord)
2 {
3
4     float2 c = float2(frac((1.0 - shadowCoord.x/shadowCoord.w) *
5         _ShadowMapTexture_TexelSize.z),
6         frac((1.0 - shadowCoord.y/shadowCoord.w) *
7             _ShadowMapTexture_TexelSize.w));
8     c.x = 1.0 - lerp(0.5 - c.x, (0.5 - c.x) + 1.0, step(0.5, c.x));
9     c.y = 1.0 - lerp(0.5 - c.y, (0.5 - c.y) + 1.0, step(0.5, c.y));
10    return c;
11
12 }
```

**Listing B.4** An algorithm to compute the sub-coordinates of a camera-view fragment in the light space in Unity.

tations using the same value.

The algorithm to compute the relative distances of the fragment to the ends of the shadow silhouette is shown in Listing B.5. RBSM computes the relative distance of the fragment with respect to the shadow silhouette to the four directions of the 2D space. For each direction (Lines 5-12), we perform the traversal over the shadow silhouette (Line 28). Then, for each shadow map texel being accessed, we check whether we step out of the lit side of the aliased silhouette. This condition is fulfilled whenever we step into an umbra texel (Lines 33-35) or step into a lit texel that does not have any discontinuity directions (*i.e.*, the texel is not neighbour of an umbra texel) (Lines 36-40). Otherwise, we increment the variable **distance** (Line 42) that represents the size of the aliasing. In Line 47, we add the sub-coordinates of the fragment into the distance previously computed to improve the accuracy of the distance computation. In Line 48, we use a linear interpolation to make the distance value signed, as already presented in Chapter 3.

To estimate the relative position  $\mathbf{r}$  in Listing B.6, we basically implement the equations (3.4) and (3.5). The same statement is held for the implementation of the conservative RBSM visibility function, that is implemented as shown in Listing B.7, following (3.6).

## B.4 SUMMARY

In this appendix, we have presented an implementation of conservative RBSM, for the Unity game engine. Since Unity uses the shadow mapping for shadow rendering, aliasing artifacts are generated along the shadow silhouette. As shown in Section 3.3, by the use of the proposed implementation of RBSM, we are able to minimize these aliasing artifacts, generating high-quality shadows at minimal additional cost.

Due to the limited source code access provided by Unity, we were not able to implement RBSM for other types of light source, such as point and directional light sources. Moreover, we could not implement RBSM for soft shadows that simulate the penumbra effect. The implementation of RBSM using the entire Unity source code, or the implementation in other game engines, may enable one to adapt the technique to support hard and soft shadow rendering for any light source. Finally, since NVIDIA GameWorks may

```

1 float4 computeRelativeDistance(float4 shadowCoord, float2 c,
2 float2 shadowMapStep, int maxSize)
3 {
4
5     float dl = computeRelativeDistance(shadowCoord, float2(1, 0),
6             (1.0 - c.x), shadowMapStep, maxSize);
7     float dr = computeRelativeDistance(shadowCoord, float2(-1, 0),
8             c.x, shadowMapStep, maxSize);
9     float db = computeRelativeDistance(shadowCoord, float2(0, 1),
10            (1.0 - c.y), shadowMapStep, maxSize);
11    float dt = computeRelativeDistance(shadowCoord, float2(0, -1),
12            c.y, shadowMapStep, maxSize);
13    if(db > 0 && dt > 0) dt = -dt;
14    return float4(dl, dr, db, dt);
15 }
16
17
18 float computeRelativeDistance(float4 shadowCoord, float2 dir, float c,
19 float2 shadowMapStep, int maxSize)
20 {
21
22     float4 tempShadowCoord = shadowCoord;
23     float foundSilhouetteEnd = 0.0;
24     float distance = 0.0;
25     float2 shadowMapDiscontinuityStep = dir * shadowMapStep;
26     tempShadowCoord.xy += shadowMapDiscontinuityStep;
27
28     for(int it = 0; it < maxSize; it++) {
29
30         float shadow = UNITY_SAMPLE_SHADOW_PROJ(_ShadowMapTexture,
31                                         tempShadowCoord);
32
33         if(shadow == 0.0) {
34             foundSilhouetteEnd = 1.0;
35             break;
36         } else {
37             float4 d = computeDiscontinuity(tempShadowCoord,
38                     shadowMapStep);
39             if((d.r + d.g + d.b + d.a) == 0.0) break;
40         }
41
42         distance++;
43         tempShadowCoord.xy += shadowMapDiscontinuityStep;
44     }
45
46     distance = distance + (1.0 - c);
47     return lerp(-distance, distance, foundSilhouetteEnd);
48
49 }
50 }
```

**Listing B.5** Computation of the relative position of a fragment inside a shadow silhouette in Unity.

```

1 float2 normalizeRelativeDistance(float4 dist, int maxSize)
2 {
3
4     float2 r = float2(0.0, 0.0);
5     r.x = normalizeRelativeDistance(float2(dist.x, dist.y), maxSize);
6     r.y = normalizeRelativeDistance(float2(dist.z, dist.w), maxSize);
7     return r;
8
9 }
10
11 float normalizeRelativeDistance(float2 dist, int maxSize) {
12
13     float T = 1;
14     if(dist.x < 0.0 && dist.y < 0.0) T = 0;
15     if(dist.x > 0.0 && dist.y > 0.0) T = -2;
16
17     float length = min(abs(dist.x) + abs(dist.y), float(maxSize));
18     return abs(max(T * dist.x, T * dist.y))/length;
19
20 }
```

**Listing B.6** Normalization of the relative position of a fragment inside a shadow silhouette in Unity.

```

1 float revectorizeShadow(float2 r)
2 {
3
4     if((r.x * r.y > 0) && (1.0 - r.x > r.y)) return _LightShadowData.r;
5     else return 1.0;
6
7 }
```

**Listing B.7** Conservative RBSM visibility function in Unity.

be used with Unity Pro, the field of shadows in game engines still needs a gentle introduction on how to integrate NVIDIA ShadowWorks with Unity Pro and an evaluation of the shadow techniques of NVIDIA ShadowWorks in the context of the Unity game engine.

The reference full implementation of RBSM for Unity is available in a public repository<sup>11</sup>

---

<sup>11</sup><https://github.com/MarcioCerdeira/GlobalIllumination/tree/master/RBSMInUnity>